Satyanarayana Kokkula

Bumper beam-longitudinal system subjected to offset impact loading

An experimental and numerical study

PhD Thesis
August 2005

Structural Impact Laboratory
Department of Structural Engineering
Norwegian University of Science and Technology
N-7491 Trondheim
Norway

Abstract

The present thesis describes an experimental and numerical study of a bumper beam-longitudinal system subjected to 40% offset impact, where longitudinals of two different alloys (AA7003 and AA6060) and two different tempers (T79 and T1) were varied along with the impact velocity. Two impact velocities 10 m/s (~36 km/h) and 15 m/s (~54 km/h) were used. The bumper beam chosen for the study was taken from the production line at Hydro Aluminium Structures (HAST), Norway, and was made out of the alloy AA7108-T6.

The experiments revealed that the robustness of the system was very dependent on the material used in the longitudinals. It was found that changing the temper condition of the longitudinals had significant influence on the collapse mode of the bumper beam-longitudinal system. The longitudinal members with considerable strain hardening had a tendency to develop lobes randomly along the length of the members. At increased impact velocity lower peak force and less fracture in the material was observed.

The numerical study was carried out with the non-linear finite element code LS-DYNA, searching for an efficient, numerically robust and accurate representation of the observed system behaviour. A comparative study of an industrial-like modelling procedure and another procedure incorporating a user-defined elasto-viscoplastic material model has been performed. The latter material model consist of state-of-the-art anisotropic plasticity, an isotropic strain and strain-rate hardening rule as well as some ductile fracture criteria, with the possibility of prescribing process dependent material characteristics.

For proper prediction of the crash performance of the bumper beam-longitudinal system, the FE-model of the bumper beam must rely upon a geometry generated from the forming simulations. Thus, forming simulations were performed to obtain a bumper beam model with required curvature, which included thickness changes.

Numerical crash results revealed good agreement with the experiments with respect to overall deformation mode and energy absorption level. The simulations predicted higher initial peaks in the force-deformation characteristics due to a different deformation mode of the longitudinal member. Thus, the number of lobes developed was less than in the experiments. However, the simulations were capable of giving relatively accurate prediction of the collapse mode found in the experimental tests, except for the bumper beam-longitudinal system with AA7003-T1 longitudinals. Application of adaptive meshing technique along with a fracture criterion helped in predicting similar fracture modes as in the tests for the bumper beam. Additional simulations were performed to investigate the influence of some key sensitivity parameters on the force level, deformation and fracture modes.

Finally, the process effects on material level were considered for the bumper beam to investigate the influence of forming history on the crash performance of the bumper beam-longitudinal system. For the present system it was found that inclusion of process effects has no influence on the crash performance.

Acknowledgements

I express my deep sense of gratitude with sincere acknowledgements to my supervisors Professor Magnus Langseth, Professor Odd Sture Hopperstad and Dr.ing. Odd-Geir Lademo for their invaluable guidance and encouragement throughout the study.

I am indebted to my fellow PhD students and colleagues at SIMLab for the enthusiastic discussions and creative working environment. Special thanks to Dr.ing. Torodd Berstad for assisting with the numerical simulations.

The experimental tests were carried out in the laboratories at the Department of Structural Engineering, NTNU. The assistance of the laboratory staff is highly acknowledged. Special credits are also given to Mr Trond Auestad, Mr Trygve Meltzer and Mr Tore Wisth for assisting with laboratory experiments. I am thankful to the institute administrators who are very keen to help.

The research was made possible by financial support from the Research Council of Norway, through the Strategic University Program “Design of Crashworthy Light Structures”, Renault, Fondation Franco-Norvégienne and Hydro Aluminium Structures.

I could able to produce this thesis because of the generous help of Professor Norman Jones, who forwarded my curriculum vitae to Professor Magnus Langseth. I salute Professor Jones with devotion always.

I am grateful to my brothers and sister, Gowri Murali family and other friends who have always supported me. I wish to thank my fellow Indians at Indian Students Forum. They have made the social life pleasurable.

Very special thanks goes to my wife, Kalpana, for her kind support and understanding especially in the last days of preparation of the thesis.

Finally, I wish to dedicate this dissertation to my parents for their constant encouragement and all the pains they were through while bringing me up to this level. The acknowledgement would not be completed without complimenting Dr. Narasimha Murthy Anishetty (Retired Senior Scientist, FAO, Italy) who elevated my career with his in time financial support.

August 2005 *Satyanarayana Kokkula*

Contents

Notations

s	engineering stress
s_u	ultimate engineering stress
s_f	engineering stress at fracture
T	axial load in tensile test
d_0	initial diameter
e	engineering strain
e_u	engineering strain corresponding to ultimate engineering stress
$\dot{e}$	engineering strain rate
e^e, e^p	elastic and plastic strains
A_0, A	undeformed and deformed (current) cross-section area
l_0, l	undeformed and deformed length
h_0, h	initial and final width
t_0	initial thickness
t	final thickness, also used as time see Equation (4.1)
V	volume
b	groove in Marciniak and Kuczynski instability theory
ω	orientation of groove angle (MK-theory)
a	homogeneous region (MK-theory)
ϕ_0	initial inhomogeneity factor (MK-theory)
e^a,e^b	thickness parameters (MK-theory)
σ	true (or Cauchy) stress
ε	true (or logarithmic) strain
$\boldsymbol{\varepsilon}$	strain tensor
$\boldsymbol{\varepsilon}^e$	elastic part of strain tensor
$\boldsymbol{\varepsilon}^p$	plastic part of strain tensor
$\boldsymbol{\sigma}$	stress tensor
$\mathbf{C}$	elastic moduli
f	yield function
$\bar{f}$	convex function
σ_0	reference yield stress
$Y(\bar{\varepsilon})$	strain-hardening variable
$\bar{\sigma}$	effective stress
$\bar{\varepsilon}$	accumulated plastic strain
Q_{Ri} , C_{Ri}	strain-hardening constants in Voce rule
$\dot{\lambda}$	plastic multiplier
$\dot{f}$	consistency condition

ψ	overstress function
η	material viscosity
$\dot{\bar{\varepsilon}}$	effective plastic strain-rate
$\dot{\varepsilon}_0$, C	material parameters for strain-rate hardening model
m	material constant in *Yld2003*
$\sigma_1, \sigma_2, \sigma_3$	principal stresses
σ_1', σ_2', σ_1'', σ_2''	principal stress transformations
G_α	flow stress in α-direction
*CFS, CFS**	critical fracture strain, isotropic and anisotropic
W_{cr}	critical specific "plastic work"
ε_{cr}	critical thickness strain
α	direction
$a_1, a_2, ..., a_8$	dimensionless anisotropy parameters in *Yld2003*
σ_{ref}	reference true stress
σ_α	true stress in α-direction
σ_2, σ_5, σ_8	true stress at 2%, 5%, 8% plastic strain
ε_x	true strain in x-direction
ε_y	true strain in y-direction
r_b	equibiaxial *r*-value
r_α	*r* in α-direction
t_t	termination time in four node element analysis (Section 3.6)
v_0	impact velocity of trolley
V_0	voltage signal from strain gauge
V	voltage output from amplifier
N	axial force in the loadcell
φ	a positive homogeneous function
K_N	axial stiffness in loadcell calibration
K_i	calibration constants
κ	curvature
M	bending moment
R_0	resistance of strain gauge
a_s	strain gauge area
l_s	length of strain gauge
ρ_R	resistivity of strain gauge
$P(t)$	total force-time history recorded by the loadcell
$F(t)$	impact force acting on test specimen
w	displacement of trolley
ς_f	rigid-body load factor
ξ_b	accuracy parameter
$E(w)$	energy absorbed
F_{avg}	mean force level

Chapter 1 Introduction

1.1 Background

Fuel economy and emission gas regulations are the primary concerns in changing over to the lightweight materials in automotive structures. Aluminium alloys are extensively used in various forms, such as extrusions and castings, due to its high strength to weight ratio. Because of the low density of aluminium compared to steel, a weight reduction of up to 300 kg is possible in a medium size vehicle (1400 kg) with the extensive use of aluminium. Thus in modern cars, aluminium alloys are employed in the front and rear bumper beams, crashboxes, longitudinals – in the extruded form, and also in other safety components such as side-door impact beams, frames, engine cradles, chassis and suspension components.

Although the use of lightweight materials helps in reducing fuel consumption and consequently lower carbon dioxide emissions, another stringent demand from the society is the passive safety obtained when employing lightweight materials. Thus the automotive industry has become increasingly more concerned about the safety of the passengers in a possible crash. To evaluate the crashworthiness of new cars, different programmes exist for example the NCAP (New Car Assessment Program). NCAP contains several standardized tests for new vehicles, where the damage to the occupants is evaluated through crash-test dummies and structural performance (Euro NCAP, 2002). Results from the NCAP tests are helping the motoring consumers to choose a crashworthy car. It is worth to note, however, conducting full-scale crash test of a car is always time consuming and expensive.

In fact, the automotive industry deals with a large variety of crash situations. The wide variety of accidents makes it desirable to consider them in groups with basic similarities. However, in practice exactly similar accidents might rarely occur. Figure 1-1 shows that the largest proportion of accidents, about 60%, occurs at the front of the vehicle and of these offset impacts are the most commonly seen accidental situations on roads, and they also give rise to the highest portion of deaths (Frank and Gruber, 1992). Oblique or side collisions are less frequent and serious in their effects, and rear impacts and "roll-overs" are relatively rare. Research has therefore concentrated mainly on front and side impacts, the former of which can be considered as the "typical" serious accident (Pugsley and Macaulay, 1978).

In a frontal or rear crash, the bumper beam is the primary component which undergoes damage and transfers the forces to the rest of the structure. Thus, the modern bumper beam systems should play a key part in the safety concept of an automobile, ensuring that minimal accelerations are transferred to the passenger. Further the automotive producers are demanding for robust bumper beam systems showing good and reproducible impact behaviour.

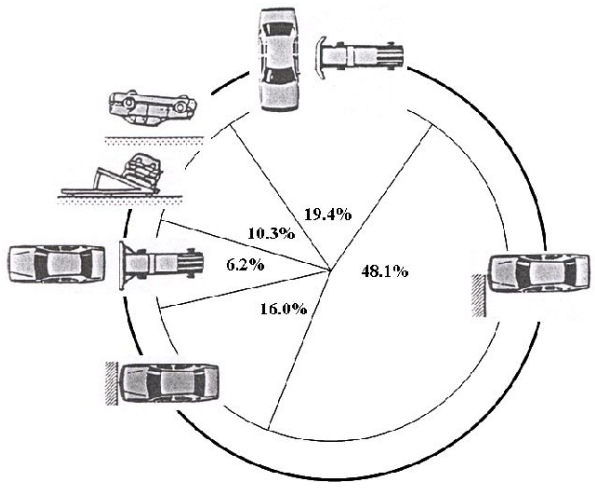

Figure 1-1 Distribution of real-world severe passenger car accidents by type of collision (Frank and Gruber, 1992).

Manufacturing of bumper beams from aluminium extrusions often involve series of forming operations performed in the soft W-temper condition, and then artificial age-hardening of the components to the material's peak hardness condition. Thus it is clear that for proper crash performance of the systems the FE-model must rely upon the geometry obtained from a simulation of the process route, i.e. including simulation of all major forming operations. Moreover, the forming operations also results in an inhomogeneous evolution of some internal variable (among others the effective plastic strain) within the shaped components. Lademo et al. (2004a) showed that plastic straining in W-temper results in significant change of the T6 work hardening curves. However, in industrial product development process effects on material are not included. Instead the homogeneous material properties of the final temper in its virgin/unformed state would be used even though the process effects may play a prominent role for the system's performance in a crash. Traditional industrial modelling procedures for the numerical analyses of bumper beam systems include the most widely used material models, i.e. MAT-24 and MAT-103, in LS-DYNA (Hallquist, 2003), but these models does not support any attempt at including process effects on the material. For the accuracy and robustness of the analyses in general it is, however, possible to include process effects in to the numerical analyses and to perform "process-based" crash simulation.

The industrially offered solutions are required to behave in a strictly controlled and robust manner in low to high velocity impacts and often the systems also include a crashbox situated in between the bumper beam and the longitudinal. The idea with this system design is that the bumper beam system should yield a specific function within different velocity regimes. At low velocity impacts up to 4 km/h the bumper beam system should absorb the impact energy entirely elastically, i.e. without any plastic deformation whatsoever. Up to 8 km/h the energy should be absorbed through plastic deformation confined to the bumper beam itself. Up to 15 km/h all the impact energy should be absorbed in the bumper beam and crashboxes

while as for higher impact velocity all components in the system should absorb an optimised part of the energy in interaction with connected units, thus contributing significantly to the safety of the vehicle's occupants. Further, zones within the system might be allowed for fracture, as long as the system does not disintegrate or deforms in a mode that reduces the energy absorption. A system is said to be "robust" if it results in the wanted controlled characteristics, even under presence of inevitable industrial variations in geometric and material properties, and also for some variations with respect to other parameters as for instance impact velocity and loading angle (Lademo et al., 2005).

The bumper beam system in this study consists of a bumper beam directly connected to a longitudinal at both ends, hereafter named a bumper beam-longitudinal system. That is, the system does not include any crashboxes. This is also the preferred system for some automotive producers, since a longitudinal will offer higher resistance to deformation, and thus give higher energy absorption than if crashboxes are used. Frontal offset crash testing has gained acceptance worldwide as an assessment of the frontal crashworthiness of vehicles. However, assessing the impact performance of bumper beam-longitudinal system through full-scale crash tests of a car is not easy as the view of the system is hidden. Thus, a separate study on the bumper beam-longitudinal system is required to understand the involved physics. This is the main motivation for the present study on bumper beam-longitudinal system at offset impact.

1.2 Problem definition

The problem studied is outlined in Figure 1-2 where a trolley, with a given initial velocity and mass, impacts the bumper beam-longitudinal system at 40% offset. The definition of 40% offset is taken as the distance from the impact point to the extreme left end of the bumper beam. At impact, the impact energy (kinetic energy) of the trolley is mainly absorbed in collapsing the bumper beam as well as the longitudinal at the impacted end,

i.e. impacted longitudinal. While the non-impacted longitudinal experiences only minor deformations.

When a system, like the one in Figure 1-2, is fitted to a vehicle and expected to perform well in a NCAP test or in a real life impact, it is important that the energy absorption capabilities are predictable. Further, these capabilities have to be evaluated in order to ensure the integrity of the passengers' compartment.

In the design process and crash assessment of vehicles Finite Element Method (FEM) is an indispensable tool. It enables new design concepts to be evaluated where the optimum interaction between materials and structural forms can be studied. The value of such numerical analysis is strongly dependent on a precise description of the mechanical behaviour of the material and also the application of enhanced material models (Lademo, 1999). This means, however, that the code has to be validated against precision tests in the laboratory to ensure proper modelling of the member

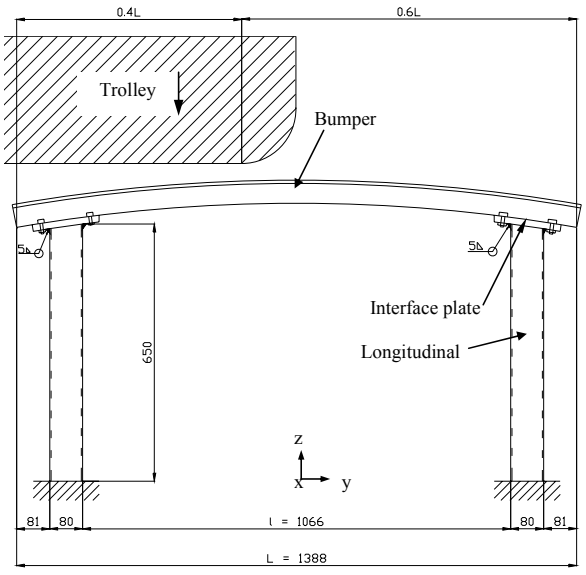

Figure 1-2 Bumper beam-longitudinal system at 40% offset impact.

geometry, boundary conditions, material properties and fracture. Thus, in order to establish a reliable experimental database for the system in Figure 1-2 only few parameters were varied. The experimental database was used for the development and validation of modelling procedures for the crash performance of the bumper beam-longitudinal system with the use of the nonlinear FE-code LS-DYNA.

In the bumper beam-longitudinal system the major part of the deformation will take place as a combination of progressive buckling and bending. It is important that the numerical model is capable of handling both these collapse modes. The numerical model should able to predict the collapse mode with a high level of certainty in order to ensure robust design.

1.3 Previous work

Thin-walled tube-like structures have been extensively studied as energy absorbing components by various researchers and comprehensive reviews can be found in the literature. (Johnson and Reid, 1978; 1986; Reid, 1993; Alghamdi, 2001; Jones, 2003; Abramowicz, 2003).

The open literature available on bumper beam studies is vast and the majority of studies carried out into bumper beam design have been related to the U.S. protection requirements. The structural performance of aluminium bumper beams is examined by Sharp et al. (1978), from the standpoint of local damage (i.e. resistance to denting and cracking), with regard to low-velocity impact (8.3 km/h). Significant cost savings can be made of being able to predict the damageability of proposed bumper beam designs from “blue prints”. This led Tang (1979) to investigate computer modelling of bumper beam impact resistance. Johnson and Walton (1983) studied a series of selected car bumper beams by quasi-static loading at their mid-span, and showed that the assumption that a bumper beam could deform through 102 mm before the body of the vehicle would become damaged was an overestimate. However, the literature available on bumper

beam systems connected to longitudinals is rather limited or non-existing. In this direction the only journal papers produced is by Hanssen et al. (2003a) and Lademo et al. (2005).

1.4 Objectives and research methodology

The objectives of this study were to increase the physical understanding of the different phenomena taking place during the offset impact of an automotive bumper beam-longitudinal system as well as to validate a modelling procedure for the system's crash performance. The specific tasks are divided into two major parts that complement each other:

- Experimental work involving the effect of:
  - Alloy and temper condition of the longitudinals
  - Trolley impact velocity
- Numerical work using the non-linear FE-code LS-DYNA (Hallquist, 2003) involving:
  - Verification of a user-defined elasto-viscoplastic material model.
  - Simulation of forming process for generating the FE-model of the bumper beam with required curvature.
  - Establishing an FE-model of the bumper beam-longitudinal system for validation purposes. Focus was placed on the force-deformation response and the ability to predict the correct deformation and fracture modes.
  - Comparison with standard industrial modelling procedures.
  - Influence of process effects, due to stretch-bending of bumper beam, on the crash behaviour of bumper beam-longitudinal system.

The research work has the following limitations:

- The problem definition given in Section 1.2
- Two impact velocities for the trolley i.e. 10 m/s (~ 36 km/h) and 15 m/s (~ 54 km/h).
- Single alloy for the bumper beam; AA7108-T6.
- Longitudinals of two different alloys (AA7003 and AA6060) and two temper conditions (T79 and T1). The longitudinals in AA7003-T79, AA7003-T1 and AA6060-T1 were selected.
- Longitudinals with constant wall thickness, span length and cross-section area of 3.2 mm, 650 mm and 95x80 mm^2 respectively.
- Trolley with constant mass; 794 kg.

To achieve the objectives the research method is based on an integrated use of experiments (both material tests and full-scale system tests) and nonlinear FE-analyses. Hence, this method has been followed in organisation of the thesis. A summary of the content of the different chapters is given below.

Chapter 2 explains the theoretical background for modelling of the material behaviour in a crash situation. The chapter gives the foundation for the work presented in the following chapters. It also introduces the chosen constitutive relation and fracture criteria that should able to represent the mechanical response of the material subjected to impact loading.

Chapter 3 contains experimental work on the material level. The chapter introduces the materials that are considered in this study for the bumper beam (AA7108, temper W and T6) and longitudinals (AA7003-T79, AA7003-T1 and AA6060-T1). Several effects were included in the study and consequently various tests were carried out; both traditional ones as the uniaxial tensile tests and others more specifically to identify certain model parameters. In order to investigate the strain-rate sensitivity, dynamic tensile

tests were carried out over a wide range of nominal strain-rates. From these tests the dynamic stress-strain behaviour was acquired.

Chapter 4 presents the overall test programme and the test set-up used for testing the bumper beam-longitudinal system at 40% offset impact. The test set-up is called the Kicking machine. The calibration procedure of the loadcells along with the instrumentation and data acquisition systems is discussed.

Chapter 5 presents the experimental work on the bumper beam-longitudinal systems. Results from the offset impact tests when using different longitudinals and impact velocities are discussed thoroughly. Comparison of results is made for similar systems with different impact velocities. A part of this work has previously been presented at the International Conference on Impact Loading of Lightweight Structures (Kokkula et al., 2005).

Chapter 6 explains how the FE-simulation of the stretch-bending and other forming operations were performed to obtain a numerical model of the rotary stretch-bent bumper beam. The other forming operations include trimming and reshaping of the holes. In the end, the assembly of a simulation model for the crash set-up is presented.

Chapter 7 presents the numerical simulations of the bumper beam-longitudinal system subjected to 40% offset impact. Numerical and experimental results are compared, and the use of different material modelling approaches for a selected bumper beam-longitudinal system is discussed.

Chapter 8 presents the sensitivity study. The sensitivity study includes both physical and purely numerical parameters. The physical parameters investigated were strain-rate, heat-affected zone (HAZ), process effects on the material and fracture criteria, while numerical parameters were element

formulation, mesh size, number of through-thickness integration points, self contact and adaptive meshing.

Chapter 9 is the final chapter where the concluding remarks are presented together with some recommendations for further work.

Chapter 2 Theory

Automotive impact is a highly complex phenomenon involving large and unstable elastic-plastic deformations. In a crash, the crash energy is dissipated by extensive plastification of the structural elements that are used as energy absorbers. Usually crash events occur at higher strain-rates, thus consideration of viscous effects might also be crucial in the analyses. The aim of this chapter is to present the basics of elasto-plastic/visco-plastic constitutive modelling, including the effect of strain-rate and plastic instability mechanisms. A further aim is to give a basic foundation for the work presented in the following chapters. Through this chapter the reader is introduced to modelling of a material subjected to impact.

2.1 Elasto-plasticity/Visco-plasticity

2.1.1 General formulation

Many of the essential features of the stress-strain behaviour of a material can be obtained from a set of stress-strain curves for the material response in a state of one-dimensional stress, i.e. uniaxial tensile test, which is widely used for characterisation of ductile materials (Dieter, 1988; Khan and Huang, 1995). Tensile testing involves gripping of the specimen at each end in a testing machine and elongated at a prescribed rate in the axial direction until it fractures. The elongation of the gauge section and the load are measured, and the engineering stress-strain curve, Figure 2-1, is constructed. The engineering stress, also known as the nominal stress, is defined by

$$s = \frac{T}{A_0} \tag{2.1}$$

and the engineering or the nominal strain is further defined as

$$e = \frac{\Delta l}{l_0} = \frac{l - l_0}{l_0} \tag{2.2}$$

where T is the applied axial load, A_0 is the undeformed area of the cross-section and l_0 and l are the initial and the current gauge length of the extensometer, respectively.

Figure 2-1 shows a typical stress-strain curve from a uniaxial tensile test for aluminium, from which important material characteristics can be extracted. Up to point A the deformation will be *elastic*, indicating that the material is able to regain its original dimensions completely after removal of the applied force. The stress-strain relationship below point A is linear and is represented by Hooke's law. The slope gives the modulus of elasticity, also called as Young's modulus. Point A is called the yield point. As the material becomes unstable at point A, the material shows non-linear elastic-plastic behaviour as seen in Figure 2-1.

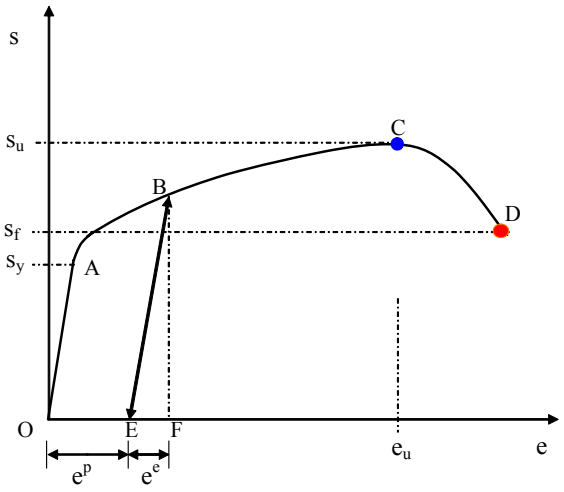

Figure 2-1 Characteristic stress-strain curve under uniaxial loading for aluminium.

The gradual transition in Figure 2-1 makes it difficult to establish a precise yield stress. For such cases a *proof stress* may be quoted. This is the stress to produce a specified amount of permanent deformation - often 0.2%, i.e. about half the elastic strain at yield. In some metals, like galvanised and bake-hardened steels, the transition from elastic to plastic deformation shows a sharp yield plateau (Marciniak et al., 2002).

The material becomes stronger with the increase in plastic deformation of the specimen, i.e. it *hardens*, implying that the load required to extend the specimen increases with further straining. Eventually the load reaches a maximum value, point C, and the *ultimate tensile strength* is obtained. After this point the engineering stress starts to decrease with increasing strain due to *instability* or *diffuse necking* in the specimen (Dieter, 1988). The condition for the formation of diffuse necking will be discussed in Section 2.2.1. The cross-sectional area of the specimen begins to decrease rapidly, so that load required during deformation drops until the specimen fractures at point D.

The initial yielding is followed by a region (elasto-plastic deformation) in which the deformation in the specimen is uniform and the stress increases. The increase is due to *work*- or *strain-hardening*, which is a phenomenon exhibited by most metals and alloys. If the material is unloaded in this region, say from point B to E, BE will be parallel to the initial loading path OA. The strain is the recovered elastic strain e^e and the rest is permanent or plastic strain e^p. Hence, according to the theory of plasticity the total strain in the elasto-plastic region consists of two parts

$$e = e^e + e^p \tag{2.3}$$

where for metals the elastic strain is normally smaller than the plastic strain.

In obtaining the *engineering stress-strain* curve from the load-extension diagram, the load was divided by initial cross-sectional area A_0 and the

extension by l_0. Thus the curve obtained was independent of the initial dimensions of the specimen, but it is still not a true material property curve. During the test, the cross-sectional area will diminish so that the true stress on the material will be greater than the engineering stress.

Alternatively, the stress-strain response is given in terms of true stress. The true stress (or Cauchy stress) is given by

$$\sigma = \frac{T}{A} \tag{2.4}$$

and the true strain (also called the logarithmic strain) is defined as

$$\mathrm{d}\varepsilon = \frac{\mathrm{d}l}{l} \Rightarrow \varepsilon = \int_{l_0}^{l} \frac{\mathrm{d}l}{l} = \ln \frac{l}{l_0} \tag{2.5}$$

where A is the current or deformed cross-sectional area and l is the current or deformed gauge length of the specimen. The relation between the nominal and the true strain is obtained by combining Equations (2.2) and (2.5) which gives

$$\varepsilon = \ln(1+e) \tag{2.6}$$

Assuming the constancy-of-volume condition due to Bridgman (1952) for ductile metals, it is possible to write

$$A_0 l_0 = Al \tag{2.7}$$

where the elastic strains, that are assumed to be small, are neglected. Hence the relationship between the nominal and the true stress may be obtained as

$$\sigma = \frac{T}{A} = \frac{T}{A_0}\frac{l}{l_0} = s(1+e) \tag{2.8}$$

As mentioned, the load, and therefore also the nominal stress, required for further deformation, falls off after reaching diffuse necking. However, the

metal continues to strain-harden all the way to fracture. This means that the true stress required to produce further deformation should also increase. Equation (2.8) is derived from assuming both constancy of volume and homogeneous distribution of strain along the gauge length of the specimen. Beyond the maximum load the true stress should be determined from actual measurements of load and cross-sectional area, while the true strain should be based on the actual area measurements.

2.1.2 Anisotropy

Materials in which the same properties are measured in any direction are termed *isotropic*, but many engineering materials produced as extrusions/sheets show a difference in properties measured in specimens aligned in different direction. This variation is known as *planar anisotropy* (Marciniak et al., 2002). In tensile tests of material in which the properties are same in all directions, one would expect, by symmetry, that the width and thickness strain would be equal; if they are different, this suggests that some *anisotropy* exists.

The state of anisotropy is usually indicated by the *r-value*. This is defined as the ratio of width strain to the thickness strain. In some cases, the thickness strain is measured directly, but it may be calculated also from the length and width measurements using the constant volume assumption, $htl = h_0 t_0 l_0 \quad or \quad \frac{t}{t_0} = \frac{h_0 l_0}{hl}$, outside the necking as (Marciniak et al., 2002; Hosford and Caddel, 1993)

$$r = \frac{\ln \frac{h}{h_0}}{\ln \frac{t}{t_0}} = \frac{\ln \frac{h}{h_0}}{\ln \frac{h_0 l_0}{hl}} \tag{2.9}$$

where h_0 and h are the initial and final width and t_0 and t are the initial and final thickness of the gauge section. It was assumed that r-ratio in Equation (2.9) is constant during the deformation. Experimental evidence supporting this way of calculating the r-value can be seen in Lademo et al. (1999). The direction in which the *r-value* is measured is indicated by a suffix, i.e. r_0, r_{45} and r_{90} for tests in the extrusion, diagonal and transverse direction respectively.

2.1.3 Strain-rate effects

In crash situations the material behaviour is deformed at high strain-rates. Experimental tests of ductile metals show that by increasing strain-rate, the flow stress is normally increased as well (Dieter, 1988). The yield stress and the flow stress at lower plastic strains are more affected by the strain-rate than the tensile strength. However, the material ductility is typically reduced with increasing strain-rate.

The strain-rate dependence of flow stress increases with increasing temperature. Decreasing the strain-rate has the same effect on the flow stress as raising the temperature (Dieter, 1988). The strain-rate sensitivity of metals is quite low at room temperature, but may increase with temperature, for steel it is slightly positive and for aluminium close to zero or slightly negative. Positive rate sensitivity usually improves forming and has an effect similar to strain-hardening (Marciniak et al., 2002). In Section 2.3 constitutive relations relating the strength of the material to strain and strain-rate will be discussed in more detail.

2.2 Plastic instability

2.2.1 Diffuse and localised necking

Diffuse necking and localised necking, shown in Figure 2-2, are two important instability phenomena that are of tremendous importance in the

study of failure of metals. Because the formation of these instabilities is an important *precursor* to *failure* of components, computational prediction of the onset and growth of these instabilities is indispensable in calculations of the ultimate ductility and strength of structures and materials (Lademo, 1999).

As soon as the material reaches the maximum load during a tensile test, the specimen becomes unstable and a neck develops, see Section 2.1.1. In this necked region the strains become highly localised. The stress in the specimen as the specimen deforms, will increase for a strain-hardening material and the cross-sectional area will decrease. At some stage, the rate of strain-hardening will fall below the rate of reduction in area and the load will reach its maximum value. At this instant,

$$\mathrm{d}T = \mathrm{d}(\sigma A) = \sigma \mathrm{d}A + A\mathrm{d}\sigma = 0 \tag{2.10}$$

or

$$-\frac{\mathrm{d}A}{A} = \frac{\mathrm{d}\sigma}{\sigma} \tag{2.11}$$

Combining the above condition with the constancy-of-volume relationship

$$\mathrm{d}V = \mathrm{d}(Al) = A\mathrm{d}l + l\mathrm{d}A = 0 \tag{2.12}$$

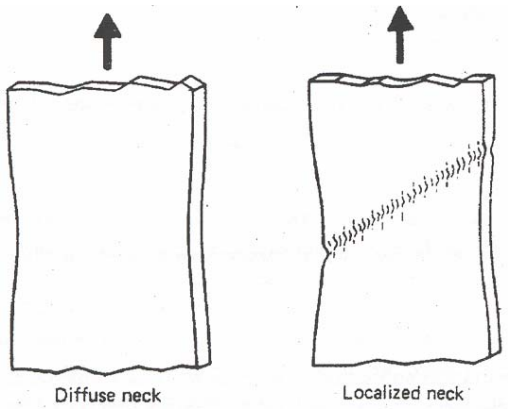

Figure 2-2 Diffuse and localised necking, (Hosford and Caddel, 1993).

and further

$$\frac{\mathrm{d}l}{l} = -\frac{\mathrm{d}A}{A} = \mathrm{d}\varepsilon \tag{2.13}$$

Hence, we obtain the point of tensile instability

$$\frac{\mathrm{d}\sigma}{\mathrm{d}\varepsilon} = \sigma \tag{2.14}$$

Equation (2.14) is the well-known Consideré condition for maximum load in a specimen in tension. A more explicit expression of the necking criterion may be obtained when using the nominal strain, i.e.

$$\sigma = \frac{\mathrm{d}\sigma}{\mathrm{d}\varepsilon} = \frac{\mathrm{d}\sigma}{\mathrm{d}\,e}\frac{\mathrm{d}\,e}{\mathrm{d}\varepsilon} = \frac{\mathrm{d}\sigma}{\mathrm{d}\,e}\frac{\mathrm{d}l/l_0}{\mathrm{d}l/l} = \frac{\mathrm{d}\sigma}{\mathrm{d}\,e}\frac{l}{l_0} = \frac{\mathrm{d}\sigma}{\mathrm{d}\,e}(1+e) \tag{2.15}$$

or by slightly re-writing it

$$\frac{\mathrm{d}\sigma}{\mathrm{d}\,e} = \frac{\sigma}{(1+e)} \tag{2.16}$$

For a sheet tensile specimen, as in Figure 2-2, where the width is much greater than thickness, there are two types of tensile instability. The first is necking that initiates according to the criterion discussed above and is called *diffuse necking*. The necking is called diffuse because its extent is much greater than the sheet thickness. Diffuse necking may terminate in fracture although it is often followed by a second instability process called *localised necking*. In this second instability the neck is a narrow band with a width about equal to the sheet thickness inclined at an angle to the specimens loading axis, as seen in Figure 2-2. There is no change in the angle and the width of the neck. The decrease in the specimen's cross-sectional area for further straining is therefore restricted to the thickness direction, which means that the localised necking corresponds to a state of plane-strain deformation. In a uniaxial tensile test, or generally at the left hand side of the Forming Limit Diagram (FLD), Marciniak and Kuczynski (1967) theory

is not required. In the next section theory of Marciniak and Kuczynski (1967) is presented to account for the failure discussed above.

2.2.2 Marciniak and Kuczynski theory

For assessing and understanding (more clearly) the plastic instability phenomenon, the classical instability analysis by Marciniak and Kuczynski (1967) is important. The discussion presented here is based on Barlat (1987) and Lademo (1999).

Marciniak and Kuczynski theory assume that an initial heterogeneity in the material thickness is present, and the assessment of plastic instability is performed using the two-zone model as in Figure 2-3. The heterogeneity is described in terms of a groove (b) oriented at an angle ω to the minor principal stress direction. The thickness inside the groove is e^b while the thickness outside is e^a. The *initial inhomogeneity factor* is defined as the ratio

$$\phi_0 = \left(\frac{e^b}{e^a} \right)_0 \tag{2.17}$$

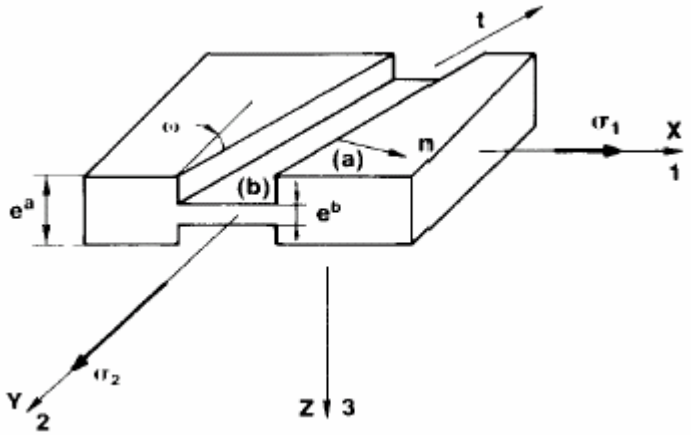

Figure 2-3 A sketch of the model of Marciniak and co-workers, Barlat (1987).

A biaxial stress state is imposed on the homogeneous region, (a), and the evolution of the strain-rates in both regions (a) and (b) is examined. The plastic strain increment in the thickness direction has to be larger inside the groove than outside to satisfy the force equilibrium across the groove. Hence, the groove will grow in a certain manner depending on among other the magnitude of the initial heterogeneity, Equation (2.17). The limiting strains are achieved when the ratio of these two strain-rates approaches a critical value corresponding to local instability. For a given path, the forming limit is obtained for the groove orientation ω that leads to the minimum calculated limiting strains. For a material exhibiting *planar isotropy and subject to a linear strain path, the critical groove orientation corresponds to an angle* $\omega = 0$ *in the whole stretching range* Barata da Rocha et al. (1984).

The *original assumptions* for the Marciniak and Kuczynski analysis are planar isotropy, Hill (1950) yield criterion, associated flow rule, and a power law strain-hardening rule. However, Barlat (1987) found that the yield surface shape has a *tremendous effect* on the predicted failure limits. Furthermore, Barlat explains the reason *why* the failure strains are so sensitive to the yield surface shape. This explanation is shortly repeated in the following.

In the case of planar isotropy, Sowerby and Duncan (1971) interpreted the process of localised necking by means of a yield locus as the one in Figure 2-4. Let us start considering the special case without any strain-hardening. In such a case, all stress states involving plastic deformation correspond to points on the locus represented by the full line. Equilibrium requires the major principal stress to be larger inside the groove than outside it, $\sigma_{b1} > \sigma_{a1}$, during the loading process. If the loading is proportional and ignoring work-hardening, the stress state in region (a) is represented by point A *during the entire straining process*. Since $\sigma_{b1} > \sigma_{a1}$, the stress in region (b) has to be represented by a point further along the σ_1-axis.

Assume that it is represented by point B_1. With the increase in strain, the relative thickness of the groove decreases. The major principal stress in the groove has to increase, and point B_1 will have to move further along the σ_1-axis until it reaches the limiting point B_0. When point B_1 reaches B_0 failure will soon occur. It is seen from Figure 2-4 that $d\varepsilon_1^b$ becomes large and $d\varepsilon_2^b \to 0$ as point B_1 approaches B_0. From the assumption of plastic incompressibility it is known that $d\varepsilon_1^b + d\varepsilon_2^b + d\varepsilon_3^b = 0$, where $d\varepsilon_3^b$ is the strain increment in thickness direction in the groove. In conclusion, $d\varepsilon_3^b = -d\varepsilon_1^b$ attains large negative values, i.e. the thickness rapidly decreases, which in reality means that the material will fracture. Even if the material strain hardens the explanation above applies. However, the rotation of point B_1 towards B_0 will be slowed down, and the material will attain a higher limiting strain. This interpretation clearly demonstrates the tremendous importance of the shape of the yield surface. Consider for instance the difference in failure strain that would be predicted using the yield stress of von Mises and Tresca. In the former case, the stress in the limiting point of plane strain is approximately 13% higher than the stress at

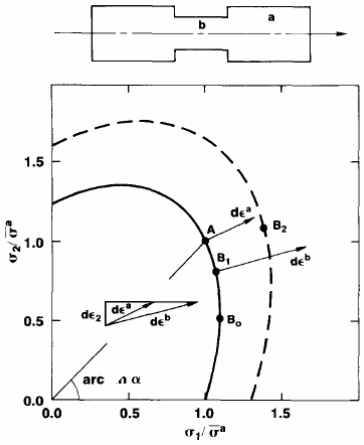

Figure 2-4 Interpretation of localised plastic flow, Barlat (1987).

balanced biaxial stress. In the latter case, however, there is no stress reserve and localisation will occur at an earlier stage.

It is further concluded, based on the considerations above, that the hardening rule adopted in the constitutive model may significantly alter the failure predictions for the material. Tvergaard (1978) found that kinematic hardening gave far better agreement with experimental results than the assumption of isotropic hardening.

Thus, accurate representation of plastic instability in LS-DYNA requires proper spatial discretisation, constitutive equations and parameters for the sheet/extrusion material at hand and possibly also some inhomogeneity in geometry or material properties. In Section 3.7, thickness inhomogeneity in the form of random Gauss-distribution has been used for simulating the tensile tests for the bumper beam material.

2.3 Constitutive model

As mentioned, the value of numerical analyses is strongly dependent on a validated modelling technology with accurate material models and fracture criteria. For the crash analyses of bumper beam-longitudinal systems, reliability and efficiency are important criteria for the choice of a constitutive model for the materials in question. In the following, the equations of a constitutive model for aluminium alloys are presented. The main ingredients of the model are a state-of-the-art anisotropic yield criterion, the associated flow rule, an isotropic strain and strain-rate hardening as well as some ductile fracture criteria (Lademo et al., 2004a).

2.3.1 General

Small strains and rotations are assumed in the presentation, while in the numerical implementation large rotations are accounted for in the co-

rotational shell elements (Belytschko et al., 2000). The strain tensor $\boldsymbol{\varepsilon}$ is decomposed into elastic and plastic parts (Lemaitre and Chaboche, 1990)

$$\boldsymbol{\varepsilon} = \boldsymbol{\varepsilon}^e + \boldsymbol{\varepsilon}^p \tag{2.18}$$

where $\boldsymbol{\varepsilon}^e$ and $\boldsymbol{\varepsilon}^p$ are the elastic and plastic strain tensors, respectively. The relation between the stress tensor $\boldsymbol{\sigma}$ and the elastic strain tensor $\boldsymbol{\varepsilon}^e$ is defined as

$$\boldsymbol{\sigma} = \mathbf{C} : \boldsymbol{\varepsilon}^e = \mathbf{C} : (\boldsymbol{\varepsilon} - \boldsymbol{\varepsilon}^p) \tag{2.19}$$

where $\mathbf{C}$ is the fourth order tensor of elastic constants.

The yield function *f*, which defines the elastic domain in stress space, is expressed in the form

$$f = \bar{f}(\boldsymbol{\sigma}) - (\sigma_0 + Y(\bar{\varepsilon})) \leq 0 \tag{2.20}$$

where σ_0 is the reference yield stress, Y is the strain-hardening variable, while the convex function $\bar{f}$ is defined below. The effective stress $\bar{\sigma}$ is defined by

$$\bar{\sigma} = \bar{f}(\boldsymbol{\sigma}) \tag{2.21}$$

The strain hardening is given by (Lemaitre and Chaboche, 1990)

$$Y(\bar{\varepsilon}) = \sum_{i=1}^{2} Q_{Ri}(1 - \exp(C_{Ri}\bar{\varepsilon})) \tag{2.22}$$

where $\bar{\varepsilon}$ is the accumulated plastic strain and Q_{Ri} and C_{Ri} are strain-hardening constants.

The generalised associated flow rule defines the evolution of the plastic strain tensor and the accumulated plastic strain as (Lemaitre and Chaboche, 1990)

$$\dot{\boldsymbol{\varepsilon}}^{p} = \dot{\lambda}\frac{\partial f}{\partial \boldsymbol{\sigma}},\ \dot{\bar{\varepsilon}} = -\dot{\lambda}\frac{\partial f}{\partial Y(\bar{\varepsilon})} \tag{2.23}$$

where $\dot{\lambda} \geq 0$ is the plastic multiplier. Equation $(2.23)_2$ leads to $\dot{\bar{\varepsilon}} = \dot{\lambda}$. The loading/unloading conditions are written in the Kuhn-Tucker form (Belytschko et al., 2000)

$$f \leq 0;\ \dot{\lambda} \geq 0;\ \dot{\lambda} f = 0 \tag{2.24}$$

These equations are used to define plastic loading and elastic unloading, while the consistency condition, $\dot{f} = 0$, is utilized to determine the plastic multiplier $\dot{\lambda}$ during a plastic process.

2.3.2 Extension to visco-plasticity

For strain-rate sensitive materials a visco-plastic model should be used. In the constitutive model described above, visco-plasticty is included by substituting Equations (2.20) and (2.24) by

$$\dot{\lambda} = \begin{cases} 0 & \text{for} \quad f \leq 0 \\ \dfrac{\psi\left(\bar{\sigma}, Y(\bar{\varepsilon})\right)}{\eta} & \text{for} \quad f > 0 \end{cases} \tag{2.25}$$

Here ψ is the overstress function and η is the viscosity, while f is the yield function (as in Equation (2.20))

$$f = \bar{f}\left(\boldsymbol{\sigma}\right) - \left(\sigma_0 + Y(\bar{\varepsilon})\right) \tag{2.26}$$

The strain-rate dependence of the effective stress will be defined by the constitutive relation

$$\bar{\sigma} = \bar{f}\left(\boldsymbol{\sigma}\right) = \left(\sigma_0 + Y(\bar{\varepsilon})\right) \cdot \left(1 + \frac{\dot{\bar{\varepsilon}}}{\dot{\varepsilon}_0}\right)^{C} \tag{2.27}$$

Solving for $\dot{\bar{\varepsilon}}$ gives

$$\dot{\bar{\varepsilon}} = \dot{\varepsilon}_0 \left[\left(\frac{\bar{\sigma}}{\sigma_0 + Y} \right)^{1/C} - 1 \right] = \frac{\psi\left(\bar{\sigma}, Y(\bar{\varepsilon})\right)}{\eta} \tag{2.28}$$

Equation $(2.23)_2$ leads $\dot{\bar{\varepsilon}} = \dot{\lambda}$.

2.3.3 Aretz yield criterion (Yld2003)

Prior studies have shown that aluminium alloys used in automotive applications have complex mechanical properties with anisotropic strength and ductility and that it may be necessary to use relatively complicated constitutive models to obtain the required accuracy in the numerical analyses (Lademo et al., 2004c). In this work the anisotropic yield criterion that is proposed by Aretz (2004) has been used for accurate and efficient representation of strong anisotropy in the materials (Lademo et al., 2004b). The criterion contains eight anisotropy parameters that can be fitted to experimental data, and has a simple mathematical form that is also efficient for computational analysis:

$$2\bar{f}^m = \left|\sigma_1'\right|^m + \left|\sigma_2'\right|^m + \left|\sigma_1'' - \sigma_2''\right|^m \tag{2.29}$$

with the generalized principal stress transformations

$$\left.\begin{matrix}\sigma_1' \\ \sigma_2'\end{matrix}\right\} = \frac{a_8 \cdot \sigma_x + a_1 \cdot \sigma_y}{2} \pm \sqrt{\left(\frac{a_2 \cdot \sigma_x - a_3 \cdot \sigma_y}{2} \right)^2 + (a_4)^2 \cdot \sigma_{xy}\sigma_{yx}} \tag{2.30}$$

and

$$\left.\begin{matrix}\sigma_1'' \\ \sigma_2''\end{matrix}\right\} = \frac{\sigma_x + \sigma_y}{2} \pm \sqrt{\left(\frac{a_5 \cdot \sigma_x - a_6 \cdot \sigma_y}{2} \right)^2 + (a_7)^2 \cdot \sigma_{xy}\sigma_{yx}} \tag{2.31}$$

where $a_1, a_2, ..., a_8$ are dimensionless anisotropy parameters. The exponent *m* can be taken as 6 or 8 for bcc or fcc sheet materials respectively. These

eight parameters can uniquely be found from eight experimental data points. If one is missing, it is also possible to simply ignore a_8 or equivalently fix it to unity (Aretz, 2004). The von Mises yield criterion is contained as a special case for $a_1 = a_2 = ... = a_8 = 1$ and $m = 2$.

2.3.4 Fracture criteria

An often used fracture criterion in the large-scale FE-simulations has been the critical equivalent plastic strain. However, it is well known that the equivalent plastic strain is not suitable as a fracture criterion when a structure is subjected to general loading modes. Two different fracture criteria have been used in the numerical analyses see Section 8.1.3, i.e. the critical thickness strain (Yeh et al., 1999) and the Cockcroft-Latham criterion (1968).

2.3.4.1 Critical thickness strain (*CFS*)

The first fracture criterion is based on the thickness strain, i.e. the element is eroded when some or all integration points of an element reaches a critical thickness strain:

$$\text{If } \varepsilon_t \le \varepsilon_{cr} \qquad \Rightarrow \qquad \boldsymbol{\sigma} = \mathbf{0} \tag{2.32}$$

2.3.4.2 Cockcroft Latham (CL)

The second fracture criterion employed here is a criterion proposed by Cockcroft and Latham (1968). The element is eroded if the term $\int_0^{\bar{\varepsilon}} \max(\sigma_1, 0)\, \mathrm{d}\bar{\varepsilon}$ obtains a value larger than a critical parameter W_{cr} in some or all integration points of an element:

$$\text{If } \int_0^{\bar{\varepsilon}} \max(\sigma_1, 0)\, \mathrm{d}\bar{\varepsilon} \ge W_{cr} \qquad \Rightarrow \qquad \boldsymbol{\sigma} = \mathbf{0} \tag{2.33}$$

Here σ_1 is the maximum principal stress, $\bar{\varepsilon}$ is the effective plastic strain, and W_{cr} is here called the critical specific plastic work.

Numerical aspects

The above discussed constitutive and fracture model is implemented in LS-DYNA as a user-defined material model in previous works (Lademo et al., 2004a; Berstad et al., 2004) and is here referred to as MAT-41. As will be seen in Chapter 7, in addition to MAT-41, crash simulations of the bumper beam-longitudinal system are also performed with widely used industrial material models, i.e. MAT-24 (*Piecewise Linear Isotropic Plasticity*) and MAT-103 (*Anisotropic Viscoplastic*) see Hallquist (2003). One difference between MAT-24 and MAT-103 is the hardening curve representation; in the former a load curve with true stress-strain values is used directly or it can be given by 8-points, hence the name "Piecewise Linear", while in the latter it is fitted with an extended Voce rule (Equation (2.22)). Another difference is the choice of yield criterion, where MAT-24 is based on the von Mises yield criterion and MAT-103 is based on the yield criterion due to Hill (1950). Note, however, that the parameters of Hill criterion have been chosen so that the yield surface is effectively the one represented by the von Mises yield criterion.

In the numerical simulations, when the fracture criterion is satisfied in one layer of a shell element this layer becomes inactive; i.e. the stress components in the layer are all taken equal to zero. When a user-defined number of integration points within an element have become inactive, the element is removed from the FE-model using the element erosion algorithm available in LS-DYNA (Hallquist, 2003). This means that it is, in principle, possible to follow the evolution of a "crack" through the structure. The fracture criterion is checked in all integration points in the structure for each time-step throughout the loading process.

Chapter 3 Material Properties

Material testing was carried out to characterize the materials. The goals of this chapter have been to identify parameters in constitutive and fracture models, see Section 2.3, that are used in numerical simulations in Chapter 7. The work presented in this chapter has been carried out in cooperation with an ongoing project titled "Modelling of Instability and Failure" (MoDIF) that has also been reported by Reyes et al. (2005).

Several effects were felt necessary to study and consequently various material characterization tests were carried out; both traditional ones as the uniaxial tensile tests and others more specifically to identify certain model parameters. The true stress-strain behaviour was obtained with standard quasi-static tensile tests in Section 3.1.2. In order to study anisotropy, tensile tests in three directions were carried out aiming at acquiring *r-values* and *flow-stress ratios*. These values were used to calibrate the constitutive model. The tensile tests also provide some knowledge about fracture, that were used to calibrate the fracture models discussed in Section 2.3.4.

With the intention of examining the strain-rate sensitivity of the materials, dynamic tensile tests were carried out. These results are discussed in Section 3.2. These data were used to include strain-rate effects in the material model. Through-thickness disk compression tests (Barlat et al., 1997b) were also conducted. The equibiaxial *r*-value that is obtained from this test was used in the calibration of the utilised yield criterion.

As mentioned in Section 1.4, one of the objectives of this work was to study the influence of process effects on the crash performance of the bumper beam-longitudinal system. Thus, a test programme following on the process effect on the material properties was carried out. In general, manufacturing

of a bumper beam from aluminium extrusions involves a series of forming operations performed in the soft W-temper condition, followed by artificial age-hardening of the components to the desired temper. After a forming operation, the material is influenced by the process, but this effect is traditionally neglected in the analyses of a formed component. The effects of forming processes have been here called “process effects” and the last test series reported here was performed with the purpose of exploring the influence of forming with simple uniaxial tensile tests. Similar tests have previously been reported by Lademo et al. (2004c). The tests were carried out in two steps; (1) Uniaxial pre-stretching of specimens in the forming state (W temper) to a given strain and (2) Uniaxial tensile tests of the pre-stretched specimens in the final state (temper T6) until fracture. An overview of the material test programme is given in Table 3-1.

3.1 Quasi-static tensile tests

3.1.1 Experimental details

All tests were applied a strain rate of $\sim 10^{-3}$ s^{-1}. The extensometer gauge length was 12.5 mm. The specimens were taken from the bumper beam (AA7108-T6) and the longitudinal materials (AA7003-T79, AA7003-T1 and AA6060-T1). In order to perform a process-based crash evaluation, tests in W-temper of AA7108 were carried out. For the interface plate (AA7003-T1) the material was taken from an extruded rectangular (82x10 mm^2) plate. The experimental program is given in Table 3-2. The specimen type is indicated in the table, and the corresponding geometry is shown in Figure 3-1. Width and thickness were measured at five different places along the gauge length prior to testing. More details on the measured width and thickness of the gauge area can be found in Reyes et al. (2005). Three parallels of each test were carried out. The specimens were machined from unformed extrusions, and taken out in 0°, 45° and 90°-direction to the extrusion.

Table 3-1 Overview of tested materials (Reyes et al., 2005).

	Alloy	Temper	Tensile tests		Compression tests	Process effects
			Quasi-static	Dynamic		
Bumper beam	AA7108	W	3 rep 0°, 45°, 90	-	5 rep	• Pre-stretching • 10 diff. plastic strains • 0° • 2 diff. lay-times in room temp. before artificial ageing
		T6	3 rep 0°, 45°, 90°	2 rep 0° 6 strain rates	5 rep	• Quasi-static tensile tests of pre-stretched specimens • 0°
Longitudinal	AA7003	T1	3 rep 0°, 45°, 90°	-	-	-
		T1 (plate)	3 rep 0°	-	-	-
		T79	3 rep 0°, 45°, 90°	2 rep 0° 6 strain rates	5 rep	-
		T79 (large)	3 rep 0°	-	-	-
	AA6060	T1	3 rep 0°, 45°, 90°	-	-	-

The test specimens from the longitudinals had to be quite small in order to acquire specimens in the 90°-direction (gauge length was 30 mm). With a width-to-thickness ratio of 5/3.2, triaxial effects after onset of necking and with respect to classical types of instability may be significant. In order to

Table 3-2 Experimental program and specimen types.

	Material						
	Bumper beam AA7108		Longitudinal AA7003				Longitudinal AA6060
Direction	W	T6	T1	T1 (plate)	T79	T79 (large)	T1
0°	B	B	A	B	A	C	A
45°	B	B	A		A		A
90°	B	B	A		A		A

Specimen type A

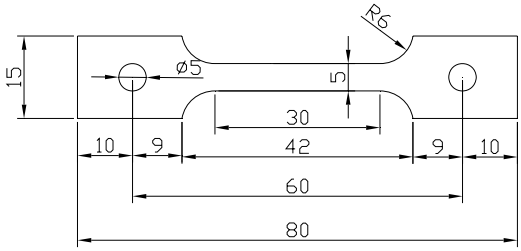

Specimen type B

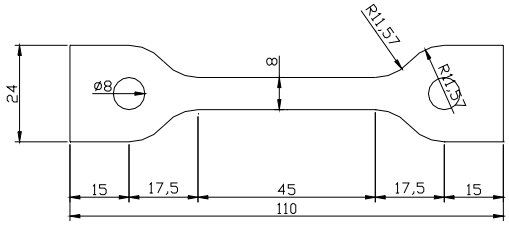

Specimen type C

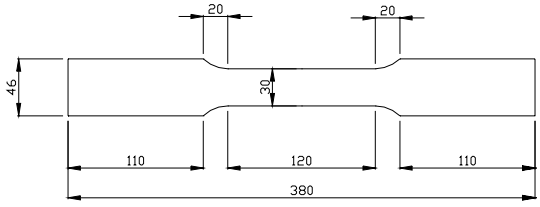

Figure 3-1 Specimen geometries for quasi-static tensile tests.

check the influence of this, large specimens ($h/t \approx 30/3.2$) (specimen type C) taken out in the 0°-direction were tested for AA7003-T79.

Temper W for the bumper beam material (AA7108) was achieved by heat treatment of specimens taken from an unformed extrusion in temper T1. The specimens were heated at 480°C for 20 min, quenched, and then tested (stretched until fracture) within 20 minutes after the heat treatment. The heat treatment and finishing times for the tests is given by Reyes et al. (2005).

3.1.2 Results

3.1.2.1 Stress-strain curves

The stress was calculated from the load measurements, while the strains were taken from the extensometer. However, after the maximum load, the strains were calculated from the crosshead displacement. This was done to achieve comparable engineering strains between the respective tests since it might vary whether localisation occurred outside or inside the extensometer gauge.

The engineering stress-strain curves from the tensile tests of the bumper beam material AA7108, temper W and T6 are shown in Figure 3-2. Curves from all three investigated directions are plotted. As seen, the anisotropy in strength and ductility is significant (respectively ±10% and up to 40% with respect to the values for the 0°-direction), and the experimental scatter is very low. For both tempers, the 90°-direction has the highest strength, and the 45°-direction has lowest strength. The strength anisotropy in the W- and T6-tempers seems to be comparable. In W-temper, the specimens in the 45°-direction are more ductile than in the other two directions, while in T6-temper, the specimens in the 0°-direction are slightly more ductile than in the 45°-direction. It is also observed from the curves that serrated flow (repeated appearance of discontinuities in the stress-strain curve) is extreme

for the material in W-temper, while almost non-existent for temper T6. This behaviour is known as the Portevin-Le Chatelier (PLC) effect (Portevin and Le Chatelier, 1923), which is widely accepted to arise from the attractive interaction between diffusing solute atoms and mobile dislocations known as dynamic strain aging (Shen et al., 2004) and may induce a macroscopic negative strain-rate sensitivity of the flow stress (Hähner and Rizzi, 2003).

The engineering stress-strain curves from the tensile tests of the longitudinal material AA7003 (temper T1 and T79) are shown in Figure 3-3. Results from the tests on large specimens in temper T79 and the plate in temper T1 are included in this figure. There is not much difference in strength between the specimens in 0°- and 90°-direction for this material, but there is a large difference in ductility (up to almost 50% of the 0°-direction). Because of the early fracture of the specimens in 90°-direction for temper T1 they also have a lower ultimate stress than the specimens in the 0°-direction. Specimens in the 45°-direction have lower strength (10-15%) than the specimens in the other two directions. The engineering stress-strain curve for the plate in temper T1 is also somewhat higher than the base curves. These differences could possibly be due to different texture in the longitudinal and plate owing to the geometry difference between the extrusions. It also seems that a small

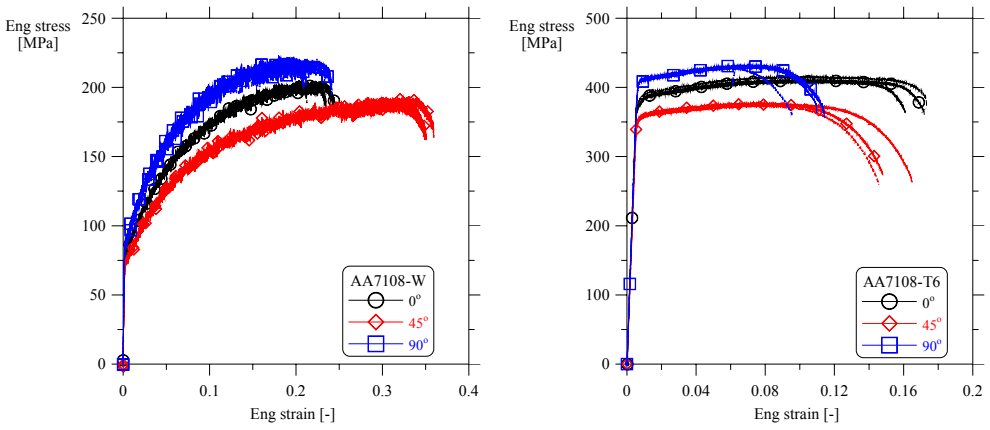

Figure 3-2 Engineering stress-strain curves for AA7108, temper W (left) and T6 (right).

PLC-effect is present for both tempers, but less for the large specimens and the specimens from the plate.

The curves from the large specimens in temper T79 are a little higher than the base curves. This could be caused by small non-linearities in the load cell characteristics that can influence the results from the large and small specimens.

For the large specimens in alloy AA7003-T79, two loading rates were checked: One (6 mm/min), corresponding to a strain rate of $\sim 10^{-3}$ s^{-1} as all the other tests, and one ten times faster (60 mm/min). Figure 3-4 provides the engineering stress vs. the crosshead displacement for the two loading rates. As seen, the strain-rate sensitivity at these rates seems negligible.

Figure 3-5 shows the engineering stress-strain curves from the tensile tests of AA6060-T1. There is not much difference in the strength levels of the three directions. However, there is a considerable anisotropy in ductility, where the 45°-direction is the most ductile, and the 0°-direction is the least. The PLC-effect is also present for the tests in this material.

3.1.2.2 r-values and flow-stress ratios

In order to identify material anisotropy from experimental tests it can be too restrictive to use yield stresses and *r*-values at yield, and these values do not give a good idea of the material behaviour for a larger strain range (Barlat et al., 2003). A more attractive method is to use the flow stresses up to a given amount of plastic work (Barlat et al., 1997a; 1997b; 2003), and *r*-values defined as the slope of the incremental width- and thickness-strain measurements (Barlat et al., 2003). Lademo et al. (1999) found that *r*-values could be represented by the slope of width strain vs. thickness strain, and guided by this and Barlat et al. (2003) *r*-values were here based on accumulated and not incremental strains. Width and thickness were measured at five different places along the parallel length of the specimen to

achieve an accurate estimate of the *r*-values. Measurements in clearly necked parts were ignored.

Furthermore, Lademo (1999) stated that for anisotropic material models, flow stresses at equal plastic work should be used in the identification of parameter rather than the flow stresses at equal plastic strain in order to be consistent with the model assumptions. The explanation for this is that the

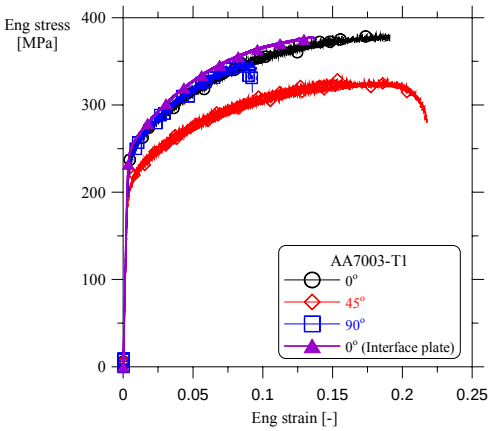

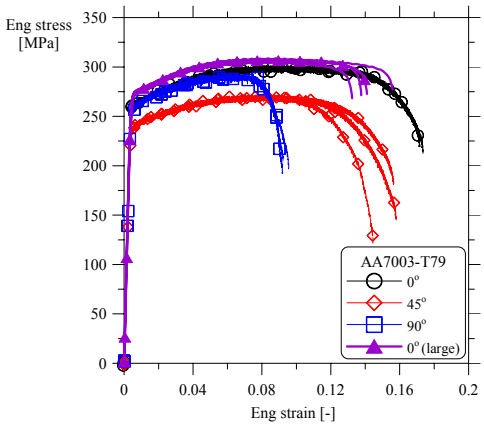

Figure 3-3 Engineering stress-strain curves for AA7003, temper T1 (left) and T79 (right).

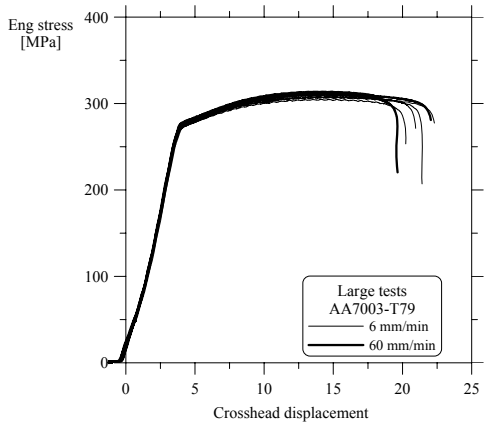

Figure 3-4 Comparison of loading velocities.

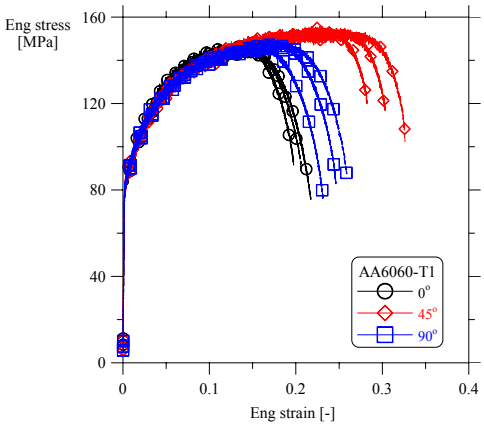

Figure 3-5 Engineering stress-strain curves for AA6060-T1.

use of the generalised associated flow rule indirectly requires the incremental plastic work to be equal for a multi-axial and a uniaxial stress state in the reference direction. Therefore, the flow-stress ratio G_α is here defined as the ratio between the flow stress in one test and a reference flow stress for the same amount of plastic work:

$$G_\alpha = \sigma_\alpha / \sigma_{ref}\big|_{W_p} \tag{3.1}$$

Here σ_α is the flow stress, σ_{ref} is the reference flow stress and W_p is the plastic work. Flow-stress ratios for varying plastic work were calculated for each test, where the flow stress in the first repetition in the 0°-direction was the reference flow stress. Slight scatter was observed between the flow-stress in the 0°-direction. The flow-stress ratios for alloy AA7108 temper W oscillated around an almost constant value for all plastic strains, while for temper T6 the flow-stress ratios varied somewhat with the plastic strain. However, this was mainly for the lower and higher plastic strains (in the tests).

The flow-stress ratios for alloy AA7003 temper T79 varied quite much with the plastic strain, while smaller variations were found for the alloy AA7003 temper T1. As the material model used in this study is not able to represent a varying flow-stress ratio, all the curves were fitted to a constant value. The average *r*-values and flow-stress ratios from the three parallels in each direction are listed in Table 3-3. The *r*-values and flow-stress ratios for temper W and T6 in AA7108 are very similar, which could indicate that the two tempers have same anisotropy, and that same yield surface is valid for both tempers (Lademo et al., 2002).

3.2 Dynamic tensile tests

In order to investigate the strain-rate sensitivity of the materials, dynamic tensile tests were carried out over a wide range of nominal strain-rates. From these tests the dynamic stress-strain behaviour was acquired.

3.2.1 Experimental details

The lower strain-rates, in the range $\dot{e} \in [6 \cdot 10^{-4}\ s^{-1}, 6\ s^{-1}]$, were obtained in a servo-hydraulic Instron testing machine, where the tests were under displacement control. Load, crosshead displacement and time were recorded, and the longitudinal strain was measured with an extensometer. A modified Split-Hopkinson tension bar (SHTB) (Clausen and Auestad, 2002) was used to achieve the highest strain rates, in the range $\dot{e} \in [1.5 \cdot 10^{2}\ s^{-1}, 1.3 \cdot 10^{3}\ s^{-1}]$. The incident, reflected and transmitted pulses were recorded in strain gauges placed on the incident and output bars. The engineering stress, strain and strain rate were calculated from this data. Two parallel tests were carried out for each strain-rate level. The details regarding the set-up and results processing are provided by Clausen and Auestad (2002).

Dynamic tensile tests were carried out for the bumper beam material AA7108-T6, and the longitudinal material AA7003-T79. The specimens in AA7108 were machined directly from an unformed bumper beam extrusion, while the specimens in AA7003 were taken from an extruded rectangular (82 x 10 mm^2) plate in temper T1, and heat treated to achieve the T79 condition. The specimen geometry is shown in Figure 3-6. The wall thickness in the bumper (at the location where the specimens were taken from) was 3.9 mm, which is smaller than the diameter on the outer parts (threaded parts) of the specimens (5 mm). As a result, the area of these outer parts of the specimens in AA7108-T6 was somewhat "shaved", and not

Table 3-3 r-values and flow-stress ratios.

			r-values			Flow-stress ratios	
	Alloy	Temper	r_0	r_{45}	r_{90}	G_{45}	G_{90}
Bumper beam	AA7108	W	0.21	1.94	1.19	0.92	1.09
		T6	0.27	1.67	1.16	0.93	1.06
Longitudinal	AA7003	T1	0.30	1.38	1.17	0.90	1.01
		T79	0.38	1.51	1.05	0.91	0.96
	AA6060	T1	0.48	0.29	1.76	1.02	1.01

completely circular (see Figure 3-6). Tests on similar specimens have been carried out previously and compared with smaller specimens, and no effect of this geometry change was observed (Enjalbert, 2003). Additionally, the threaded parts of the specimens were carefully inspected after the tests, and they were perfectly intact.

3.2.2 Results

Material data for the dynamic tensile tests are given in Table 3-4. "BA" in the test name refers here to the tests in the Instron machine, while "sh" refers to the tests in the SHTB. The initial diameter in the test region was measured before testing, and is given in the table as d_0. Mean strain-rates, both engineering and true values, are also stated in the table. The true values are found from the known relations between engineering and true values. True stresses were found for plastic strains of 2%, 5% and 8%, and these stresses together with ultimate engineering stress and corresponding engineering strain are also specified in the table.

The engineering stress-strain curves from all tests are shown in Figure 3-7, while the true stress-strain curves until diffuse necking are given in Figure 3-8. As one can see, there is a significant influence of the strain-rate with respect to strength, strain-hardening (as seen from the point of diffuse necking) and the local ductility. The stress-strain curves from the quasi-

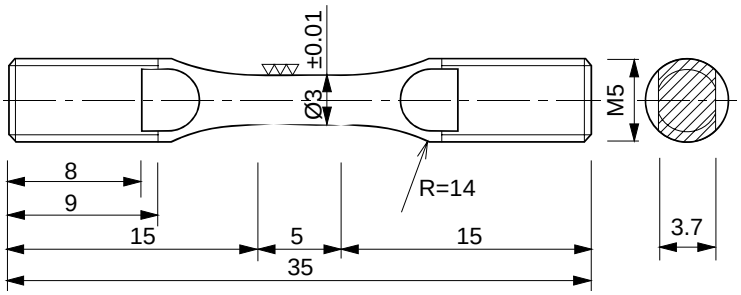

Figure 3-6 Specimen geometry for dynamic tensile tests.

static tensile tests of flat specimens are also included in the figure. As one can see, these curves are quite close to the corresponding curves on small specimens. For AA7003-T79 the curves from the flat specimens are somewhat lower than the curves from the small specimens. This is probably because the flat specimens were taken directly from the longitudinal while the small specimens for the dynamic tests were taken from the extruded plate and heat treated. For AA7003-T1 it was found that the stress-strain curves corresponding to the specimens from the plate were somewhat higher than for the specimens from the longitudinal.

The true stress was found for different plastic strains (i.e. 2%, 5% and 8%), and the true stress corresponding to a plastic strain of 2% and 5% are plotted vs. the true strain rate in Figure 3-9. The strain-rate effect is quite small until

Table 3-4 Material data for dynamic tensile tests.

		diameter	Strain rates		True stress at given plastic strain			Max stress	Corr.strain
			Eng.	True	$\varepsilon_p = 2\%$	$\varepsilon_p = 5\%$	$\varepsilon_p = 8\%$		
	Test	d_0 [mm]	$\dot{e}$ [s^{-1}]	$\dot{\varepsilon}$ [s^{-1}]	σ_2 [MPa]	σ_5 [MPa]	σ_8 [MPa]	s_u [MPa]	e_u
Bumper beam AA7108-T6	*T6-BA1*	3.01	$6.30 \cdot 10^{-4}$	$6.20 \cdot 10^{-4}$	422	444	456	428	0.0669
	T6-BA2	3.01	$8.50 \cdot 10^{-4}$	$8.40 \cdot 10^{-4}$	418	445	462	432	0.0759
	T6-BA3	3.01	$9.10 \cdot 10^{-2}$	$8.95 \cdot 10^{-2}$	426	453	471	434	0.0944
	T6-BA4	3.01	$7.70 \cdot 10^{-2}$	$7.60 \cdot 10^{-2}$	430	459	474	438	0.0795
	T6-BA5	3.02	$5.80 \cdot 10^{0}$	$5.70 \cdot 10^{0}$	431	466	486	448	0.0885
	T6-BA6	3.02	$4.15 \cdot 10^{0}$	$4.10 \cdot 10^{0}$	440	474	485	453	0.0758
	T6-sh1	3.01	$3.84 \cdot 10^{2}$	$3.46 \cdot 10^{2}$	469	495	515	470	0.1441
	T6-sh2	3.01	$1.19 \cdot 10^{3}$	$1.07 \cdot 10^{3}$	471	500	518	474	0.1226
	T6-sh3	3.01	$1.16 \cdot 10^{3}$	$1.02 \cdot 10^{3}$	476	506	-	474	0.1031
	T6-sh4	3.01	$5.10 \cdot 10^{2}$	$4.60 \cdot 10^{2}$	472	502	-	478	0.1025
	T6-sh5	3.01	$4.47 \cdot 10^{2}$	$4.02 \cdot 10^{2}$	473	507	527	479	0.1177
	T6-sh6	3.01	$1.56 \cdot 10^{2}$	$1.39 \cdot 10^{2}$	465	496	-	470	0.1086
	T6-sh7	3.01	$1.72 \cdot 10^{2}$	$1.55 \cdot 10^{2}$	467	499	520	472	0.1321
Longitudinal AA7003-T79	*T79-BA3*	3.04	$6.80 \cdot 10^{-4}$	$6.70 \cdot 10^{-4}$	316	343	349	330	0.0756
	T79-BA4	3.04	$7.10 \cdot 10^{-4}$	$7.00 \cdot 10^{-4}$	301	329	340	329	0.0796
	T79-BA5	3.04	$6.60 \cdot 10^{-2}$	$6.50 \cdot 10^{-2}$	327	357	366	339	0.0789
	T79-BA6	3.04	$6.90 \cdot 10^{-2}$	$6.80 \cdot 10^{-2}$	348	374	379	356	0.0603
	T79-BA7	3.06	$3.15 \cdot 10^{0}$	$3.10 \cdot 10^{0}$	340	368	369	350	0.0709
	T79-BA8	3.06	$4.35 \cdot 10^{0}$	$4.30 \cdot 10^{0}$	325	360	373	350	0.0591
	T79-BA9	3.06	$6.50 \cdot 10^{-4}$	$6.40 \cdot 10^{-4}$	339	360	364	348	0.0594
	sh1	3.05	$1.23 \cdot 10^{3}$	$1.10 \cdot 10^{3}$	380	411	-	392	0.0935
	sh2	3.05	$1.82 \cdot 10^{2}$	$1.61 \cdot 10^{2}$	333	370	393	363	0.1283
	sh4	3.05	$1.26 \cdot 10^{3}$	$1.12 \cdot 10^{3}$	350	385	409	374	0.1180
	sh5	3.05	$4.68 \cdot 10^{2}$	$4.12 \cdot 10^{2}$	351	385	409	374	0.1335
	sh6	3.05	$4.71 \cdot 10^{2}$	$4.26 \cdot 10^{2}$	371	405	425	389	0.0970
	sh7	3.05	$1.73 \cdot 10^{2}$	$1.52 \cdot 10^{2}$	336	372	399	364	0.1265

a strain rate of 10^{-2} s^{-1}, and the true stress increases linearly after this with the logarithmic strain rate. The increase in true stress is around 15% for AA7108-T6 and 25% for AA7003-T79, Figure 3-9. As one can also see from the figure, the results from tests on AA7003-T79 are slightly more scattered than the results from the tests on AA7108-T6. The fracture modes observed in the dynamic tensile tests are discussed by Reyes et al. (2005).

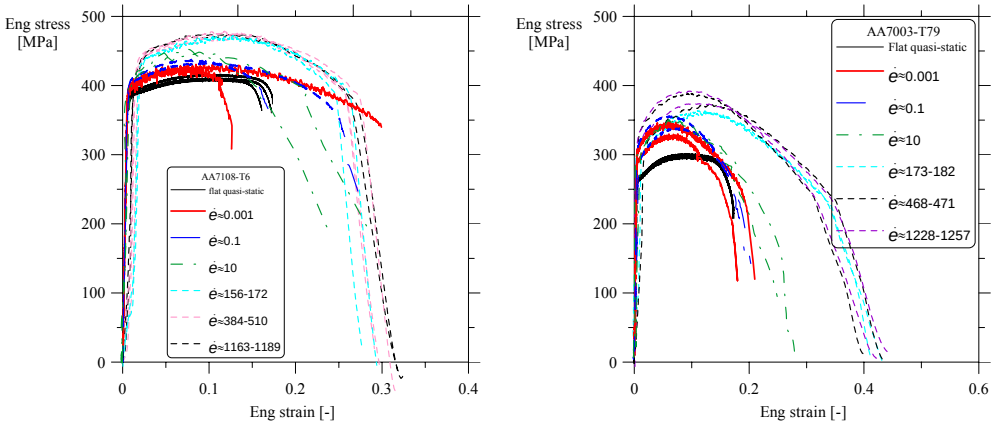

Figure 3-7 Engineering stress-strain curves from dynamic tensile tests.

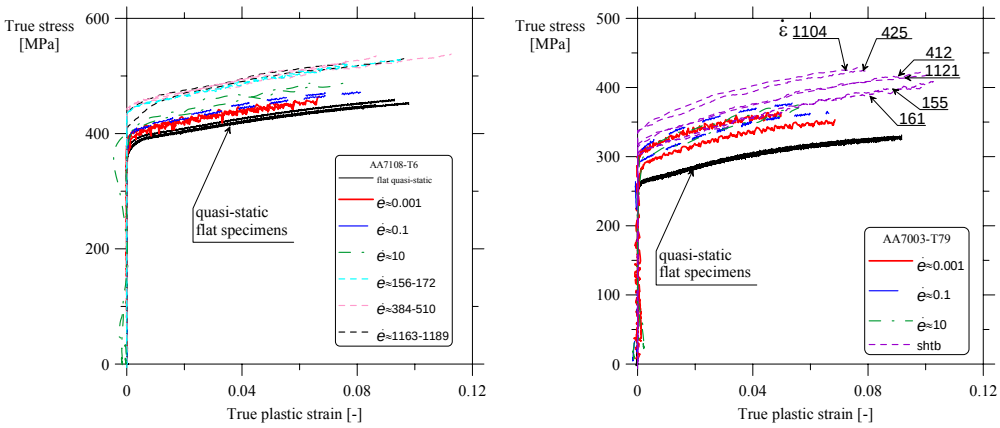

Figure 3-8 True stress-strain curves from dynamic tensile tests.

3.3 Compression tests

The equibiaxial *r*-value r_b can be found from through-thickness disk compression tests (Barlat et al., 1997b). In the present work r_b is needed in order to calibrate the yield criterion *Yld2003* (Aretz, 2004). The through-thickness compression test is a simple test where a circular disk is compressed in the thickness direction.

When a circular disk is loaded with a compressive force in one direction, one can imagine that the disk can be loaded with a tensile hydrostatic load with the same magnitude as the compressive load, see Figure 3-10. For metals, the hydrostatic load will not influence the plastic behavior, and

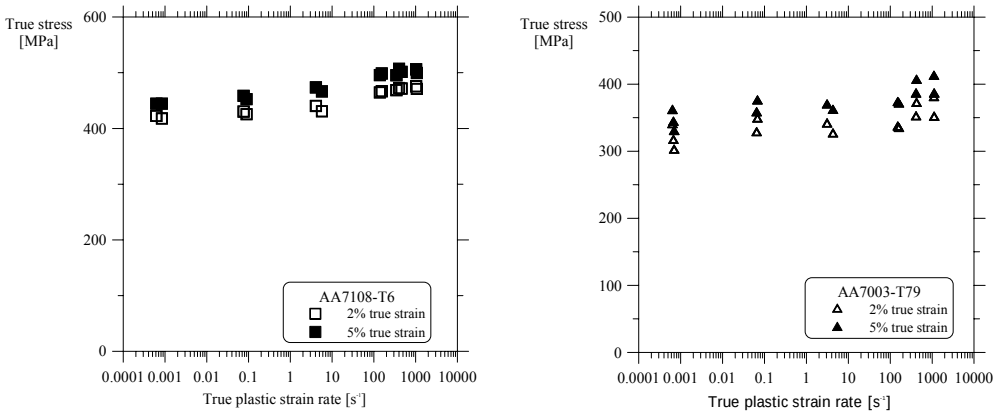

Figure 3-9 The effect of strain-rate on the true stress.

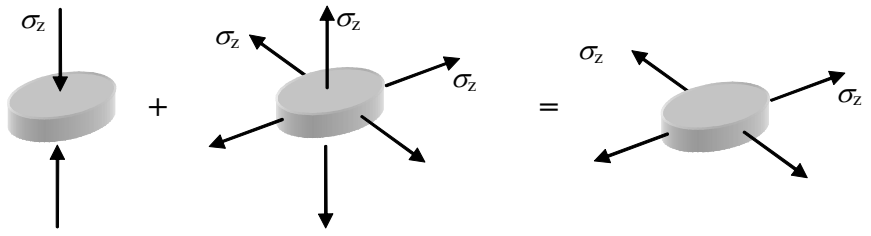

Figure 3-10 Through-thickness disk compression test.

therefore, the stress state in a through-thickness compression test is equivalent to the stress-state of an equibiaxial tensile test in terms of plasticity theory.

3.3.1 Experimental details

Compression tests on circular specimens with a diameter of 14 mm were carried out on the bumper beam material AA7108 in temper W and T6, and the longitudinal material AA7003-T79. The specimens were taken from unformed bumpers in tempers T1 and T6. The specimens in temper T1 were heat treated to achieve W temper following the same procedure as for the specimens in the quasi-static tensile tests. After testing, the increase in width in two perpendicular directions were measured (Δx and Δy), and the true strains in the same directions were calculated as

$$\varepsilon = \ln\left(\text{final dimension} / \text{initial dimension}\right) \tag{3.2}$$

From this, the equibiaxial strain ratio was found, as

$$r_b = \varepsilon_y / \varepsilon_x \tag{3.3}$$

Where x corresponds to the reference direction (in this case the extrusion direction) and y is the transverse direction.

In this study, it was chosen to only to measure the balanced biaxial strain ratio and not the corresponding stress, because friction will influence the load levels. However, it is assumed that the strain-ratio is not affected by the friction because it is isotropic and relatively low in the present case. Due to the higher scatter in experimental results it was chosen to perform five parallel tests for each material so that a reasonable average value could be obtained.

3.3.2 Results

The results from the compressions tests are given in Table 3-5. Here the increase in width in the x- and y-direction are included, together with the corresponding true strains and strain ratios. The transverse strain ε_y are plotted vs. the longitudinal (extrusion direction) strain ε_x in Figure 3-11, and there is obviously some scatter in these results. The average true strain ratios were found and are also given in Table 3-5. As one can see, there is a relatively large difference between the equibiaxial r-value for W and T6 temper.

3.4 Parameter identification

The motivation for the material tests was to determine parameters in the material model. In this section it is explained in detail how these parameters were found from the results of the material tests.

3.4.1 Strain and strain-rate hardening

Voce parameters, σ_0, Q_{Ri} and C_{Ri} (i = 1, 2) in Equation (2.22) were found by curve fitting to all the true stress-strain curves. For use in the numerical models only the curve parameters in the 0°-direction are necessary. There was not much scatter between the test repetitions (Reyes et al., 2005), and therefore, representative values from the 0°-direction are given in Table 3-6. True stress-strain curves from tests and the corresponding fitted curves are shown in Figure 3-12 and Figure 3-13.

Table 3-5 Results from compression tests (Reyes et al., 2005).

	Alloy	Temper	Initial width h_0 [mm]	Test no	Increase in width Δx [mm]	Increase in width Δy [mm]	True strain ε_x	True strain ε_y	True strain ratio $\frac{1}{r_b}=\frac{\varepsilon_x}{\varepsilon_y}$	Average true strain ratio $\frac{1}{r_b}=\frac{\varepsilon_x}{\varepsilon_y}$
Bumper beam	AA7108	W	14.0	1	1.70	0.908	0.115	0.0628	1.824	2.38
				2	1.950	0.768	0.130	0.0534	2.442	
				3	1.925	0.635	0.129	0.0444	2.904	
				4	1.888	0.680	0.127	0.0474	2.667	
				5	1.922	0.893	0.129	0.0618	2.081	
		T6	14.0	2	1.005	0.825	0.0693	0.0573	1.211	1.49
				3	1.230	0.767	0.0842	0.0533	1.579	
				4	1.218	0.768	0.0834	0.0534	1.562	
				5	1.155	0.714	0.0793	0.0497	1.594	
Longitudinal	AA7003	T79	14.0	1	1.025	0.635	0.0707	0.0444	1.593	1.55
				2	1.295	0.832	0.0885	0.0577	1.533	
				3	1.338	0.884	0.0913	0.0612	1.491	
				4	1.430	0.897	0.0973	0.0621	1.566	

In order to include strain-rate dependency, Equation (2.27) was used, where the parameters to be determined are $\dot{\varepsilon}_0$ and C. The parameters were found by minimizing the sum of squares between the model and the experimental data, i.e.:

$$\sum_{i=1}^{n}\left(\frac{\bar{\sigma}_i}{(\sigma_0 + Y(\bar{\varepsilon}))} - \left(1+\frac{\dot{\bar{\varepsilon}}_i}{\dot{\varepsilon}_0}\right)^C\right)^2 = \min \tag{3.4}$$

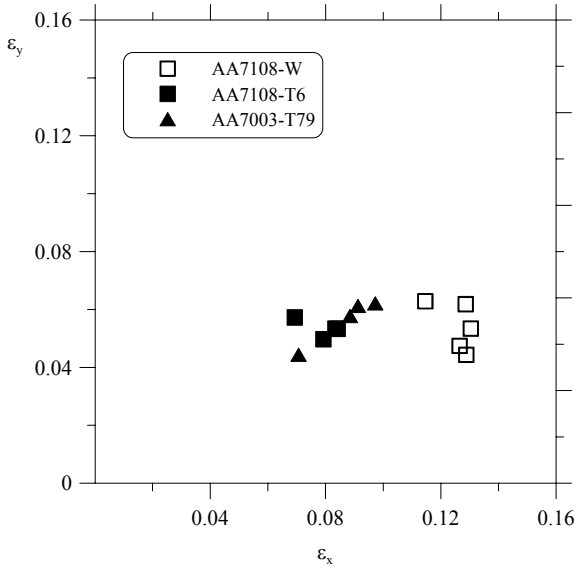

Figure 3-11 Transverse strain ε_y vs. longitudinal strain ε_x in the disk compression test.

Table 3-6 Chosen Voce parameters for numerical analyses.

				Curve parameters				
	Alloy	Temper	Angle	σ_0 [MPa]	Q_{R1} [MPa]	C_{R1} [-]	Q_{R2} [MPa]	C_{R2} [-]
Bumper beam	AA7108	W	0°	41.9	37.7	2828	204	8.51
		T6	0°	347	37.0	1017	113	9.99
Longitudinal	AA7003	T1	0°	210	35.7	457	279	7.86
		T1 (plate)	0°	202	47.7	1432	237	11.4
		T79	0°	239	20.4	4822	83.7	18.4
	AA6060	T1	0°	72.2	7.46	1405	91.6	17.8

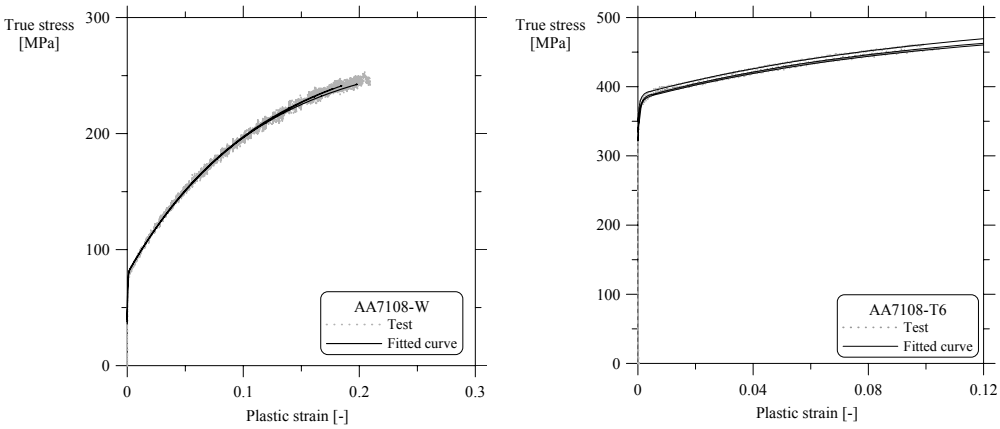

Figure 3-12 True stress-strain curves, and fitted hardening curves for bumper beam materials.

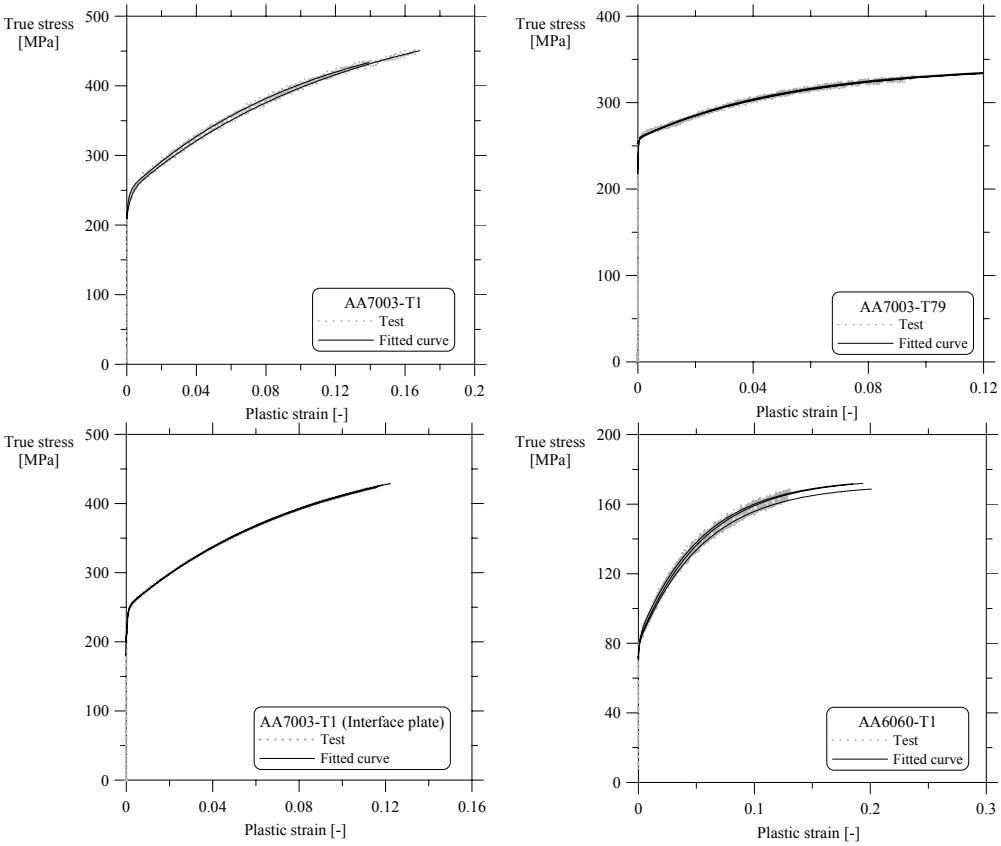

Figure 3-13 True stress-strain curves, and fitted hardening curves for the longitudinal materials and interface plate.

Here $\bar{\sigma}_i$ is the true stress at 2% plastic strain for each test while $\dot{\bar{\varepsilon}}_i$ is the corresponding strain rate. $(\sigma_0 + Y(\bar{\varepsilon}))$ is taken as the true flow stress at 2% plastic strain for the quasi-static case. The parameters are listed in Table 3-7, and in Figure 3-14 one can see that the model corresponds well with the experimental data.

3.4.2 Yld2003 parameters

The calibration of the anisotropic yield criterion is presented in the following. There are eight parameters (a_1, a_2,$\cdots$ a_8) to be determined in *Yld2003* (Equations (2.30) and (2.31)). Additionally, the exponent *m* can be taken as 6 or 8 for bcc or fcc sheet materials, respectively (Aretz, 2004). As the materials in this study are fcc sheet materials *m* is taken as 8 here.

Table 3-7 Strain-rate parameters.

			$(\sigma_0 + Y(\bar{\varepsilon}))$	$\dot{\varepsilon}_0$	C
	Alloy	Temper	[MPa]	[s^{-1}]	[-]
Bumper beam	AA7108	T6	420	0.26641	0.01518
Longitudinal	AA7003	T79	319	0.00126	0.00813

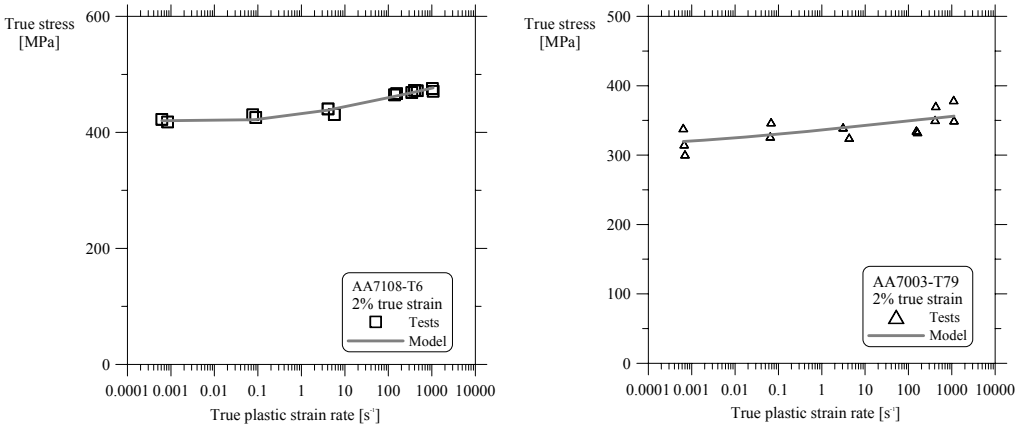

Figure 3-14 True stress at 2% plastic strain vs. true plastic strain rate, from tests and material model.

The *r*-values and flow-stress ratios in Table 3-3 give six experimental measurements, and additionally the equibiaxial *r*-ratio r_b found from the through-thickness compression tests (see Section 3.3) gives a seventh measurement. As there are eight parameters to be determined the equibiaxial stress could have been used as the eighth measurement. However, this property was not measured in the current study. According to Aretz (2004), a_8 could be taken as 1.0. This however may result in atypical yield surfaces. It was here chosen to fix the point $\sigma_x/\sigma_0 = \sigma_y/\sigma_0 = 1.0$ and $\sigma_{xy}/\sigma_0 = 0.0$ in the calibration.

The yield criterion can be written as

$$g = \left[\frac{1}{2}\left(\left|\sigma_1'\right|^m + \left|\sigma_2'\right|^m + \left|\sigma_1'' - \sigma_2''\right|^m\right)\right]^{\frac{1}{m}} - \bar{f}_0 = \left[g_n\right]^{\frac{1}{m}} - \bar{f}_0 = 0 \tag{3.5}$$

where σ_1', σ_2', σ_1'', and σ_2'' are defined in Equations (2.30) and (2.31), and $\bar{f}_0$ represents the flow stress in the reference direction.

The *r*-value for a general direction α can be found as

$$r_\alpha = -\frac{\frac{\partial g}{\partial \sigma_x}\sin^2\alpha + \frac{\partial g}{\partial \sigma_y}\cos^2\alpha - \frac{\partial g}{\partial \sigma_{xy}}\cos\alpha\sin\alpha}{\frac{\partial g}{\partial \sigma_x} + \frac{\partial g}{\partial \sigma_y}} \tag{3.6}$$

Furthermore, the stress components σ_x, σ_y and σ_{xy} can be expressed by the uniaxial stress σ_α in a general direction α:

$$\begin{aligned} \sigma_x &= \sigma_\alpha \cos^2\alpha \\ \sigma_y &= \sigma_\alpha \sin^2\alpha \\ \sigma_{xy} &= \sigma_\alpha \sin\alpha\cos\alpha \end{aligned} \tag{3.7}$$

These relationships can be used in the yield criterion in Equations (2.29), and (2.30) the stress ratio for each direction can then be found as:

$$G_\alpha = \left.\frac{\sigma_\alpha}{\bar{f}_0}\right|_{\text{model}} = \frac{1}{\frac{1}{2}\left(\frac{1}{2}\left(\left|\sigma_1'^*\right|^m + \left|\sigma_2'^*\right|^m + \left|\sigma_1''^* - \sigma_2''^*\right|^m\right)\right)^{\frac{1}{m}}} \tag{3.8}$$

here, $\sigma_1'^*$, $\sigma_2'^*$, $\sigma_1''^*$, and $\sigma_2''^*$ are defined as $\sigma_1'^* = \sigma_1'/\sigma_\alpha$, $\sigma_2'^* = \sigma_2'/\sigma_\alpha$, $\sigma_1''^* = \sigma_1''/\sigma_\alpha$, and $\sigma_2''^* = \sigma_2''/\sigma_\alpha$.

The equibiaxial *r*-ratio can be found as

$$r_b = \frac{\frac{\partial g}{\partial \sigma_y}}{\frac{\partial g}{\partial \sigma_x}} \tag{3.9}$$

$\frac{\partial g}{\partial \sigma_x}$, $\frac{\partial g}{\partial \sigma_y}$ and $\frac{\partial g}{\partial \sigma_{xy}}$ are found from the yield criterion as:

$$\begin{aligned}
\frac{\partial g}{\partial \sigma_x} &= \frac{1}{m}\left[g_n\right]^{\left(\frac{1}{m}-1\right)}\left[\frac{\partial g_n}{\partial \sigma_1'}\frac{\partial \sigma_1'}{\partial \sigma_x} + \frac{\partial g_n}{\partial \sigma_2'}\frac{\partial \sigma_2'}{\partial \sigma_x} + \frac{\partial g_n}{\partial \sigma_1''}\frac{\partial \sigma_1''}{\partial \sigma_x} + \frac{\partial g_n}{\partial \sigma_2''}\frac{\partial \sigma_2''}{\partial \sigma_x}\right] \\
\frac{\partial g}{\partial \sigma_y} &= \frac{1}{m}\left[g_n\right]^{\left(\frac{1}{m}-1\right)}\left[\frac{\partial g_n}{\partial \sigma_1'}\frac{\partial \sigma_1'}{\partial \sigma_y} + \frac{\partial g_n}{\partial \sigma_2'}\frac{\partial \sigma_2'}{\partial \sigma_y} + \frac{\partial g_n}{\partial \sigma_1''}\frac{\partial \sigma_1''}{\partial \sigma_y} + \frac{\partial g_n}{\partial \sigma_2''}\frac{\partial \sigma_2''}{\partial \sigma_y}\right] \\
\frac{\partial g}{\partial \sigma_{xy}} &= \frac{1}{m}\left[g_n\right]^{\left(\frac{1}{m}-1\right)}\left[\frac{\partial g_n}{\partial \sigma_1'}\frac{\partial \sigma_1'}{\partial \sigma_{xy}} + \frac{\partial g_n}{\partial \sigma_2'}\frac{\partial \sigma_2'}{\partial \sigma_{xy}} + \frac{\partial g_n}{\partial \sigma_1''}\frac{\partial \sigma_1''}{\partial \sigma_{xy}} + \frac{\partial g_n}{\partial \sigma_2''}\frac{\partial \sigma_2''}{\partial \sigma_{xy}}\right]
\end{aligned} \tag{3.10}$$

where

$$\begin{aligned}
\frac{\partial g_n}{\partial \sigma_1'} &= \frac{m}{2}\left|\sigma_1'\right|^{m-1} & \frac{\partial g_n}{\partial \sigma_1''} &= \frac{m}{2}\left|\sigma_1'' - \sigma_2''\right|^{m-1} \\
\frac{\partial g_n}{\partial \sigma_2'} &= \frac{m}{2}\left|\sigma_2'\right|^{m-1} & \frac{\partial g_n}{\partial \sigma_2''} &= -\frac{m}{2}\left|\sigma_1'' - \sigma_2''\right|^{m-1}
\end{aligned} \tag{3.11}$$

and

$$\left.\begin{matrix}\frac{\partial\sigma_1'}{\partial\sigma_x}\\ \frac{\partial\sigma_2'}{\partial\sigma_x}\end{matrix}\right\} = \frac{a_8}{2} \pm \frac{a_2}{4}\frac{a_2\cdot\sigma_x - a_3\cdot\sigma_y}{\sqrt{\left(\frac{a_2\cdot\sigma_x - a_3\cdot\sigma_y}{2}\right)^2 + (a_4)^2\cdot\sigma_{xy}\sigma_{yx}}}$$

$$\left.\begin{matrix}\frac{\partial\sigma_1'}{\partial\sigma_y}\\ \frac{\partial\sigma_2'}{\partial\sigma_y}\end{matrix}\right\} = \frac{a_1}{2} \mp \frac{a_3}{4}\frac{a_2\cdot\sigma_x - a_3\cdot\sigma_y}{\sqrt{\left(\frac{a_2\cdot\sigma_x - a_3\cdot\sigma_y}{2}\right)^2 + (a_4)^2\cdot\sigma_{xy}\sigma_{yx}}} \qquad (3.12)$$

$$\left.\begin{matrix}\frac{\partial\sigma_1'}{\partial\sigma_{xy}}\\ \frac{\partial\sigma_2'}{\partial\sigma_{xy}}\end{matrix}\right\} = \pm\frac{(a_4)^2\cdot\sigma_{xy}}{\sqrt{\left(\frac{a_2\cdot\sigma_x - a_3\cdot\sigma_y}{2}\right)^2 + (a_4)^2\cdot\sigma_{xy}\sigma_{yx}}}$$

and

$$\left.\begin{matrix}\frac{\partial\sigma_1''}{\partial\sigma_x}\\ \frac{\partial\sigma_2''}{\partial\sigma_x}\end{matrix}\right\} = \frac{1}{2} \pm \frac{a_5}{4}\frac{a_5\cdot\sigma_x - a_6\cdot\sigma_y}{\sqrt{\left(\frac{a_5\cdot\sigma_x - a_6\cdot\sigma_y}{2}\right)^2 + (a_7)^2\cdot\sigma_{xy}\sigma_{yx}}}$$

$$\left.\begin{matrix}\frac{\partial\sigma_1''}{\partial\sigma_y}\\ \frac{\partial\sigma_2''}{\partial\sigma_y}\end{matrix}\right\} = \frac{1}{2} \mp \frac{a_6}{4}\frac{a_5\cdot\sigma_x - a_6\cdot\sigma_y}{\sqrt{\left(\frac{a_5\cdot\sigma_x - a_6\cdot\sigma_y}{2}\right)^2 + (a_7)^2\cdot\sigma_{xy}\sigma_{yx}}} \qquad (3.13)$$

$$\left.\begin{matrix}\frac{\partial\sigma_1''}{\partial\sigma_{xy}}\\ \frac{\partial\sigma_2''}{\partial\sigma_{xy}}\end{matrix}\right\} = \pm\frac{(a_7)^2\cdot\sigma_{xy}}{\sqrt{\left(\frac{a_5\cdot\sigma_x - a_6\cdot\sigma_y}{2}\right)^2 + (a_7)^2\cdot\sigma_{xy}\sigma_{yx}}}$$

The flow-stress ratios and *r*-values from the model for the 0°-, 45°- and 90°-direction were found from Equations (3.6), (3.9) and (3.8). The eight

parameters were found by fixing the point $\sigma_x/\sigma_0 = \sigma_y/\sigma_0 = 1.0$ and $\sigma_{xy}/\sigma_0 = 0.0$ (as mentioned earlier), and minimizing the sum of squares between the model and the experimental data. However, since a small difference in the flow-stress ratio is more significant than in the *r*-values (which are additionally less accurately measurable than the flow stresses) (Aretz, 2004), it was desirable to let the flow-stress ratios have more weight than the *r*-values when minimizing the sum of squares between the model and the experimental data. But a systematic method of weighting was preferred, and therefore the *r*-values was raised to the power of 1/(*m*-1). This fraction was chosen based on a very simple reflection: The yield function is a function of the m^{th} root of stresses raised to the power of *m* (see Equation (3.5)). The *r*-value is expressed as a function of derivatives of different stress components (see Equation (3.6)). Very simplified, one could say that the *r*-value is a function of stresses raised to the power of (*m*-1), or that the *r*-value could systematically be weighted by raising the *r*-value to the power of 1/(*m*-1). The weighting and minimizing of the sum of squares between the model and the experimental data can be summarized in the following equation. Thus, the *r*-values was raised to the power of 1/(m-1) to let the flow-stress ratios have more weight than the *r*-values

$$\sum_{\alpha}^{0^\circ,45^\circ,90^\circ}\left(G_\alpha^{\exp}-\left.\frac{\hat{\sigma}_\alpha}{\bar{f}_0}\right|_{\text{model}}\right)^2+\sum_{\alpha}^{0^\circ,45^\circ,90^\circ}\left(\left(r_\alpha^{\exp}\right)^{\frac{1}{m-1}}-\left(r_\alpha^{\text{model}}\right)^{\frac{1}{m-1}}\right)^2+\left(\left(r_b^{\exp}\right)^{\frac{1}{m-1}}-\left(r_b^{\text{model}}\right)^{\frac{1}{m-1}}\right)^2=\min \quad (3.14)$$

The measured flow-stress ratios and *r*-values together with the results from the calibration are given in Table 3-8. The compression tests in this study were carried out for only three materials i.e. AA7108-W, AA7108-T6 and AA7003-T79, the equibiaxial parameters, however, for the longitudinals of AA7003-T1 and AA6060-T1 were taken from the study of Achani et al. (2005) for temper T6 for both materials. Thus, it was possible to determine the model parameters for all the materials. The identified yield surfaces for the different materials and tempers are given by Reyes et al. (2005).

3.4.3 Fracture parameters

3.4.3.1 Critical thickness strain (*CFS*)

Yeh et al. (1999) suggested that a critical fracture strain *CFS* can be used as the critical thickness strain (i.e. $\varepsilon_{cr} = CFS$). *CFS* is defined as

$$CFS = -\ln(1-e_t) = -\ln\left[\left(1-\frac{e_u}{2}\right)\frac{s_f}{s_u}\right] \tag{3.15}$$

where

$$e_t = \frac{e_u}{2} + \left(1-\frac{e_u}{2}\right)\left(1-\frac{s_f}{s_u}\right) \tag{3.16}$$

Table 3-8 Measured values used to calibrate *Yld2003*, and corresponding material parameters.

		Bumper beam		Longitudinal		
	Alloy	AA7108		AA7003		AA6060
	Temper	W	T6	T79	T1	T1
Flow-stress ratio	G_0	1.00	1.00	1.00	1.00	1.00
	G_{45}	0.92	0.93	0.91	0.89	1.02
	G_{90}	1.06	1.06	0.96	0.99	0.99
r-value	r_0	0.21	0.27	0.38	0.30	0.48
	r_{45}	1.94	1.67	1.51	1.38	0.29
	r_{90}	1.19	1.16	1.05	1.17	1.76
Equibiaxial *r*-value	$1/r_b$	2.38	1.49	1.55	1.79*	2.23*
Yld2003 parameters	a_1	0.842	0.839	0.980	0.924	0.923
	a_2	0.998	0.979	1.103	1.061	1.029
	a_3	0.920	0.969	1.050	1.002	0.936
	a_4	1.081	1.087	1.154	1.229	1.086
	a_5	0.839	0.055	0.897	0.874	0.932
	a_6	0.952	0.979	1.059	1.035	1.047
	a_7	1.120	1.103	1.116	1.131	0.868
	a_8	1.147	1.161	1.015	1.069	1.062
	m	8	8	8	8	8

*Values taken from Achani (2005) for T6 temper condition.

where, s_u is the ultimate engineering stress, e_u the corresponding engineering strain and s_f is the engineering stress at fracture, see Figure 2-1. As the parameters are given from a standard tensile test, the *CFS* parameter is very easy to use and calibrate.

The following three assumptions were basis for the development of *CFS* (Yeh et al., 1999):

$$\begin{aligned} &\text{i)} \quad \varepsilon_2 = \varepsilon_3 && \text{for} \quad e \le e_u \\ &\text{ii)} \quad \varepsilon_2 = \text{constant} && \text{for} \quad e \ge e_u \\ &\text{iii)} \quad \sigma_1 = \sigma_{1u} && \text{for} \quad e \ge e_u \end{aligned} \tag{3.17}$$

In order to include anisotropy, the first assumption can be modified to

$$\varepsilon_2 = r\varepsilon_3 \quad \text{for} \quad e \le e_u \tag{3.18}$$

where r is the r-value for the actual test specimen. By using these three assumptions it can be shown that

$$CFS^* = -\ln\left[\left(1+e_u\right)^{-\frac{1}{1+r}} \cdot \frac{s_f}{s_u} \right] \tag{3.19}$$

For an isotropic material ($r = 1$) the exponent $-1/(1+r)$ equals -½. By expanding the term $(1+e_u)^{-1/2}$ as a binomial series, assuming $|e_u| \ll 1$, and retaining only the first two terms in the series, *CFS** for an isotropic material can be approximated to *CFS* in Equation (3.15). *CFS** is easily calculated from the engineering stress-strain data and the r-values (from Table 3-3). *CFS** was calculated for all repetitions, and the selected values for bumper beam and longitudinals in 0°-direction are given in Table 3-9. The variation in *CFS** is discussed by Reyes et al. (2005).

3.4.3.2 Cockcroft Latham (CL)

The critical "plastic work" W_{cr} as defined by Cockcroft and Latham (1968) reads

$$W_{cr} = \int_0^{\bar{\varepsilon}_f} \max\left(\sigma_1, 0\right) \mathrm{d}\bar{\varepsilon} \tag{3.20}$$

and can e.g. be estimated from a uniaxial tension test by using the three assumptions in Equation (3.17) (Reyes et al., 2004). The integral can be divided in two parts; for $e \le e_u$ and $e \ge e_u$:

$$W_{cr} = \int_0^{\bar{\varepsilon}_u} \sigma_1 \mathrm{d}\bar{\varepsilon} + \int_{\bar{\varepsilon}_u}^{\bar{\varepsilon}_f} \sigma_1 \mathrm{d}\bar{\varepsilon} = \int_0^{\bar{\varepsilon}_u} \sigma_1 \mathrm{d}\bar{\varepsilon} + s_u \left(1 + e_u\right)\left[\bar{\varepsilon}_f - \bar{\varepsilon}_u\right] \tag{3.21}$$

Here, the effective strain at maximum stress equals the true strain in the tensile direction:

$$\bar{\varepsilon}_u = \ln\left(1 + e_u\right) \tag{3.22}$$

and the effective strain at fracture follows from Equation (3.17)$_{(ii)}$:

$$\bar{\varepsilon}_f = \ln\left(1 + e_u\right) + \frac{2}{\sqrt{3}} \ln\left(\frac{s_u}{s_f}\right) \tag{3.23}$$

It is consequently possible to calculate the critical "plastic work" from the stress-strain data from a uniaxial tensile test. If the true stress-strain curve is fitted to the extended Voce rule in Equation (2.22), one can also use this equation for σ_1 in the first integral in Equation (3.21). The following estimate for W_{cr} is then found (Reyes et al., 2004):

$$\begin{aligned} W_{cr} = {} & \left(\sigma_0 + Q_{R1} + Q_{R2}\right) \ln\left(1 + e_u\right) - \frac{Q_{R1}}{C_{R1}} - \frac{Q_{R2}}{C_{R2}} + \\ & \left(1 + e_u\right) s_u \frac{2}{\sqrt{3}} \ln\left(\frac{s_u}{s_f}\right) + \frac{Q_{R1}}{C_{R1}} \left(1 + e_u\right)^{-C_{R1}} + \frac{Q_{R2}}{C_{R2}} \left(1 + e_u\right)^{-C_{R2}} \end{aligned} \tag{3.24}$$

Here, it is assumed that $C_{Ri} > 0$, but $Q_{Ri} \geq 0$, and that the material is isotropic. The selected values for Cockcroft-Latham parameter (W_{cr}) are also given in Table 3-9 (Reyes et al., 2005).

3.5 Process effects

When a component is formed, the material is usually in the soft W-temper state, which means lower force requirement, increased ductility, less springback and a more controlled forming operation. After forming the part, it is heat treated to achieve the desired strength/ductility properties (i.e. the desired temper for the finished product). Traditionally, in numerical simulations of such components, the homogenous material properties of the final temper in its virgin/undeformed state would be used. However, it is possible to include the process effects in numerical analyses to perform "process-based" crash simulations. This can be very important in regard to accuracy of analyses in general. Additionally, it can be especially important in connection with fracture modelling, as forming operations lead to a significant variation in thickness and in material properties, i.e. *inhomogeneity* that can promote strain localisation.

One aspect regarding the process-based crash simulation is to represent the reduced strength and ductility in itself. However, it might be equally or even more important to include the resulting inhomogeneity in the structure. This inhomogeneity in geometry (thickness), yield stress and hardening (thus ductility) might cause totally different deformation patterns than if

Table 3-9 Critical fracture values for bumper beam and longitudinal materials.

	Bumper beam		Longitudinal		
Alloy	AA7108		AA7003		AA6060
Temper	W	T6	T79	T1	T1
CFS^* parameter	0.24	0.19	0.36	0.12	0.63
W_{cr}	66	108	159	71	113

homogenous properties were present/assumed. From a perspective of robust performance it is also of interest to understand and control the resulting inhomogeneity and possibly design alternative forming or heating sequences.

An experimental program was carried out: (1) to investigate the effect of forming in W-temper on the stress-strain behaviour of a tensile test in temper T6 and (2) use the results to model this effect in LS-DYNA, similar to the previous work of Lademo et al. (2004c). The test programme and experimental details are given by Reyes et al. (2005). The results from the tests are presented in the following.

3.5.1 Results

Engineering stress-strain curves from the uniaxial tensile tests of the pre-stretched specimens are given in Figure 3-15, while true stress-strain curves are shown in Figure 3-16. There is a well-defined effect of the amount of pre-stretching, especially for the batch that only had one hour in room

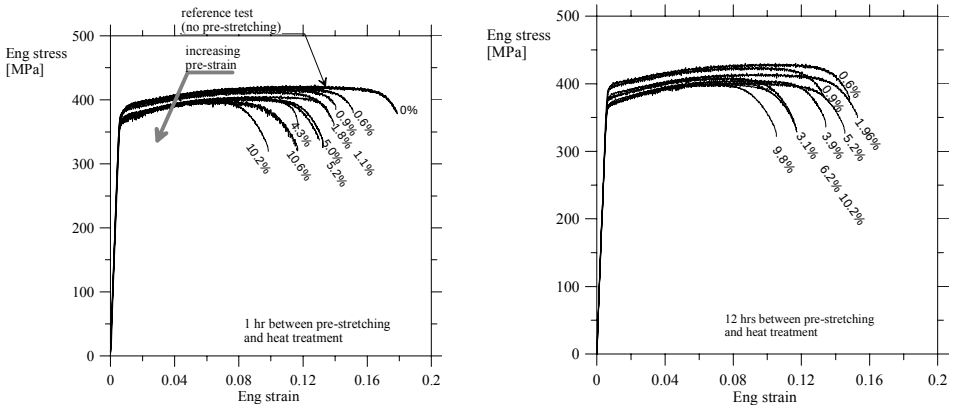

Figure 3-15 Engineering stress-strain curves for specimens in T6 temper after stretching until fracture; specimens with 1 (left) and 12 (right) hours in room temperature between pre-stretching and heat treatment.

temperature before heat treatment; the stress levels and ductility decrease for increasing pre-strain. The trend is the same for the 12-hour-batch; however, the ductility does not necessarily decrease for increasing pre-strain for all the tests. Furthermore, the onset of diffuse necking in the specimen deformed to 10% plastic strain occurs as early as 6% opposed to 12% in the reference test.

In Figure 3-17 the engineering stress-strain curves from the quasi-static uniaxial tensile tests presented in Section 3.1 are shown together with some of the curves from the pre-stretched specimens. As one can see, the curve for the reference test that was not pre-stretched, but given the same heat treatment as the pre-stretched specimens, is very close to the curves from the uniaxial tests on specimens taken directly from an unformed bumper beam. This confirms that the heat treatment given to the pre-stretched specimens is comparable to the heat treatment of the extrusions.

The true flow stresses at 2% strain of the pre-stretched specimens were observed from the curves and are given in Table 3-10 and Table 3-11 as σ_2. The normalized stresses, i.e. the ratio between the considered flow stress

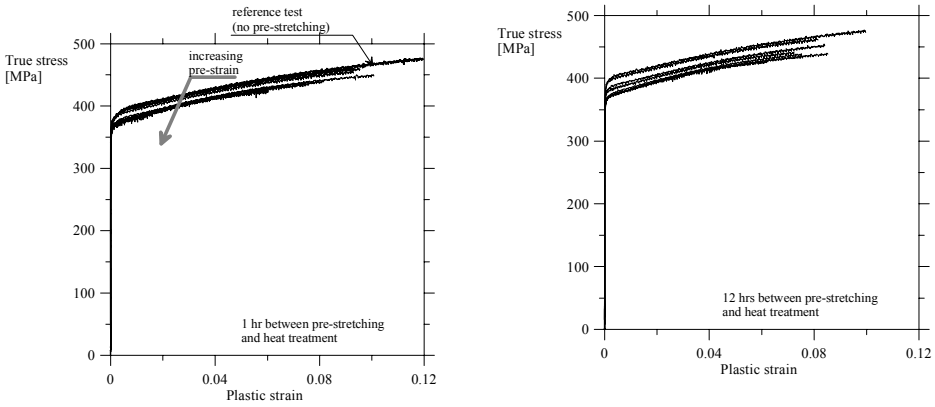

Figure 3-16 True stress-strain curves for specimens in T6 temper after stretching until fracture; specimens with 1 (left) and 12 (right) hours in room temperature between pre-stretching and heat treatment.

and the flow stress for 0% pre-strain vs. the plastic pre-strain are shown in Figure 3-18. Here it is obvious how the flow stress decreases with increasing amount of pre-strain. For the batch that was in room temperature only one hour, the flow stress flattens off already after approximately 2% of pre-strain. The flow stresses of the specimens in the second batch that lay in room temperature for 12 hours, continues to drop until approximately 4% before the curve flattens.

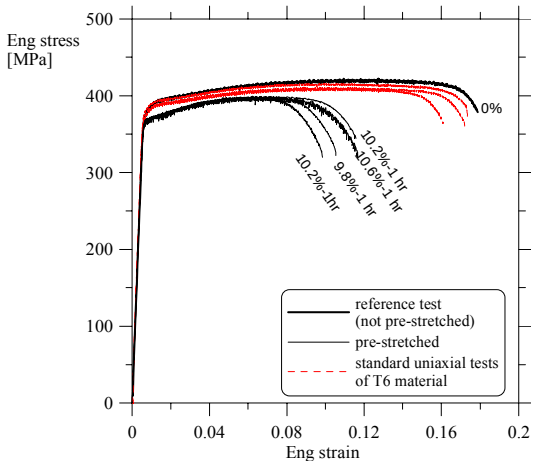

Figure 3-17 Comparison with the standard uniaxial test from the same material.

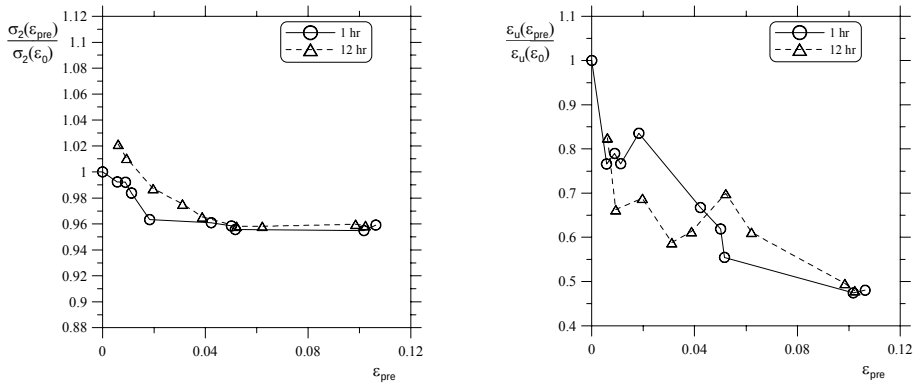

Figure 3-18 Normalized true flow stress vs. plastic pre-strain (left) and normalized true strain at diffuse necking vs. plastic pre-strain (right).

3.5.2 Parameters to be used in process-based crash analyses

The simplest method assumes that only the yield stress is influenced by the pre-strain and the strain-hardening is unaffected, Lademo et al. (2004c; 2005). If this option is chosen, the input data in the model should be a curve of the pre-strain versus the yield stress, which for instance could be σ_2 in Table 3-10 and Table 3-11.

A more refined method assumes that also the strain-hardening is influenced by the pre-strain. The input is in that case fitted Voce parameters for different pre-strains. The program generates stress-strain curves corresponding to these Voce parameters for the given pre-strains, and linearly interpolates between the prescribed curves to find the correct curve for an intermediate value of pre-strain. Therefore, the true stress-strain curves were fitted to the Voce hardening rule (Equation (2.22)), and the different curve parameters are listed in Table 3-10 and Table 3-11.

Table 3-10 Yield stress and Voce-parameters for tests that lay one hour in room temperature between pre-stretching and heat treatment.

plastic pre-strain	Stress at 2% strain	Curve parameters					
	σ_2	σ_0	Q_{R1}	C_{R1}	Q_{R2}	C_{R2}	$\sigma_0+\Sigma Q$
[%]	[MPa]	[MPa]	[MPa]	[-]	[MPa]	[-]	[MPa]
0	411	355	34.5	714	136	8.41	525
0.572	408	356	30.8	1478	126	9.39	513
0.889	408	354	30.3	1563	116	10.9	500
1.828	396	328	45.2	3576	105	12.8	478
4.228	395	326	44.4	4501	97.1	15.3	467
5.163	393	309	60.2	4501	100	14.8	470
10.64	394	307	59.2	4501	89.2	17.5	456
1.123	404	333	48.2	4200	111	11.8	492
5.011	394	315	51.6	4199	98.5	15.4	465
10.17	392	312	52.6	4728	87.4	19.4	452

3.6 Verification of user-defined material model (MAT-41)

To verify the user-defined material model in LS-DYNA, simulations were performed on a four node element as shown in Figure 3-19(a), at different strain-rates. As the experimental data at different strain-rates was available, see Section 3.2, at 2% and 5% of deformation, the considered element is thus only subjected to uniaxial tension with 2% deformation. Numerical simulations were performed at strain-rates of 10^{-3}, 10^{-2}, 10^{-1}, 10, 10^{2} and 10^{3} s^{-1}. To have closely constant strain-rate within each simulation a time dependent deformation was applied on the 3-4 edge of the element. The displacement-time curve is shown in Figure 3-19(b). Constraints applied at the four nodes of the element are given in Table 3-12.

The termination time for the simulations is obtained in the following manner:

Table 3-11 Yield stress and Voce-parameters for tests that lay twelve hours in room temperature between pre-stretching and heat treatment.

plastic pre-strain	Stress at 2% strain	Curve parameters					
	σ_2	σ_0	Q_{R1}	C_{R1}	Q_{R2}	C_{R2}	$\sigma_0+\Sigma Q$
[%]	[MPa]	[MPa]	[MPa]	[-]	[MPa]	[-]	[MPa]
0.607	420	340	57.8	3552	128	9.50	526
1.964	406	313	69.5	5719	112	11.7	494
3.115	401	314	63.4	5115	101	14.1	478
3.881	397	316	54.4	5115	97.9	15.6	468
5.213	394	318	49.1	3782	95.1	16.5	462
5.163	394	318	49.8	4764	85.6	18.8	454
9.845	415	332	62.4	4594	120	10.4	514
0.929	394	306	61.9	4583	92.8	16.9	461
6.208	394	323	46.5	4708	88.4	18.6	455
10.23	420	340	57.8	3552	128	9.50	526

$$\dot{e} = \frac{\Delta l}{l_0 \cdot T_t} \quad \Rightarrow \quad T_t = \frac{\Delta l}{l_0 \cdot \dot{e}} \tag{3.25}$$

where $\dot{e}$ is the required strain-rate, l_0 is the original length (2 mm), Δl is the change in length (0.04 mm) and T_t termination time. Thus calculated simulation termination times at different strain-rates are given in Table 3-13.

From Table 3-13, at 10^{-3} s^{-1} strain-rate the calculated termination time is 20 seconds which is a very long time in running the simulation. Hence mass-scaling was employed for this simulation only. After mass-scaling the new

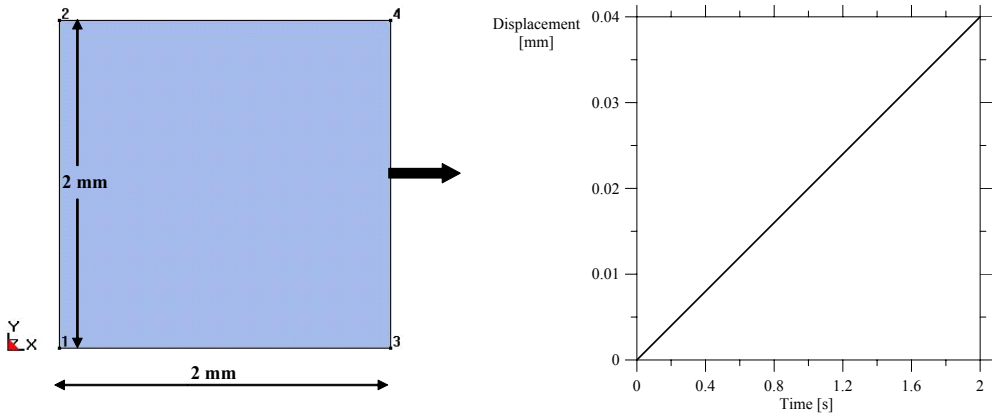

(a) (b)

Figure 3-19 (a) Four node element used in verifying the user-defined material model and (b) Displacement time plot for deforming the four node element at ~10^{-2} s^{-1} strain rate.

Table 3-12 Constraints applied at the nodes of four node element.

Node number	Translational constraints	Rotational constraints
1	x, y and z	x and y
2	x, and z	x and y
3	y and z	x and y
4	z	x and y

termination time was $T_t = 2$ seconds. In simulations care has been taken such that there is no addition of kinetic energy because of mass-scaling.

For the uniaxial loading condition the effective stress and the stress in the loading direction i.e. in x-direction, should be equal. The simulation results for the four node element analysis at a strain-rate of ~10^{-3} s^{-1} with mass-scaling are presented in Figure 3-20(a), while Figure 3-20(b) shows the simulation results at ~10^{3} s^{-1} strain-rate. In these figures the effective stress

Table 3-13 Four node element simulation termination time at different strain-rates.

Strain-rate $\dot{e}$ (s^{-1})	Deformation Δl (mm)	Termination time T_t (s)
10^{-3}	0.04	20
10^{-2}	0.04	2
10^{-1}	0.04	$2x10^{-1}$
10	0.04	$2x10^{-3}$
10^{2}	0.04	$2x10^{-4}$
10^{3}	0.04	$2x10^{-5}$

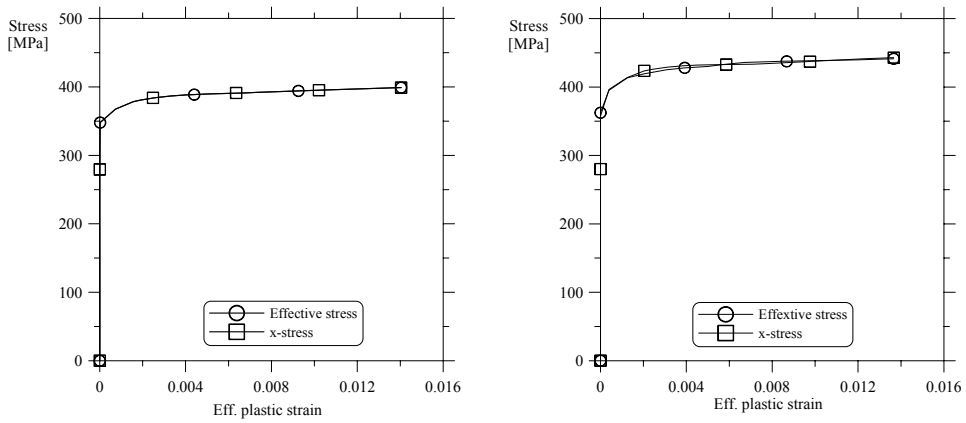

Figure 3-20 Comparison of stresses in the four node element analyses at (a) ~10^{-3} s^{-1} and (b) ~10^{3} s^{-1} strain-rates.

and stress in x-direction are compared with respect to effective plastic strain.

Stress levels predicted, at 2% plastic deformation, at different strain-rates in the analyses of the four node element are compared with the experimentally obtained values in Figure 3-21. The stress level predicted in the four node element analyses at different strain-rates is close to the experimental results. This shows that the user-defined material model is capable of representing the strain-rate sensitivity of the material accurately.

3.7 Simulation of quasi-static tensile test with shell elements

An FE-model was made to simulate the tensile tests of only bumper beam material in T6 temper condition i.e. AA7108-T6. For the geometry modelling of tensile test specimen in simulations, specimen type B as shown in Figure 3-1 was utilised, which is the same as that used in quasi-static tests. The specimen was modelled with shell elements having an initial random Gauss-distributed thickness (Berstad et al., 2004) with a coefficient of variation of the thickness CoV(t) = 0.0315, see Figure 3-22. For the

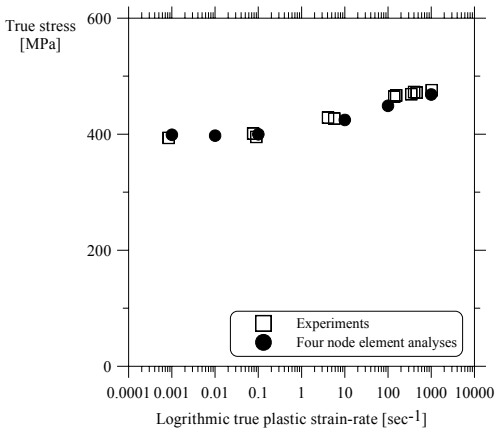

Figure 3-21 Comparison of four node element analyses results with experiments at 2% true strain.

simulation of a uniaxial tensile test the inhomogeneity in thickness is not strictly required. However, modelling of thickness variations might improve the prediction of strain localisation and thus fracture in the specimen. The tensile test specimens in the experiments were taken from the back face of the bumper beam, see Figure 4-2(a), whose nominal thickness was 4 mm. The properties used in running the tensile test simulations are given in Table 3-14.

3.7.1 Explicit simulations

The specimens were simulated with the *CFS** fracture criterion. Two mesh sizes and two types of element formulations were applied, as given in Table 3-15, with five through-thickness integration points. Two cylindrical contact entities (option available in LS-DYNA) as shown in Figure 3-22(b) were employed in deforming the tensile test specimen (Hallquist, 2003). For the left contact entity all degrees of freedom were fixed, while the right contact

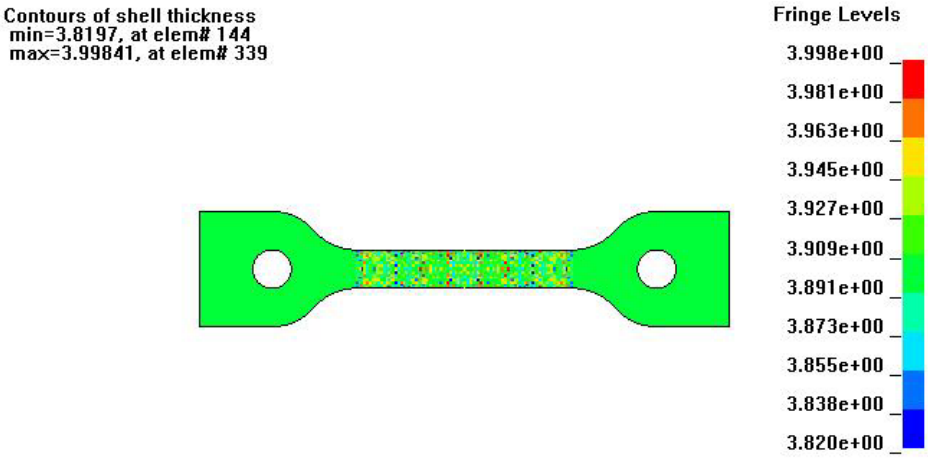

(a) Top view

(b) Front view

Figure 3-22 FE-model with initial thickness inhomogeneity for tensile test analysis.

entity was loaded with a ramping velocity to avoid spurious noise, see Figure 3-23.

Table 3-14 Material parameters used in running tensile test simulations.

Parameter	Value	
σ_0	347	[MPa]
Q_{R1}	37	[MPa]
C_{R1}	1017	[-]
Q_{R2}	113	[MPa]
C_{R2}	9.99	[-]
a_1	0.839	
a_2	0.979	
a_3	0.969	
a_4	1.087	
a_5	0.055	
a_6	0.979	
a_7	1.103	
a_8	1.161	

Table 3-15 Mesh sizes and element type applied in tensile test simulation.

	Element type		
	Belytschko-Tsay		Fully-integrated
Mesh	Fine (mm)	Coarse (mm)	Coarse (mm)
Mesh size in the gage section	0.25	0.5	0.5

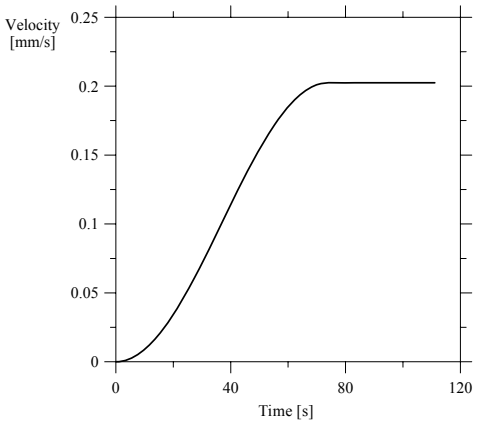

Figure 3-23 Ramping velocity signal used in loading the tensile test specimen in explicit analysis.

As can be seen from Figure 3-24, in all the simulations the localisation occurred much too early compared to the tests and thus under-prediction of the specimen's ductility. Further, one can also observe that neither the element size nor the element formulation type has any effect on the predicted curves. The reason for the early localisation is probably due to the presence of dynamic effects in the explicit simulation, although the total change in kinetic energy was small. Due to the presence of dynamic effects in the system, whenever the localisation occurs the deformation cannot be spread over and thus an entire row of elements get localised. Thus the force-displacement curve drops soon after the localisation. Furthermore, the thickness of the material probably influences the localisation in simulations. Similar behaviour was observed when the specimen was modelled without a coefficient of variation in thickness CoV(t).

3.7.2 Implicit simulations

As seen in the above section explicit simulations failed to predict the specimen's ductility due to the dynamic effects. With an intention to predict

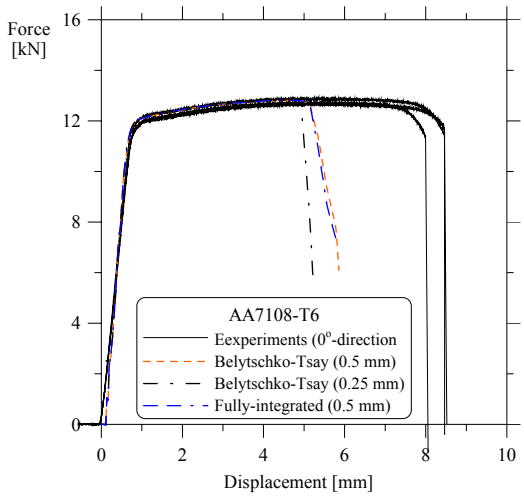

Figure 3-24 Comparison of the force-deflection curves from the tests and explicit simulation of tensile test specimen.

the exact material behaviour as in the tests, implicit simulations were performed with the same input. To avoid the contact problems during the implicit simulations (Kokkula et al., 2003) the contact entities were switched off. The deformation is induced by applying the time dependent displacement to the nodes at the location of contact entity on the right side of the specimen, while at the left-hand side of the specimen nodes at the location of contact entity were fixed. The implicit simulations were performed only with the fully-integrated element formulation see Table 3-15.

Figure 3-25 compares the force-displacement curves from the implicit simulation with the experiments. If we consider the flexibility of the testing machine both the experimental and simulated curves are on top of each other. The reason for accurate prediction of material ductility in the implicit simulation compared to the explicit simulations is due to the spreading of deformation over a large area even after the onset of diffuse necking.

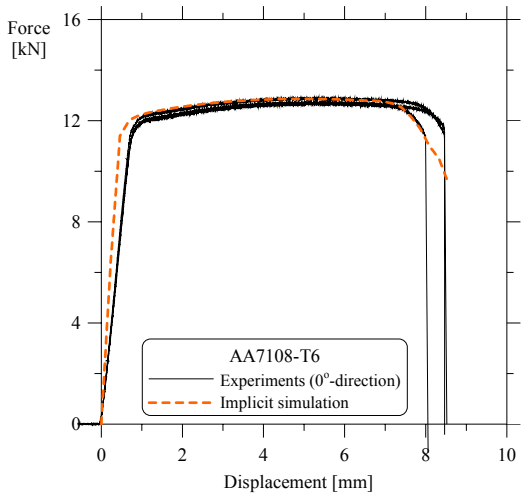

Figure 3-25 Comparison of the force-deflection curves from tests and implicit simulation.

Chapter 4 Experimental Programme

In this chapter the test programme and test set-up of bumper beam-longitudinal system are presented. The overall test programme is discussed in Section 4.1. The penultimate Section 4.2 describes the test set-up. The loadcells used for measuring the force signals as a function of time in the experiments were calibrated prior to the tests; the calibration procedure of the loadcells is presented in Section 4.3. In Section 4.4 the instrumentation and data acquisition systems are discussed.

4.1 Test programme

The bumper beam is a box-like structure produced from an aluminium extrusion that was plastically formed to the required curvature by stretch-bending in a soft condition (W-temper), obtained by solid-solution heat treatment and quenching. After forming, the bumper beams are artificially age-hardened to T6 peak hardness condition. The configuration of the bumper beam-longitudinal system at 40% offset that was tested in this work is shown in Figure 4-1. The cross-section details of the bumper beam at section A-A in Figure 4-1 are shown in Figure 4-2(a). The longitudinal cross-section details at section B-B (in Figure 4-1) are shown in Figure 4-2(b), while Figure 4-2(c) provides the interface plate details. It is interesting to note that the vertical face of the bumper beam, see Figure 4-2(a), is concave in the vertical plane - a feature which Tang (1979) found to be associated with the highest resistance to denting.

During testing the free length of the longitudinals was kept constant at 650 mm, and the longitudinal was cut to 8° inclination at one end, Figure 4-2(d). This cut ensured that the longitudinal after welding to the interface plate

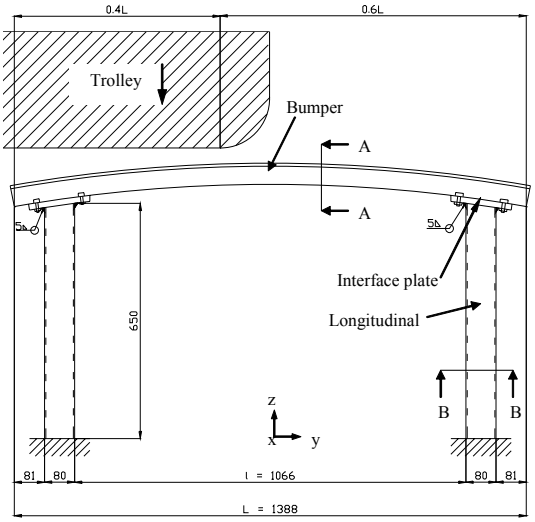

Figure 4-1 Configuration of the bumper beam-longitudinal system at 40% offset impact.

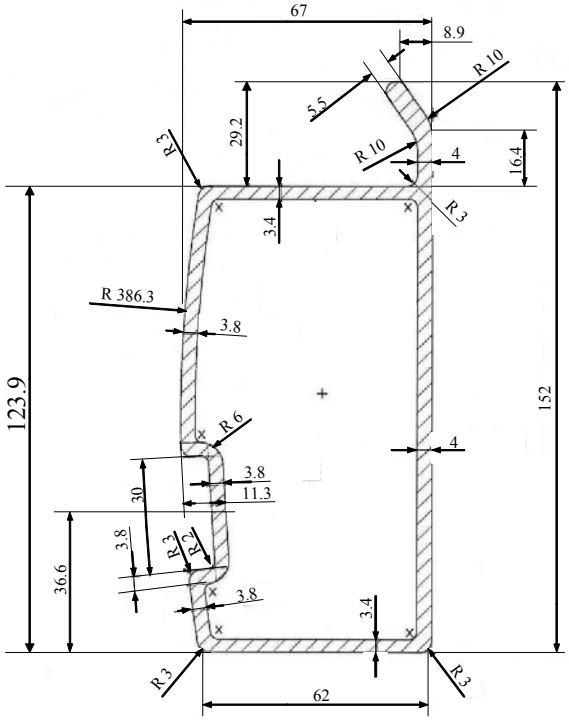

(a)

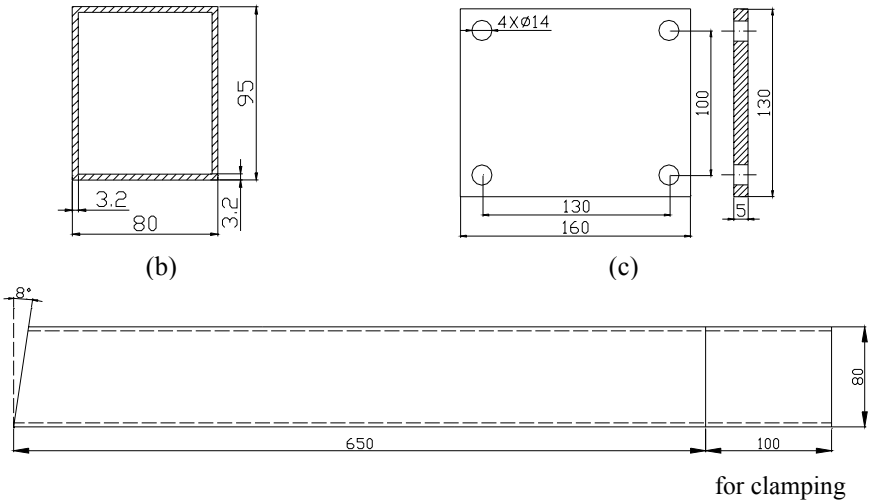

Figure 4-2 Cross-section and detailed dimensions of (a) bumper beam at section A-A (Figure 4-1) rotated by 90°, (b) longitudinal at section B-B, (c) interface plate details and (d) longitudinal.

Table 4-1 Test programme for testing bumper beam-longitudinal system.

Test	Longitudinals	Impact velocity v_0 (m/s)	SIMLab Reference
Series **A**			
A1	AA7003-T79	10	TEST-1-T79
A2			TEST-2-T79
A3			TEST-3-T79
A4			TEST-4-T79
A5			TEST-5-T79
Series **B**			
B1	AA7003-T1	10	TEST-1-AT1
B2			TEST-2-AT1
B3			TEST-3-AT1
Series **C**			
C1	AA6060-T1	10	TEST-1-BT1
C2			TEST-2-BT1
C3			TEST-3-BT1
Series **D**			
D1	AA7003-T79	15	HS-1
D2			HS-2
D3			HS-3
Bumper beam in alloy AA7108-T6			

was positioned properly on the back face of the bumper beam. The bumper beam was fixed to the longitudinals by using M12 bolts via the interface plate. The lower 100 mm of the longitudinal was used for clamping in the test rig.

A summary of the test programme is presented in Table 4-1. As mentioned, longitudinals of two different alloys (AA7003 and AA6060) and two temper conditions (T79 and T1) were tested, while using a single alloy (AA7108-T6) for the bumper beam. None of the longitudinals were triggered to initiate a particular deformation mode. Prior to testing, the width, height, length and wall thickness of the extruded longitudinals were measured. The impact velocity (v_0) was chosen as 10 m/s (~ 36 km/h) and 15 m/s (~ 54 km/h). The impactor (trolley) mass was kept constant at 794 kg, thus the kinetic energy (hereafter called impact energy) was also kept constant at 39.7 kJ and 89.3 kJ, respectively.

4.2 Test set-up

4.2.1 The kicking machine

The kicking machine, Figure 4-3, is the name of the device used for testing the bumper beam-longitudinal systems. Hanssen et al. (2003a) have discussed thoroughly the working procedure of the kicking machine for high-speed offset (50%) testing of automotive bumper beam systems. Jensen (2005) used the kicking machine to study the axial loading of hollow extrusions (interaction between local and global buckling). Axial crushing of self-pierce riveted double hat sections is analysed by Hanssen et al. (2003b) utilising the test data from kicking machine. This section provides a brief overview of the kicking machine and is mostly based upon Hanssen et al. (2003a).

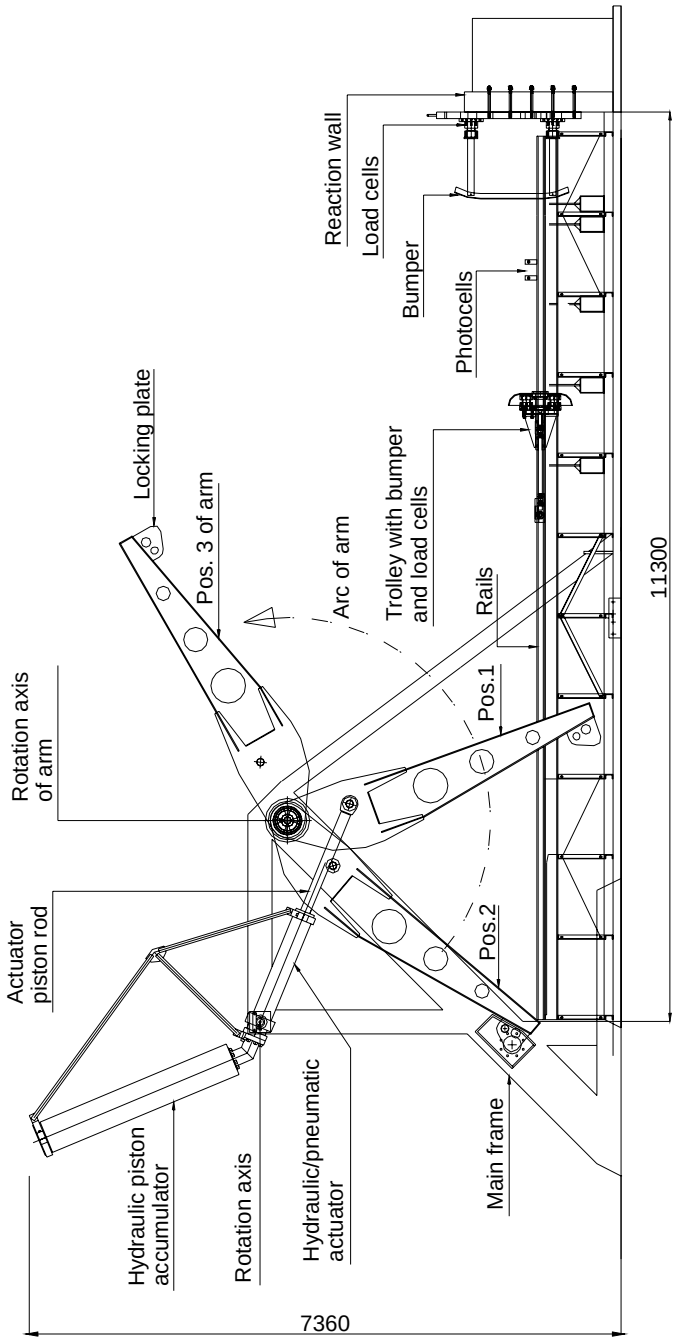

Figure 4-3 Illustration of kicking machine at SIMLab, NTNU.

The bumper beam-longitudinal system was fixed to the reaction wall of the kicking machine using a fixture and loadcell at the bottom end of the longitudinal on both sides. Two loadcells were fixed to the reaction wall with six M16 bolts for each loadcell. The loadcell details are shown in Figure 4-9 and will be discussed thoroughly in Section 4.3. The frontal flange of the loadcell has a square cross section and was fitted with four 11 mm holes, one in each corner, to accommodate the fixture.

Details of the fixture are shown in Figure 4-4(a). The longitudinal along with the interface plate was inserted into the fixture through the rectangular slot at its centre. This slot (80x95 mm^2) in the fixture was machined such that the longitudinal easily fits inside. Three tapered sliding blocks, see Figure 4-4(b), were placed inside the longitudinal and hammered from the other end of the longitudinal. As the tapered blocks slide one over the other a rigid clamping of the longitudinal inside the fixture was ensured (over a length of 100 mm). A circular hole was made in the interface plate for the purpose of hammering the tapered blocks. However, this hole was not

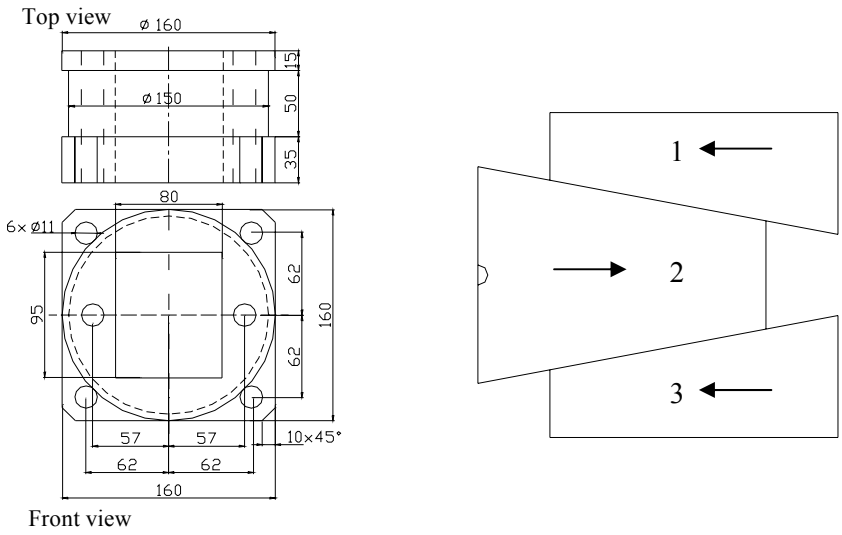

(a) (b)

Figure 4-4 (a) Fixture details, (b) Sliding blocks used for fixing the longitudinal inside the fixture

shown in Figure 4-2(c).

The accelerating system consists of an arm that rotates around a set of bearings, i.e. the arm is free to rotate in the plane of Figure 4-3. Note that the arm is open like a crankshaft at the bearing end. The arm itself is connected to a hydraulic/pneumatic actuator system, which provides the moving force. This system accelerates the trolley up to the desired impact velocity.

The trolley traverses the length of the rails and hits the test specimen located at far end. The impact velocity of the trolley is measured by means of a photocell system located directly in front of the test specimen. In general, the test specimen will not have enough capacity to absorb all the impact energy of the trolley by itself, a secondary energy absorbing system was required to prevent the damage to the loacell. For this reason the trolley has rigid buffer plates on both sides of the loadcell. These buffer plates hit the crashboxes fixed to the reaction wall, which ensure the integrity of the loadcells, see Figure 4-5.

Four loadcells were employed, two on the trolley and one at each end of the longitudinal. The front end details of the trolley are shown in Figure 4-6. The loadcells fixed to the reaction wall measure the axial force as well as two orthogonal bending moments see Figure 4-7. As the loadcell is made of high strength steel, it is assumed to behave elastically during impact. The force-voltage characteristics are obtained statically using a hydraulic actuator and are calibrated as described in Section 4.3.

4.2.2 Equations of motion

The acceleration, velocity and displacement history of the trolley was obtained from the total force signal of the loadcells on the trolley. Let

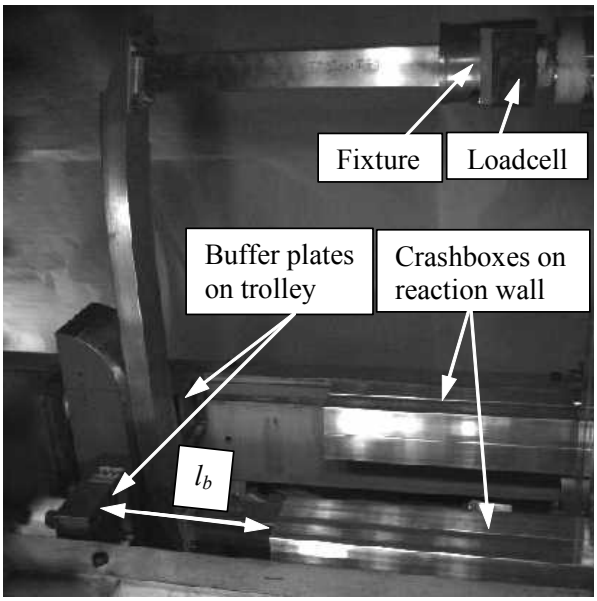

Figure 4-5 Pre-crash photo of bumper beam-longitudinal system showing the buffer plates on trolley, crashboxes on reaction wall, fixture, loadcell and the measurement of distance between the buffer plates and crashboxes on the reaction wall.

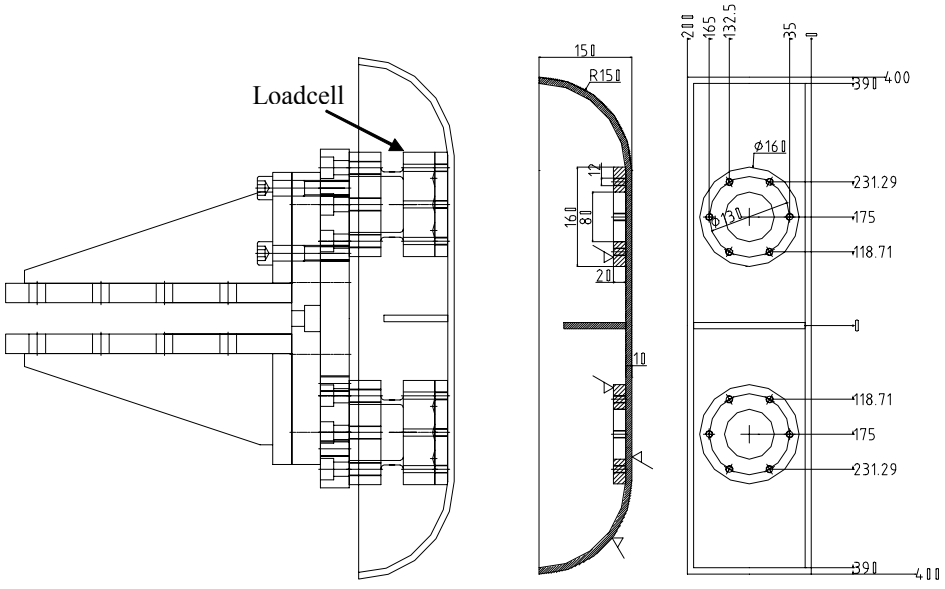

Figure 4-6 Details of trolley front end.

M_B (742 kg) and M_N (52 kg) denote the mass of the trolley located at the rear and in front of the strain gauges of the loadcells respectively, see Figure 4-8. The total force-time history recorded by the loadcells on the trolley is $P(t)$, whereas the impact force acting on the test specimen is $F(t)$. Equations of motion for the backing mass M_B and front mass M_N are obtained by assuming unidirectional rigid-body motion of the system shown in Figure 4-8.

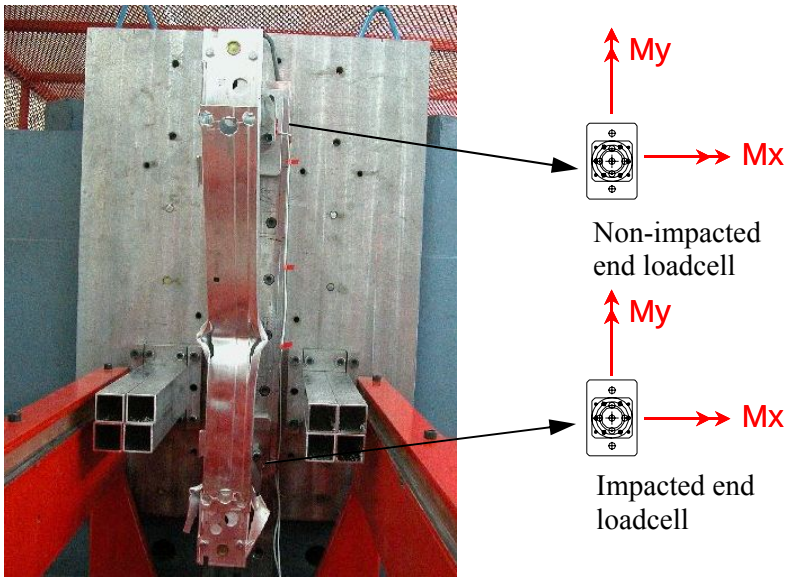

Figure 4-7 Post-crash photo of bumper beam-longitudinal system.

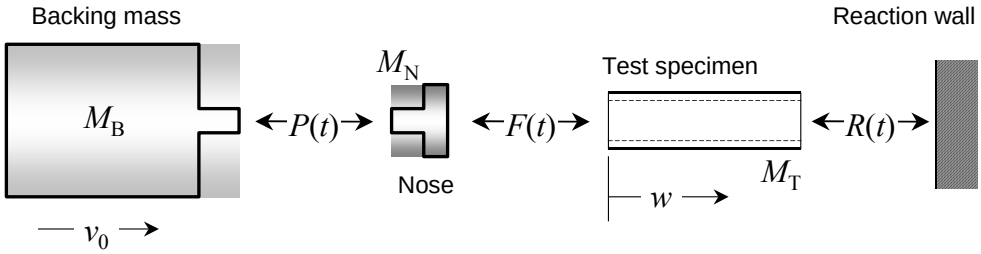

Figure 4-8 Rigid-body diagram of generalised test set-up.

The equations are:

$$\ddot{w} = -\frac{P(t)}{M_B} \tag{4.1}$$

and

$$F(t) = P(t) - M_N \ddot{w} \tag{4.2}$$

where w is the displacement of the trolley measured from the moment of impact.

When the above equations are combined, the relation between $F(t)$ and $P(t)$ is obtained as

$$F(t) = \varsigma_f \cdot P(t) \tag{4.3}$$

$$\varsigma_f = 1 + \frac{M_N}{M_B} \tag{4.4}$$

Here ς_f is the rigid-body load factor. For the selected backing mass of 742 kg and 52 kg mass for the loadcell in front of the trolley, giving a rigid-body factor of 1.07. The velocity $\dot{w}(t)$ and displacement $w(t)$ of the rigid body can be expressed as

$$\dot{w}(t) = v_0 - \int_0^t \frac{P(t)}{M_B} \mathrm{d}t \tag{4.5}$$

$$w(t) = \int_0^t \dot{w}(t) \, \mathrm{d}t \tag{4.6}$$

Assuming that the impact started at time $t = 0$ and that the trolley activated the crashboxes on the reaction wall at time $t = t_b$. The displacement of the trolley was found from Equation (4.6), hence

$$w(t_b) = \int_0^{t_b} \dot{w}(t)\,\mathrm{d}t \tag{4.7}$$

Note that the time when the crashboxes were activated was obtained from video recordings see Section 4.2.3. The distance from test specimen activation until the trolley hits the crashboxes on the reaction wall l_b is easily measured prior to each test. The measurement of l_b is shown in Figure 4-5. Hence, a reliable measurement is ensured if $w(t_b) = l_b$, and the following accuracy parameter is defined

$$\xi_b = \frac{w(t_b)}{l_b} \tag{4.8}$$

When the deformation w has been obtained at each time step, the absorbed energy E and the mean force level F_{avg} are calculated as

$$E(w) = \int_0^{w} f(w)\,dw \tag{4.9}$$

$$F_{avg} = \frac{1}{w} \cdot E(w), w > 0 \tag{4.10}$$

The formulas given above assume that the only force acting on the trolley during impact arises from the test specimen and measured by the loadcells. Friction of any source was neglected (from trolley wheel bearings, from rail-wheel interface, etc.). However, when the trolley activates the crashboxes on the reaction wall at time $t = t_b$, the results given by the equations above are no longer valid.

4.2.3 High speed video camera

Two types of high speed video cameras were used to record the impact events. The cameras are Phantom v5.0 and Photron's ultima APX. In the following sections information on the resolution, frame rate and the recording mode for both cameras is presented.

4.2.3.1 Phantom v5.0

A Phantom v5.0 high speed monochrome digital video camera was used to record the impact events. The monochrome model offers a higher sensitivity and better image resolution than the colour model. The camera has a maximum frame rate of 64 000 pictures per second and a maximum resolution of 1024x1024 pixels. The frame rate is dependent on the choice of resolution, the higher the resolution the lower the frame rate will be. For recording the impact events of test series **A**, **B** and **C**, see Table 4-1, a resolution of 1024x1024 pixels were used, giving a maximum frame rate of approximately 1 100 frames per second (Phantom, 2004). When recording at 1 100 pictures per second and higher, image blur can be a problem with fast moving objects without the aid of additional shuttering. The Phantom's SR-CMOS sensor allows continuously variable shutter speeds down to 10 micro seconds (1/100 000 second) with intervals of 5 micro seconds (Phantom, 2004). The shutter is a true "snap-shot" or synchronous shutter. A standard Nikon AF Zoom-Nikkon lens with focal length 20-35 mm was used. The camera has one gigabyte of image memory. At the chosen frame rate and resolution the camera memory can store 1 second of film.

4.2.3.2 Photron's ultima APX

The camera has 10-bit monochrome, 30-bit colour CMOS sensor with large pixels and 4 micro seconds global electronic shutter that provide excellent light sensitivity and sharp imagery. The APX provides full resolution

(1024x1024 pixels) up to 2 000 frames per second, and reduced resolution all the way up to 120 000 frames per second (Photron, 2005). The APX memory can be expanded to facilitate 3 second record duration at maximum resolution and a rate of 2 000 frames per second. Further, the camera enables recording speed to be changed, up or down by a factor of four, during a recording (Photron, 2005).

Two APX cameras were used to record test series **D** tests with maximum resolution and at 2000 frames per second. Of the two cameras used, one camera was used to capture the deformation mode of the complete system and the other camera use was used to capture the folding process i.e. buckle development in the longitudinal at the impacted end and the failure process at the non-impacted end of the bumper beam.

For both cameras, the picture sequence is stored in the camera during recording and transferred to a PC after the test using FireWire data transfer. Prior to the test, the camera is set to continuously film using a FIFO (first in first out) memory buffer system. Manual post-triggering was used, i.e. the camera was triggered after the test was completed and all pictures already in the memory were transferred to the computer used to store the films from the experimental tests.

4.2.4 Operation of kicking machine

The operation of the kicking machine will now be described (Hanssen et al., 2003a). Assume that the arm is in its neutral position, a little to the right of the vertical (Pos. 1, Figure 4-3). The arm is connected to the piston rod of a hydraulic/pneumatic actuator that is directly connected to a hydraulic accumulator of the piston type. The volume between the actuator piston and the accumulator piston is filled with hydraulic oil. When preparing for a test, a valve is opened to let pressurised air from the house mains into the piston rod side of the actuator. The arm will now move slowly back as the excess oil flows back to the tank of the hydraulic power supply. When the

arm reaches it's starting position (Pos. 2, Figure 4-3) two hydraulic cylinders, one on each side, will lock the arm by pressing against the locking plate.

The gas (nitrogen) pressure in the accumulator is normally much higher than the air pressure from the house main. Therefore the accumulator piston remains in its lowest position (against the bottom stop) while the arm is moved from Pos. 1 to Pos. 2. After the arm has been locked, a valve is opened so that the volume on the rod side of the actuator is vented to the air. The trolley is now brought up snug against the arm. A thrust roller mounted at the rear of the trolley is in direct contact with the arm to ensure a perfect transfer of forces. The machine is then charged by pumping in hydraulic oil until the accumulator piston reaches its top position (against the top stops). This is indicated by a sudden rise in the oil pressure. The gas (nitrogen) volume in the accumulator has now been reduced by approximately 20% with a corresponding increase in pressure (the maximum gas volume is about 200 litres, whereas the minimum gas volume is approximately 161 litres). This compressed gas is the energy source for the accelerating system. Hence, it is the initial gas pressure in the accumulator that determines the force that can be produced. The test is now started by releasing the hydraulic cylinders that lock the arm and the arm now pushes the trolley forward along its rails. The connection of the actuator piston rod to the arm introduces a 1:5 lever action, i.e. the force acting on the trolley is 1/5 of the piston rod force, but the velocity at the trolley level is 5 times greater. Once the arm has passed the useful part of its arc a sensor applies disc brakes in the arm hubs to stop the arm. After the test, the brakes are released and the arm dropped to its neutral position. Note that the actuator/accumulator assembly has to be able to rotate around an axis trough the end of the actuator, Figure 4-3.

The maximum change in gas volume of the 200-litre gas section of the hydraulic accumulator is 39 litres. The maximum working pressure of the accumulator is 200 bar. A constant pressure of 200 bar expanding by 39

litres (from 161 litres to 200 litres) yields an energy output of 720 kJ. However, the trolley leaves the arm after about 2/3 the stroke. Hence, the maximum energy delivered to the trolley is approximately 500 kJ. For the current trolley with a mass of M_T = 794 kg, this indicates a maximum speed of approximately 35 m/s (125 km/h).

4.3 Calibration of loadcells

This section describes the calibration procedure of the loadcells that were used in the kicking machine see Section 4.2. The basis for the description is by Hanssen et al. (2005). In order to measure the interface force between the specimen and the trolley, a special purpose loadcell was designed. The loadcell design is shown in Figure 4-9. Basically, the load cell is a stocky cylinder with thick end flanges machined in one piece of high strength steel with a minimum yield stress of σ_0 = 600 MPa (proportionality limit). The load measurement system is based upon four evenly distributed strain gauges, glued on to the central shaft.

The signal from each strain gauge was sampled separately and used to compute the axial force and bending moments. The shaft is a stocky cylinder of circular section and with a wall thickness and outer diameter of 7 and 100 mm respectively. Both the ends of the central shaft are connected to thick flanges (80 mm). Such a thickness is necessary in order to realise a linear strain distribution (Euler-Bernoulli) over the cross-section in the central shaft. The loadcell has five spherical indents machined into the front flange, which are for calibration purposes. A compressive load was applied to the loadcell through a steel ball successively located in all five holes, see Figure 4-9. This yields sufficient information to fully calibrate the load cell.

Figure 4-10 shows the assumed linear-strain distribution in the loadcell for a general eccentric loading condition. Let the original voltage signal from the four strain gauges be $\mathbf{v}_0 = \left\{ v_1^0, v_2^0, v_3^0, v_4^0 \right\}^T$ where the subscripts specifies the

strain gauge. The output from the amplifier is then $\mathbf{v} = \mathbf{a}\mathbf{v}_0 = \left\{a_1 v_1^0, a_2 v_2^0, a_3 v_3^0, a_4 v_4^0\right\}^T = \left\{v_1, v_2, v_3, v_4\right\}^T$. The axial strain in the location of the strain gauges is proportional to voltage, hence $\boldsymbol{\varepsilon} = \left\{\varepsilon_1, \varepsilon_2, \varepsilon_3, \varepsilon_4\right\}^T = \mathbf{k}\mathbf{v} = \left\{k_1 v_1, k_2 v_2, k_3 v_3, k_4 v_4\right\}^T$. The four voltage signals of $\mathbf{v} = \left\{v_1, v_2, v_3, v_4\right\}^T$ were sampled separately and post-processed in order to determine the reaction forces on the load cell.

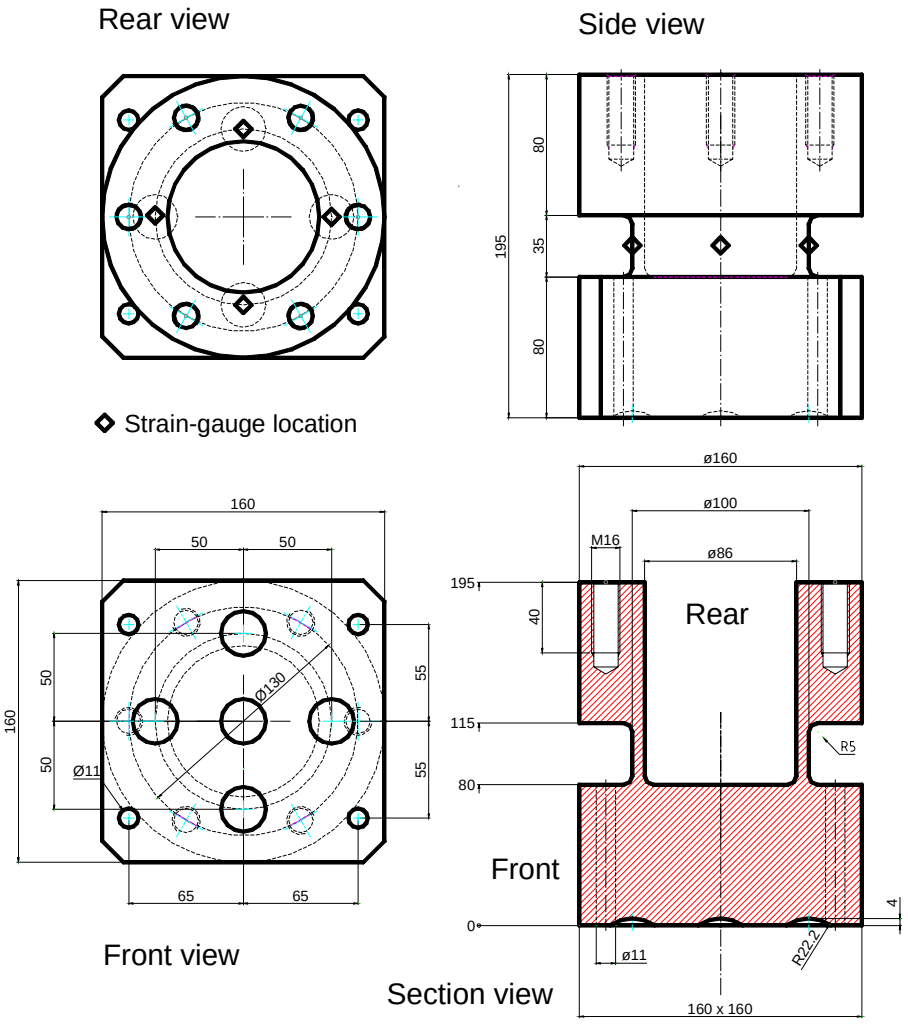

Figure 4-9 Loadcell details.

4.3.1 Calibration step 1: Axial force

Assume a state of pure-axial loading ($e=0$). The axial force N is related to the axial strain ε by $N=\bar{K}_N\varepsilon$ where $\bar{K}_N$ is the axial stiffness. For this loading condition there are four measures for the axial strain, $\varepsilon=\varepsilon_i=k_i v_i$, $i=1..4$. In this way there are also four measures for the axial force, $N=\bar{K}_N\varepsilon_i=\bar{K}_N k_i v_i=K_i v_i$, $i=1..4$. The state of pure-axial loading will provide data for calibration of the constants K_i, $i=1..4$, see Section 4.3.3, Figure 4-12(a)-(d).

An eccentrically applied normal force can be decomposed into an axial force and two-orthogonal bending moments around the x- and y-axis, Figure 4-10. It is evident from this figure that four strain gauges will be sufficient

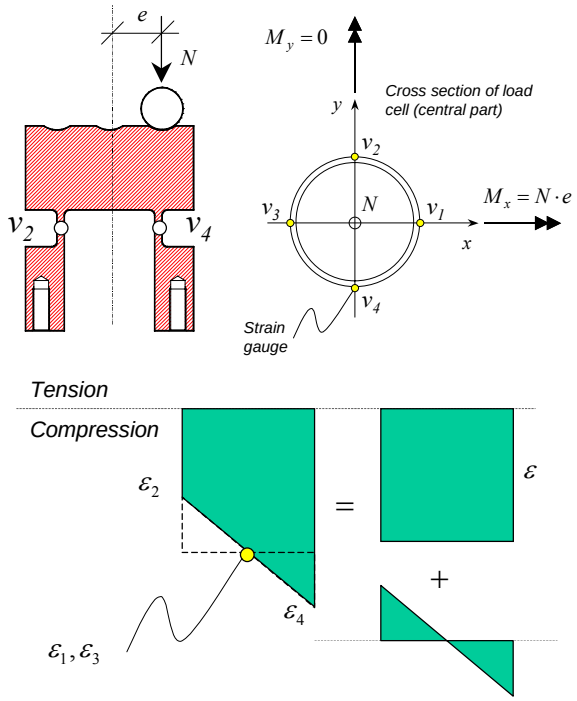

Figure 4-10 Strain distribution for development of calibration formulas.

in order to capture the information from such a loading condition. The average axial strain is taken as $\varepsilon = \frac{1}{4}\bar{K}_N(\varepsilon_1+\varepsilon_2+\varepsilon_3+\varepsilon_4) = \frac{1}{4}\bar{K}_N(k_1v_1+k_2v_2+k_3v_3+k_4v_4)$. However, the pure axial calibration has determined the constants $K_i = \bar{K}_N k_i$, $i = 1..4$ and the expression for the axial force is written as

$$N = \frac{1}{4}(K_1v_1 + K_2v_2 + K_3v_3 + K_4v_4) \tag{4.11}$$

4.3.2 Calibration step 2: Bending moments

Assume a state of eccentric loading so that $M_y = 0$ and $M_x = N \cdot e$, Figure 4-10. The bending moment M_x is proportional to the curvature κ_x of the cross-section, viz. $M_x = \bar{K}_M \kappa_x$. The curvature is again proportional to the difference in axial strains in the following manner, $\kappa_x = k_x(\varepsilon_4 - \varepsilon_2)$ and one can write

$$\begin{aligned} M_x &= \bar{K}_M k_x(\varepsilon_4 - \varepsilon_2) = \bar{K}_M k_x(k_4v_4 - k_2v_2) \\ &= \frac{\bar{K}_M}{\bar{K}_N} k_x(\bar{K}_N k_4v_4 - \bar{K}_N k_2v_2) = K_x(K_4v_4 - K_2v_2) \end{aligned} \tag{4.12}$$

Hence, $M_x = K_x(K_4v_4 - K_2v_2)$ where the constants K_2 and K_4 have already been determined by the pure-axial loading condition in Section 4.3.1. Eccentric loading around the x-axis will provide data for determination of K_x. The same consideration can be used for eccentric loading around the y-axis and one arrives at $M_y = K_y(K_1v_1 - K_3v_3)$. The results from the load cell are given in Section 4.3.3, Figure 4-12(i)-(j).

If the strain gauges are not correctly positioned, a moment around the x-axis will induce strains in the strain gauges used for calculation of moment around the y-axis and vice-versa, Figure 4-11. However, this coupling effect

can also be taken into consideration by the calibration formulas. The graph of Figure 4-11 illustrates this. Assume that the loadcell has been subjected to an axial force and moment only around the x-axis. The computed bending moment around the x-axis is then $M_x = K_x(K_4 v_4 - K_2 v_2)$. The calculated moment around the y-axis is $M_y^0 = K_y(K_1 v_1 - K_3 v_3)$, where the super index is used to indicate that this is a residual moment. This error can be related to the computed bending moment M_x in the following manner $M_y^0 = K_y^0 M_x = K_y^0 \cdot K_x(K_4 v_4 - K_2 v_2)$ which easily determines K_y^0. The residual moment M_y^0 has to be subtracted from the original expression $M_y = K_y(K_1 v_1 - K_3 v_3)$. In this way, the complete formulas for the bending moment around the x- and y-axis read

$$M_x = K_x(K_4 v_4 - K_2 v_2) - K_x^0 \cdot K_y(K_1 v_1 - K_3 v_3) \tag{4.13}$$

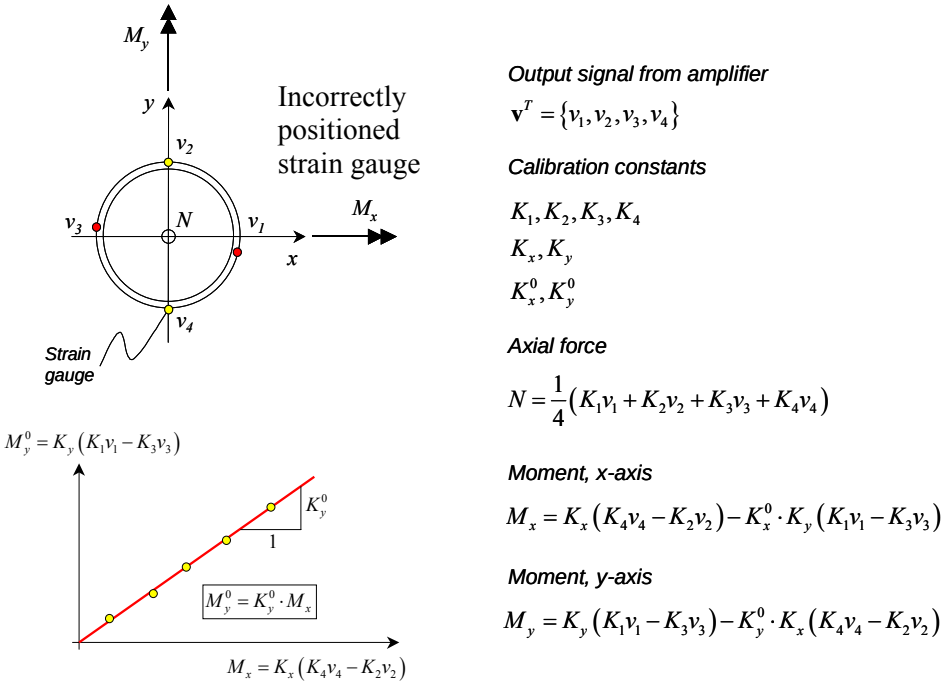

Figure 4-11 Correction for incorrect positioning of strain gauges and summary of signal processing.

and

$$M_y = K_y(K_1 v_1 - K_3 v_3) - K_y^0 \cdot K_x(K_4 v_4 - K_2 v_2) \tag{4.14}$$

A summary of the load signal processing is given in Figure 4-11.

4.3.3 Calibration results

The loadcells were calibrated in a Dartec 500 kN static testing machine (accuracy ± 1% of applied load) using the approach described above. The compressive load was applied cyclically at a frequency of 5 Hz. The force level from the Dartec testing machine and the signal from the four strain gauges were sampled digitally. All relevant data for one selected loadcell is given in Figure 4-12. Figure 4-12(a)-(d) give the relation between force level and signal from each strain gauge for pure-axial loading. The relation is clearly linear although some hysteresis is evident from Gauge 2 and 3. The hysteresis, or reversibility error, is the difference between the loadcell's output when a force following a monotonic decrease from its rated load (Robinson, 1997). Robinson (1997) gives four hysteresis mechanisms for loadcells. These are 1) metallurgical hysteresis, 2) local yielding effects, 3) hysteresis in strain-gauge backing and adhesive layer and finally 4) slip at the interface between loadcell support conditions. Given the axisymmetry of the current loadcell and support conditions, hysteresis in the strain-gauge backing and adhesive layer could be a possible explanation for the hysteresis observed for Gauge 2 and 3 only.

Four eccentric loading conditions were applied to the loadcell, namely loading by the steel ball through the four eccentrically placed holes in the top flange, Figure 4-9. First, this load condition can be used to check the performance of the calibration formula for the total axial force given by Equation (4.11) and defined by the constants K_i, $i = 1..4$ of Figure 4-12(a)-(d). The results can be seen in Figure 4-12(e)-(h). The formulas appear to give good results, although the force levels are somewhat underestimated by

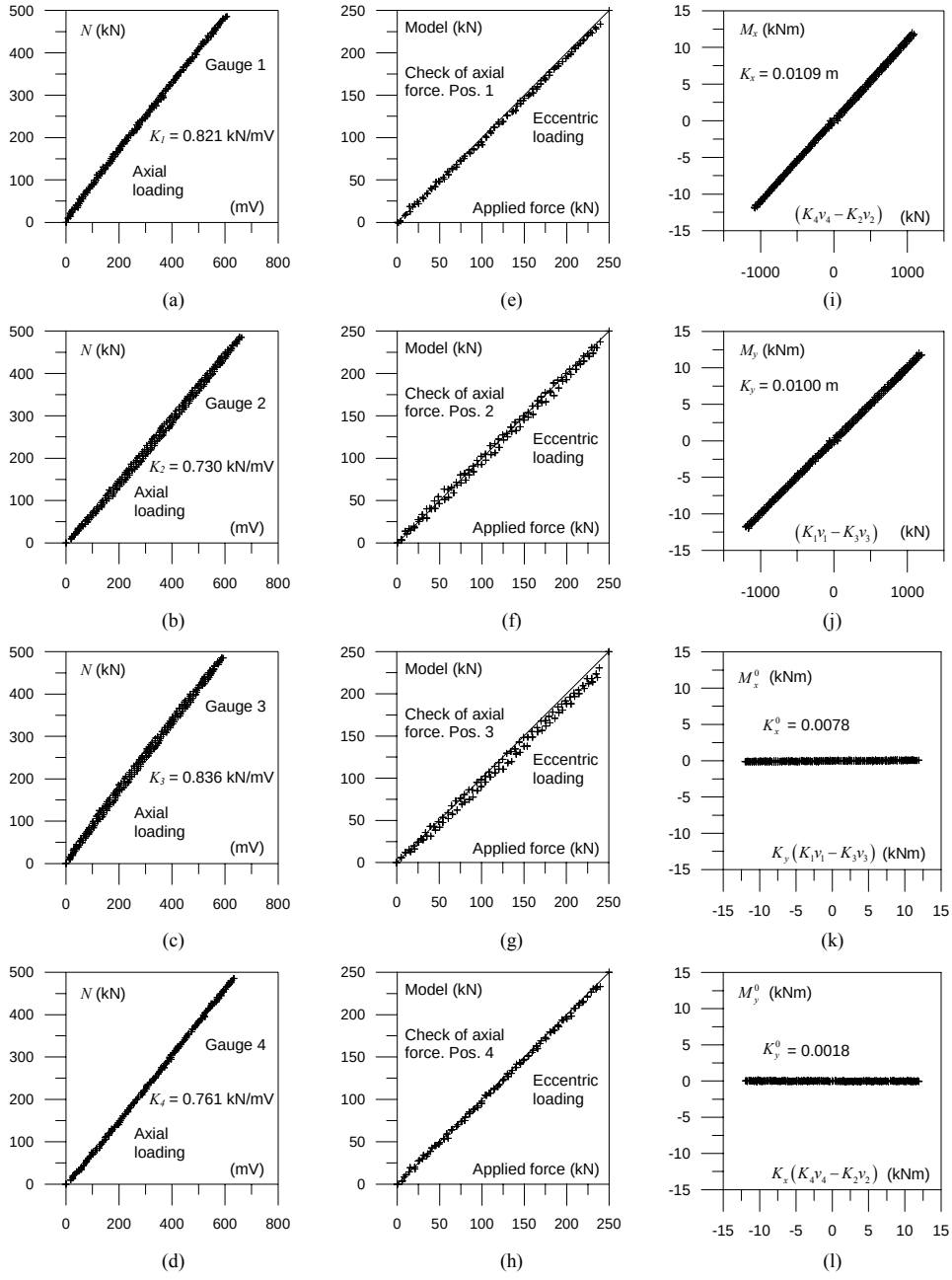

Figure 4-12 Results from calibration procedure.

the calibration formula for loading position 3 (which is the hole directly above Gauge 3). The calibration results relating to the two bending moments M_x and M_y are shown in Figure 4-12(i)-(j). The corresponding correction for the coupling error between the two bending moments is given in Figure 4-12(k)-(l) and is less than 1% for both cases.

4.4 Instrumentation and data acquisition

Figure 4-13 shows a block diagram of the signal path from the strain gauges on the loadcell to the logging card in a PC. The strain gauges used have a resistance of $R_0 = 350\Omega$ and a gauge factor of 2.10 (FLA-3-350-11-4L, Tokyo Sokki Kankyujo Co. Ltd. JAPAN). Strain gauge consists of a metal filament mounted on paper or a synthetic material. When a strain gauge is elongated, the area a_s of the metal filament will decrease while the length l_s increases. Thus, the resistance of the filament is changed, i.e. $\Delta R = \rho_R \frac{\Delta l_s}{\Delta a_s}$. The resistivity ρ_R of a strain gauge is temperature dependent, but for the current application (short duration impact loading) it can be regarded as a constant.

A Wheatstone's measuring bridge was used to measure the strain from each strain gauge, Figure 4-14, i.e. to convert the difference in resistance to a difference in volts. In Figure 4-14, the resistance R_1 refers to the strain gauge with resistance $R_0 + \Delta R$ after elongation. R_2, R_3 and R_4 are fixed

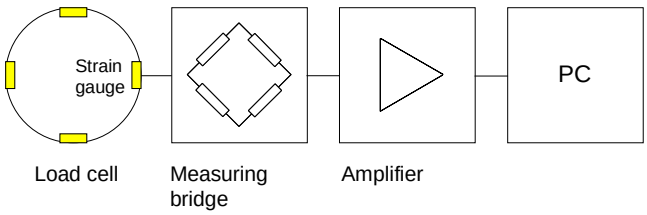

Figure 4-13 Block diagram of measuring system.

resistances equal to R_0. The relation between resistances and voltage V in a Wheatstone's quarter bridge is

$$\begin{aligned}\Delta V &= V_0\left(\frac{-R_2}{R_1+R_2}+\frac{R_3}{R_3+R_4}\right)=V_0\left(\frac{-R_0}{R_0+\Delta R+R_0}+\frac{R_0}{R_0+R_0}\right)\\ &= V_0\left(\frac{\Delta R}{2\cdot\Delta R+4\cdot R_0}\right)\end{aligned} \tag{4.15}$$

The signals from the strain gauges are very small and need to be amplified. It is also an advantage to put the amplifier as close to the strain gauges as possible to prevent the signals from picking up electrical noise. Owing to the test set-up it is difficult to locate the measuring bridge and the amplifiers directly beside the loadcells. However, the wires from the loadcell are shielded in order to reduce the effect of electrical noise.

The amplifiers were specially made for the purpose of the present study. Each amplifier was built up of three high-speed programmable gain-

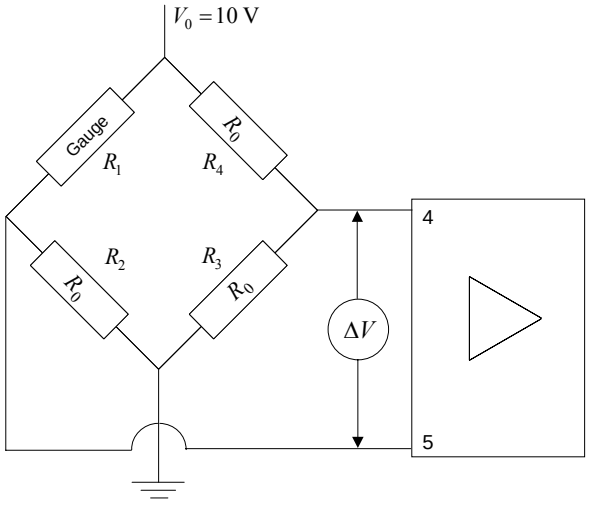

Figure 4-14 Wheatstone's measuring bridge and first instrumentation amplifier (U1).

instrumentation amplifiers of type PGA207 from Burr-Brown. These are denoted U1-U3 in Figure 4-15. In short, an instrumentation amplifier increases the difference between the two input signals on pin 4 and pin 5, Figure 4-14. Each of the three instrumentation amplifiers has a gain that can be changed digitally. The change is made by S1-S3, which each contains two switches. With these switches it is possible to get four different gains for each instrumentation amplifier, the actual factors being 1, 2, 5 and 10. There are two potentiometers P1 and P2 in each amplifier. The first (P1) is used to set the zero point level. This is necessary because there is a small deviation in the zero-point level due to drift in the strain gauges and the amplifier. The other potentiometer (P2) is used for step less control of the gain. The bandwidth is an important feature of the amplifiers. If the bandwidth is too small, important high-frequency information in the signal may be lost. The multiple of gain and bandwidth of instrumentation is close to constant. An amplification of 5x5x5 = 125, which will be used in the current test set-up, will give a bandwidth of 1.0 MHz (from data sheet of PGA207). This is more than enough for impact testing of bumper beam-longitudinal systems.

4.4.1 Logging

The signals from the strain gauges were sampled separately, i.e. four channels were needed per loadcell. The logging card of the PC was

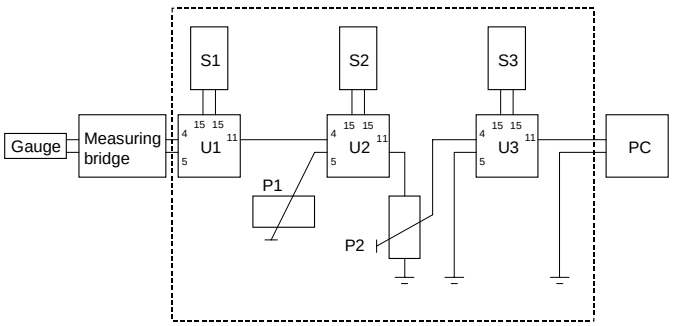

Figure 4-15 Block diagram of amplifier.

delivered by Computer Boards, type PCI-DAS4020/12. The maximum sampling frequency of one channel was 20 MHz. This value will decrease with use of more than two channels. Each logging card had four input channels. For the bumper beam-longitudinal system set-up in Figure 4-1, ten channels were used, requiring the use of three logging cards (the two rear load cells require eight channels, whereas the two load cells on the trolley require two channels). The maximum sampling frequency for this configuration (and up to 12 channels in total) was 5 MHz. The logging card can use two sensitivities ±1 V and ±5 V, depending on the level of input signal. This gives a resolution of 0.488 mV or 2.441 mV respectively with 12 bits A/D converters. Special in-house software was developed using Visual Basic to control the logging cards. The sampling frequency used with the logging program was 500 kHz and the sensitivity used was ±5 V. The data collection of the logging program was initiated by signals from a photocell system mounted directly in front of the impact area.

4.4.2 Filtering

In the tests there are a lot of elastic stress waves in the loadcells propagating through the strain gauges, see Figure 4-16. All the experimentally obtained force-time curves were smoothed using a moving-point average algorithm of 1250 points, roughly corresponding to a low-pass filter with a cut-off frequency of 400 Hz. The smoothing algorithm starts the averaging gradually, i.e. in the beginning of the signal the first data point is the original one, the next point is the average of the foregoing point, itself and the subsequent point. This process is continued until reaching the maximum number of smoothing points, here 1250. Then 1250 points is used in the smoothing of the main signal until approaching the end of the signal. At the end of the signal, the number of averaging data point is reduced in the same manner as was done at the start of the signal. The moving-point average algorithm reduced the oscillations in force level, but the absorbed energy will be correctly estimated. No other filtering methods were investigated.

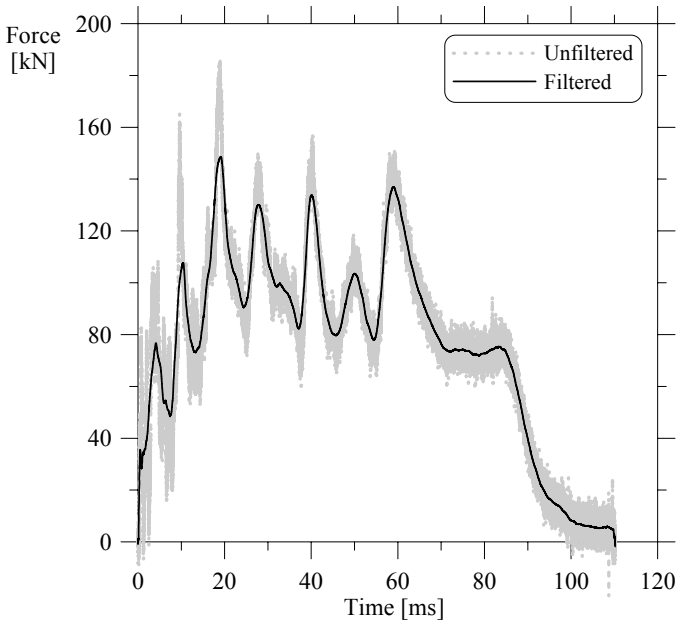

Figure 4-16 Filtering of measured force-time curves.

Chapter 5 Experimental Results

In this chapter experimental results on the bumper beam-longitudinal systems are presented. Four series (see Table 4-1) of tests were performed viz. test series **A**, **B**, **C** and **D**. Five parallel tests were performed for test series **A**, whereas for other test series three parallels were tested. The purpose of these tests is to establish an experimental database for the bumper beam-longitudinal system at 40% offset impact and to validate an FE-model.

The test conditions were similar; the variables being the strength of the longitudinal and impact velocity, to provide further information about the repeatability and robustness of the bumper beam-longitudinal system at offset impact.

Load transfer is the key element influencing the energy absorption capability of a system/structure during the impact. Normally the load is transferred from one structural compartment to the next as the crash event progresses and the load path could be an axial, bending, shear, or a combination.

For the bumper beam-longitudinal system at offset impact, the load path is neither pure axial nor bending collapse, but rather a combination of the two modes. The impact energy of the trolley is to be absorbed by the collapse of the bumper beam and crushing and bending of the longitudinal members. For the collapse of the longitudinal member at the impacted end both an axial load and a bending moment is to be transferred from the bumper beam to the longitudinal.

The succeeding sections presents the results from test series **A**, **B** and **C** with varying longitudinals strength and test series **D** at increased impact velocity. The force-deformation plots obtained from the loadcells on the trolley with the corresponding photographs of the deformed test specimens are given for each test series.

5.1 Test series A

The response data obtained for test series **A**, i.e. with an impact velocity of 10 m/s and with AA7003-T79 material used in the longitudinals, are presented in Figure 5-1. Filtered force-deformation plot for each of the test is shown on the left side of the deformed test specimen. For the five parallel tests filtered force-deformation curves are plotted in Figure 5-2. The force-deformation characteristics are similar for the five parallels, Figure 5-2, even though their deformation pattern varies. A photo gallery of the deformation history is given in Figure 5-3 for test specimen **A1** based on the high speed video camera recording. The corresponding loadcell data is given in Figure 5-4. Note that the given time refers to the image taken closest to the assumed time of impact.

The sequence of events, see Figure 5-3, for test specimen **A1** during the impact was as follows (the selected times were denoted with dots on the force-time curves in Figure 5-4). The impact event started at time t_1. By the time t_2 the bumper beam cross-section was completely collapsed and buckling in the impacted longitudinal was initiated. At time t_3 the bumper beam has developed a plastic hinge in the mid-section. A crack developed at the non-impacted end of the bumper beam at time t_4, as folding in the impacted longitudinal continued. Note the significant curvature of the non-impacted longitudinal as it was strained by the bumper beam. It is evident that this loading caused the development of a local buckle at its clamped end, prior to time t_5. The trolley almost activated the crashboxes on the reaction wall at time t_6.

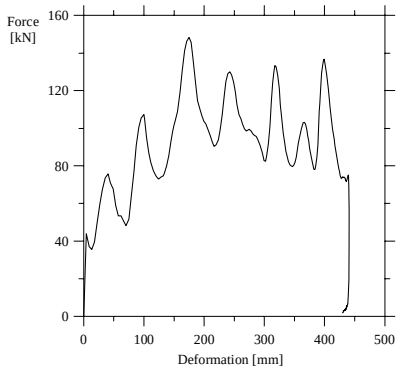
Force
[kN]
160
120
80
40
0
0
100
200
300
400
500
Deformation [mm]

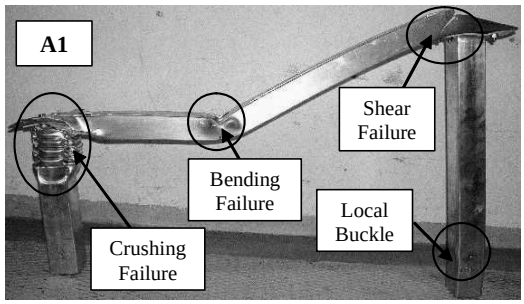
A1
Shear Failure
Bending Failure
Local Buckle
Crushing Failure

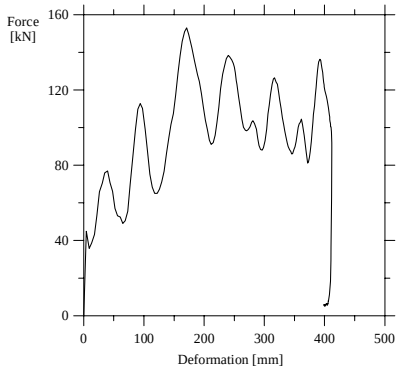
Force
[kN]
160
120
80
40
0
0
100
200
300
400
500
Deformation [mm]

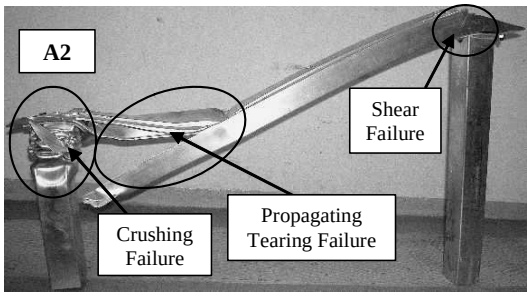
A2
Shear Failure
Crushing Failure
Propagating Tearing Failure

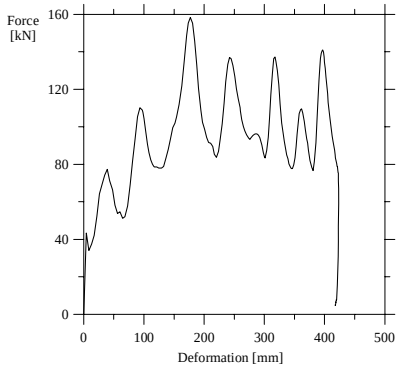
Force
[kN]
160
120
80
40
0
0
100
200
300
400
500
Deformation [mm]

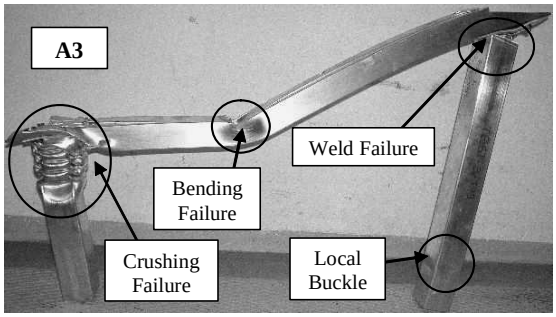
A3
Weld Failure
Bending Failure
Crushing Failure
Local Buckle

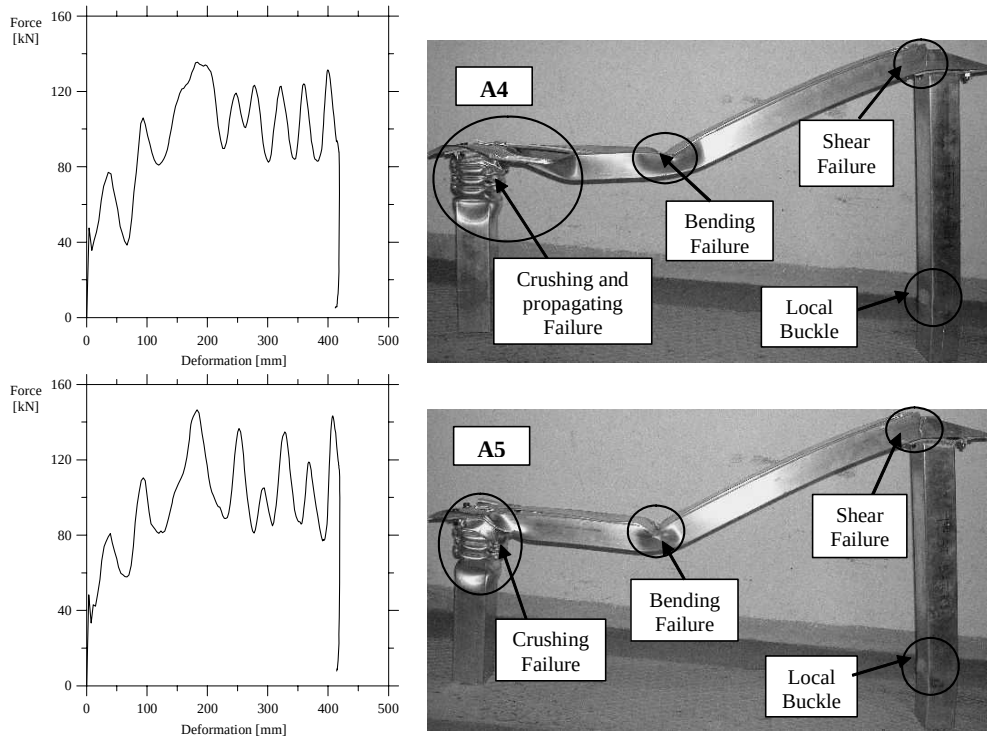

Figure 5-1 Experimental results for test series **A**.

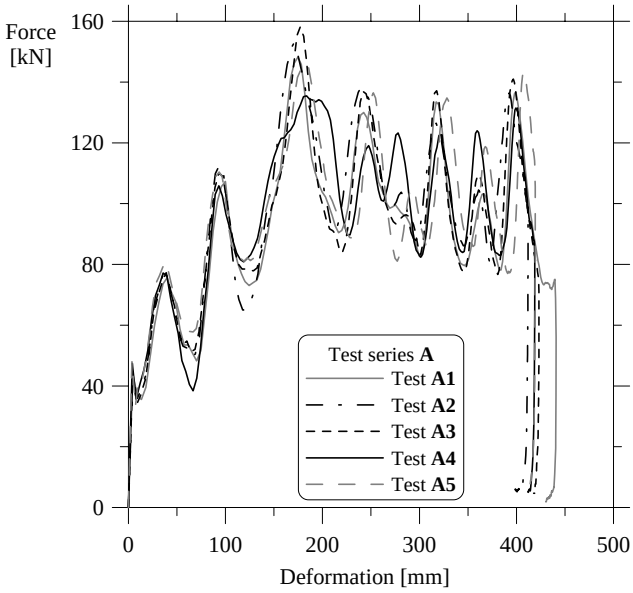

Figure 5-2 Filtered force-deformation plots for test series **A**.

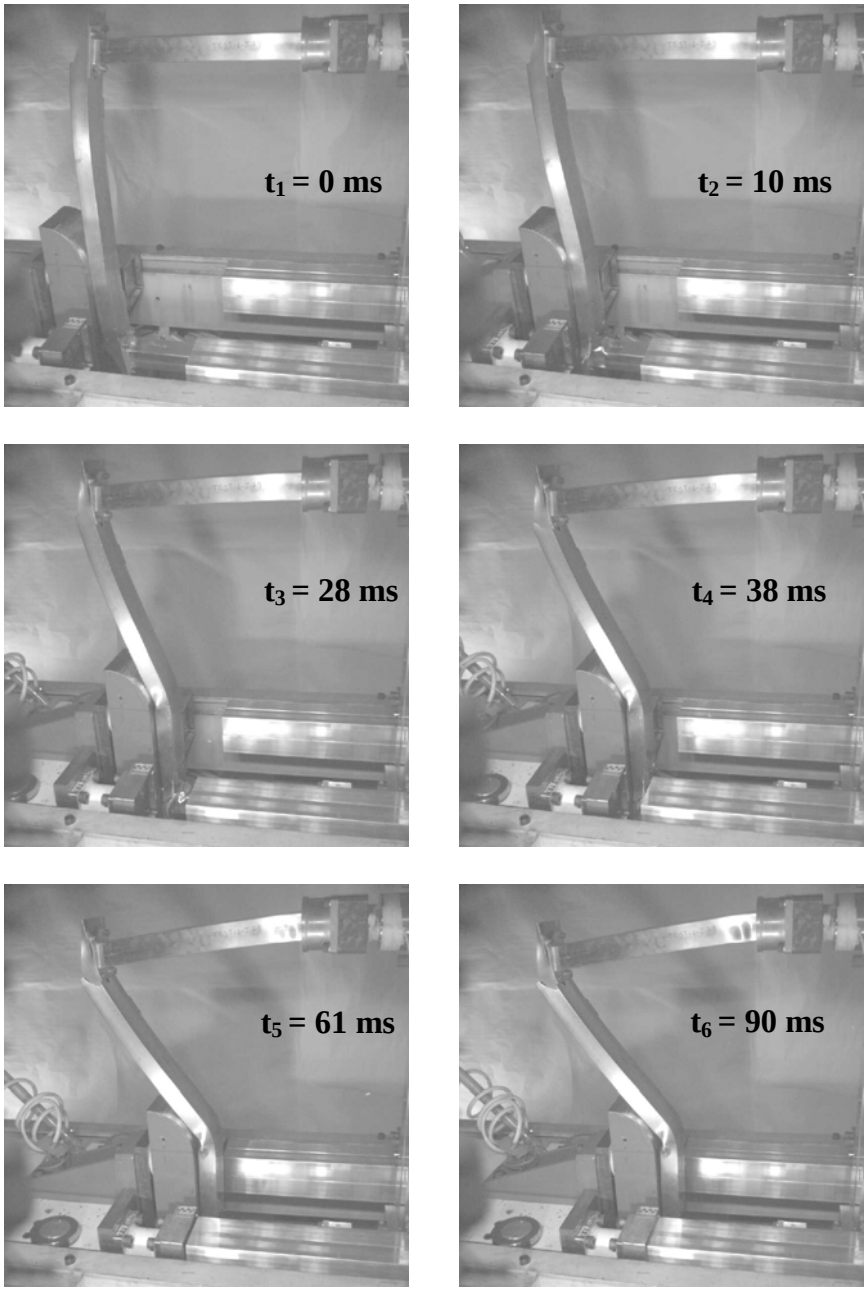

Figure 5-3 Photos taken from high speed video recording for test specimen **A1**.

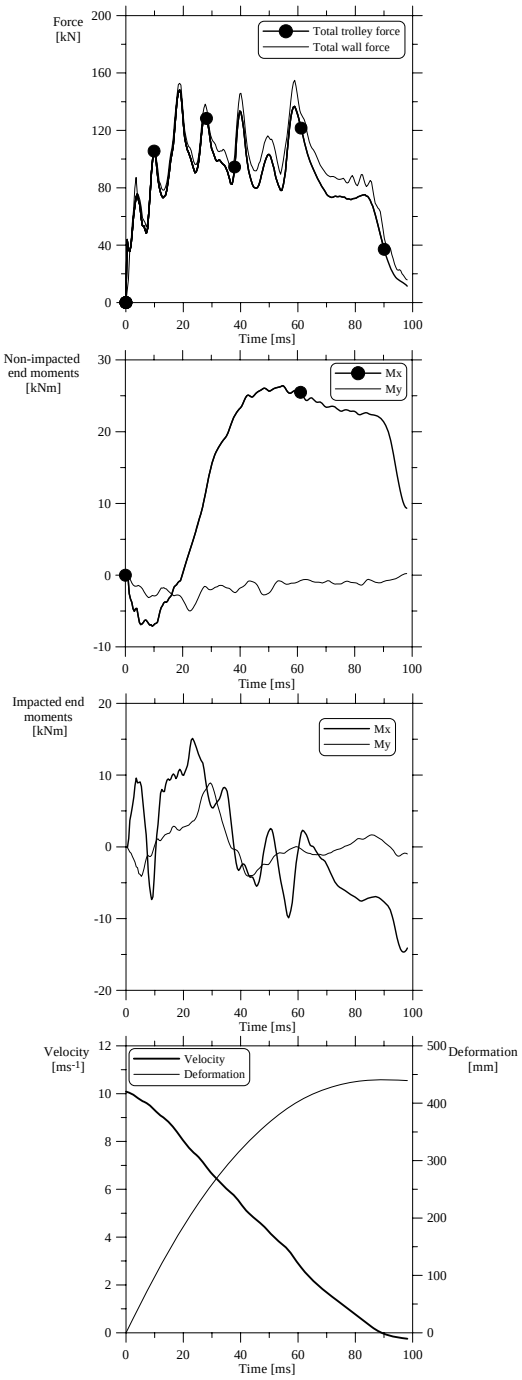

Figure 5-4 Loadcell data for test specimen **A1**.

If no inertia effects were present, the total forces measured on the trolley should correspond to the total forces on the reaction wall. As seen from Figure 5-4, the force levels recorded on the reaction wall are in general somewhat higher than the trolley force due to the inertia of the bumper beam-longitudinal system.

When the trolley impacts the bumper beam-longitudinal system, the impact energy was initially used in crushing the bumper beam cross-section completely. The crushing of the bumper beam corresponds to a deformation of about 60-70 mm. A close view of the crushed bumper beam cross-section is shown in Figure 5-5(a). The collapse of the bumper beam cross-section was accompanied with the bending of the interface place. As soon as the collapse of the bumper beam was completed, the force acting between the trolley and the system was mainly governed by the folding mechanism(s) in the longitudinal member.

The interface plate was welded to the longitudinal, thus it was assumed that a softer zone would develop at the welded end in the longitudinal. Hereafter, this softer zone is called a heat-affected zone (HAZ).

Initiation of the first buckle in the impacted longitudinal led to a rise in the force level. This happened at a deformation of 100 mm see Figure 5-2, which corresponds to 10 ms in Figure 5-3 (second image). The following highest peak in the force-deformation plots in Figure 5-2, at a deformation of about 160 mm, was due to the formation of a second buckle in the impacted longitudinal. This was observed from the video camera recordings.

The reason for these two different peaks in the force-deformation plots was as follows. The first buckle in the impacted longitudinal developed just below the HAZ and thus requiring a moderate increase in the force level to cause buckling. On the other hand, the location of the second buckle is (assumed to be) outside the HAZ, at least for the tested systems here, where

the material properties in the longitudinal are not affected by the welding process and this resulted in a significant rise in the force level.

The subsequent crushing of the impacted longitudinal was by progressive folding with an axisymmetric deformation mode, Figure 5-5(a). In the figure the numbers represents the lobes developed in the impacted longitudinal. The axisymmetric mode is here defined as the mode where two opposing walls move inwards and the other two move outwards, which is referred to as one lobe. This progressive folding mode was observed in all the five parallel tests. The failure events related to the progressive folding in the impacted longitudinal together with the collapse of the bumper beam is denoted as “crushing failure” in Figure 5-1 and Figure 5-5(a).

The longitudinals of test series **A** had smaller strain hardening properties compared to the longitudinals of test series **B**, see Section 3.4.1. The smaller strain hardening properties aided in the easy localisation of strains leading to progressive buckle development (Jones, 2003) in the impacted longitudinal.

A plastic hinge developed in the mid-section of the bumper beam. As the hinge developed the upper flange of the bumper beam experienced an inward motion. At this point a kinematic mechanism developed. This inward movement of the upper flange caused the side walls (webs) to move outward. Simultaneously, rupture in the folded flange and webs took place which resulted in the bending failure, see Figure 5-5(b).

Due to the bolted connection between the bumper beam and the longitudinals, crushing of the impacted longitudinal made the bumper beam to rotate about the plastic hinge at mid-section with the development of a tensile force along the length axis of the bumper beam. This tensile force in the bumper beam increased further with the crushing of the longitudinal and caused localisation of strains at the non-impacted end. In ductile materials, like aluminium, modes of plastic instability and strain localisation will normally occur before the fracture strain in tension is reached. These modes

will tend to localise the strains in the material, and this will eventually produce a fracture. The crack resembled a through-thickness shear instability mode (Bressan and Williams, 1983; Hooputra et al., 2004). A close view of the through-thickness shear crack is shown in Figure 5-5(c).

As can be seen from Figure 5-5(c), there is a propagating tearing crack at the intersection between the lower flange and the web. However, from the video camera recordings the time of occurrence was not clear as the view was hidden from the camera angle, see Figure 5-3. It is presumed that the propagating tearing crack occurred before the development of the through-thickness shear crack.

Note the significant curvature change in the non-impacted longitudinal as it was strained by the bumper beam and a local buckle was developed at the clamped end of the longitudinal. This buckle was observed for all the five parallel experiments, see Figure 5-1.

The development of a local buckle in the non-impacted longitudinal can also be seen from the moment-time curve (M_x) data from the loadcell at the non-impacted end in Figure 5-4, where the curve started to drop from its

(a) (b) (c)

Figure 5-5 Typical deformation and failure modes for test series **A**: (a) Crushing failure, (b) Bending failure and (c) Through-thickness shear and propagating tearing cracks.

peak position at 61 ms. However, in the same figure the moment-time curve (M_y) data from the loadcell at the impacted end recorded a moment of 9 kNm about the y-axis approximately at 30 ms. This effect has not been investigated, but is probably due to bending of the system about y-axis.

From the post-crash test specimens a considerable amount of failure zones has been observed in the folds of the longitudinal. However, these failure events are not critical since they do not propagate or significantly reduce the energy absorption of the system.

From the high speed video camera recordings for the five parallels it seemed that the trolley barely touched the crashboxes on the reaction wall, as no plastic deformation was observed in the crashboxes. This can also be seen from the velocity-time curve in Figure 5-4. The velocity of the trolley reached zero at about 90 ms, and further increase of velocity in the negative direction is due to the retardation of the trolley, see the last graph of Figure 5-4. In case the trolley had activated the crashboxes, the velocity curve should have been parallel to the abscissa from the activation time onwards. Such types of curves can be found for test series **B**, **C** and **D** in the forth-coming sections.

Thus the impact energy of the trolley was fully absorbed by the bumper beam-longitudinal system, which can also be observed from the energy-deformation plots. The energy absorption performance of test series **A** is summarised in Figure 5-6(a) where the absorbed energy is shown as a function of the deformation. The mean force-deformation plots are shown in Figure 5-6(b), where it is seen that the mean force increases as the folding in the impacted longitudinal increased.

In test specimen **A2** the lower flange of the bumper beam encountered an unacceptable failure mode, whereas in test specimen **A3** fracture in the weld was observed see Figure 5-1. However, the failure events did not show any significant influence on the force-deformation characteristics, Figure 5-2.

All the five repetitions of test series **A** showed similar force-deformation characteristics with little scatter, i.e. in this sense a robust performance.

The deformation modes for the remaining four test specimens of test series **A**, i.e. **A2**, **A3**, **A4** and **A5**, are given in Appendix-A along with the images from the high speed video camera recordings and loadcell data.

Assuming that the trolley just hit the crashboxes on the reaction wall the accuracy parameter, defined by Equation (4.8), calculated for the five parallel is shown in Table 5-1. For a reliable measurement the ideal value of this accuracy parameter should be one. From the variations in the accuracy parameter, it was possible to conclude that the average force level on the trolley fall well within ± 5 %.

5.2 Test series B

The response data obtained for test series **B**, i.e. with an impact velocity of 10 m/s and with AA7003-T1 material used in the longitudinals, are shown in Figure 5-7. Unlike the case of test series **A**, the three parallel tests

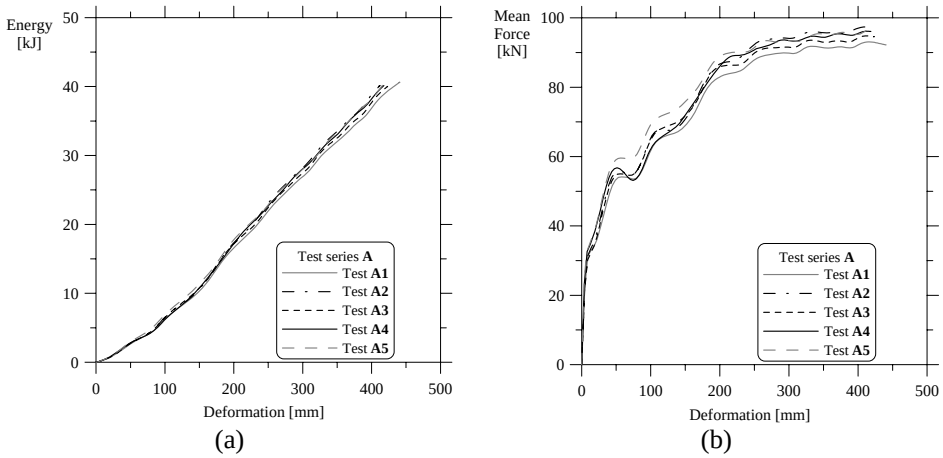

(a) (b)

Figure 5-6 (a) Energy-deformation, (b) Mean force-deformation plots for test series **A**.

resulted in three significantly different deformation modes. Thus, a non-robust performance of the bumper beam-longitudinal systems was experienced when the test series **B** longitudinals were used, see Table 4-1. Due to the difference in the deformation and failure modes for the three test specimens, only one test specimen i.e. **B1** is studied thoroughly. Further, it is not possible to generalise the typical failure modes in the systems as like test series **A**.

In this case also, the impact energy in the initial stage was used for crushing of the bumper beam cross-section, and later in deforming the longitudinals.

A sequence of photos showing the deformation history for test specimen **B1** is shown in Figure 5-8 together with the corresponding results from the loadcell in Figure 5-9. The dots in the force-time curves, Figure 5-9, represent the different deformation stages shown in the photos. The sequence of events in Figure 5-8 for test specimen **B1** was as follows. The impact process started at time $t_1 = 0$.

Table 5-1 Accuracy parameter Equation (4.8) for test series **A**.

Test Series **A**	Length prior to testing l_b (mm)	Calculated displacement $w(t_b)$ (mm)	Reaction wall crashboxes activation time t_b (ms)	Accuracy parameter ξ_b
A1	421	438.2	81	1.040
A2	420	411.6	76	0.980
A3	420	423.2	84	1.007
A4	422	418.9	83	0.992
A5	421	419.1	81	0.995

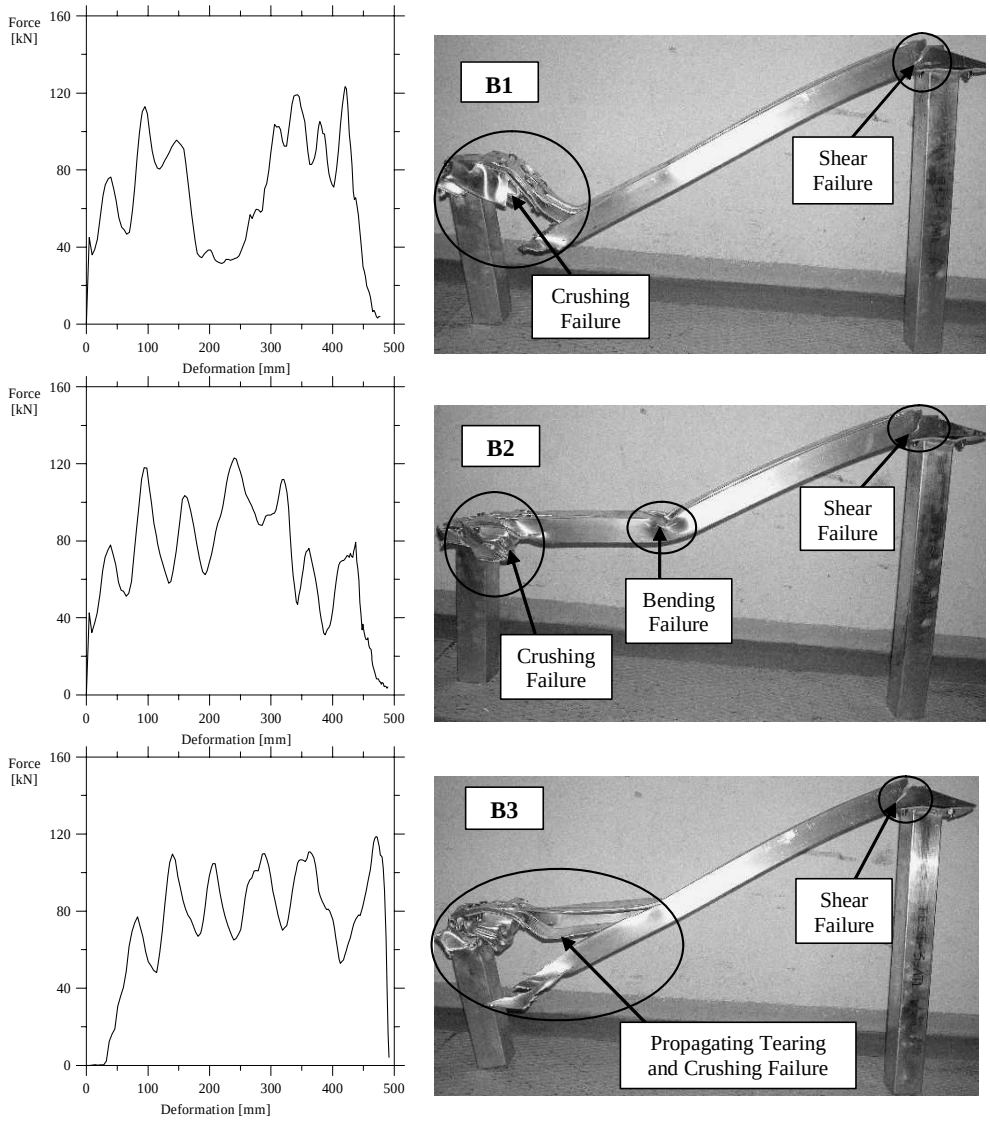

Figure 5-7 Experimental results for test series **B**.

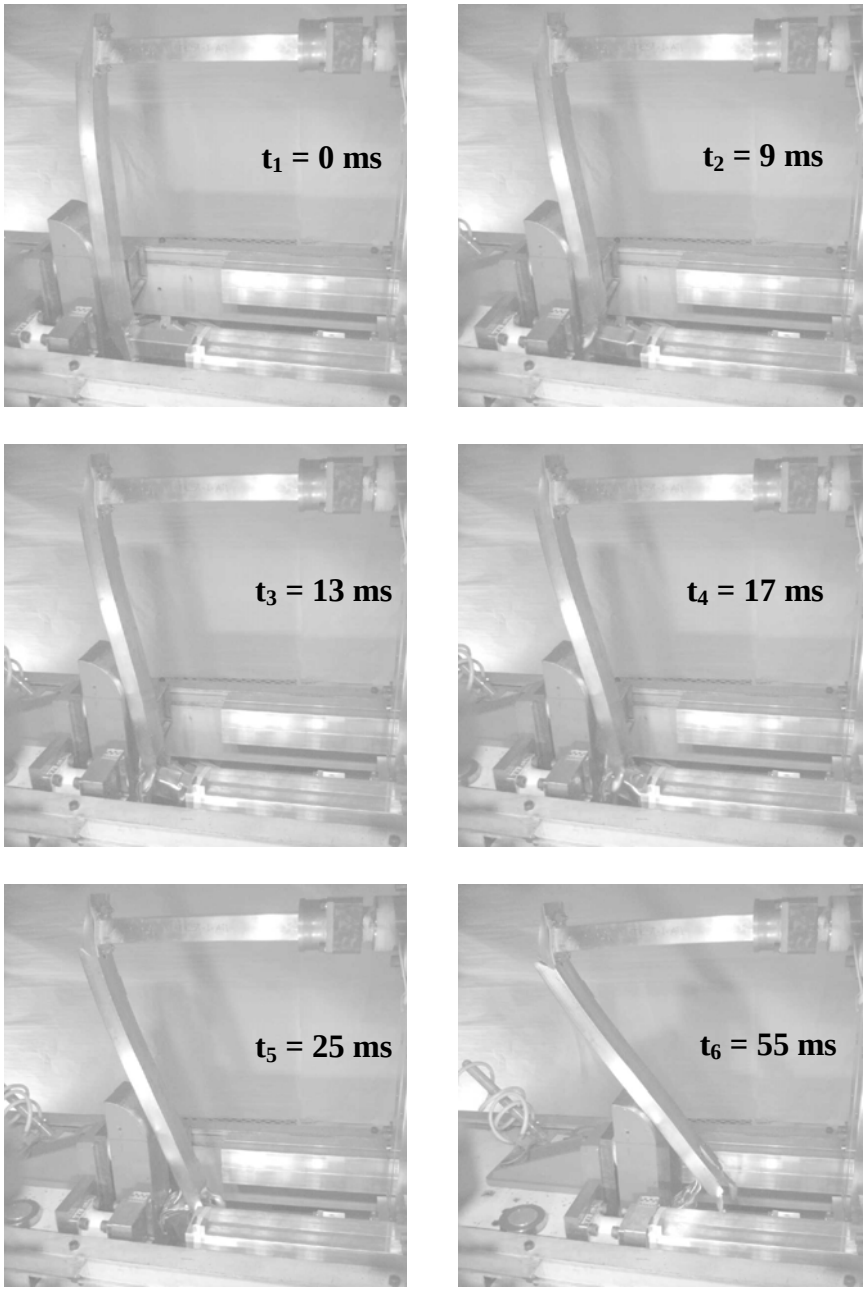

Figure 5-8 Photos taken from high speed video recording for test specimen **B1**.

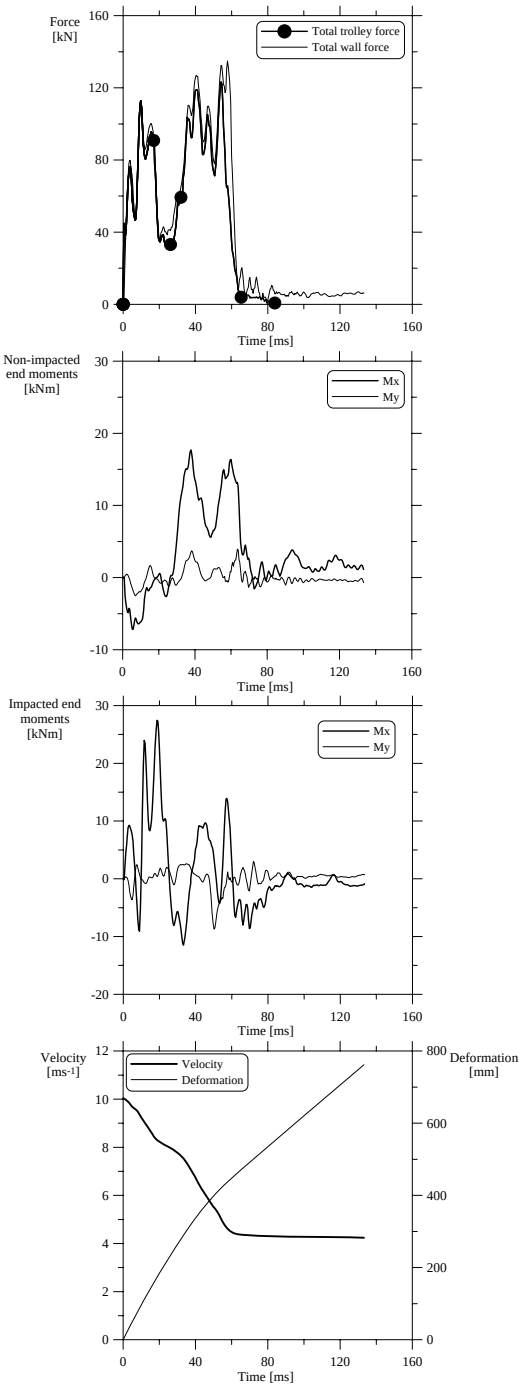

Figure 5-9 Loadcell data for test specimen **B1**.

Before time t_2 the bumper beam cross-section had collapsed completely and the buckling in the impacted longitudinal started. Propagating tearing crack in the bumper beam appeared before time t_3. Prior to time t_4 the deformed end of the impacted longitudinal started to rotate about the buckle that developed during the time t_2. The failure events at the non-impacted end of the bumper beam have fully developed at time t_5. The trolley activated the crashboxes on the reaction wall at time t_6.

Transition from progressive buckling to global bending was observed in the impacted longitudinal for test specimens **B1** and **B3**. This collapse mode was characterized by large lateral displacements. The large lateral displacements included localised sectional collapse of the mid- and end sections of the longitudinal member.

As can be seen in the second image of Figure 5-8, the first buckle (lobe) in the impacted longitudinal developed in the mid-section, approximately at a distance of 200 mm from the impacted end of the longitudinal. The first buckle acted as a hinge, making the longitudinal to bend globally upon further crushing. The sudden drop in force level at 17 ms in Figure 5-9 corresponds to this transition of the deformation mode. Further crushing of the impacted longitudinal caused a rise in the force level as new buckles were created on both sides of the hinge. The combined propagating tearing/through-thickness shear fracture events at the non-impacted end of the bumper beam occurred in a similar fashion as for test series **A**.

As mentioned, the load transfer from the bumper beam to the impacted longitudinal is caused by axial and bending modes. But for test specimen **B1** the bending collapse in the longitudinal dominated over the axial collapse mode. Further, this can also be linked to the bending stiffness of the longitudinal, as the longitudinals of test series **B** had lower yield strength and higher strain hardening, see Section 3.4.1. However, it was observed that the longitudinal members had a tendency to develop lobes randomly along the length of the members, thus making the member more unstable

and increasing the probability of a transition from progressive buckling to global bending.

The deformation modes for three parallel tests were different with significant scatter in the force-deformation plots, i.e. a non-robust performance of the bumper beam-longitudinal systems. All the filtered force-deformation plots of test series **B** are shown in Figure 5-10. It was not clear from the experiments, why there is no rise in the force level although there was some deformation for test specimen **B3**, see Figure 5-7 and Figure 5-10. The energy-deformation plots are shown in Figure 5-11(a).

The video camera recordings for the three parallels showed that the trolley activated the crashboxes on the reaction wall. Further, this can also be clearly seen from the velocity-time curve in Figure 5-9. After the activation of the reaction wall crashboxes the velocity became constant and parallel to the abscissa at 55 ms, which corresponds to a deformation of about 420 mm. For this reason the energy-deformation plots in Figure 5-11(a) are shown only up to a deformation of 500 mm.

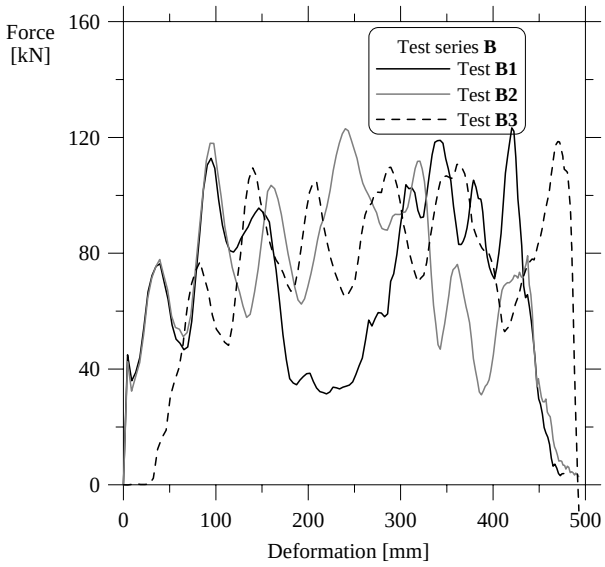

Figure 5-10 Filtered force-deformation plots for test series **B**.

Due to the unacceptable failure modes in the bumper beam and impacted longitudinal, the system had reduced energy absorption capability. And thus a low mean force. The mean force-deformation plots are shown in Figure 5-11(b). The accuracy parameter, defined by Equation (4.8), calculated for the three parallels is shown in Table 5-2. For test specimen **B3** the average force level on the trolley was underestimated by 9%, while the other two tests were with in $\pm 5\%$. The deformation history in the form of image galleries from the video camera recordings and the corresponding loadcell data for test specimens **B2** and **B3** are given in Appendix-B.

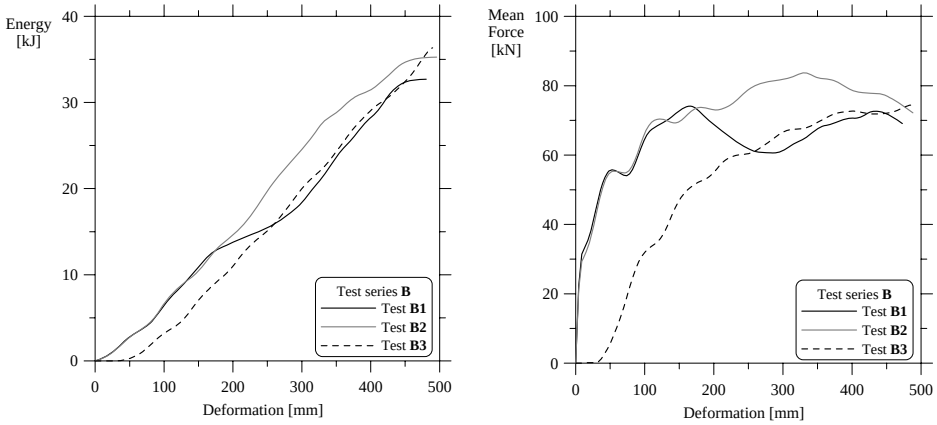

(a) (b)

Figure 5-11 (a) Energy-deformation, (b) Mean force-deformation plots for test series **B**.

Table 5-2 Accuracy parameter Equation (4.8) for test series **B**.

Test Series **B**	Length prior to testing l_b (mm)	Calculated displacement $w(t_b)$ (mm)	Reaction wall crashboxes activation time t_b (ms)	Accuracy parameter ξ_b
B1	420	424.4	55	1.010
B2	426	442.1	65	1.037
B3	431	473.6	65	1.098

5.3 Test series C

The response data for test series **C**, i.e. with an impact velocity of 10 m/s and with AA6060-T1 material used in the longitudinals, are presented in Figure 5-12.

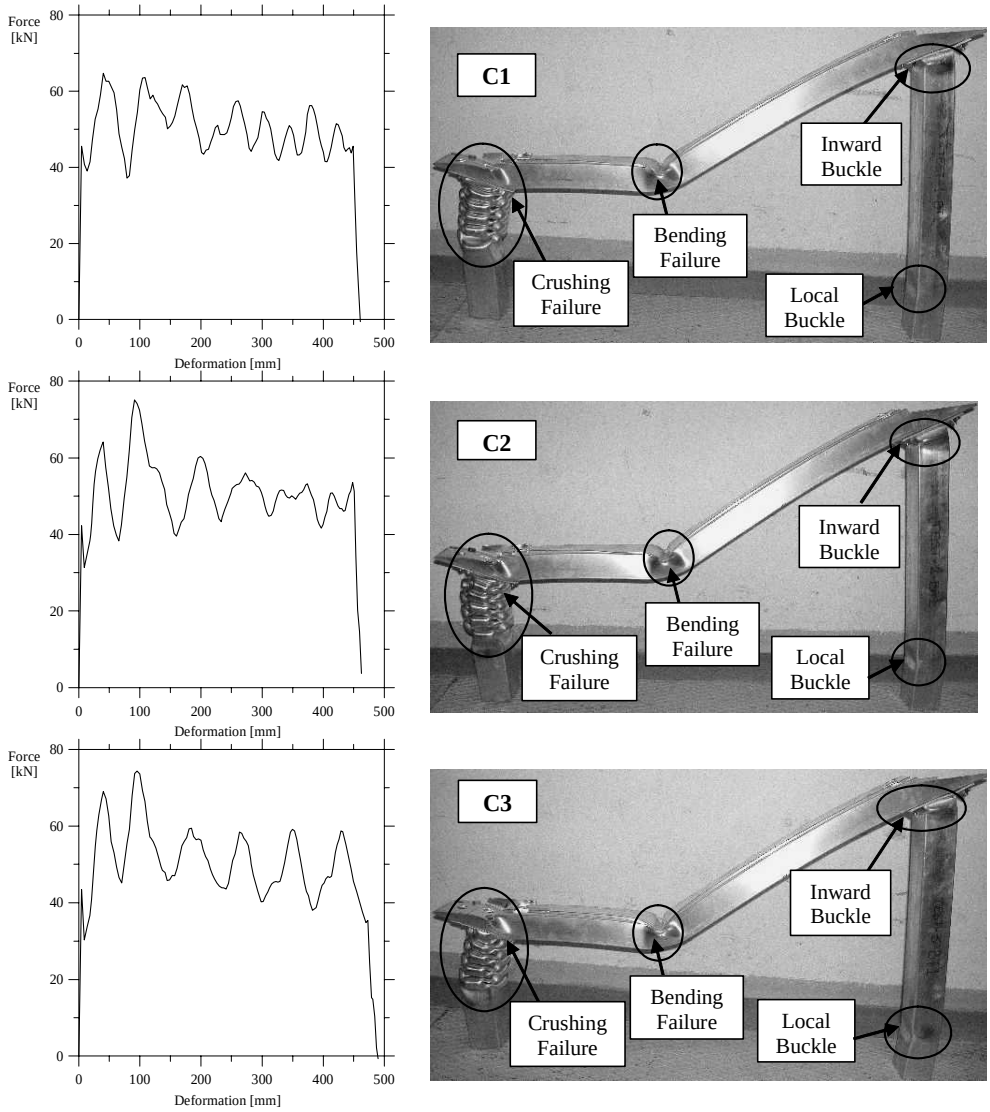

Figure 5-12 Experimental results for test series **C**.

All the tested specimens of this series obtained the same deformation mode. The bumper beam's cross-section in this series was not completely collapsed, Figure 5-12, as the longitudinals of test series **C** had a reduced strength, Section 3.4.1, when compared to the longitudinals of other test series. However, the impact energy absorbed by the bumper beam-longitudinal system was also much lower.

A photo gallery of the deformation history based on the high-speed video recordings for test specimen **C1** is given in Figure 5-13. The corresponding results from the loadcell data are shown in Figure 5-14.

The discussion on the sequence of events for test specimen **C1** in Figure 5-8 is presented below. The selected times are denoted with dots on the force-time curves in Figure 5-14. The impact started at time $t_1 = 0$. Initiation of buckling in the impacted longitudinal started with minor deformation of the bumper beam cross-section at time t_2. At time t_3 a central plastic hinge in the mid-section of bumper beam developed. At time t_4 the non-impacted longitudinal had a buckle very close to the HAZ due to the straining caused by the bumper beam, whereas another local buckle in the non-impacted longitudinal has developed at its clamped end at time t_5. The reaction wall crashboxes were activated by the trolley at time t_6, with notable amount of plastic deformations in the crashboxes.

Before complete crushing of the bumper cross-section, activation of the impacted longitudinal took place with the development of a buckle just below the HAZ. The position of the first buckle along the length of the longitudinal member appeared to be below the HAZ for all three parallels.

With the increase in impact force, the web of the bumper beam buckled outwardly at the impacted end and simultaneously a plastic hinge developed in the mid-section. The rest of the impact energy of the trolley was used in progressive folding of the impacted longitudinal and continued bending of the bumper beam.

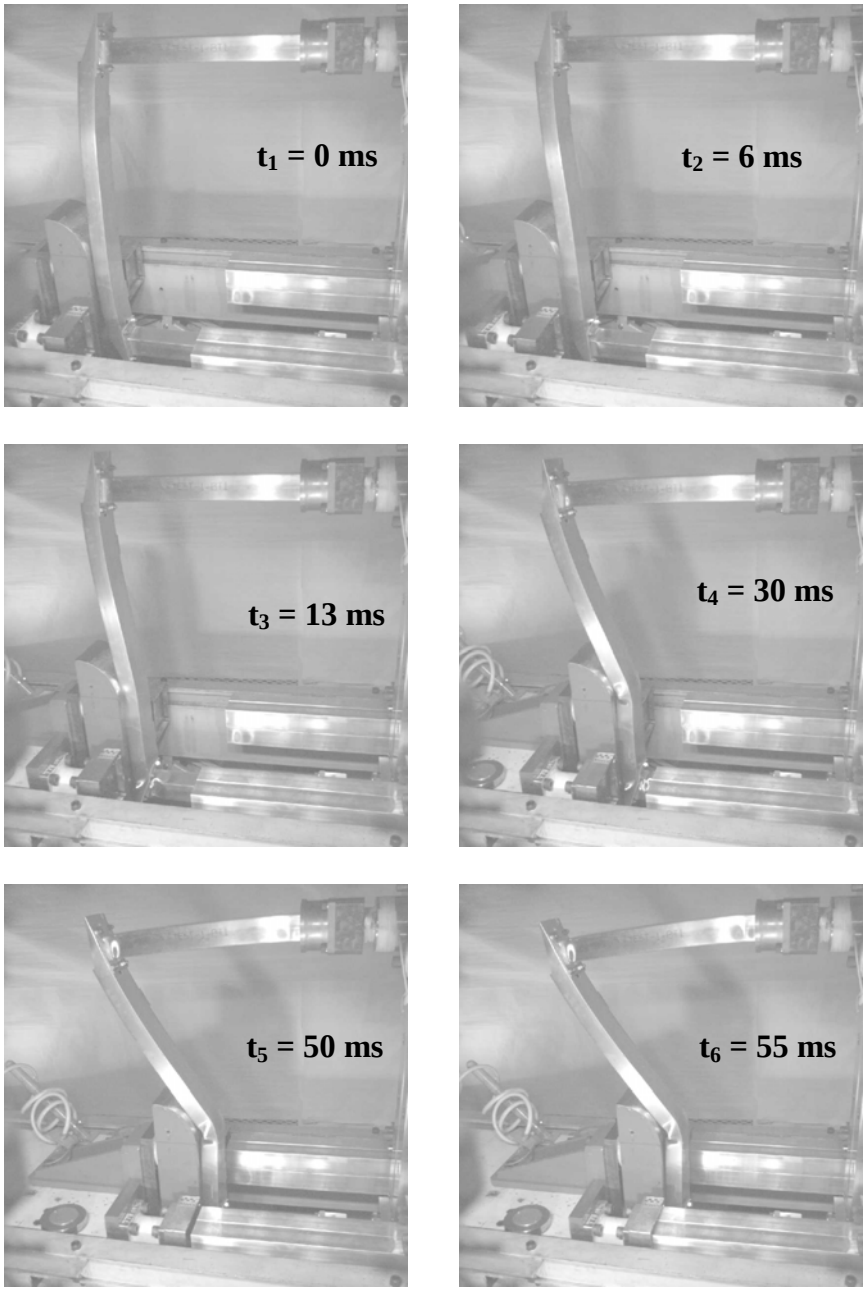

Figure 5-13 Photos taken from high speed video recording for test specimen **C1**.

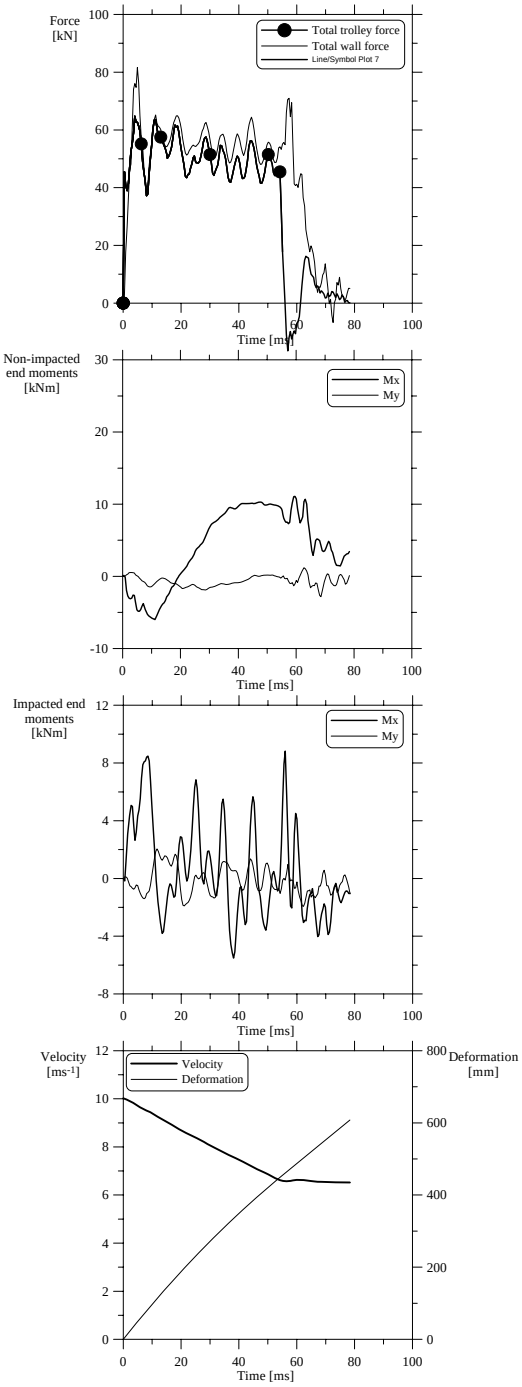

Figure 5-14 Loadcell data for test specimen **C1**.

A close view of the buckled bumper beam and the progressive folding in the impacted longitudinal is shown as “crushing” in Figure 5-15(a), while the bending at the mid-section of the bumper beam is shown in Figure 5-15(b).

As the crushing of the impacted longitudinal progressed further, the bumper beam curvature changed significantly. There was enough force in the axial direction of the bumper beam to localise the strains at the non-impacted end for the development of a through-thickness shear crack, but due to the soft nature of the longitudinal members an inward buckle developed below the HAZ. A close view of this buckle is shown in Figure 5-15(c).

This can also be observed from the peak in moment-time curve (M_x) data from the loadcell at non-impacted end in Figure 5-14 at about 30 ms. The moment was almost constant until the formation of another plastic hinge at its clamped end. The drop in the moment-time curve at 50 ms represented this event. These two buckles on the non-impacted longitudinal can be observed in all the three test specimens in Figure 5-12.

The filtered force-deformation plots for the three tests in this series are shown in Figure 5-16. When compared to test series **B**, Figure 5-10, the test series **C** showed good repeatability. No high peaks in the force-deformation plots are found as for test series **A** in Section 5.1. Owing to less strength and

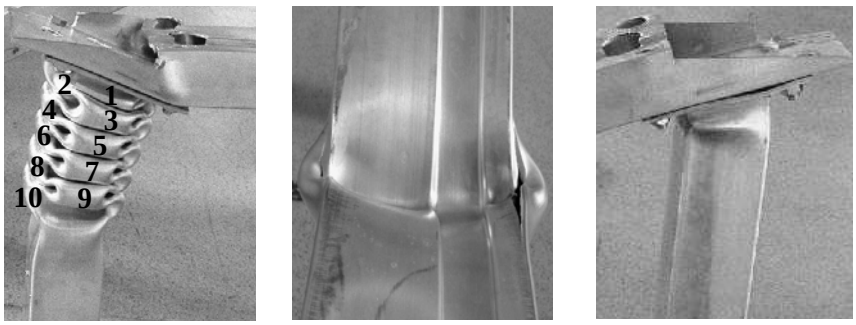

(a) Crushing (b) Bending (c) Inward buckle

Figure 5-15 Typical deformation and failure modes for test series **C**.

moderate strain hardening, see Section 3.4.1, the energy absorbed by the bumper beam-longitudinal system was, however, very small, see Figure 5-17(a). About 23 kJ of the impact energy has been absorbed by the bumper beam-longitudinal systems before the trolley activated the crashboxes on

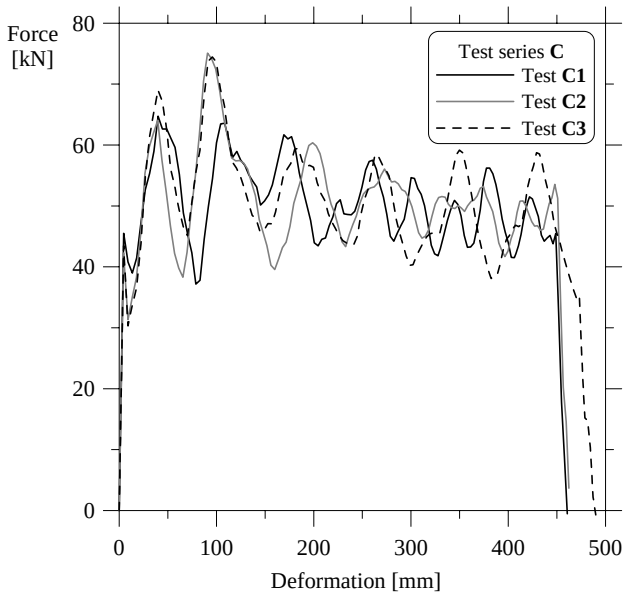

Figure 5-16 Filtered force-deformation plots for test series **C**.

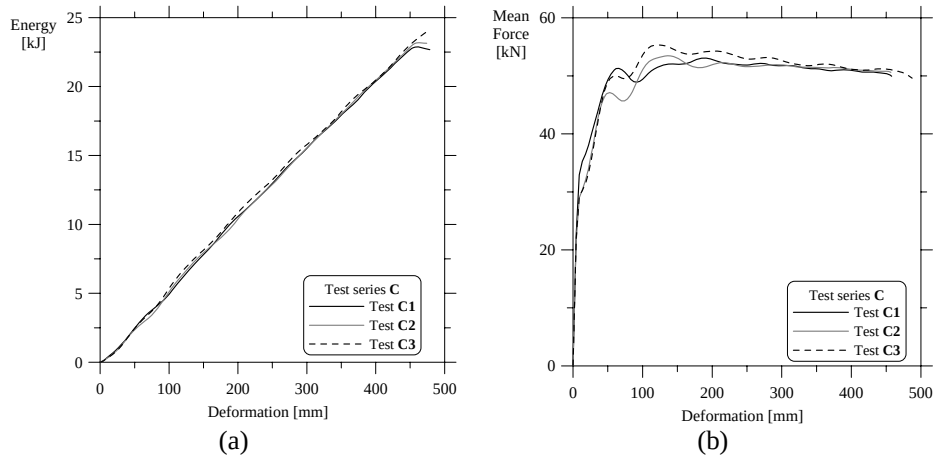

Figure 5-17 (a) Energy-deformation, (b) Mean force-deformation plots for test series **C**.

reaction wall. The activation of reaction wall crashboxes can also be recognised from the velocity-time curve in Figure 5-14. The cracks in the folds of the longitudinal and in the plastic hinge were not that notable. The mean force of the system, Figure 5-17(b), was low when compared to the other two test series **A** and **B**.

The accuracy parameter, defined by Equation (4.8), calculated for the three parallels is shown in Table 5-3. The average force level on the trolley was underestimated in all the tests but with in ± 5%. The deformation history in the form of an image gallery from the video camera recordings and the corresponding loadcell data for test specimens **C2** and **C3** are given in Appendix-C.

5.4 Test series D

In Section 5.1 experimental results for test series **A** were presented, where the impacting velocity was 10 m/s. Another set of experimental tests were performed at 15 m/s impact velocity (test series **D**, see Table 4-1). The longitudinals used for testing the bumper beam-longitudinal system at the increased speed were the same as those used in test series **A**, i.e AA7003-T79. In the following test results for test series **D** will be presented and discussed.

Table 5-3 Accuracy parameter Equation (4.8) for test series **C**.

Test Series **C**	Length prior to testing l_b (mm)	Calculated displacement $w(t_b)$ (mm)	Reaction wall crashboxes activation time t_b (ms)	Accuracy parameter ξ_b
C1	443	454.2	55	1.025
C2	448	453.4	55	1.012
C3	471	479.5	59	1.018

The response data obtained for test series **D** are shown in Figure 5-18. Filtered force-deformation plot for each test is shown together with corresponding final deformed shape. All the tested specimens of this series obtained the same deformation mode. As mentioned earlier (see Section 4.2.3) the experiments of test series **D** were recorded with two high speed cameras.

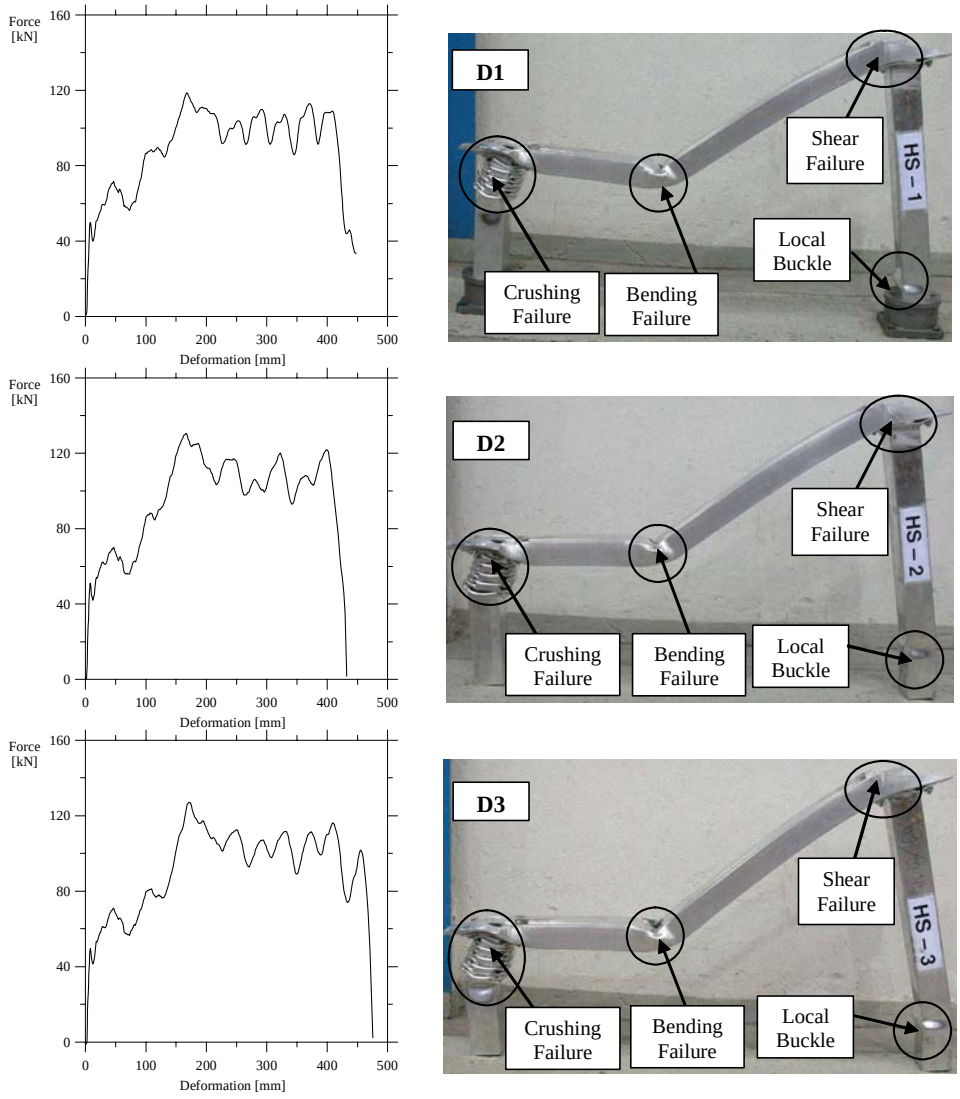

Figure 5-18 Experimental results for test series **D**.

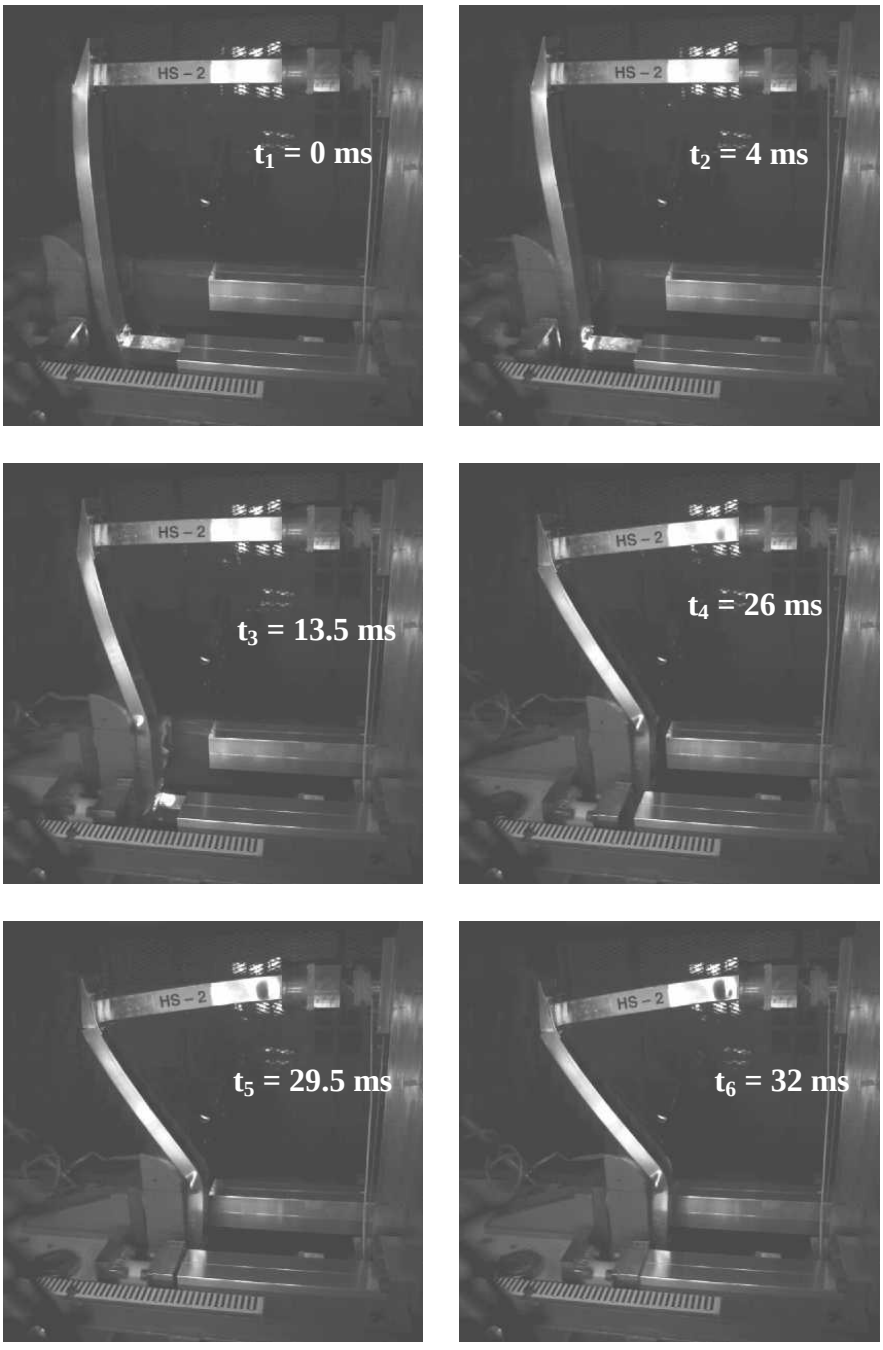

Figure 5-19 Photos taken from high speed video recording (first camera) for test specimen **D1**.

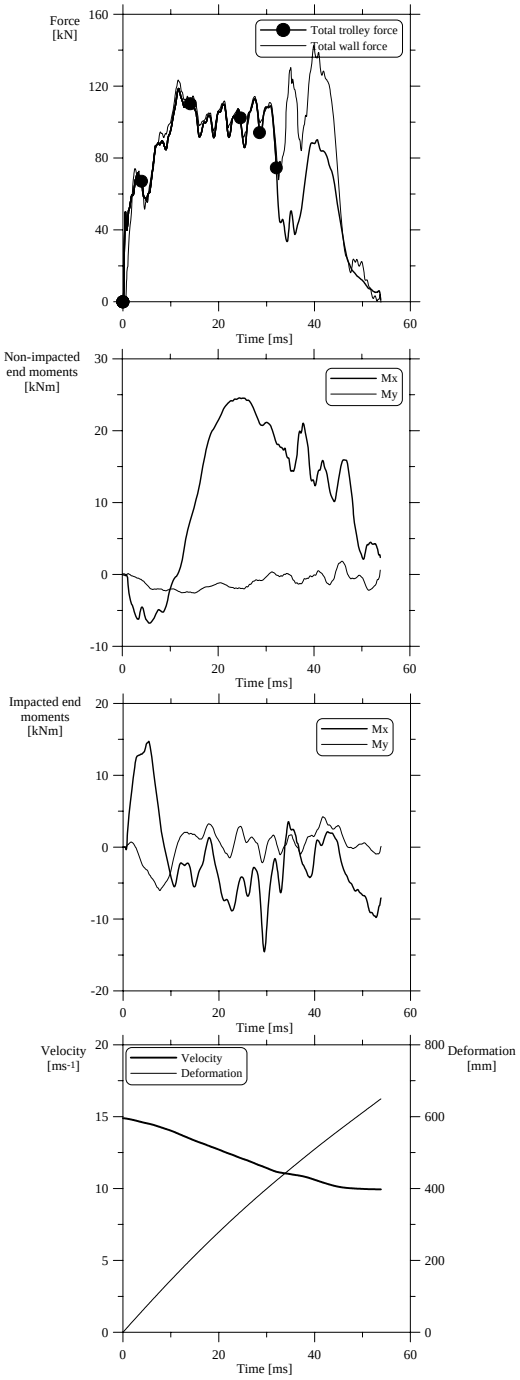

Figure 5-20 Loadcell data for test specimen **D1**.

The first and second camera recordings are shown respectively in Figure 5-19 and Figure 5-21. A photo gallery of deformation history is shown in Figure 5-19 for test specimen **D1**. The corresponding results from the loadcell data is presented in Figure 5-20. Filtered force-deformation plots for the three parallels are plotted in Figure 5-22.

The sequence of events in Figure 5-19, for test specimen **D1** was as follows. The selected times were denoted with dots on the force-time curves in Figure 5-20. The impact event started at time $t_1 = 0$. Buckling initiation in the impacted longitudinal started at time t_2. Development of a central plastic hinge in the bumper beam started at time t_3, before this time complete development of the first buckle in the impacted longitudinal took place. As the folding in the impacted longitudinal continued and also due to the change in the curvature of the bumper beam, a combined propagating tearing and through-thickness shear crack developed at the non-impacted end of the bumper beam. This happened at time t_4. A local buckle developed at time t_5 in the non-impacted longitudinal at its clamped end. The trolley activated the crashboxes on the reaction wall at time t_6.

(a) (b)

Figure 5-21 Images captured by second camera for test specimen **D1** (a) Buckling initiation, (b) complete formation of first buckle in the impacted longitudinal.

The second camera was mainly used to understand the deformation process (folding) which happened in the impacted longitudinal. From the camera recordings in Figure 5-21(a) it was clear that the buckling initiation in the impacted longitudinal started below the HAZ. The completely developed first buckle in the impacted longitudinal is shown in Figure 5-21(b).

During the initial phase of the impact process the bumper beam did not collapse completely as for test series **A**. Before complete crushing of the cross-section of the bumper beam, the initiation of a lobe in the impacted longitudinal took place. The first buckle in the impacted longitudinal started to develop at a deformation of 50-60 mm, see Figure 5-22. This corresponds to 4 ms in the second image of Figure 5-19 and is marked with a dot on the force-time curve in Figure 5-20. Crushing of the bumper beam cross-section and bending of the interface plate continued with the complete development of the first buckle in the impacted longitudinal, resulting in rise in the force level. The second buckle that developed in the impacted longitudinal led to

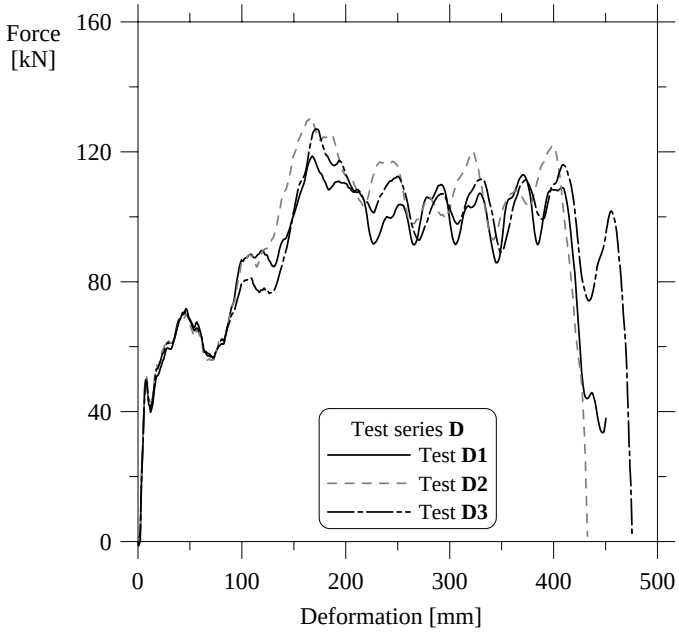

Figure 5-22 Filtered force-deformation plots for test series **D**.

the highest peak in the force-deformation plots in Figure 5-22, at about 160 mm deformation.

Subsequent crushing of the impacted longitudinal was by progressive folding with an axisymmetric deformation mode. For the three parallels, there was little scatter in the force-deformation data with respect to the highest peak force level see Figure 5-22.

The crushed bumper beam together with the progressive folding mode in the impacted longitudinal can be seen in Figure 5-23(a). Of the three systems tested, test specimens **D1** and **D2** obtained the same amount of deformation, while slightly higher deformation was observed for test specimen **D3**. The reason for this higher deformation in test specimen **D3** could be due to the use of pre-deformed crashboxes on the reaction wall.

The development of a plastic hinge in the mid-section of the bumper beam, see Figure 5-23(b), and the propagating tearing and through-thickness shear cracks at the non-impacted end followed the same course as for test series **A**. A close view of the propagating tearing/through-thickness shear crack is

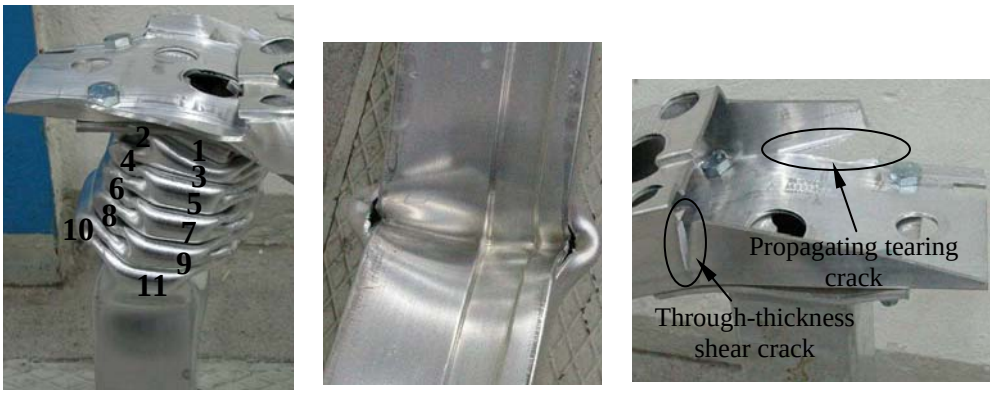

(a) (b) (c)

Figure 5-23 Typical deformation and failure modes for test series **D**: (a) Crushing failure, (b) Bending failure and (c) Through-thickness shear and propagating tearing cracks.

shown in Figure 5-23(c). For test specimen **D3** the location of the second camera was changed to capture the fracture events that were happening at the non-impacted end of the bumper beam. It was revealed that the propagating tearing crack at the intersection between the lower flange and the web started much earlier than the through-thickness shear crack.

From the post-crash test specimens a considerable amount of failure zones was observed in the folds of the longitudinal. However, these failure events are not critical since they do not propagate.

From the video recordings it was observed that the trolley activated the crashboxes on the reaction wall. The energy-deformation and mean force-deformation plots for test series **D** are plotted in Figure 5-24(a) and (b) respectively. It was clear from these figures that, for the same amount of deformation test specimens **D1** and **D3** absorbed almost the same amount of energy, while slightly increased energy absorption was found for test specimen **D2**. Furthermore, it was not clear from the high speed video recordings why there was an increased peak force level for the test specimen **D2** in Figure 5-22.

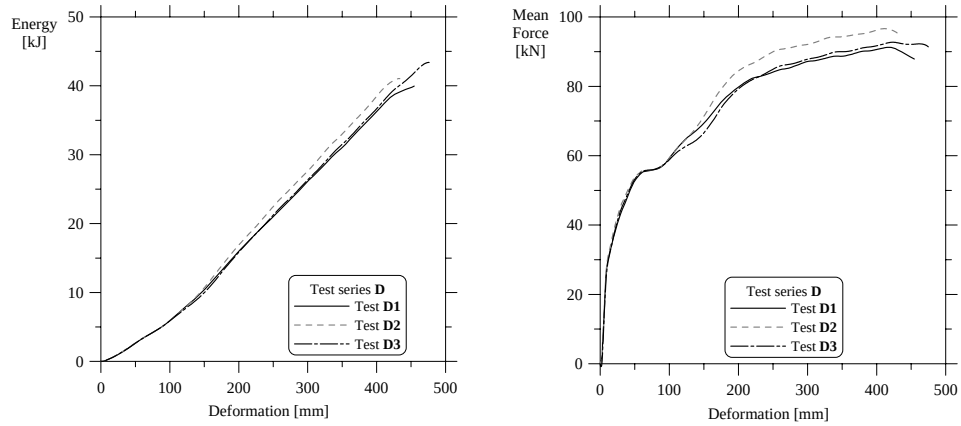

Figure 5-24 (a) Energy-deformation, (b) Mean force-deformation plots for test series **D**.

The accuracy parameter defined by Equation (4.8) for the three parallels of test series **D** is shown in Table 5-4. The parameter was within the rage of 0.99-1.007, indicating a very good accuracy of the recorded force. The deformation history of test specimens **D2** and **D3** obtained from the high speed video camera recordings and the loadcells are given in the Appendix-D.

5.5 Comparison of test series A and D

The longitudinals used in the test series **A** and **D** were the same, i.e. AA7003-T79, and the only difference being the impact velocity of 10 and 15 m/s for test series **A** and **D**, respectively**.**

5.5.1 Force-deformation

The total impact energy available for test series **A** and **D** was 39.7 kJ and 89.3 kJ, respectively. Thus for test series **D** the impact energy was more than double that of test series **A**. A much higher peak force was expected due to the influence of inertia and material strain-rate hardening, as instantaneous plastic strains develop at the beginning of the response. The typical force-deformation plots for selected test of test series **D** is plotted together with test series **A** in Figure 5-25.

Table 5-4 Accuracy parameter Equation (4.8) for test series **D**.

Test Series **D**	Length prior to testing l_b (mm)	Calculated displacement $w(t_b)$ (mm)	Reaction wall crashboxes activation time t_b (ms)	Accuracy parameter ξ_b
D1	423	422.0	32	0.997
D2	420	423.1	32	1.007
D3	456	458.4	35	1.005

In the beginning of the deformation process, test series **A** and **D** behaved quite differently. For test series **A** complete collapse of the bumper beam cross-section occurred first and then the buckling initiation in the impacted longitudinal started, whereas in test series **D** the bumper beam did not collapse completely before the initiation of buckling in the impacted longitudinal.

The development of the second buckle in the impacted longitudinal caused to the highest peak in both test series. However, the peak force level was lower for test series **D** than for test series **A**, see Figure 5-25. The subsequent crushing of the impacted longitudinal was by a progressive folding mode in both series systems.

The energy-deformation and mean force-deformation plots for test series **A** and **D** are shown in Figure 5-26(a) and (b), respectively. From Figure 5-26(a) one can clearly observe that the amount of energy absorbed by both

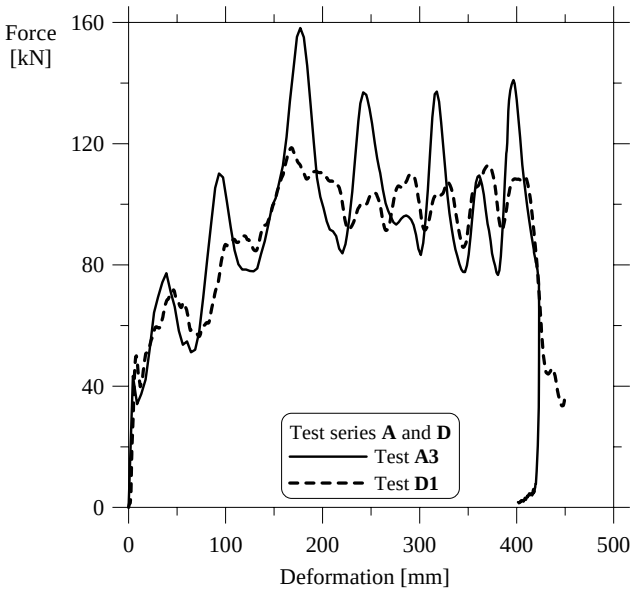

Figure 5-25 Comparison of typical force-deformation curves for test series **A** and **D**.

test series was almost the same before the impactor activated the crashboxes on the reaction wall.

5.5.2 Deformation shape

A comparison of the impacted end of the bumper beam-longitudinal systems for test series **A** and **D** in Figure 5-1 and Figure 5-18, respectively, reveals that the number of lobes developed in the impacted longitudinal was different. The number of lobes developed in test series **D** was ten, Figure 5-23, while the corresponding number for test series **A** was nine Figure 5-5 (a).

In test series **D**, the impact energy was not completely absorbed by the bumper beam-longitudinal system. Thus even after the activation of the crashboxes on the reaction wall the system deformed further together with the crashboxes using the rest of the impact energy. Hence, the impacted longitudinal had an extra lobe in test series **D** than in test series **A**. Thus, it is clear that the number of lobes developed in the impacted longitudinal of such a system was dependent on the impact velocity, at least for the systems

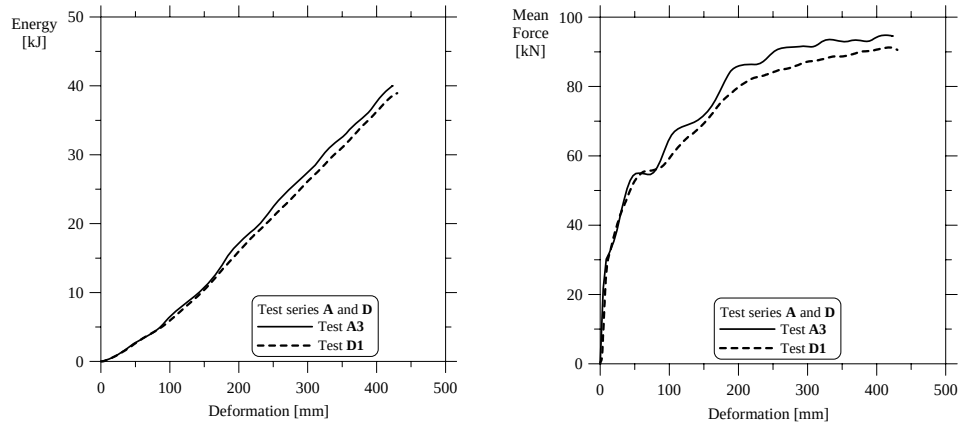

Figure 5-26 Comparison of (a) Energy-deformation, (b) Mean force-deformation plots for test series **A** and **D**.

tested here. Jones (1997) also noticed that there is an increase in the number of lobes developed with the increase in impact velocity.

From Figure 5-23 one can also clearly observe that the deformed end of the impacted longitudinal has some rotation towards the non-impacted end, in test series **D**. Whereas no such rotation was observed in test series **A**, see Figure 5-1. The rotation of the deformed end of the impacted longitudinal in test series **D** might be due to the inertia of the system at the increased impact velocity. Moreover, the lobes developed in test series **D** were much more compressed than in test series **A**.

Figure 5-27 shows the comparison of the propagating tearing and through-thickness shear cracks which occurred at the non-impacted end of the bumper beam in test series **A** and **D**. In the figure test specimen **A3** is not shown, since it had encountered weld fracture instead of developing a through-thickness shear crack. The through-thickness shear crack in test series **A** was not consistent compared to test series **D**. In test specimens **A1** and **A2** the through-thickness crack occurred at an angle to the axis of the longitudinal Figure 5-26, whereas in test specimens **A4** and **A5** the crack was almost parallel to the initial axis of the longitudinal. One possible

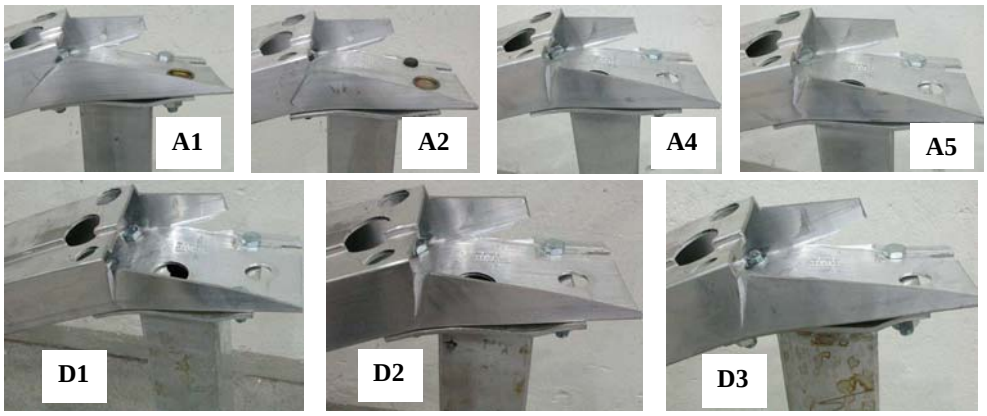

Figure 5-27 Comparison of through-thickness shear crack at the non-impacted end of bumper beam for test series **A** and **D**.

reason for this inconsistency in the development of through-thickness shear crack in test series **A** is the manner in which the non-impacted end of the bumper beam was strained due to the offset loading.

5.6 Summary

Test results on the bumper beam-longitudinal systems at 40% offset impact have provided guidelines on the influence of alloy, temper condition and also the impact velocity on the crash performance.

Test series **A** revealed that the total impact energy was effectively utilised in crushing the bumper beam as well as the longitudinal at the impact end, without the activation of the crashboxes on the reaction wall. However, test series **B**, **C** and **D** have shown the activation of crashboxes on the reaction wall. The force-deformation characteristics seemed to be similar for all the test specimens of test series **A**, see Section 5.1, even though their deformation pattern varied. For test specimens **A2** and **A5** the bumper beam encountered unacceptable failure modes. Of the 14 tests carried out weld fracture was observed only in test specimen **A3**.

In test series **B** three significantly different deformation modes were observed for the bumper beam-longitudinal system (see Section 5.2) i.e. the tendency to unacceptable failure modes of the bumper beam and longitudinal was higher. The only difference between test series **A** and **B** was the temper condition of the longitudinals. Series **B** (AA7003-T1) longitudinals had less strength with significant strain-hardening compared to series **A** (AA7003-T79) longitudinals, which had higher strength and moderate strain-hardening. Moreover, the results for test series **B** have shown that the deformation mode of the system can change from progressive folding mode to global bending mode. Thus, the temper condition of the chosen longitudinal has significant effect on the crash performance and energy absorption of the bumper beam-longitudinal system. For a chosen impact velocity, Jensen (2005) found by numerical

simulations of axially loaded aluminium extrusions a change in collapse mode when the temper condition of AA6060 is changed from T6 to T4.

It is shown that test series **C** bumper beam-longitudinal systems obtained the same deformation mode in the three parallel tests, see Section 5.3, namely progressive folding in the impacted longitudinal. Moreover, the propagating tearing and through-thickness shear cracks at the non-impacted end of the bumper beam was not observed. The failure observed in the folds of the impacted longitudinals was much less for test series **C** than for other test series.

Test series **D** showed highly repetitive and robust performance at the increased impact velocity. Comparison of test series **A** and **D** revealed that the deformed end of the impacted longitudinal in test series **D** had some rotation towards to the non-impacted end. Further, by increasing the impact velocity test series **D** experienced less material failure compared to test series **A**, see Figure 5-5 and Figure 5-23 the bending failure in the mid-section of the bumper beam.

Based on the experimental results of bumper beam-longitudinal system at 40% offset it can be concluded that for a given amount of deformation, test series **A** and **D** absorbed almost the same amount of energy for the same amount of deformation which is higher than for test series **B** and **C**, see Figure 5-28.

In 40% offset impacts the bumper beam undergoes considerable bending due to the direct impact of the impactor and the energy absorption was mainly concentrated in the impacted longitudinal only. The non-impacted longitudinal, however, experienced only minor deformations in the form of plastic hinges.

In general it appears that the behaviour of the bumper beam-longitudinal systems in the current study is dependent on the collapse mode of the impacted longitudinal. For the entire test series the impacted longitudinal collapsed progressively, except in test series **B**.

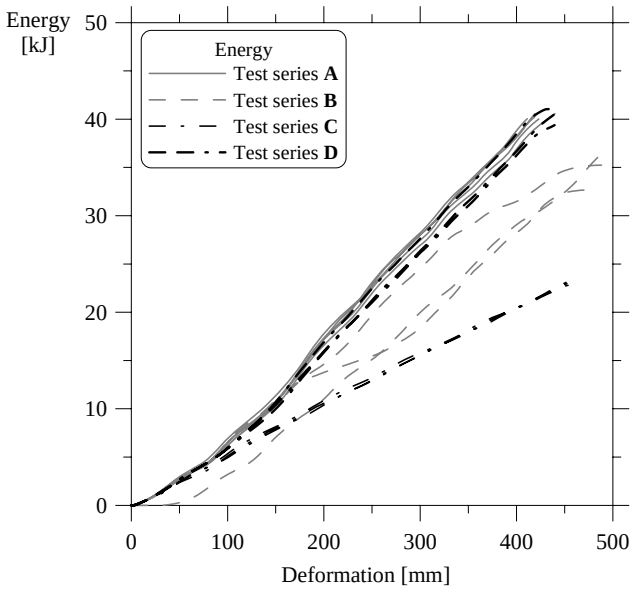

Figure 5-28 Comparison of energy-deformation plots for the entire test series.

Chapter 6 Finite Element Modelling

The objective of this chapter is to generate the FE-model of the bumper beam as well as the test set-up as shown in Figure 1-2, in order to predict the response of the bumper beam-longitudinal system.

As mentioned earlier, manufacturing of bumper beams from aluminium extrusions often involves series of forming operations performed in a soft condition (W-temper), which is obtained by soft solid-solution heat treatment. Subsequently, the bumper beams are artificially age-hardened to T6 peak hardness condition. Thus it is clear that for proper crash performance of the systems the FE-model must rely upon the geometry obtained from a simulation of process route, i.e. including simulation of all major forming operations. Moreover, the forming operations also result in an inhomogeneous evolution of some internal variables (among others the effective plastic strain) within the shaped components, Lademo et al. (2004c). Stretch-bending is a well-suited process, Clausen et al. (2000), for the plastic forming of bumper beams. The intention here is to explain how the numerical stretch-bending and other forming operations were performed to obtain the shape of the bumper beam. The other forming operations include trimming and reshaping of the holes.

The process of forming a component changes the properties of the material being used. This is generally ignored in the design and validation process of automotive structures even though the changes in material strength and thickness may be substantial. Although the forming effects on the performance of individual components have been reported in the literature (Dutton et al., 1999; Reid, 1996; Kim et al., 2003; Bottcher and Frik, 2003; Lee et al., 2001; Kim and Huh, 2003; Dagson, 2001), there are few papers reporting the consequence of including formed properties in full vehicle

models (Dutton et al., 2001; Cafolla et al., 2003). However, in the above studies the component never undergoes the artificial ageing treatment as the bumper beam in this study.

The accuracy of any simulation depends on how accurately the modelling work has been carried out. The process route for the production of the bumper beam from the straight extrusion to the final product is demonstrated in more detail using the flow chart in Figure 6-1. At the end of this flow chart an FE-model of the test set-up, see Figure 1-2, is generated.

Efforts were taken in constructing the numerical model of the bumper beam as similar as possible to the reality. The bumper beam and all other components in the system was modelled and meshed in order to make a precise model using TrueGrid® pre-processor (2001). Thus, this chapter basically deals with the modelling of the components of the bumper beam-longitudinal system. The basis for modelling lies upon an analysis model obtained from Hydro Aluminium Structures (HAST).

The same mesh size and constitutive model, see Section 2.3, is used for both the forming and crash analyses. Anisotropy development due to pre-stretching is not included in the model, but no experiments have been performed to verify this assumption.

6.1 Geometry model of the test set-up

6.1.1 Stretch-bending of bumper beam

When studying the FE-analyses of stretch-bending of aluminium extrusions, Hopperstad et al. (1998) found that the shape of yield surface has significant influence on the local deformation pattern of the cross-section. Thus, in order to predict a reliable final geometry of the bumper beam, the stretch-bending and other forming operations in the present chapter were performed

only with the user-defined material model (MAT-41) discussed in Chapter 2.

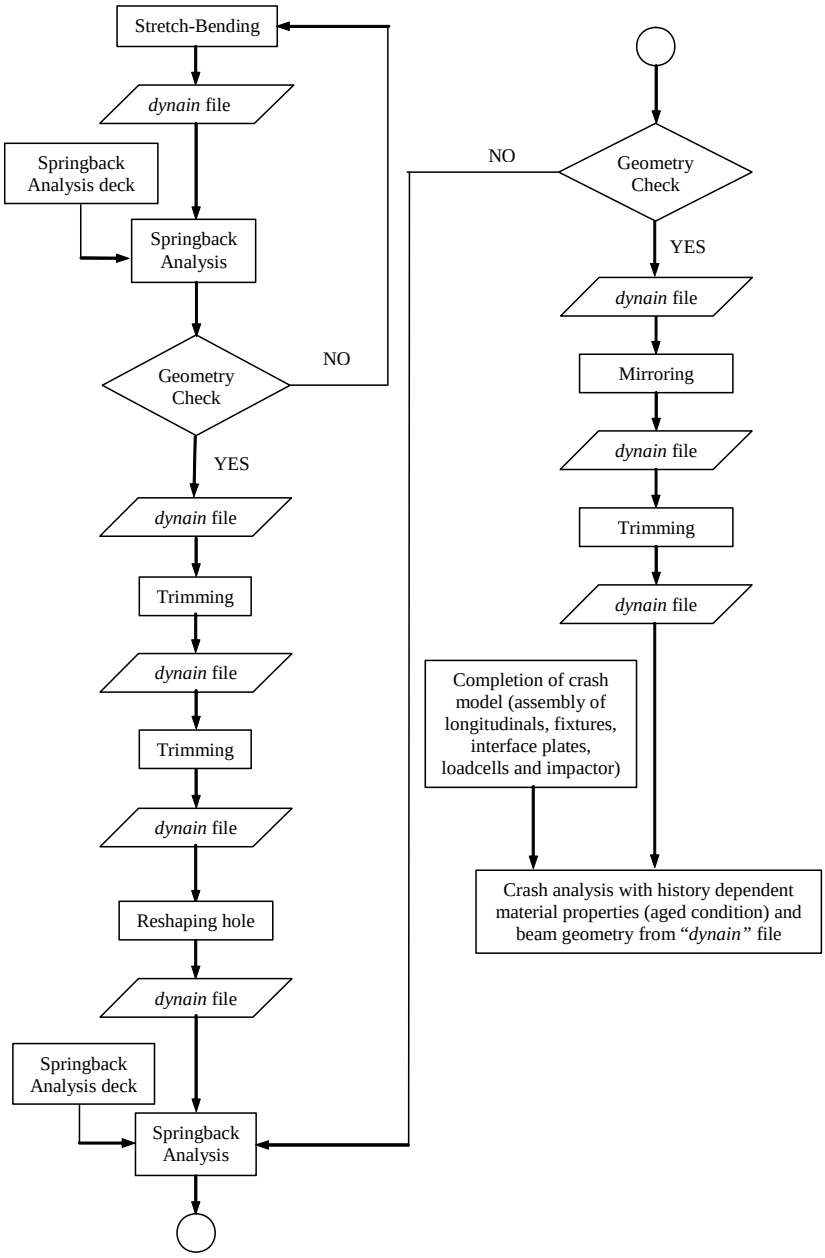

Figure 6-1 Flow chart showing the various operations in the development of FE geometry model of the test set-up.

From the flow chart shown in Figure 6-1 it is seen that the first operation is stretch-bending of the bumper beam to the required curvature. Due to symmetry of the bumper beam only a model of half of the process was constructed. Various views of the bumper beam model are shown in Figure 6-2 for the input to the stretch-bending operation, while the FE-modelled cross-section is compared with the original drawing in Figure 6-3. The tooling used to perform the stretch-bending operation is shown in Figure 6-4. As can be seen the tooling is shown in the absence of bumper beam; this is done intentionally to avoid colour confusion between the bumper beam and tooling parts.

The mandrel is inserted into the bumper beam through the cut-out on the left end, which firmly fixes inside the bumper beam, and rotates about its own centre-of-rotation. Rotation of the mandrel takes care of sagging on the upper flange of the bumper beam at the cut-out section. The stretch-bending operation initiated when the clamp started to move in x-direction i.e. towards to the lower die. Initial and final positions of the stretch-bending tools are shown in Figure 6-5(a) and (b), respectively. As mentioned, the stretch-bending operation is usually performed in W-temper condition. The

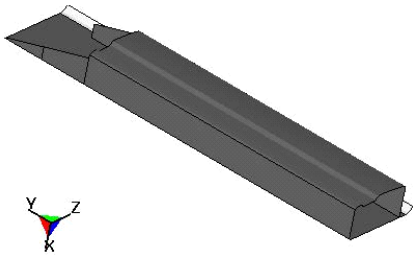

(a)

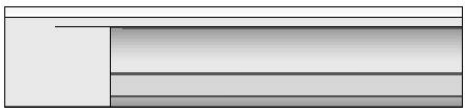

(b)

Figure 6-2 Various views of the bumper beam; (a) Isometric View, (b) Top View.

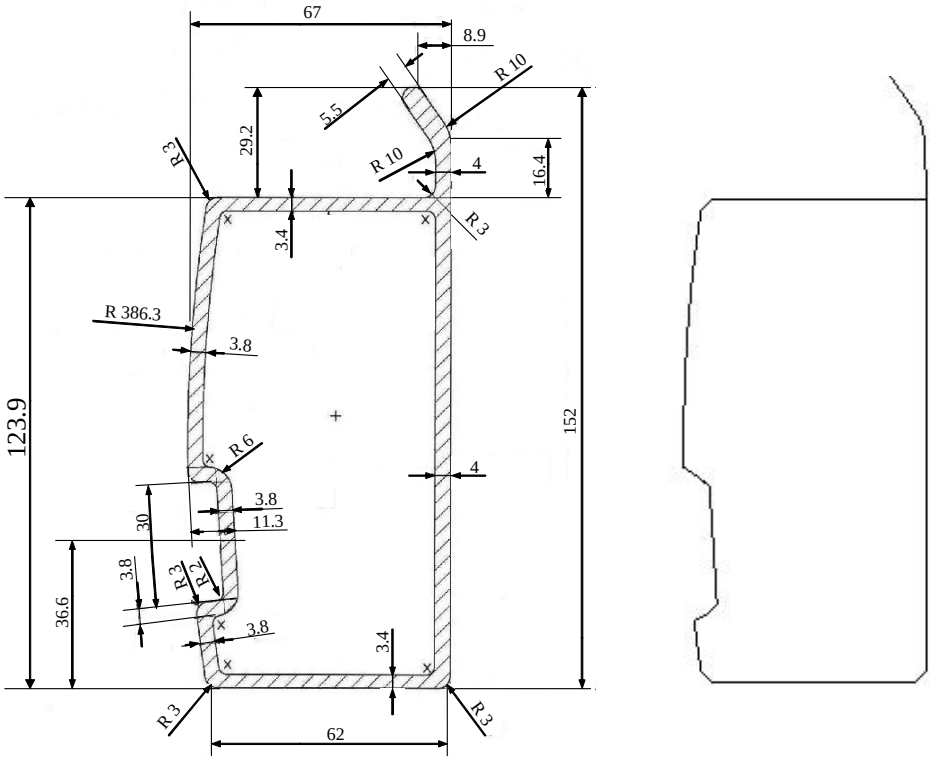

Figure 6-3 Comparison of bumper beam cross-section: (a) original dimensions, (b) FE-model.

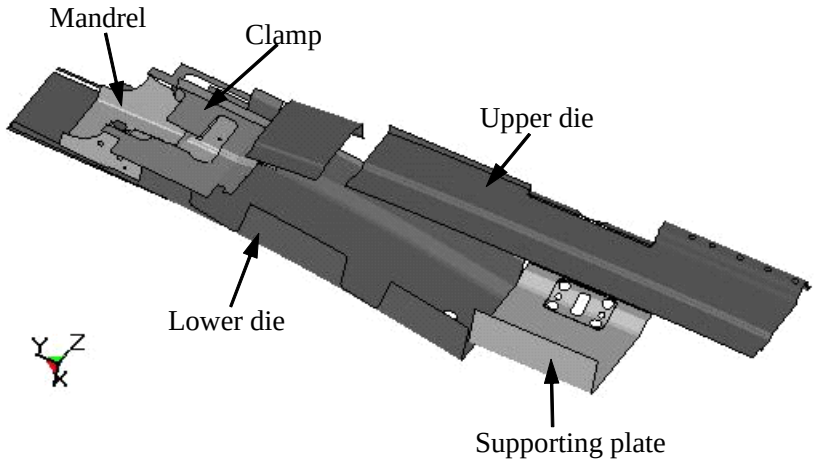

Figure 6-4 Tooling used for stretch-bending of bumper beam.

W-temper properties of the bumper beam are given in Table 3-6. A solution time of 0.1 s was chosen for the explicit analyses of the stretch-bending operation.

The movements of the upper die, lower die and clamp are described by cosine functions and are shown in Figure 6-6. The supporting plate was fully-constrained so that it does not move or rotate through out the stretch-bending operation. Movement of the clamp in x-direction was stopped when it touched the upper flange of the bumper beam and the lower die, this happened at 0.05 s.

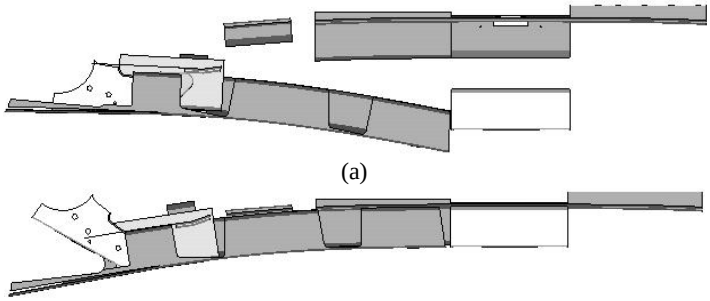

(a)

(b)

Figure 6-5 Stretch-bending tool (a) initial position, (b) final position.

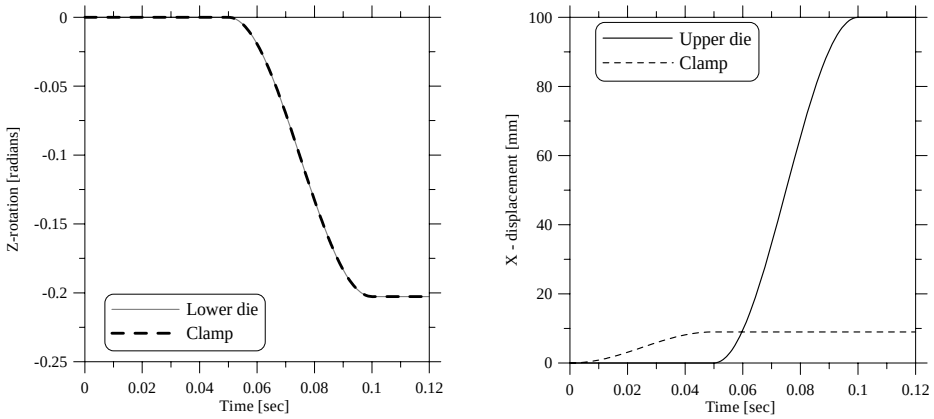

(a) (b)

Figure 6-6 Displacement of the dies in stretch-bending of bumper beam (a) z-rotation of lower die and clamp, (b) x-displacement of upper die and clamp.

As and when the clamp movement was stopped the lower die started rotating about its pivot point, together with the stopped clamp, clearly seen from Figure 6-6(a). At this time the upper die also started to move in x-direction, see Figure 6-6(b). In the forming simulations care has been taken such that there was no addition of kinetic energy.

Modelling aspects for the stretch-bending of the bumper beam and the boundary conditions that are applied at the right end of the bumper beam, see Figure 6-2(b), are listed in Table 6-1. The bumper beam obtained the desired curvature when the rotation of the lower die was stopped.

Table 6-1 Modelling aspects for the stretch-bending of bumper beam.

Modelling aspects	Description
Bumper beam AA7108	
Element type:	Quadrilateral (Belytschko-Lin-Tsay shell) (default)
Integration points:	1 in-plane and 5 through-thickness
Hourglass control:	Stiffness form
No. of elements in half model:	9577
Element size (approx.):	5.0x5.0 mm^2
Stretch-bent length (half):	692.00 mm before stretch-bending 694.21 mm after stretch-bending
Cross section geometry:	See Figure 6-2 and Figure 6-3
Material models:	**MAT-41** User-defined material model with W-temper properties, see Table 3-6
Material strain-rate effects:	Neglected
Geometrical imperfections:	None
Nodal constraints:	**Forming**: Translation in y-direction is constrained at right end. Rotations about x- and z- direction are constrained
Total mass (half model)	2.264 kg
Tooling for stretch-bending	
Element type:	Not applicable
Integration points:	Not applicable
Hourglass control:	Not applicable
No. of elements:	Large number of elements are required to represent the surfaces
Element size (approx.):	Min. 3.5 mm and Max. 6 mm
Cross section geometry:	See Figure 6-4
Material models:	**MAT-20** (rigid body)

Nodal constraints:	Lower die : x, y and z-displacements; x- and y- rotations Upper die : y- and z- displacements; x, y and z- rotations Clamp : y- and z-displacements; x- and y- rotations Mandrel : x, y, and z-displacements; x- and y- rotations Supporting plate : x, y, and z-displacements and rotations
Contact	
Bumper beam (S)	Single surface, penalty based, friction coefficient 0.2
Clamp (M) – Bumper beam upper flange (S)	Automatic nodes to surface, penalty based, friction coefficient 0.2
Mandrel (M) – Bumper beam upper flange (S)	Automatic nodes to surface, penalty based, friction coefficient 0.2
Mandrel (M) – Bumper beam lower flange (S)	Automatic nodes to surface, penalty based, friction coefficient 0.2
Lower die (M) – Bumper beam lower flange (S)	Automatic nodes to surface, penalty based, friction coefficient 0.2

S stands for slave set nodes and M for master set nodes

The bumper beam will have some residual stresses because of the stretch-bending operation; these stresses will try to relax elastically, when the stretch-bending tools are removed, to reach an equilibrium state. The elastic recovery of stresses corresponds to an unloading phase; in general implicit codes are more effective to represent this phase, see Mercer et al. (1995). Hence, an implicit springback simulation was performed. The springback analysis was performed on the *dynain*[1] file obtained at the end of stretch-bending operation. It was observed from the simulation that there was a shortening along the length of the bumper beam in the axial direction. The axial-length of the bumper beam before and after springback analysis was measured to be 694.88 and 694.21 mm, respectively. Figure 6-7 shows the bumper beam geometry obtained after performing implicit springback simulation. At the end of the implicit springback analysis a new *dynain* file was created.

[1] LS-DYNA optionally generates different types of output files. One of them is the *dynain* file which can be used as an input file for the next process. The *dynain* file is a simple text file including geometry, shell thickness, stresses and history variables.

6.1.2 Results from stretch-bending of bumper beam

The results from the stretch-bending operation indicating percentage thickness reduction and effective plastic strains are shown in Figure 6-8 and Figure 6-9, respectively. It is notable that the thickness reduction is mostly limited to the thinning of the upper flange, Figure 6-8. Near by the cut-out region of the upper flange there has been considerable amount of work-hardening, as indicated by the plastic strain data, showing more than 5% strain. The extreme left end of the bumper beam has undergone no straining at all, Figure 6-9.

6.1.3 Trimming, reshaping and mirroring

The next operation in sequence as per the flow chart (Figure 6-1) is trimming. The *dynain* file created at the end of the implicit springback analysis is used as a basis and the trimming option of LS-DYNA (Hallquist, 2003) was used to trim holes on the upper flange of the bumper beam, by defining three curves at the three specified locations. At the end of this trimming operation a new *dynain* file was created that is carried further to the next operation. The geometry of the bumper beam obtained after trimming the holes is shown in Figure 6-10.

Following the sequence in Figure 6-1, the next operation is also trimming. The material in white colour attached to the back face of bumper beam in Figure 6-10, was trimmed away by using two trim curves. The earlier *dynain* file was called while performing the present trimming operation and the geometry of the bumper beam is shown in Figure 6-11.

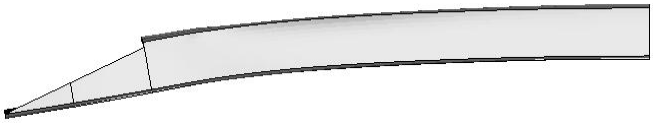

Figure 6-7 Bumper beam geometry after springback analysis.

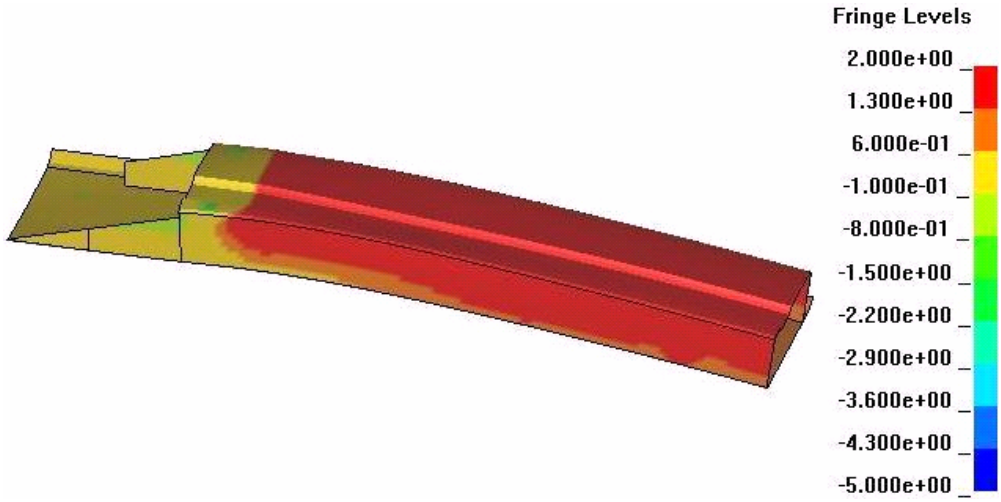

Figure 6-8 Contours of percentage thickness reduction.

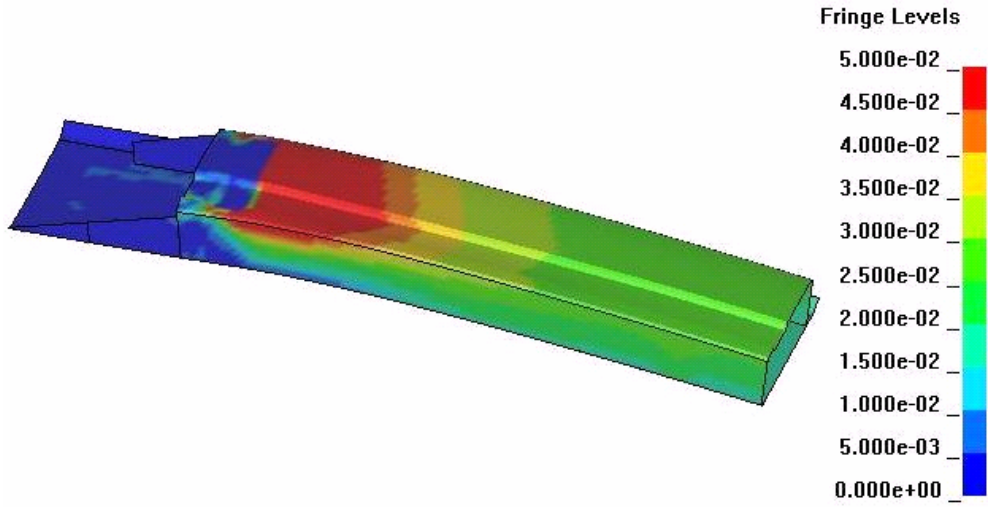

Figure 6-9 Contours of effective plastic strain.

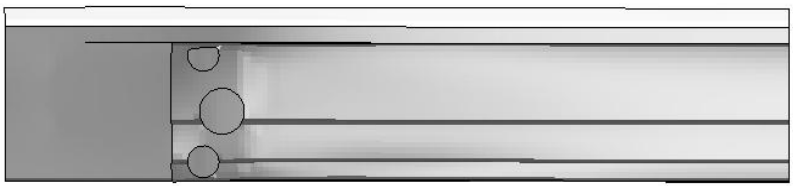

Figure 6-10 Bumper beam after trimming holes.

The next operation according to Figure 6-1 is reshaping; the top hole, which can be seen on the upper flange of the bumper beam, was reshaped using a reshaping tool shown in Figure 6-12. Here also the expansion tool is shown in the absence of bumper beam to avoid colour confusion.

The expansion tool (white colour) moves in the direction of the arrow and at the same time the material around the top hole, i.e. on the side wall, of the bumper beam was expanded Figure 6-10. After this operation again an implicit springback analysis was performed on the last *dynain* file. The expanded hole in the bumper beam after springback analysis is shown in Figure 6-13.

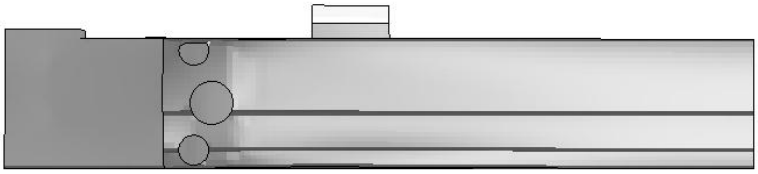

Figure 6-11 Bumper beam after trimming back face material.

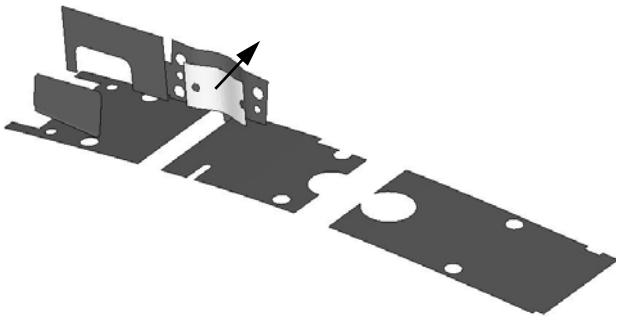

Figure 6-12 Reshaping tool for the expansion of the side walls of the bumper beam.

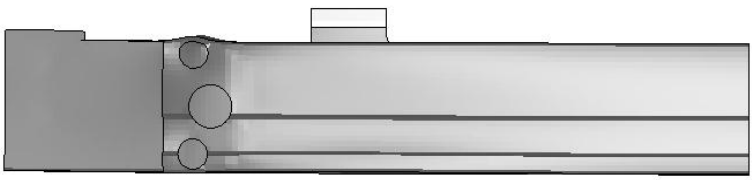

Figure 6-13 Geometry of the bumper beam after reshaping of the top hole.

The stretch-bending and other trimming operations were performed only on a half section of the bumper beam. The shift to a full bumper beam model was performed by mirroring the first half that contained all the data as the parent section. The full model of the bumper beam was obtained by executing a purpose-built programme called *mirror*. When this was executed a new file named *new.k* (which is also in the format of a *dynain* file, but called with a different name) was created. This file was again called upon when performing the rest of the trimming operations. The full bumper beam after the mirroring operation is shown in Figure 6-14.

Following the flow chart, Figure 6-1, the next operations were trimming of holes on the lower flange and a hole on the upper flange of the bumper beam, respectively. These holes were trimmed by using trim curves at the respective locations on the *dynain* file obtained at the end of the *mirroring* operation. The complete geometry of the bumper beam is shown in Figure 6-15.

The obtained bumper beam only includes the thickness variations resulting from the stretch-bending process. The cross-section of the rotary stretch-bent bumper beam is shown in Figure 6-16. The outward flange (circled in Figure 6-16), should ideally be bent perpendicularly i.e. 90° to the lower flange of the bumper beam during the hole expansion process. However, the analysis model failed to predict this event properly. It has been observed

Figure 6-14 Full model of the bumper beam after mirroring.

Figure 6-15 Complete model of the bumper beam.

from the experiments that this outward flange was not involved in the crash process.

The geometry of the bumper beam obtained from numerical simulations was able to represent the global behaviour satisfactorily with respect to the cross-section and stretch-bent length. The full length of the stretch-bent bumper beam measured on the test specimen was 1388 mm, while that obtained from simulation was 1388.42 mm. No attempt was made to measure the amount of springback during the unloading phase.

6.2 Modelling of system components

Modelling aspects for other components like the longitudinals, interface plates, loadcells, fixtures and impactor used in the crash analysis are summarised in Table 6-2. The interface plate is shown in Figure 6-19(a), in which numbers from 1 through 4 represent the fastening locations. The coordinates at these fastening locations are given in Figure 6-21.

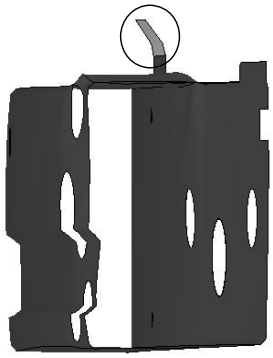

Figure 6-16 Cross-section of the stretch bent bumper beam.

Table 6-2 Modelling aspects of components used in crash analysis.

Modelling Aspects	Description
Longitudinal and HAZ	
Element type:	Quadrilateral, Belytschko-Lin-Tsay shell (default)
Integration points:	1 in-plane and 5 through-thickness

Hourglass control:	Stiffness form
No. of elements in full model:	Longitudinal: 8448 , HAZ: 264
Element size (approx.):	5.0x5.0 mm^2
Effective extrusion length:	Longitudinal: 630 mm, HAZ width: 20 mm
Cross section geometry:	See Figure 6-17 and Figure 4-2(b)
Material models	**MAT-24**, **MAT-103** and **MAT-41**
Material strain-rate effects:	Neglected
Geometrical imperfections:	None
Nodal constraints:	All degrees of freedom free – lower nodes are merged with the fixture, upper nodes are merged with interface plate
Total mass(full model):	2 kg
Fixture and Loadcell (including bottom plate and bolts)	
Element type:	Hexahedron brick (default)
Integration points:	1
Hourglass control:	Full Flanagan-Belytschko stiffness form with exact volume integration
Geometry:	See Figure 6-18
Material models:	**MAT-3,** (load cell and bolts) elastic-plastic, bilinear kinematic hardening. 210000 MPa, tangential modulus 700 MPa, yield stress 600 Mpa, density 7850 kg/ m^3, Poisson's ratio 0.33 **MAT-20,** (fixture bottom plate) rigid body
No. of elements in model:	78016 – load cell, 1368 – bottom plate, 2784 – bolts, 414 – fixture
Element size (approx.):	min: 1 mm, max: 5mm (Load cell) min: 5.1 mm, max: 100 mm (fixture)
Material strain-rate effects:	Neglected
Nodal constraints:	Fixture, Load cell and bolts: all degrees of freedom free Bottom plate : all degrees of freedom are constrained
Total mass (full model):	Load cell (including bottom plate and bolts): 48.378 kg Fixture: 40 kg
Interface plate	
Element type:	Quadrilateral, Belytschko-Lin-Tsay shell (default)
Integration points:	1 in-plane and 5 through-thickness
Hourglass control:	Stiffness form of type 3
No. of elements in full model:	910
Element size (approx.):	5.0x5.0 mm^2
Material models	**MAT-103**
Cross section geometry:	See Figure 6-19(a)
Material strain-rate effects:	Neglected
Nodal constraints:	All degrees of freedom free – lower nodes are merged with HAZ
Total mass(full model):	0.289 kg
Impactor	
Element type:	Not applicable
Integration points:	Not applicable
No. of elements in full model:	1210

Element size (approx.):	min: 7.5 mm, max: 13.5mm
Material models:	**MAT-20,** rigid body
Cross section geometry:	See Figure 6-19(b)
Nodal constraints:	All degrees of freedom are constrained, except the x-direction translation degree is set free and all the nodes have an initial impact velocity.
Total mass(full model):	794 kg

Figure 6-17 Details of longitudinal and heat-affected zone (HAZ).

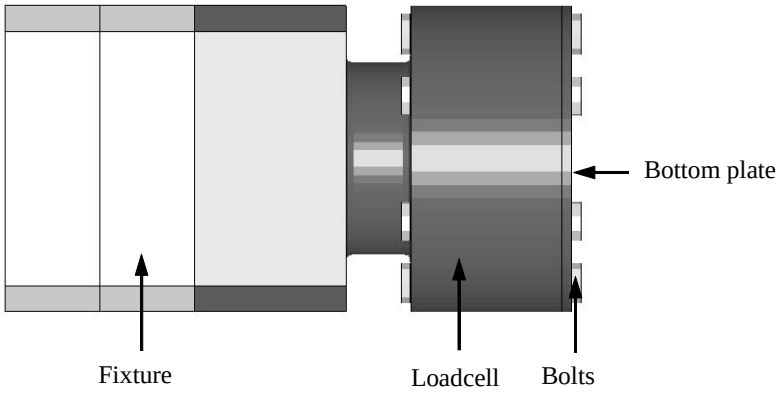

Figure 6-18 Loadcell together with fixture.

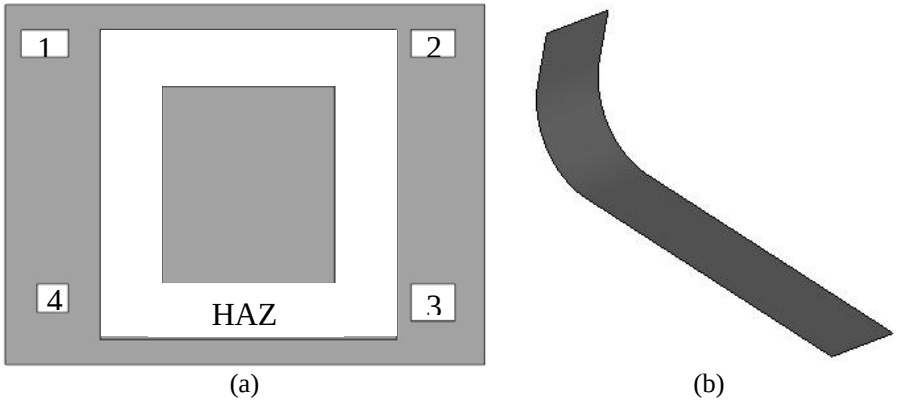

Figure 6-19 (a) Interface plate, (b) Impactor.

6.3 Assembly of test set-up

After performing the last trimming operation a new *dynain* file was created that is used as a basis for the FE-model for the crash analysis. Two sets of longitudinals, interface plates, fixtures and loadcells are required to connect them on the back face of the bumper beam, so they are copied and called with a different file name. All the components were assembled with respect to the location of the stretch-bent bumper beam. Finally the impactor was positioned carefully so that it did not penetrate into the bumper beam's upper flange. The FE-model of the test set-up after the assembly of all components and ready for crash simulation is shown in Figure 6-20.

For the various contact conditions in the system, different types of contact algorithms were employed, ensuring that minimum penetration of parts occurred nor resulting in any numerical problems. The contact types employed are summarised in Table 6-3.

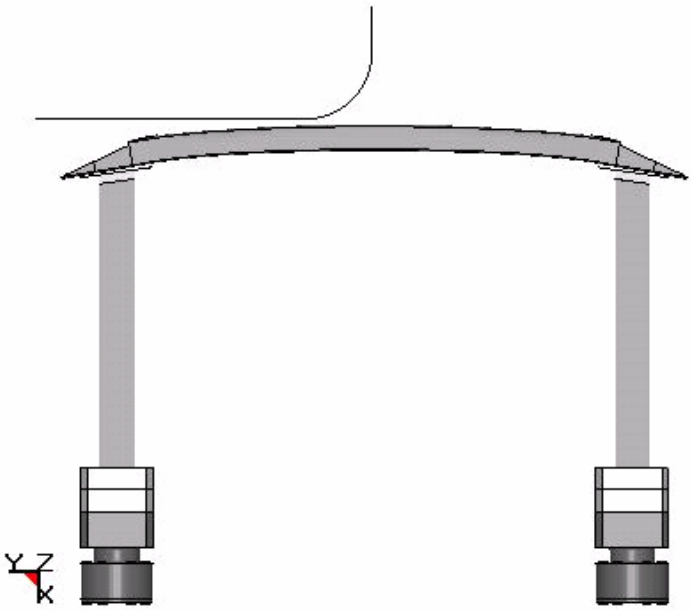

Figure 6-20 FE-model of the bumper beam-longitudinal system.

6.4 Modelling of connections

In the tests the bumper beam was connected to the longitudinals via the interface plates using a bolted connection, whereas the longitudinals were connected to the interface plate through MIG welding. The modelling of this bolted connection is clearly shown in Figure 6-21. The connections used in simulations are summarised in Table 6-4.

The interface plate and the longitudinal were connected by welding. Thus, it was assumed that a part of the extruded longitudinal member was affected by the heat due to welding. This part is usually called a heat-affected zone and is denoted by HAZ see Figure 6-17.

Bjørneklett and Myhr (2003) used a local material design to initiate a favourable buckling mode as a means of controlling the energy absorption in a product during crash. It was showed that the yield stress can be reduced over a very limited area. The borders between the areas with different yield strength are relatively sharp. Bjørneklett and Myhr (2003) used a heat induced trigger with a width of 20 mm situated a small distance below the upper end of the extrusion. They found the heat induced trigger to function

Table 6-3 Modelling of contact in the crash analysis.

Modelling Aspects	Description
Contact	
Bumper beam (S)	Automatic single surface, penalty based, friction coefficient 0.2
Longitudinal and HAZ (S)	Automatic single surface, penalty based, friction coefficient 0.2
Impactor (M) – Bumper beam (S)	Automatic nodes to surface, penalty based, friction coefficient 0.6
Interface plate (M) – Bumper beam (S)	Automatic nodes to surface, penalty based, friction coefficient 0.0
Interface plate (M) – Longitudinal (S)	Automatic surface to surface, penalty based, friction coefficient 0.0

well, as the deformation was initiated at the location of the heat trigger.

Thus, in the present study the HAZ length was modelled with a length of 20 mm, as in the work of Bjørneklett and Myhr (2003). The reduced true stress-

Table 6-4 Modelling of connection in the crash analysis.

Modelling Aspects	Description
Connection	
Bumper beam and interface plate	Bolt connection was used between the bumper beam upper flange and interface plate in the test. In the numerical simulations this was done as follows; in each bolting position, four elements are made as rigid in bumper beam and in the interface plate. The same rigid material is used for both bumper beam and interface plate elements for the same bolt, but different rigid material in the different bolt locations, so that the different bolts are not connected to each other, see Figure 6-21.
Longitudinal and interface plate	The nodes in the HAZ of the longitudinal were merged with the nodes of interface plate.

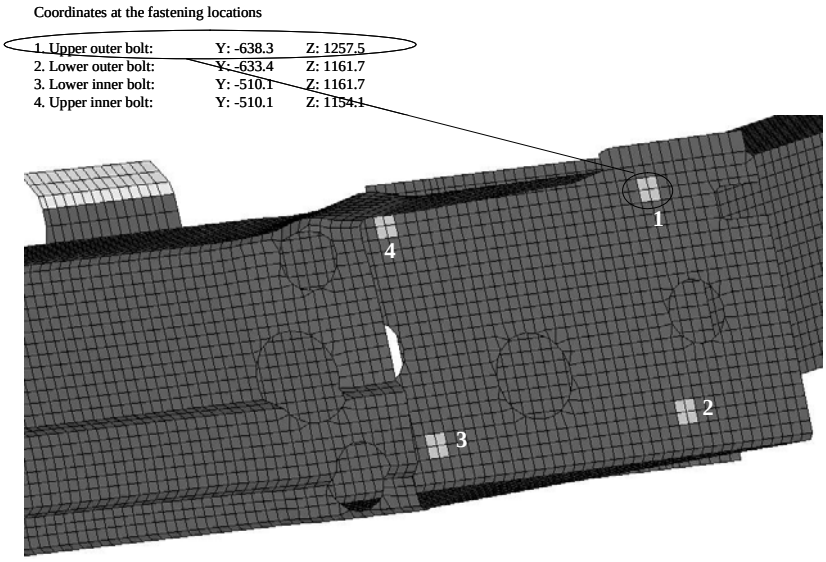

Figure 6-21 Modelling of bolted connection between the bumper beam back face and the interface plate.

strain curve used for the HAZ is shown in Figure 6-22. This is the same as that used to represent the base material (longitudinal) but with 30% shift in the true stress-strain curve according to Eurocode 9 (2004) specifications. The HAZ modelled here represents a thermal trigger as in the work of Bjørneklett and Myhr (2003).

As will be seen in Section 8.1.2.1, in the absence of proper modelling of the HAZ the deformation increases while the mean force (and thus energy absorption rate) of the bumper beam-longitudinal system decreases.

6.5 Summary

Many experimental and simulation results have already been published for the forming of bumper beams using variety of bending techniques. For example, Welo (1996) provides an overview of different relevant bending processes such as rotation bending, press bending and stretch-bending.

A priori it is known that a geometry obtained from forming simulation, and not from idealised CAD drawings, is a pre-requisite for accurate crash

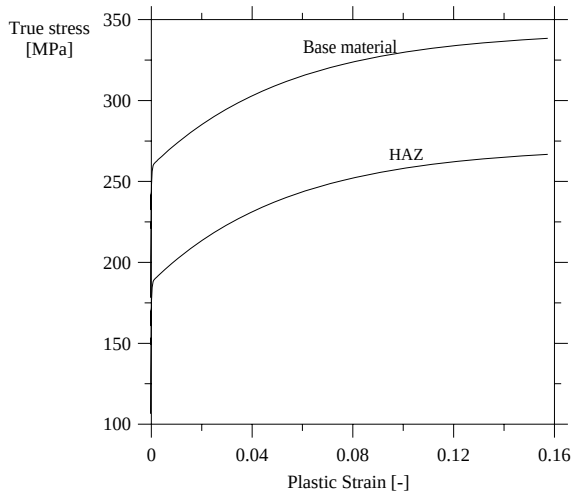

Figure 6-22 Stress-strain curves used in the base material and HAZ.

prediction of these bumper beam systems. To achieve a bumper beam with geometric variations due to the forming operations, here numerical simulations of all the forming operations were performed to obtain a rotary stretch-bent bumper beam with the aid of the flow-chart. The obtained geometry was able to represent the global behaviour of the bumper beam satisfactorily with respect to the cross-section and stretch-bent length. However, no attempt was made to measure the amount of springback during the unloading phase.

Modelling of other components which are used in the crash analysis for example, longitudinals, loadcells, etc., has been carried out with care. Also care has been taken in modelling the test set-up of FE-model, such that there would not be any numerical robustness problems in the crash analysis. However, the development of a numerically robust model is always critical and time consuming.

Chapter 7 Full-scale Simulations of Bumper Beam-Longitudinal Systems

The need for computer crash simulations with high degrees of fidelity and robustness is becoming increasingly important for use in parametric studies and early design analysis. The numerical simulations also enable new design concepts to be evaluated where there is a need to establish an optimum design with interaction between materials and structural forms. The main objective of this chapter is to investigate the ability of the non-linear FE-code LS-DYNA (Hallquist, 2003) to predict the response of the bumper beam-longitudinal system. The main focus is placed on accurate prediction of the observed system behaviour with respect to force-deformation characteristics and fracture modes.

The impact tests presented in Chapter 5 show that the energy absorption of the bumper beam-longitudinal system decreases with decreasing yield strength of the longitudinals. Furthermore, the energy absorption was found to depend on the temper condition (and thus strain-hardening of the material) and the collapse mode of the longitudinal being used.

The effect of sampling frequency on the simulation results is presented in Section 7.2. For a selected bumper beam-longitudinal system the crash response is predicted using the material models that are most widely used in the industry (MAT-24 and MAT-103 (Hallquist, 1998)) and the current user-defined material model (MAT-41) are compared directly with the experimental results in Section 7.3. As will be seen, there is some influence of the material model, and thus the choice of yield criterion.

Simulations were performed following the sequence of the presentation of the experimental results in Chapter 5, i.e. test series **A**, **B**, **C** and **D**. For each

test series the simulation results are compared with the experimental results in Sections 7.4 through 7.7. The numerical simulations aid(s) in understanding the energy absorption process. The amount of energy mitigated through different parts of the bumper beam-longitudinal system is presented in Section 7.8. All the crash analyses were, however, based upon the geometry of the bumper beam obtained from the forming simulations, see Section 6.1. Furthermore, no strain-rate effects were taken in to consideration in this chapter. The strain-rate effects as well as process effects on material properties are studied separately in Chapter 8.

7.1 Explicit simulations

Only explicit crash simulations were performed in this study. However, implicit dynamic simulations of the bumper beam-longitudinal system can also be performed but the convergence becomes critical due to the number of contact definitions, which requires lot of simulation time (Kokkula et al., 2003). The simulations were performed on a single Linux processor. LS-DYNA uses a central difference operator for time integration, requiring a limitation on the time-step size. To obtain numerical stability during the crash simulations, the time-step size is typically in the order of one microsecond. All the simulations were executed with a variable time-step. It is also possible to execute the simulations with a fixed time-step, which generally has the potential of yielding large errors in analyses including inertia effect. For the present bumper beam-longitudinal system in Figure 6-20, the loadcells are also modelled. Because of the fine mesh in the loadcells the time-step size is often controlled by these elements and thus an initial time-step size of 0.168 microseconds was generated by LS-DYNA. The numerical model has a variety of complex contact conditions which are modelled using different contact algorithms (Table 6-3) based on the penalty method to avoid penetrations of structural parts during the crash process.

7.2 Effect of sampling frequency

There can be danger for the loss of important physical information in the numerical simulations (as in the experiments), when sampling is performed with low frequency. To study the effect of sampling frequency on the simulation results of such large-scale systems, two simulations were performed with two sampling frequencies i.e. 500 and 4 kHz. The sampling frequency of 500 kHz corresponds to the one used for sampling in the experiments, see Section 4.4.1. The force-time curves obtained using these two frequencies are shown in Figure 7-1. The force-time signal at low frequency (4 kHz) follows the other frequency (500 kHz) without any significant loss of information. Based on this it was decided to use 4 kHz as the sampling frequency in all the simulations.

7.3 Influence of yield criterion

In order to check the influence of the choice of yield criterion, simulations were performed with the most widely used industrial material models in LS-

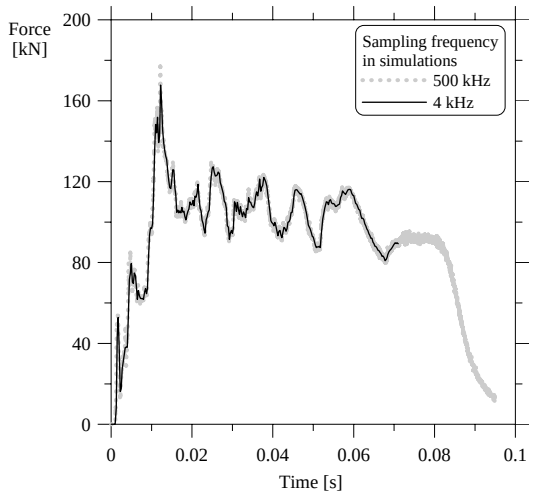

Figure 7-1 Effect of sampling frequency in simulations.

DYNA as well as the user-defined material model (MAT-41) presented in Chapter 2. In this section, the predicted numerical results for the bumper beam-longitudinal system when using MAT-24, MAT-103, MAT-41 and MAT-41(*CFS**) models are presented. The difference between the analyses denoted with MAT-41 and MAT-41(*CFS**) is that the former analyses are run without an activated fracture criterion and the latter are run with critical thickness strain fracture criterion, see Section 2.3.4.1. It is possible to use a fracture criterion in MAT-24 based on the effective plastic strain (Hallquist, 2003). However, no attempt is made to use this fracture criterion in connection with MAT-24. Further, when using MAT-103 the abilities of representing the planar anisotropy using the quadratic yield criterion was not exploited. Moreover, all the simulations in this section were run for test series **A**, i.e. longitudinals out of the AA7003-T79 material and at 10 m/s impact velocity.

The force-deformation curves are filtered like the test results using the same low-pass filter with a cut-off frequency. The force-deformation and mean force-deformation plots in Figure 7-2 clearly depict that the response of the bumper beam-longitudinal system predicted by MAT-24 and MAT-103

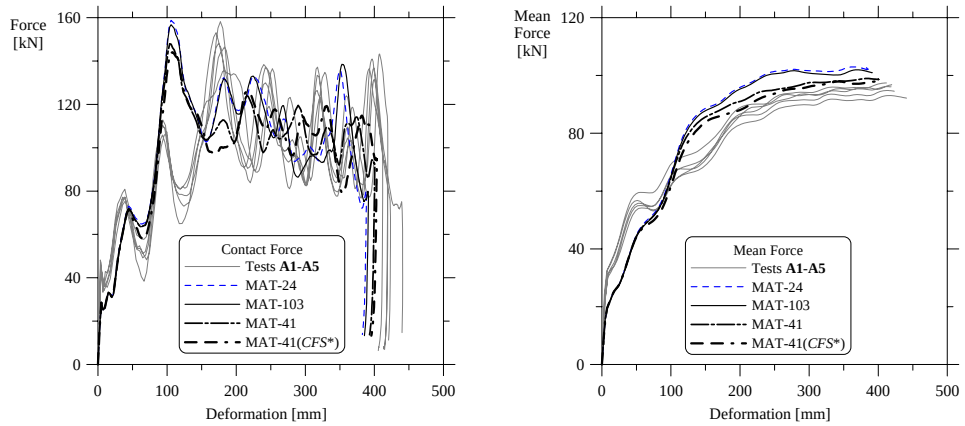

Figure 7-2 Comparison of (a) force-deformation and (b) mean force-deformation plots from the tests and simulation results with different material models for series **A** system.

material models is slightly “stiffer” than what is predicted by MAT-41 and MAT-41(*CFS**).

As mentioned earlier, the main difference between MAT-24 and MAT-103 is the hardening curve representation; in the former model the measured true stress-stain values was used, while in the latter the measured values were fitted with a five parameter Voce strain-hardening rule (Equation (2.22)). Obviously this can over-predict the energy that can be dissipated, since actual materials will fail at some deformation. As will be seen latter in this section, material models MAT-24 and MAT-103 over-predict the energy absorption, due to lack of fracture criterion.

The behaviour of the bumper beam-longitudinal system predicted by MAT-41 is similar to that predicted by MAT-24 and MAT-103, but with an increased amount of permanent deformation. The increase in the predicted permanent deformation is due to the consideration of anisotropy in the yield criterion. Further, when the *CFS** fracture criterion is considered in MAT-41, the predicted behaviour of the system is slightly improved compared to the one without fracture criterion. The deformation in the system is mainly controlled by collapse of the bumper beam cross-section and buckling of the impacted longitudinal. After the buckling load has been reached, the plastic deformation in the buckles increases rapidly. As the buckles develop further fracture occurs and at some stage some elements are deleted. Thus, the amount of deformation in the system is increased.

The permanent deformation of the bumper beam-longitudinal system in the tests varied from 412 to 440 mm with nine fully developed lobes in the impacted longitudinal, see Figure 5-5(a). The highest deformation was observed for test specimen **A1**. The predicted permanent deformation, energy absorption, number of lobes developed and the CPU time consumed for running the simulation when using different material models are given in Table 7-1. The number of lobes developed in the impacted longitudinal in the simulations when using different material models is compared to the one

observed in the experimental tests in Figure 7-3. As seen the number of lobes developed in the impacted longitudinal was three shorter with MAT-24 and MAT-103 models, whereas it was two shorter with MAT-41. The development of lobes depend on the initiation of the buckling pattern in the longitudinal, this is explained more detail in Section 7.4.2. However, the lobes developed with MAT-41 were rather of a mixed mode than progressive mode as observed in the tests. The under-prediction of lobes in the simulations may be due to the mesh size and also the lack of modelling the initial imperfections in the extruded member. Table 7-1 show that the predicted permanent deformation when using MAT-24 is 10 mm less than that predicted by MAT-41(*CFS**), while the permanent deformation predicted by MAT-103 is almost the same as that of MAT-24. This shows that the impact energy is absorbed completely over a shorter deformation of the impacted longitudinal. However, when using MAT-41 with and without a fracture criterion the difference in maximum permanent deformation is only 5 mm. The increase in permanent deformation when using MAT-41(*CFS**) is due to the removal of seventeen elements in the bumper beam.

The impacted longitudinal started to buckle at its clamped end when using MAT-41, this can be clearly seen in Figure 7-3. However, no such buckle was observed in the tests. From the second column in Table 7-1 it is also clear that the impactor has highest displacement when using MAT-41 with critical thickness strain fracture criterion (*CFS**). Furthermore, one should

Table 7-1 Predicted permanent deformation, energy absorption and number of lobes from simulations when using different material models for test series **A**.

Material model	Permanent deformation (mm)	Energy absorbed (kJ)	Number of lobes	CPU time consumption (Hrs)
MAT-24	395	38.32	6	53
MAT-103	400	38.38	6	54
MAT-41	400	38.17	7	74
MAT-41(*CFS**)	405	38.01	7	77

also remember that the nodes between the longitudinal and the fixture (modelled as a rigid-body, see Table 6-2) were merged in the FE-model. In the tests the longitudinals were fixed inside a rectangular slot in the fixture, using a sliding block mechanism, see Figure 4-4.

The CPU time consumed for running the bumper beam-longitudinal system simulation with MAT-41 is more than that used by the MAT-24 and MAT-103 material models. The amount of time consumed for completing a simulation depends on physical time of the event and the time-step size used in the analysis. Further, the computational time is affected both by the element size and number of elements. However, the implementation of a particular material model in LS-DYNA also plays a significant role on the time consumption. The increase in computational time when using MAT-41 is due to the complex nature of the yield criterion, see Section 2.3.3, and also the use of a fracture criterion.

Another important observation is the energy absorbed by different components in the bumper beam-longitudinal system. This is easily

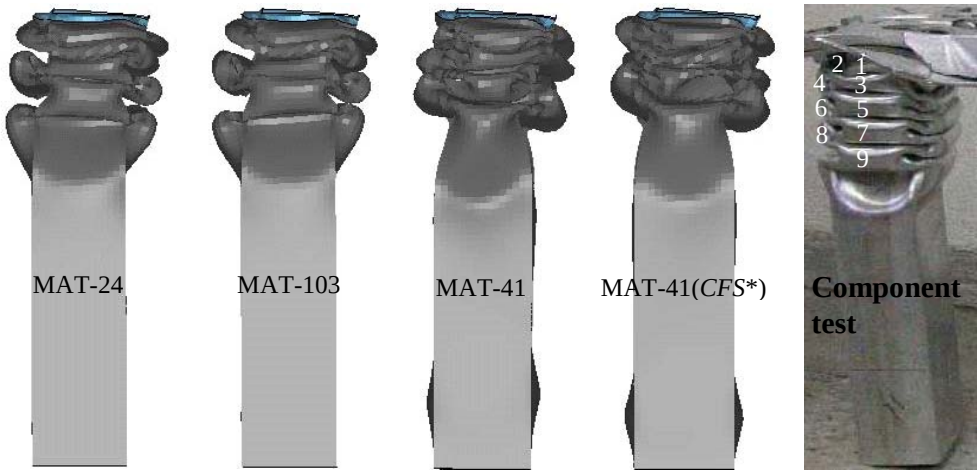

Figure 7-3 Development of lobes in the impacted longitudinal in simulations and test.

obtained from the simulations by observing the internal energy in the different materials. Table 7-2 shows the percentage of energy absorbed by different components in the bumper beam-longitudinal system when using different material models. This data is also important for determining the importance of the respective components to the fidelity of the overall simulation. From Table 7-2 it is clear that the energy absorbed by the impacted longitudinal varied between 75.07% and 76.03% of the total energy absorbed.

For the same amount of deformation the predicted energy absorption using the current material models is higher than that from tests, Figure 7-2. The predicted mean force is close to the tests when using the user-defined material model, the permanent deformation predicted, however, is slightly higher than that of MAT-24 and MAT-103. From the above discussion it is clear that there is some influence of the chosen material model, and thus the yield criterion, on the predicted behaviour of the bumper beam-longitudinal

Table 7-2 Material internal energy for test series **A** with different material models.

Part	MAT-24		MAT-103		MAT-41		MAT-41(*CFS**)	
	Internal energy (kJ)	Percen-tage (%)	Internal energy (kJ)	Percen-tage (%)	Internal energy (kJ)	Percen-tage (%)	Internal energy (kJ)	Percen-tage (%)
Total system	38.32	100	38.38	100	38.17	100	38.01	100
Bumper beam	7.30	19.05	7.24	18.86	7.25	18.99	6.9	18.11
Impacted longitudinal	28.77	75.07	28.88	75.25	28.68	75.13	28.96	76.03
Non-impacted longitudinal	0.77	2.00	0.78	2.03	0.78	2.04	0.82	2.15
Impacted interface plate	1.02	2.66	1.03	2.68	1.01	2.65	0.98	2.57
Non-impacted interface plate	0.43	1.12	0.43	1.12	0.43	1.13	0.40	1.05

system. In this section, however, only overall predicted behaviour of test series **A** is compared. A more detailed analysis of test series **A** with respect to force-deformation characteristics and deformation shape is discussed in the following.

7.4 Simulation of test series A

7.4.1 Force-deformation comparison: tests and simulations

The bumper beam-longitudinal system obtained maximum permanent deformation when the impactor was stopped, i.e. when all the impact energy was absorbed. In the simulations the impact energy is converted to plastic work by bending and stretching of the bumper beam as well as crushing the longitudinal at the impacted end and also bending of the non-impacted longitudinal. This is similar to that observed in the experiments. In the initial stage of crushing, the active longitudinal members locally squeezes and the stretch-bent bumper beam starts to flatten so that the upper and lower flanges of the bumper beam will experience compression and tension, respectively. The contact force (between the impactor and the bumper beam) versus displacement of the impactor from experiments and simulations are plotted in Figure 7-2(a). The corresponding mean force-versus-deformation curves are shown in Figure 7-2(b).

From the force-deformation curves, Figure 7-2(a) several crash events can be identified. The force level in the initial stages of crushing corresponds to the collapse of the bumper beam cross-section. After the collapse of the bumper beam cross-section at the impacted end, the force level is governed by the initiation of the folding mechanism in the impacted longitudinal. It transpires from Figure 7-2(a) that an initial high peak force was predicted for the first buckle formation in the impacted longitudinal. The reason for this peak may be that the assumed length and mechanical properties of the HAZ are not sufficiently close to the reality. In the tests the first buckle developed well within the HAZ and required a force of about 100 kN. In

this case the next (i.e. highest) peak in tests was due to the development of a second buckle in the impacted longitudinal.

The force level dropped after reaching the maximum peak at a deformation of 100 mm in the simulations, Figure 7-2. At this deformation the first buckle development completed in the impacted longitudinal.

The asymmetric loading conditions and also the connection between the bumper beam and the longitudinals made the bumper beam to stretch in the axial direction. As the loading at the impacted end increased, the bumper beam curvature changed significantly and stretched the non-impacted longitudinal considerably. Hence, bending of the non-impacted longitudinal occurred with the formation of a plastic hinge (local buckle) at its clamped end. As the crash event progressed the impacted longitudinal folded (deformed) by absorbing the rest of the impact energy.

7.4.2 Deformation shape

The fidelity and accuracy of the simulations can be studied in several ways. Firstly, the general deformations at the impact regions were compared visually to the images captured with the high speed camera. Secondly the permanent deformations were compared. A sequence of deformation shapes obtained from the numerical simulation when using MAT-41(*CFS**) is shown in Figure 7-4. The selected times are denoted with dots on the force-time curve in Figure 7-5.

The impact event started at time $t_1 = 0$. By the end of time t_2 the bumper beam cross-section at the impacted end collapsed and simultaneously the development of a plastic hinge in the mid-section of the bumper beam started. The state at time t_3 was selected because it represented the stage at which the first buckle developed in the impacted longitudinal at the interface of HAZ and base material. A close view of the first buckle in the

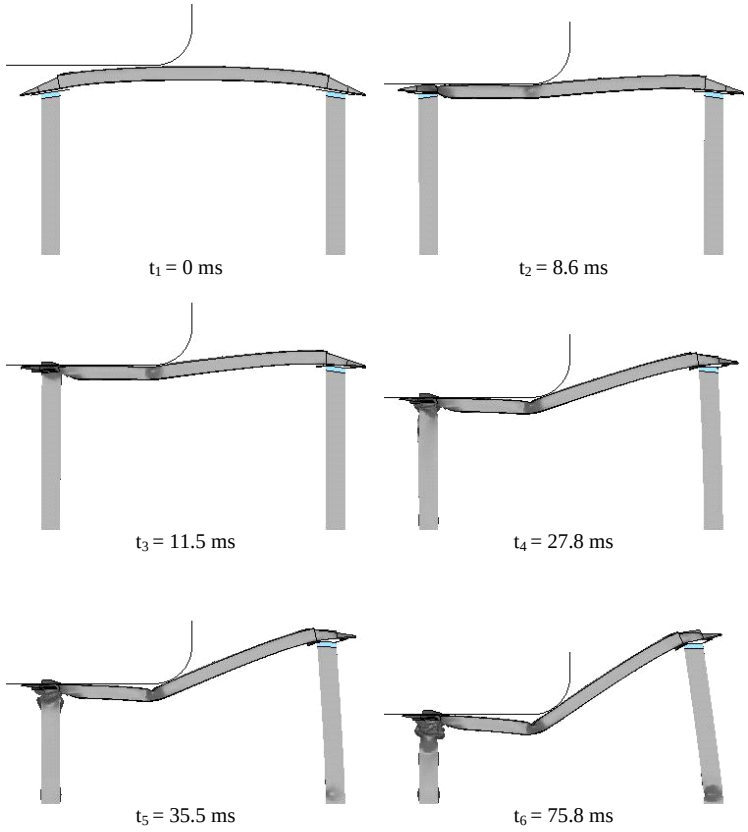

Figure 7-4 A sequence of deformation shapes from the simulation for test series **A** with MAT-41(*CFS**).

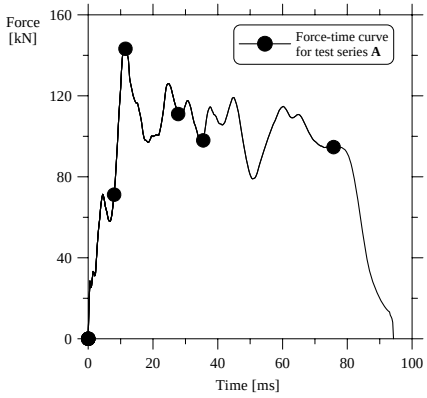

Figure 7-5 Force-time curve from simulation – showing the selected times in Figure 7-4 for test series **A**.

impacted longitudinal is shown in Figure 7-6(a). The figure clearly shows that an *asymmetric* folding mode (usually called as an *extensional* mode) developed as the first buckle, since the two adjacent walls of the impacted longitudinal buckled inwardly. However, in the tests an *axisymmetric* folding mode is observed for the first buckle. At time t_4 the elements at the non-impacted end of the bumper beam started to erode, to represent the propagating tearing crack at the intersection between the lower flange and the web. The crack is clearly shown in Figure 7-6(b) with a circle. Note the significant curvature of the non-impacted longitudinal, fifth image in Figure 7-4, as it is being stretched by the bumper beam. It is evident that this loading caused the development of a local plastic hinge in the non-impacted longitudinal at its clamped end prior to time t_5. The last image at time t_6 represented the stage at which much of the plastic deformation occurred in the bumper beam-longitudinal system.

Deformation shapes from the simulation and the experiments are compared in Figure 7-7. It is clear from Figure 7-7(a) that the non-impacted longitudinal in the simulations had a more dominant local buckle near by its clamped end than in the tests. The probable reason, as mentioned earlier, is the merging of nodes between the longitudinal and the fixture. The bending failure in the mid-section of the bumper beam is compared in Figure 7-7(b), and is poorly predicted in the simulations. In Figure 7-7(c), it is seen that

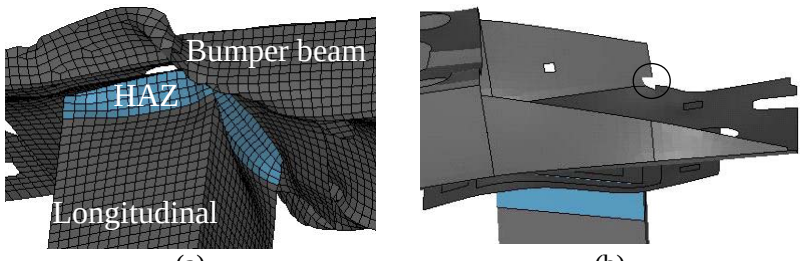

(a) (b)

Figure 7-6 (a) Close view of the first buckle developed in the impacted longitudinal at time t_3 = 11.5 ms and (b) start of element deletion at the intersection between the lower flange and the web at t_4 = 27.8 ms.

neither the through-thickness shear crack at the cut-out region of the non-impacted end of the bumper beam is predicted in the simulation. Further, the propagating tearing crack at the intersection between the lower flange and the web is poorly predicted.

From the post-crash test specimens of test series **A**, a considerable number of failure zones have been observed in the folds of the impacted longitudinal. A direct view of the geometry does not reveal direct erosion of any element in the same zones. However, element deletion occurs only when the three through-thickness (see Table 6-2) integration points reaches the fracture criterion.

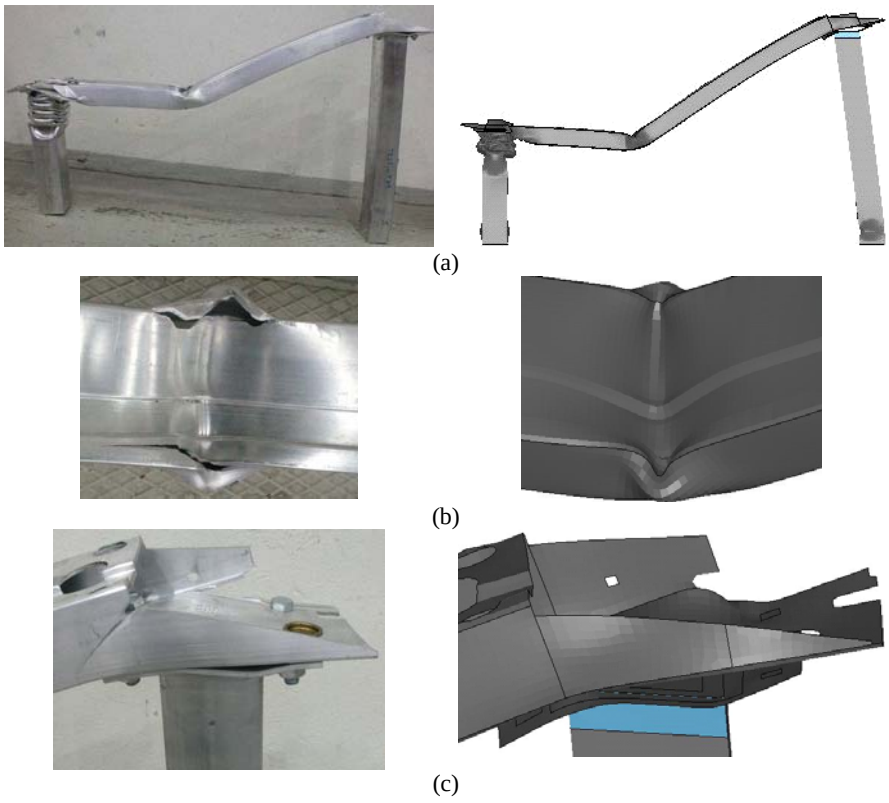

Figure 7-7 Comparison of permanent deformation shapes of test specimen **A1** and that obtained from simulation with MAT-41 (*CFS**).

The elements that reached the fracture criterion in different through-thickness integration points for the impacted longitudinal are shown in Figure 7-8. Be aware that in the figure the deformation is greatly reduced to show the elements. Further, the HAZ is not included in the figure. If one considers that the first integration point belongs to the outer layer then the fifth integration point represents the inner layer of the element or vice-versa. The elements in which the integration point reached the fracture criterion are denoted by light colour (red). Thus, the surface cracks which are observed in the folds of the impacted longitudinal can aptly be represented by these failed integration points. However, in none of the elements the third through-thickness integration point reached the fracture criterion and hence no element was deleted.

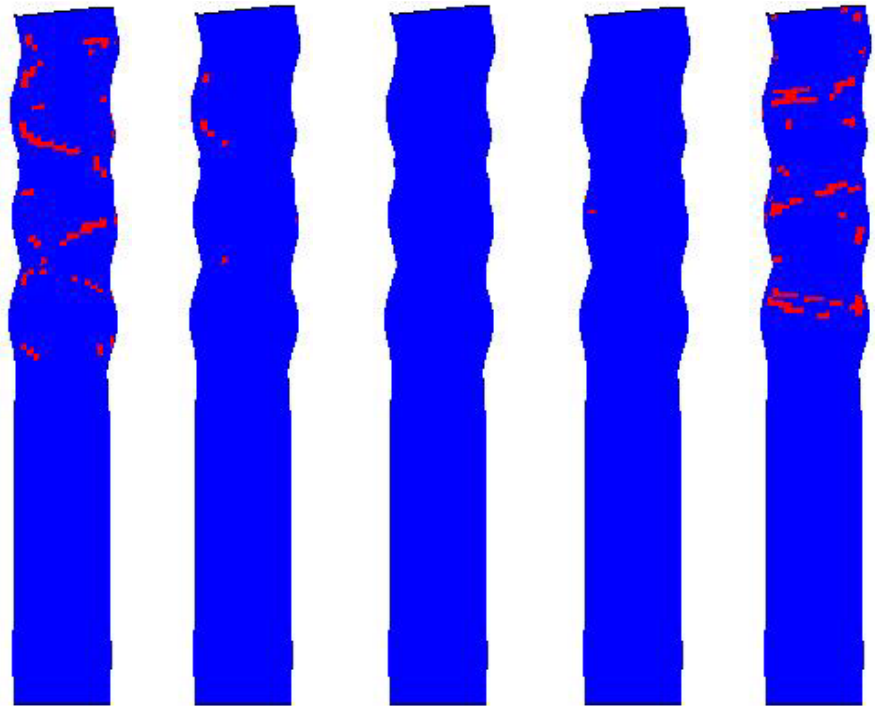

Figure 7-8 Elements that reached the critical thickness strain fracture criterion (*CFS**) in the impacted longitudinal for each integration point for test series **A** in the simulation.

The bending failure in the folded elements of the bumper beam in the simulations is shown in Figure 7-9. The elements in light colour (red) represent the integration points that reached the critical thickness strain fracture criterion. As in the impacted longitudinal, only two integration points reached the fracture criterion and thus no elements were removed.

None of the integration point in the elements near by the cut-out region reached the fracture criterion to represent the through-thickness shear crack at the non-impacted end of the bumper beam, see Figure 7-7(c). Thus, no integration point data is presented from this region.

7.5 Simulation of test series B

7.5.1 Force-deformation comparison: tests and simulations

The experiments of test series **B** resulted in significantly different deformation modes than for test series **A**. Transition from progressive buckling to a global bending mode was observed in the impacted longitudinal for test specimens **B1** and **B3**, whereas a progressive folding mode was observed for test specimen **B2**.

Simulations were performed only with the user-defined material model with and without the *CFS** fracture criterion. As with test series **A**, a 30% shift

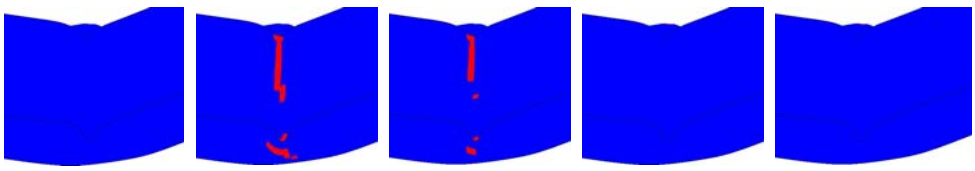

Figure 7-9 Elements that reached the critical thickness strain fracture criterion (*CFS**) in the bumper beam for each integration point for test series **A** in simulation.

(decrease) in the true stress-strain curve, Figure 6-22, of the base material was used to model the HAZ. In the experiments it was observed that the crashboxes on the reaction wall were activated. The activation was mainly due to the unacceptable failure modes in the impacted longitudinal. However, the simulations were run up to the termination time at which the impactor velocity became zero.

The force-deformation and mean force-deformation curves obtained from the numerical simulations, with and without a failure criterion, are plotted against the test results in Figure 7-10. During the initial stages of the crushing process, i.e. the collapse of the bumper beam cross-section and initiation of buckling in the impacted longitudinal, the force-deformation curves from the simulations followed the experimental curves of test specimens **B1** and **B2**. This corresponds to a deformation of 100 mm, see Figure 7-10(a). However, the peak force predicted in the numerical simulations was much higher than that of the tests, and is related to the development of the first buckle in the impacted longitudinal.

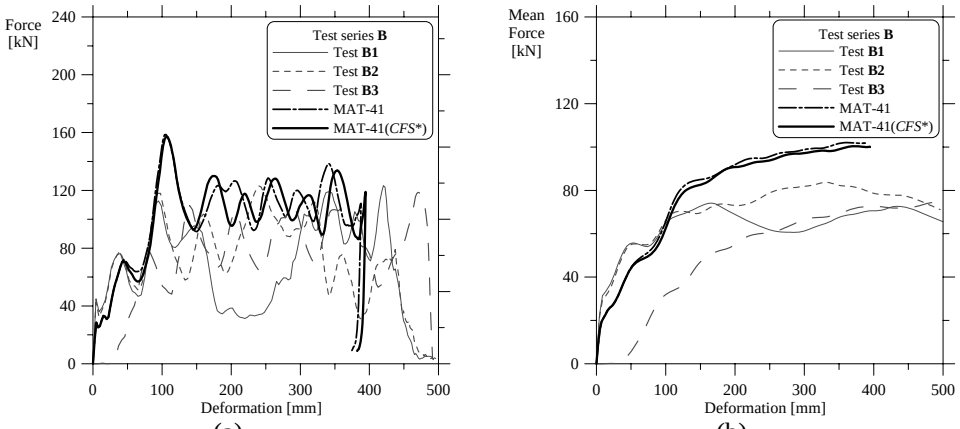

Figure 7-10 Comparison of (a) force-deformation and (b) mean force-deformation plots from the tests and simulation results for test series **B**.

In test specimen **B1** the first buckle in the impacted longitudinal developed in the mid-section of the extruded member and acted as a hinge. Next, the deformed end of impacted longitudinal started to rotate about this hinge and as a consequence the force level dropped at about 150 mm deformation (Figure 7-10(a)). Further crushing of the impacted longitudinal caused a rise in the force level as new buckles were created on both sides of the hinge.

In the simulations a progressive folding mode developed in the impacted longitudinal. One can easily note this from the oscillations of curves around a mean value, after the maximum peak in the force-deformation curves Figure 7-10(a). The figure clearly depict that the simulations terminated at a deformation of about 400 mm. At this deformation the impact energy was absorbed by the bumper beam-longitudinal system. This indicates that if the unacceptable failure in the impacted longitudinal had not prevailed, the longitudinal might have deformed progressively up to the deformation predicted in the simulations (i.e. 400 mm). From the mean force-deformation curves in Figure 7-10(b), one can note that there is no difference between the simulation results with and without a fracture criterion. However, the predicted mean force is significantly higher than in the tests.

7.5.2 Deformation shape

A snap-shot sequence of deformation shapes from the numerical simulation for test series **B** is shown in Figure 7-11. The selected times are denoted with dots on the corresponding force-time curve in Figure 7-12. The selected times here are the same as that selected for test series **A** in Figure 7-4, except for time t_4.

The impact process initiated at time $t_1 = 0$. The bumper beam cross-section collapsed at the impacted end by time t_2 and simultaneously the development of a plastic hinge in the mid-section of the bumper beam

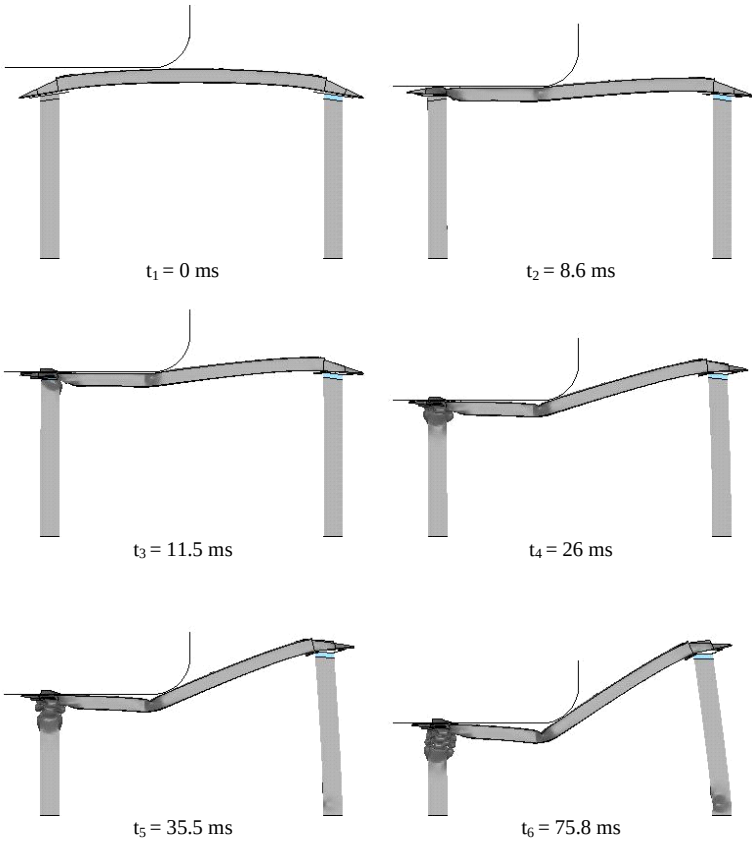

Figure 7-11 A sequence of deformation shapes from the simulation for test series **B** with MAT-41(*CFS**) model.

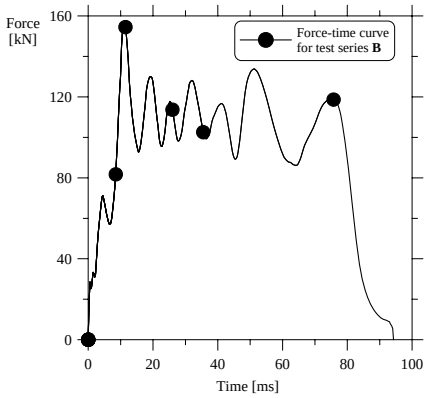

Figure 7-12 Force-time curve from simulation – showing the selected times in Figure 7-11 for test series **B**.

started. Time t_3 represented the stage at which the first buckle developed in the impacted longitudinal at the interface of HAZ and base material. A close view of this first buckle in the impacted longitudinal is shown in Figure 7-13(a). The figure clearly shows that the first buckle developed was asymmetric. At time t_4 the elements at the non-impacted end of the bumper beam were eroded to represent the propagating tearing crack at the intersection between the lower flange and the web. This crack is clearly shown in Figure 7-13(b) with a circle. A local plastic hinge developed in the clamped end of the non-impacted longitudinal prior to time t_5. The last image at time t_6 represents the stage at which the velocity of the impactor has become zero.

No attempt is made here to compare the experimental images and numerically predicted deformation modes as in test series **A**, Figure 7-7. This is because the numerical simulations failed to predict the deformation and fracture modes observed in the experimental tests.

7.6 Simulation of test series C

Simulations were performed only with the user-defined material model, with and without a fracture criterion (*CFS**). Experiments of test series **C**

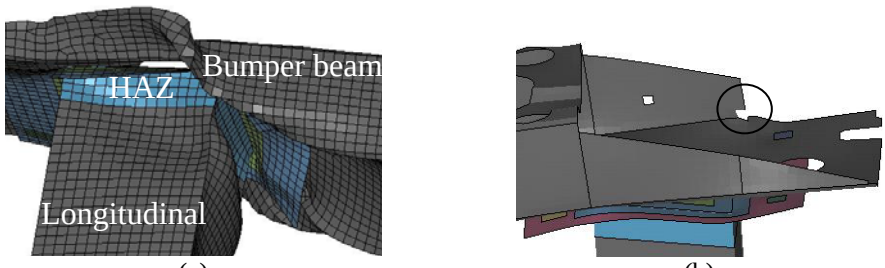

(a) (b)

Figure 7-13 (a) Close view of the first buckle developed in the impacted longitudinal at time t_3 = 11.5 ms and (b) start of element deletion at the intersection between the lower flange and the web at t_4 = 26 ms.

revealed that the bumper beams in this series were not completely crushed, as the longitudinals had less strength than in test series **A** and **B**. Consequently, absorbed energy was much lower. From the high-speed video recordings it was observed that the crashboxes on the reaction wall were activated in all the three parallels. To represent this activation in the numerical simulations, the key word *TERMINATION_BODY available in LS-DYNA (Hallquist, 2003) was used. With the use of this keyword the impactor was stopped at the desired displacement.

7.6.1 Force-deformation comparison: tests and simulations

When performing the simulations of test series **C**, the HAZ as shown in Figure 6-20 was not modelled. It was observed from the simulations that when the HAZ was modelled (as in test series **A** and **B**) the bumper beam-longitudinal system ran into a global buckling mode. Hence, the HAZ was avoided to obtain the stable behaviour as in the tests. The force-deformation and mean force-deformation curves from the experiments and simulations with and without the fracture criterion are shown in Figure 7-14.

As with the tests, the longitudinal at the impacted end started to buckle before the complete collapse of the bumper beam cross-section. With the increase in force the web of the bumper beam buckled outwardly at the impacted end and simultaneously a plastic hinge developed in its mid-section. This can be noted from the first peak in the force-deformation plots, Figure 7-14(a), at a deformation of about 50 mm. A progressive folding mode developed in the impacted longitudinal with further increase in the impact force. The oscillations in the force-deformation plots around the mean value are due to the formation of new lobes in the impacted longitudinal.

The mean force-deformation plots in Figure 7-14(b) clearly show that there was no difference between the curves obtained from simulations with and without fracture, but the predicted mean force level was somewhat too low.

The lower mean force level recorded in the simulations may be due to strain-rate effects that have been ignored. The strain-rate effects in test series **C** is studied as a sensitivity parameter in Section 8.2. As will be seen the predicted mean force level was close to the experiments when the strain-rate effects are considered in the simulations. In the experiments it was observed that there were no significant fracture events in the bumper beam-longitudinal systems in accordance with the simulations. Thus the predicted curves with and without fracture criterion are on top of each other.

7.6.2 Deformation shape

Some snap-shots of various stages of deformation shapes obtained from the numerical simulation of test series **C** are shown in Figure 7-15. The corresponding force-time curve is plotted in Figure 7-16 with the selected times. The impact event started at time $t_1 = 0$. Without considerable collapse of the bumper beam cross-section, buckling initiation in the impacted longitudinal took place before the time t_2. At time t_3 the web of the bumper beam buckled and simultaneously a plastic hinge developed in the mid-section of bumper beam. Due to the stretching caused by the bumper beam a

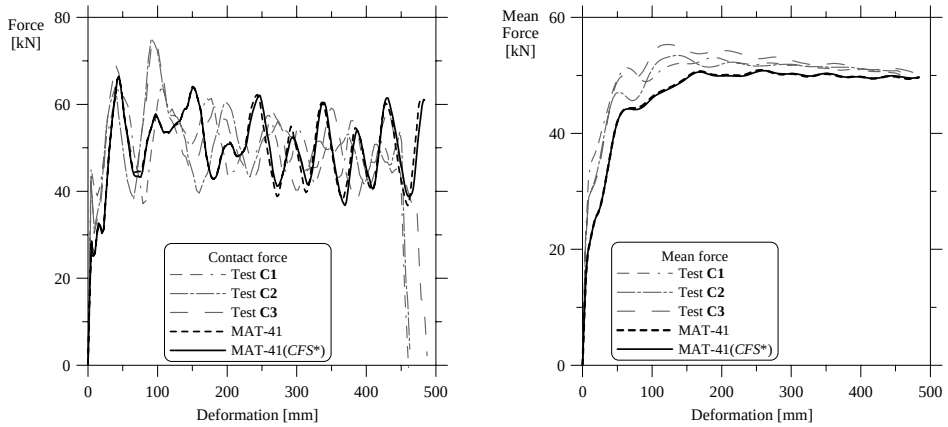

Figure 7-14 Comparison of (a) force-deformation and (b) mean force-deformation plots from the tests and simulation results for test series **C**.

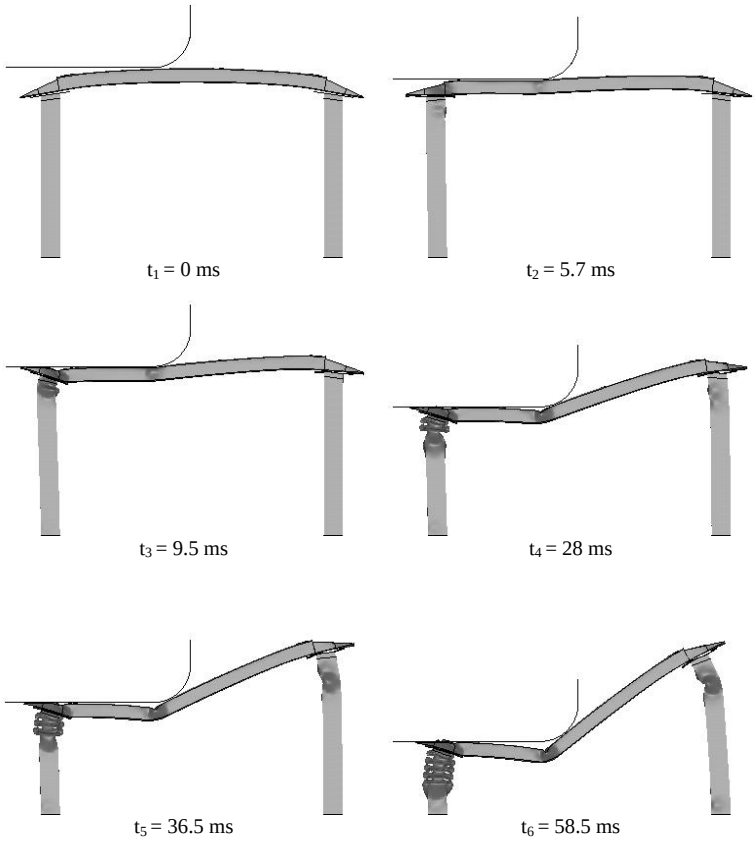

Figure 7-15 A sequence of deformation shapes from the simulation for test series **C** with MAT- 41(*CFS**) model.

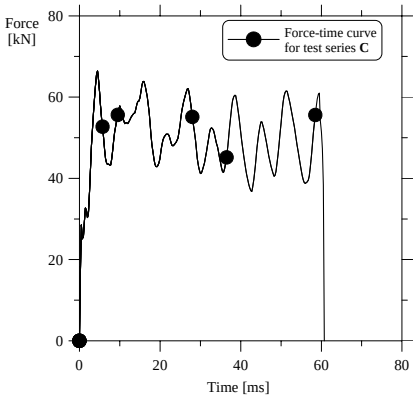

Figure 7-16 Force-time curve from simulation – showing the selected times in Figure 7-15 for test series **C**.

local plastic hinge started to develop in the non-impacted longitudinal at time t_4. At time t_5 the upper end of the non-impacted longitudinal started to rotate about the plastic hinge that developed at time t_4. Another plastic hinge started to develop at the clamped end of the non-impacted longitudinal at time t_6. The simulation terminated at about 61 ms by the time the impactor reached the given *TERMINATION_BODY condition.

Deformation shapes from the numerical simulation and experimental images are compared in Figure 7-17. As can be seen in Figure 7-17(a), the non-impacted longitudinal in the numerical simulations had a more dominant buckle than in the tests. Moreover, in the tests the upper hinge was developed close to the interface plate, and in the simulation it was predicted far away from the interface plate. This kind of over-prediction of buckling in the simulations may be attributed to the lack of modelling initial imperfections in the extruded member but also be attributed to the HAZ in the experiments. Progressive folds in the impacted longitudinal are compared in Figure 7-17(b). The number of lobes developed in the simulation and test are the same. However, the rupture in the folded compression flange and the webs of the bumper beam is poorly predicted in the simulations, Figure 7-17(c), although some integration points in the elements reached the fracture criterion.

7.7 Simulation of test series D

Results for the bumper beam-longitudinal systems at increased impact velocity i.e. test series **D** (Table 4-1) is presented below. As with the other series; the simulations of test series **D** were performed with the user-defined material model, with and without the *CFS** fracture criterion. Experiments on test series **D** revealed that the trolley activated the crashboxes on the reaction wall. The simulations of test series **D** were run up to the permanent deformation measured on the test specimens, i.e. 491 mm. Thus, the simulation terminated when the impactor reached the above displacement value using the keyword *TERMINATION_BODY.

7.7.1 Force-deformation comparison: tests and simulations

Force-deformation curves from the experiments and simulations are plotted in Figure 7-18(a), while the mean force-deformation plots are shown in Figure 7-18(b).

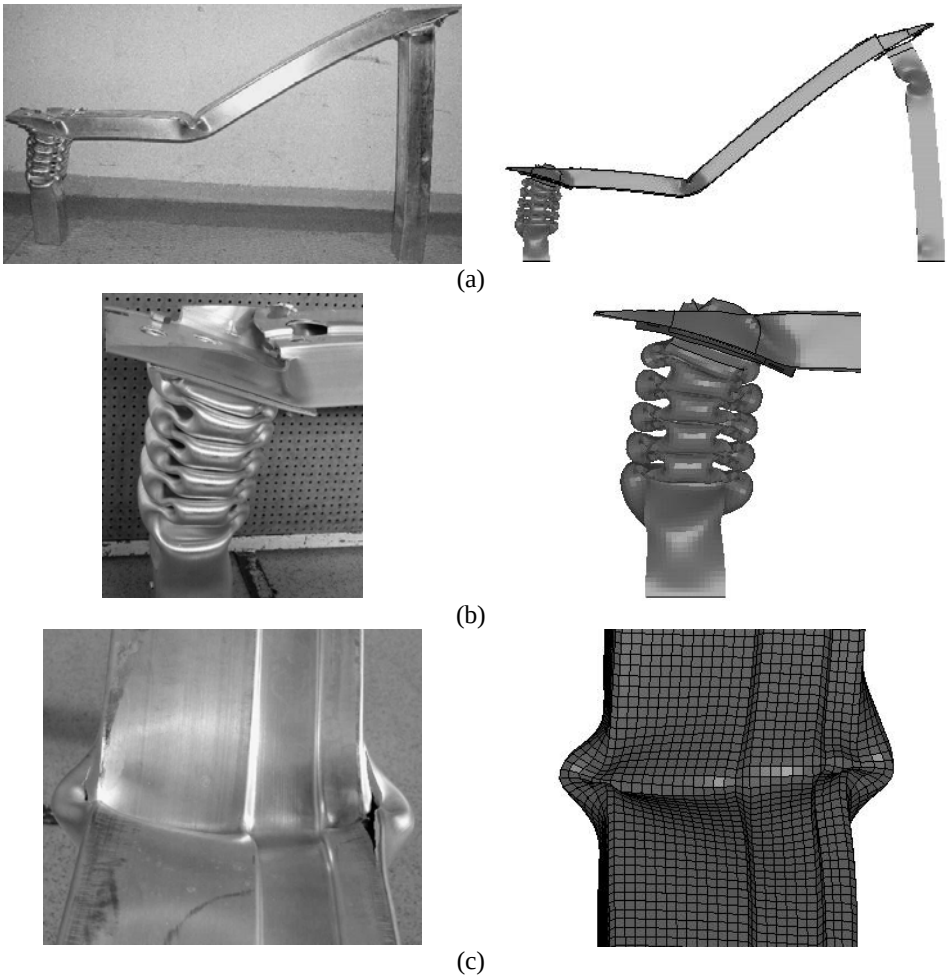

Figure 7-17 Comparison of permanent deformation shapes of test specimen **C1** and that obtained from simulations with MAT-41 (*CFS**) model.

In the simulations the bumper beam cross-section collapsed at the impacted end before the initiation of longitudinal buckling. From Figure 7-18(a) one can observe that the force-deformation curves obtained from the simulations deviate from the experimental curves before 100 mm deformation. The collapse of the bumper beam cross-section is accompanied by the bending of the interface plate and the observed difference might be due to different attributes of this plate. The peak force seen in the force-deformation plots corresponds to the buckling initiation in the impacted longitudinal. Compared to the tests this peak force is much higher in the simulations. Regarding these matters the discussion in Section 7.4.1 is still valid.

The plastic hinge in the mid-section of the bumper beam developed before the buckle in the impacted longitudinal. In further accordance with the experiments a progressive folding mode of the impacted longitudinal was observed. Figure 7-18(b) clearly depict that the predicted mean force level in the simulations too high. This is mainly due to the higher initial peak load.

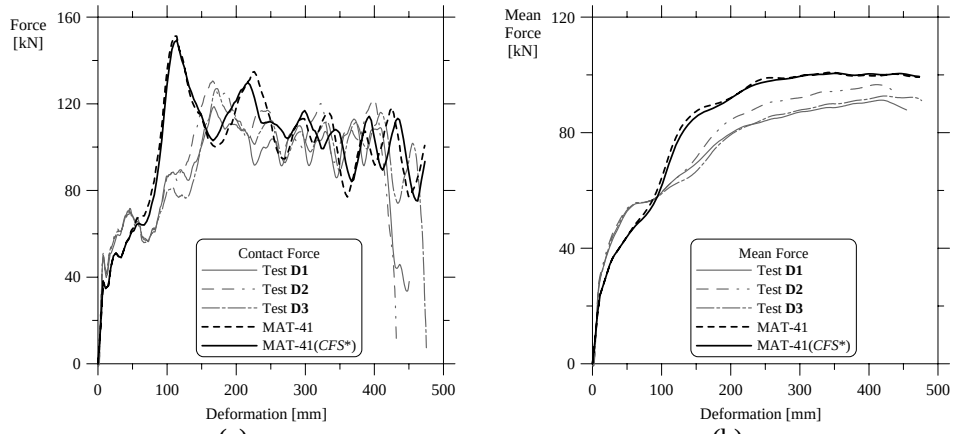

Figure 7-18 Comparison of (a) force-deformation and (b) mean force-deformation plots from the tests and simulation results for test series **D**.

7.7.2 Deformation shape

Snap-shots at various stages of the deformation process obtained from the numerical simulations for test series **D** are shown in Figure 7-19. The selected times are denoted with dots on the corresponding force-time curve in Figure 7-20. The impact event started at time $t_1 = 0$. By the end of time t_2 the bumper beam cross-section at the impacted end collapsed and simultaneously the development of a plastic hinge in the mid-section of the bumper beam started. At time t_3 the first buckle developed in the impacted longitudinal (at the interface of HAZ and base material). A close view of this first buckle in the impacted longitudinal is shown in Figure 7-21(a). This figure clearly shows the initial asymmetric folding mode developed. This is not in agreement with the tests where an axisymmetric folding mode was observed. At time t_4 the elements at the non-impacted end of the bumper beam were eroded. The crack is clearly shown in Figure 7-21(b) with a circle. A local plastic hinge in the non-impacted longitudinal developed at its clamped end prior to time t_5. The simulation stopped at time t_6 as the impactor reached the termination displacement specified on the *TERMINATION_BODY keyword card. Thus, the impact events of test series **D** and **A** follow each other, but at different times due to different impact velocity.

The final deformed shapes from the numerical simulation and experiments are compared in Figure 7-22. In Figure 7-22(a), the overall deformation mode of the bumper beam-longitudinal system is compared. As can be seen, the local plastic hinge developed at the clamped end of the non-impacted longitudinal is more consistent with the experiments compared to the other test series simulations (i.e. test series **A**, **B** and **C**). The crushed bumper beam at the impacted end and the progressive folding mode in the impacted longitudinal is compared in Figure 7-22(b). In the simulations also the deformed end of the impacted longitudinal has some rotation towards the

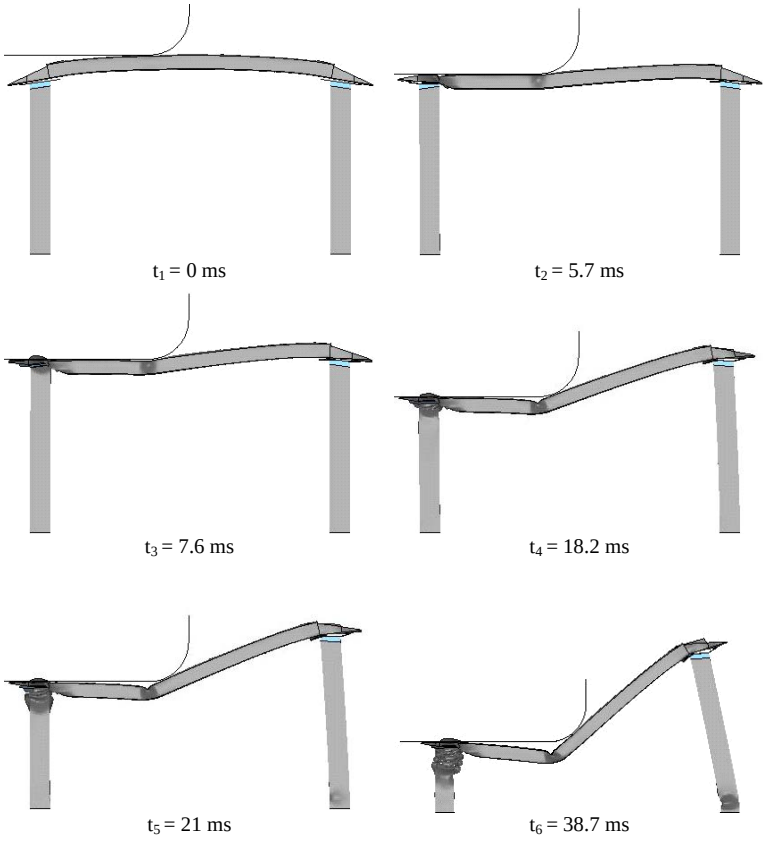

Figure 7-19 A sequence of deformation shapes from the simulation for test series **D** with MAT-41(*CFS**) model.

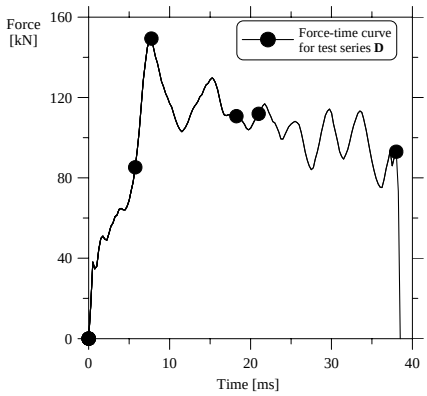

Figure 7-20 Force-time curve form simulation – showing the selected times in Figure 7-19 for test series **D**.

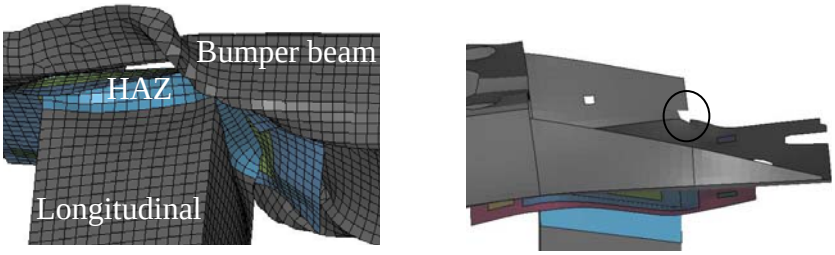

(a) (b)

Figure 7-21 (a) Close view of the first buckle developed in the impacted longitudinal at time t_3 = 7.6 ms and (b) start of element deletion at the intersection of the lower flange and the web t_4 = 18.2 ms.

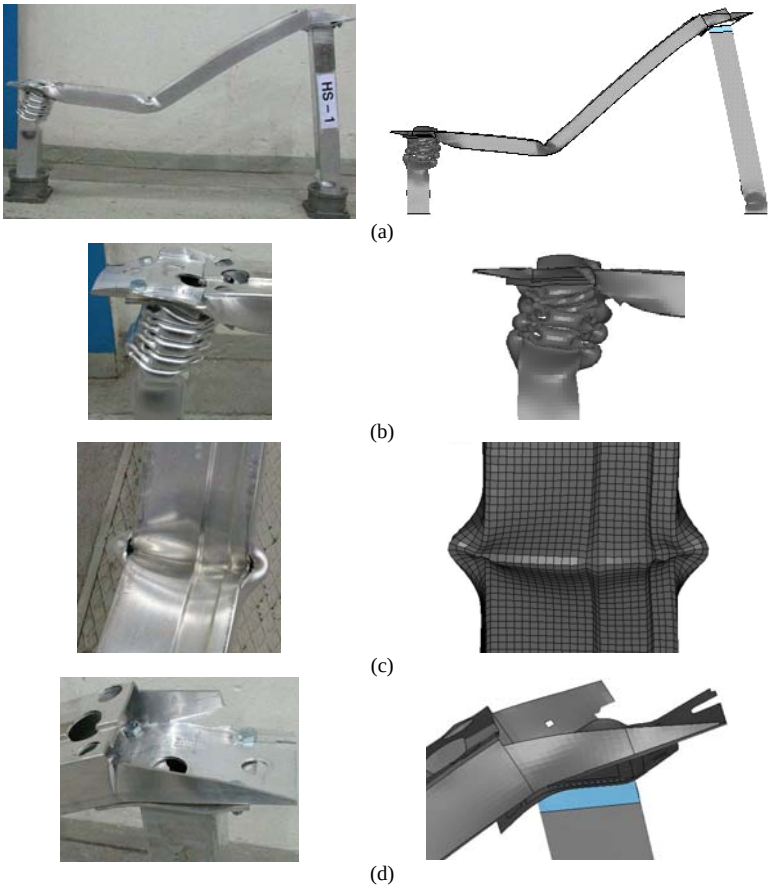

(a)

(b)

(c)

(d)

Figure 7-22 Comparison of permanent deformation shapes of test specimen **D1** and that obtained from simulations with MAT- 41(*CFS**) model.

non-impacted longitudinal as in the test. The number of lobes developed was two shorter in the simulations (eight) compared to the tests (ten).

The failure in the folded compression flange and webs of the bumper beam was poorly predicted, Figure 7-22(c), although some integration points reached the fracture criterion. The numerical simulation failed to predict the through-thickness shear crack at the cut-out region of the non-impacted end of the bumper beam.

7.8 Energy absorption

Numerical simulations make it possible to understand how the energy has been distributed in the system with the progress of deformation. The amount of energy mitigated through different parts of the bumper beam-longitudinal system when using the user-defined material model are summarised in Table 7-3, Table 7-4, Table 7-5 and Table 7-6 for test series **A**, **B**, **C** and **D**, respectively. Figure 7-23 shows the energy-deformation plots for all the components in the bumper beam-longitudinal system. The force-deformation curves from the numerical simulations are also shown on the top of the same figure.

For test series **A**, **B** and **D**, the energy absorption in the impacted longitudinal started at a deformation of 100 mm. Prior to this deformation the energy is absorbed in collapsing the bumper beam cross-section at the impacted end. This point strongly supports that in experimental test series **A** and **B**, the bumper beam collapsed before the buckling initiation in the impacted longitudinal started, see Chapter 5. Thus, it is clear that the initiation of buckling in the impacted longitudinal has led to the high peak in the force-deformation plots for test series **A**, **B** and **D**. It was concluded that this peak probably can be reduced by modelling initial geometric imperfections or by increasing the assumed length of the HAZ. The simulations with increased HAZ length can be found in Sections 8.1.2.2 and 8.3.2 for test series **A** and **D**, respectively.

Table 7-3 Material internal energy for test series **A** (same as in Table 7-2).

Part	Impact energy = 39.7 kJ, MAT-41(*CFS**)	
	Internal energy (kJ)	Percentage %
Total system	38.01	100
Bumper beam	6.9	18.11
Impacted longitudinal	28.96	76.03
Non-impacted longitudinal	0.82	2.15
Impacted interface plate	0.98	2.57
Non-impacted interface plate	0.40	1.05

Table 7-4 Material internal energy for test series **B**.

Part	Impact energy = 39.7 kJ, MAT-41(*CFS**)	
	Internal energy (kJ)	Percentage %
Total system	38	100
Bumper beam	6.79	17.87
Impacted longitudinal	28.96	76.21
Non-impacted longitudinal	0.81	2.13
Impacted interface plate	0.99	2.60
Non-impacted interface plate	0.39	1.03

Table 7-5 Material internal energy for test series **C**.

Part	Impact energy = 39.7 kJ, MAT-41(*CFS**)	
	Internal energy (kJ)	Percentage %
Total system	23.36	100
Bumper beam	4.90	20.98
Impacted longitudinal	16.73	71.62
Non-impacted longitudinal	1.15	4.92
Impacted interface plate	0.35	1.49
Non-impacted interface plate	0.22	0.94

Table 7-6 Material internal energy for test series **D**.

Part	Impact energy = 89.325 kJ, MAT-41(*CFS**)	
	Internal energy (kJ)	Percentage %
Total system	46.05	100
Bumper beam	7.58	16.46
Impacted longitudinal	35.80	77.74
Non-impacted longitudinal	1.14	2.48
Impacted interface plate	1.034	2.24
Non-impacted interface plate	0.46	0.99

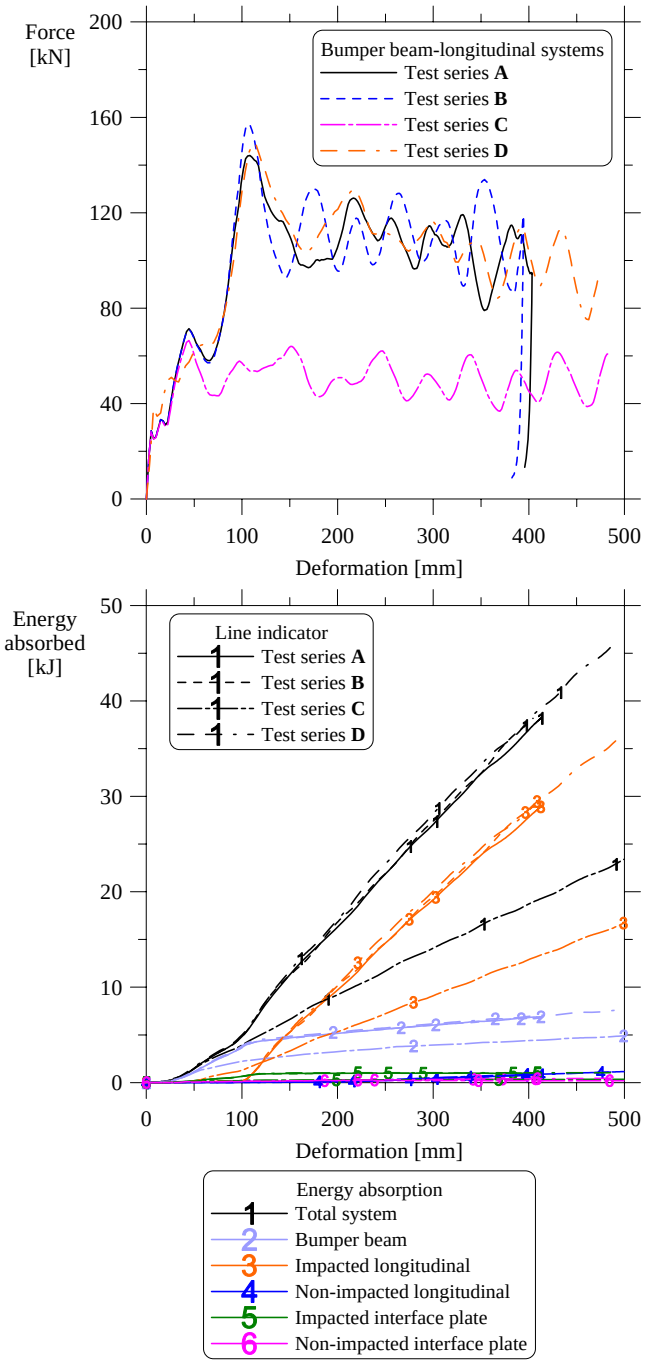

Figure 7-23 Force-deformation plots, energy distribution with respect to deformation for test series **A**, **B**, **C** and **D**.

Contrary to other test series, the energy absorption in the impacted longitudinal of test series **C** started at a deformation of 50 mm, see Figure 7-23. As the buckling in the impacted longitudinal started, the bumper beam cross-section did not collapse completely and the high peak which was observed in other test series was not observed here.

The energy absorbed by the bumper beam in test series **A**, **B** and **D** varies between 6.79 kJ and 7.58 kJ. The percentage of energy being absorbed by the bumper beam compared to the total energy absorbed was 16.5% in test series **D** (Table 7-6), whereas this was 18% in test series **A** (Table 7-3).

The energy absorption by the impacted interface plate started at a deformation of 50 mm in the test series **A**, **B** and **D**. This corresponds to 50% collapse of the bumper beam cross-section. The energy absorbed by the non-impacted interface plate in test series **A**, **B**, **C** and **D** is almost the same and is close to 1% of the total energy absorbed. The energy absorbed in developing the plastic hinge(s) in the non-impacted longitudinal varies from 2.13% to 4.92% (see Tables 7-3 to 7-6). The lowest being in test series **B** while the highest in test series **C**. In the latter case the non-impacted longitudinal had two buckles.

The energy absorbed by the impacted longitudinal in test series **A** and **B** was the same with 76% (Table 7-3 and Table 7-4). This shows that in the offset impacts the longitudinals are the key structural elements for absorbing the impact energy. Thus the longitudinals deserves a closer look since it contributes to great percentage of the total energy absorbed. From Table 7-5 it is clear that the impacted longitudinal absorbed only 71% of the total energy absorption for test series **C**. This is mainly due to the lower yield strength of the material, see Table 3-6.

From Table 7-6 it is clear that the impacted longitudinal in test series **D** absorbed approximately 78% of the total energy absorbed before the impactor was stopped at a displacement of 491 mm. The total energy

absorbed by test series **D** is slightly higher than that of test series **A**, Figure 7-23. This increase in the total energy absorption is due to increased inertia effects in test series **D**.

7.9 Summary

Numerical simulations were performed and compared with the experimental results for each test series **A**, **B**, **C** and **D**. The simulations of test series **A** was performed using different material models. The results revealed that for a given amount of deformation the predicted energy absorbed was higher with the currently available material models in LS-DYNA than with user-defined material model (MAT-41).

For test series **B** the simulations failed to predict the behaviour that was observed in the tests. Thus, no comparison was performed between the simulated and experimentally obtained permanently deformed specimens.

The predicted mean force level for test series **C** was lower than in the tests. Further, a more dominant buckle was predicted on the non-impacted longitudinal. If the HAZ was modelled the system showed a tendency of running into an unstable deformation mode.

At the increased impact velocity for test series **D**, the numerical simulations predicted a much higher peak force compared to the tests.

The simulations failed to predict the through-thickness shear crack that was observed at the cut-out region of the non-impacted end of the bumper beam in test series **A**, **B** and **D**.

In general, good agreement was found between the experiments and simulations when using the user-defined material model with the critical thickness strain fracture criterion (*CFS**), e.g. the mean force-deformation

plots in Figure 7-2(b) for test series **A**. The following points can be noted from the present chapter:

For test series **A**, **B** and **D**

- The deformation mode in the impacted longitudinal deviated from the experiments, i.e. for the first buckle instead of developing an *axisymmetric* mode an *asymmetric* folding mode developed. Thus, the number of lobes developed was less.
- The change in deformation mode caused a higher peak force in the force-deformation characteristics.

For test series **C**

- The predicted deformation mode in the impacted longitudinal was similar to that observed in the experiments. However, the mean force level was underestimated and with a more dominant buckle in the non-impacted longitudinal.

Chapter 8 Sensitivity Studies and Process Effects on Material Level

Sensitivity studies have been carried out for each test series using the respective baseline model. The sensitivity studies include both physical and purely numerical parameters. The physical parameters investigated were strain-rate, heat-affected zone (HAZ) and fracture criteria, while the numerical parameters investigated were element formulation type, mesh size, number of through-thickness integration points, self-contact and adaptive meshing. The sensitivity study for test series **A** is much wider than for the other series. For test series **B** no sensitivity study was performed, since the simulations failed to predict the observed behaviour in the tests. In the present chapter, unless otherwise mentioned the critical thickness strain fracture criterion (*CFS**) will be considered as a default in all the simulations.

8.1 Test series A

For test series **A**, the numerical response of the bumper beam-longitudinal system predicted by different material models was discussed in Section 7.3. It is reasonable to use the user-defined material model as a basis of the sensitivity study, since it includes many possible important features. Thus, the user-defined material model with critical thickness strain fracture criterion was chosen as the "baseline" model for test series **A**.

8.1.1 Strain-rate

In the analysis of the dynamic plastic response of automobile bumper beam structures subjected to crash loading, strain-rate sensitivity effects may be

important. Failure to account for such effects in the analysis may result in completely unrealistic results (Shieh, 1975).

In the baseline model the material is assumed to be strain-rate insensitive. However, the material tests presented in Section 3.2 showed that there is some strain-rate sensitivity on the strength of the bumper beam material (i.e. AA7108-T6), as well as for the longitudinal material in AA7003-T79. The strength variation of the bumper beam (AA7108-T6) and the longitudinal (AA7003-T79) at different strain-rates is shown in Figure 3-14. Strain-rate effects are included in the constitutive model as explained in Chapter 2.

The numerical response (force-deformation) of the bumper beam-longitudinal system when considering strain-rate sensitivity is compared with the baseline model in Figure 8-1. The figure clearly depicts that with the consideration of strain-rate sensitivity the average force level increases. The deformation mode predicted in the numerical simulations for both cases, i.e. with and without consideration of strain-rate sensitivity, was the same, but the amount of deformation is less when strain-rate sensitivity is taken into account.

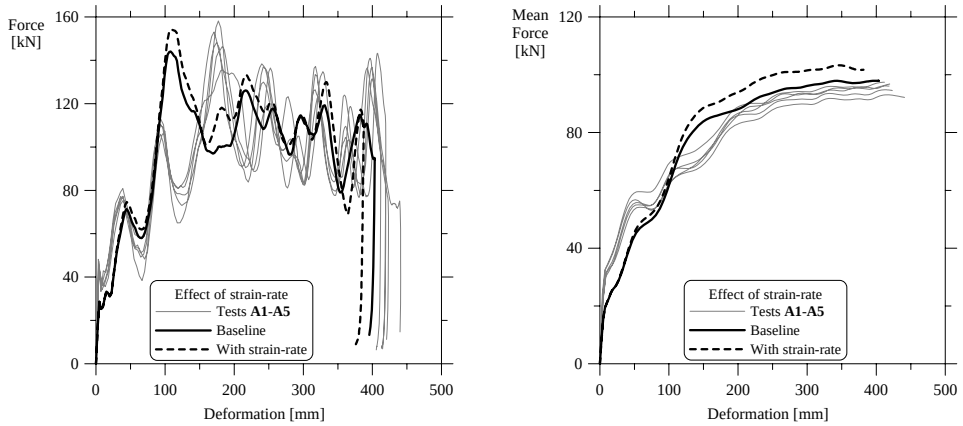

Figure 8-1 Strain-rate effects on the response of test series **A**, (a) force-deformation and (b) mean force-deformation.

In other words, this implies that the total impact energy of the impactor was absorbed over a smaller deformation which can also be noted from the mean force-deformation plot in Figure 8-1(b). The mean force predicted is higher for the system with strain-rate effects. From the simulations it can be concluded that strain-rate effects are of importance and without inclusion of these effects, the peak moments (and thus, peak decelerations) might be considerably underestimated, see Figure 8-1(a).

8.1.2 Heat-affected zone (HAZ)

In the FE-model (Figure 6-20) a length of 20 mm and a 30% reduction factor in the true stress-strain curve (Figure 6-22) were assumed in modelling the HAZ. To study the influence of the HAZ on the crash behaviour of the bumper beam-longitudinal systems the following additional simulations were performed. The first case is without the HAZ, in the second case the 20 mm HAZ length is increased to the elastic local buckling length, and in the final case the thickness of two rows of elements in the HAZ is increased to represent the fillet material addition due to welding.

8.1.2.1 Without the HAZ

Figure 8-2 shows the response of the bumper beam-longitudinal system with the baseline model, without any HAZ, but with and without strain-rate effects. The final permanent deformation shapes are compared in Figure 8-3.

When the HAZ was not modelled the deformation mode changed. One would expect that when the HAZ was not modelled the force level in the system should increase, due to the increased stiffness of the longitudinals.

On the contrary, a lower force level with increased permanent deformation was observed in the simulations, Figure 8-2(a). Thus the mean force as well

as the energy absorbed by the bumper beam-longitudinal system decreased, Figure 8-2(b), when the rate effects were ignored. However, the behaviour was opposite when the rate effects were taken into consideration.

The reasons for such behaviour of the system are as follows. With the initiation of buckling in the impacted longitudinal in the baseline simulation the deformation was concentrated in the soft zone, i.e. in the HAZ itself. The formation of a second buckle led to rise in the force level at a deformation of 200 mm, see Figure 8-2(a). When the HAZ was not modelled, however, a higher force was required to initiate the buckling in the impacted longitudinal. Of this reason the deformation was not concentrated, as in the baseline model, and simultaneously the buckling pattern was developed over the entire length of the longitudinal. This pattern helped in the easy formation of buckles with the progress of the deformation process. The above is also applicable when the strain-rate effects are taken into consideration. However, there was a much higher peak force in the simulations when the rate effects were considered, as in previous section.

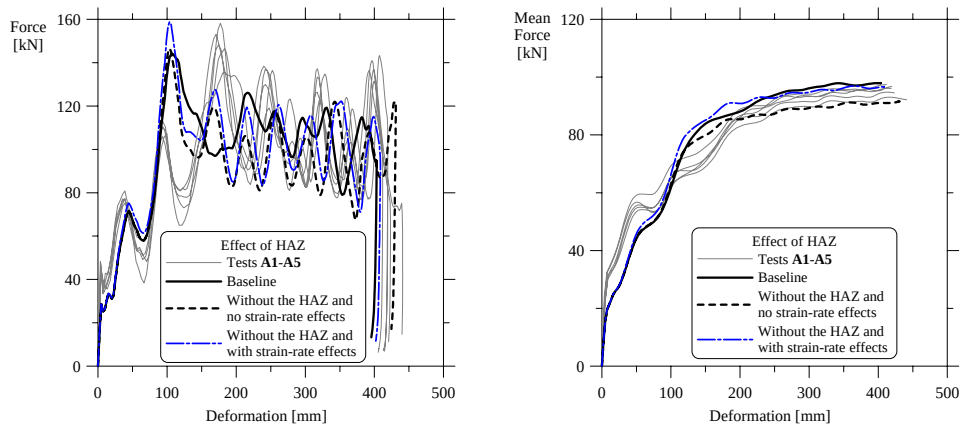

Figure 8-2 Influence of HAZ on the crash behaviour of test series **A**, (a) force-deformation and (b) mean force-deformation.

A clearer progressive buckling mode developed in the impacted longitudinal when the HAZ was not modelled (Figure 8-3(b) and (c)), and the permanent deformation of the system increased without the rate effects. The predicted permanent deformation without the HAZ, but with rate effects was close to the tests, see Figure 8-2(a). When the HAZ was not modelled, it can further be seen that there are some rotational effects on the deformed end of the impacted longitudinal. On the other hand, no local buckle developed at the clamped end of the impacted longitudinal, which is in better accordance with the experiments.

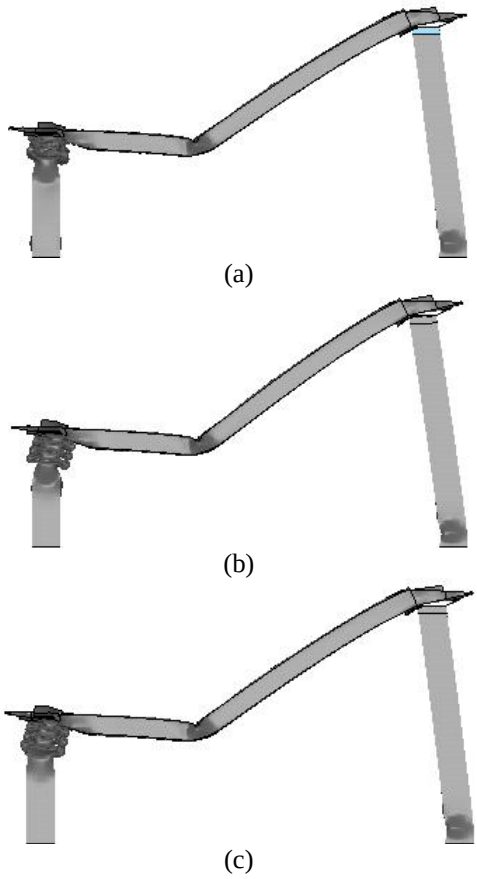

Figure 8-3 Final deformation shapes of test series **A** from the simulations (a) with the HAZ (baseline model), (b) without the HAZ, no strain-rate effects and (c) without the HAZ, with strain-rate effects.

It can be concluded that without the modelling of the HAZ the behaviour of the bumper beam-longitudinal system deviated from the experiments, in the absence of strain-rate effects. On the other hand the system behaviour was close to that observed in the tests when rate effects were considered.

8.1.2.2 Increasing the HAZ length

In the previous section, the initial high peak force existed in the force-deformation plots when the HAZ was modelled with 20 mm width, Figure 8-2(a). Here it is questioned/investigated whether the peak force can be reduced by assigning the HAZ a different (even unphysical) length. Presently the HAZ length is increased to the elastic local buckling length of the longitudinal. Thus, as the buckling initiation in the impacted longitudinal starts on the 95 mm wall (see Figure 1-2), the HAZ length was taken as 95 mm.

The 95 mm HAZ was modelled only in the impacted longitudinal. Force-deformation plots from the simulations are compared in Figure 8-4(a). The

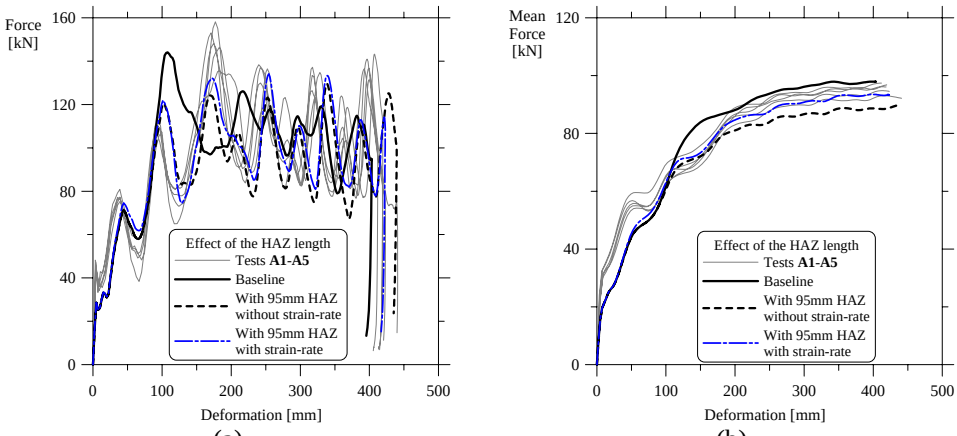

Figure 8-4 Influence of increasing the HAZ length from 20 mm to 95 mm, on the crash behaviour of test series **A**, (a) force-deformation and (b) mean force-deformation.

analyses were performed with and without strain-rate effects. The peak force that existed in the 20 mm HAZ system is clearly reduced when a 95 mm HAZ was modelled. The peak force was the same both with and without the strain-rate effects. This reduction in the peak force is due to the "availability" of a sufficient length for the formation of the first buckle in the impacted longitudinal within the weaker HAZ. This further aids in the easy formation of the rest of the buckles outside the HAZ region, and thus the mean force of the system decreased (without strain-rate effects) in Figure 8-4(b). With rate effects the mean force level increased and was on the top of the experimental curves, see Figure 8-4(b).

The folding mode developed in the impacted longitudinal with a 20 mm HAZ is a mixed mode, Figure 8-5(a). In Figure 8-5(b) and (c) the folding mode developed with a 95 mm HAZ in the system is more clearly progressive, i.e. similar to that observed in the tests. However, there are some rotational effects on the deformed end of the impacted longitudinal due to the reduced stiffness of the longitudinal. As in the case without the HAZ in the previous section, the impacted longitudinal did not develop any buckle at its clamped end. On the other hand one has to sacrifice for the poor prediction of fracture in the critical areas.

To summarise; assigning the HAZ an unphysical length of 95 mm, i.e. about the elastic local buckling length, led to accurate prediction of the force level and the deformation mode in the system. Do remember that the HAZ of 95 mm is unphysical and that this modelling approach must be considered as a "trick". The author belives that more tests are required to verify that this approach "holds" also in other cases.

8.1.2.3 Increasing the thickness of the elements in the HAZ

For accurate prediction of fracture modes, the numerical model should be constructed as close as possible to the physical test set-up. As mentioned earlier, the longitudinal and the interface plate were MIG welded in order to

connect the longitudinal to the bumper beam's back face. Because of welding some extra material is added in the form of a fillet in the welded section. To represent this material the thickness of selected rows of elements in the HAZ are assigned an increased thickness.

The increased thickness was assigned to the two rows of elements in the HAZ closest to the interface plate and two rows in the interface plate (Figure 6-20). Three simulations were performed with 1.5, 2 and 2.5 times the original thickness of the respective elements. Only with a thickness

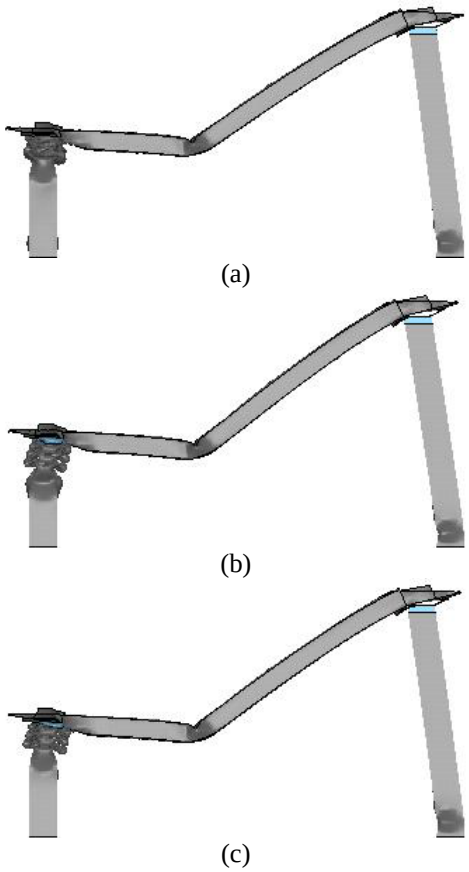

(a)

(b)

(c)

Figure 8-5 Final deformation modes from the simulations for test series **A**, (a) baseline model (b) 95 mm HAZ model without strain-rate effects and (c) 95 mm HAZ model with strain-rate effects.

increase by 2.5 times change in the fracture mode was observed. The predicted response is compared with the baseline model in Figure 8-6.

As can be seen from Figure 8-6(a), the response of the system changed significantly after the formation of first buckle in the impacted longitudinal, i.e. after the initial high peak in the force-deformation plots. One can clearly see that the impact energy is absorbed over a shorter deformation, i.e. the mean force level, is over-predicted when compared to the baseline model. The final deformed shape of the bumper beam-longitudinal systems is shown in Figure 8-7. In the present case, the simulation was able to predict the through-thickness shear crack at the cut-out region of the non-impacted end of the bumper beam. A close view of the crack is shown in Figure 8-7. However, the propagating tearing crack at the intersection between the lower flange and the web was not influenced by increasing the thickness of the selected elements. The predicted through-thickness shear crack path is parallel to the axis of the longitudinal which is similar to that observed in the test specimens **A4** and **A5**, see Figure 5-27. It may be possible to predict the crack path as in the test specimens **A1** and **A2**, Figure 5-27, if the

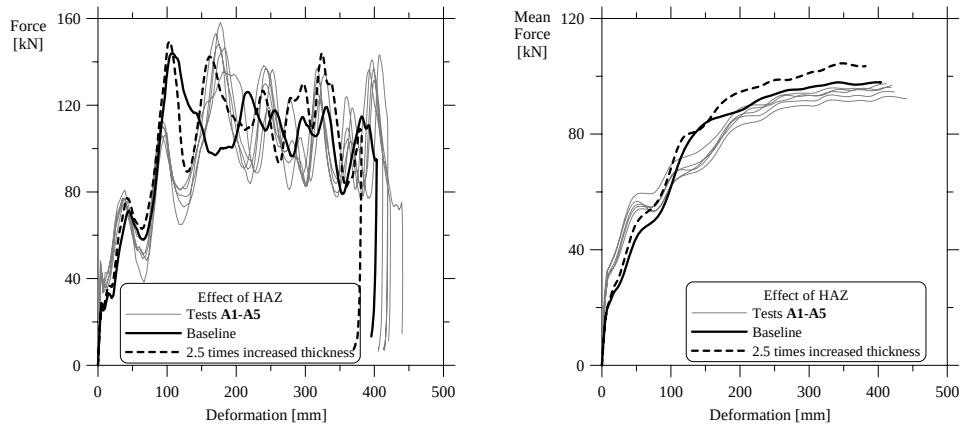

Figure 8-6 Influence of increasing the thickness of selected elements to represent weld material addition (a) force-deformation and (b) mean force-deformation.

element splitting could be done along the diagonal direction when employing fission based adaptive meshing, see Section 8.1.8.

8.1.3 Fracture criteria

In addition to the critical thickness strain fracture criterion (*CFS**) that was used in the baseline model, the user-defined material model includes the fracture criterion due to Cockcroft and Latham (CL), Equation (2.33). The CL fracture parameters are tabulated in Table 3-9.

The response of the system obtained from the simulations when using the two different fracture criteria is shown in Figure 8-8. As can be seen, there is no significant influence on the predicted behaviour of the system, i.e. the response of the system is the same when either of the two of fracture criteria is used. However, there is a slight increase in the permanent deformation of the system when the Cockcroft-Latham fracture criterion is used. The increase in deformation is due to more extensive failure events and the deletion of a larger number of elements in the analysis performed with CL fracture criterion. When using the *CFS** and CL fracture criteria in the simulations, a total of 17 and 67 elements were eroded, respectively. The fracture limits for the bumper beam material (AA7108-T6) is shown in Figure 8-9. As can be seen, especially in the stretch-stretch region the CL

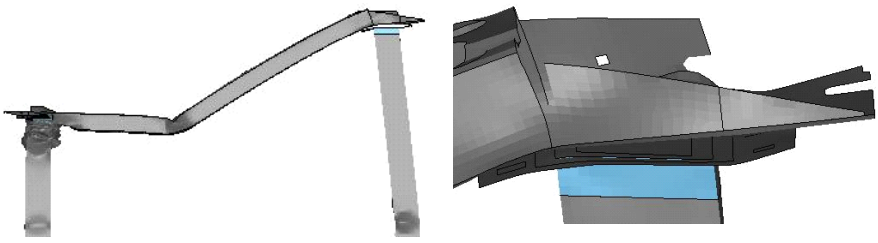

Figure 8-7 Final deformed shape (left) of the bumper beam-longitudinal system when the thickness of selected elements in the HAZ is increased by 2.5 times, close view of the through-thickness shear crack (right) at the non-impacted end of the bumper beam.

criterion is greater than the *CFS** criterion representing that a state of fracture is more easily reached. Hence, the response of the bumper beam-longitudinal system differs.

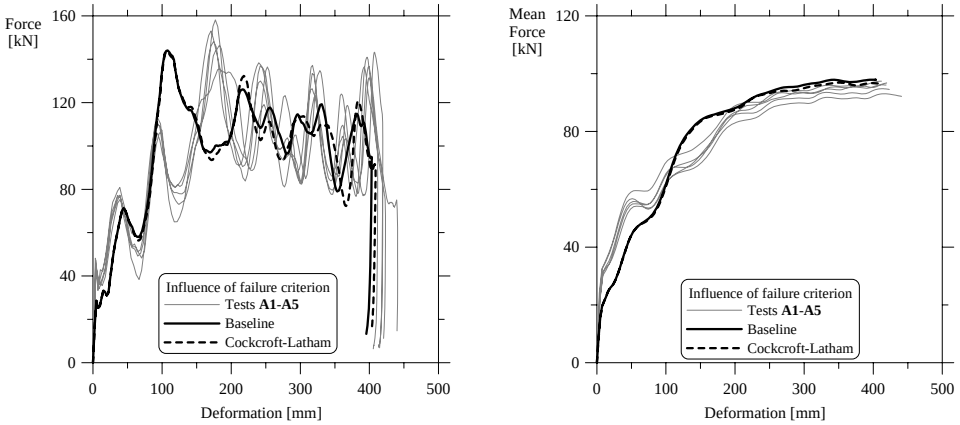

Figure 8-8 Influence of fracture criteria on the crash performance of bumper beam-longitudinal system (a) force-deformation and (b) mean force-deformation.

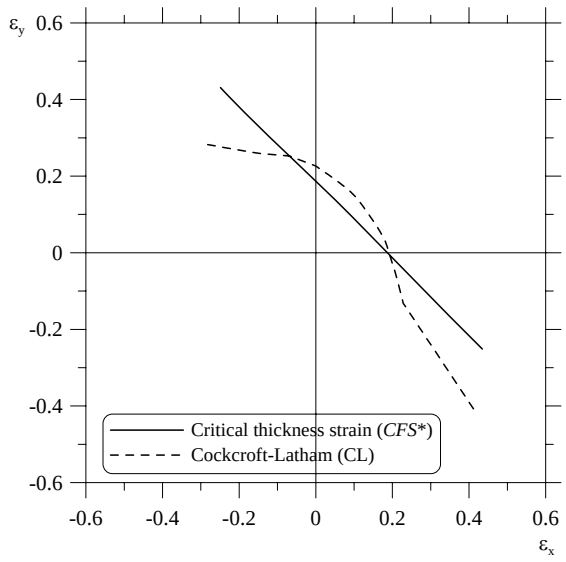

Figure 8-9 Fracture limits predicted for the bumper beam material by the user-defined constitutive model.

8.1.4 Self contact

As the extruded longitudinal deforms, contact between the lobes will occur. Thickness offsets are not included in the surface to surface and node to surface contact algorithms, whereas in single surface contact algorithms they are always included. The default thickness $t_{contact}$ used in the contact formulation is given by (Hallquist, 2003)

$$t_{contact} = \min(t_{initial}, 0.4 \cdot l_{edge}) \tag{8.1}$$

where $t_{initial}$ is the initial shell thickness and l_{edge} is the length of the shell element. In thin shells this is not a problem as the thickness of the shell is much smaller than other dimensions, but for thick shells the thickness and the length of the side edge can be of similar size and the thickness used in the contact formulation will be much smaller than the real thickness.

In the current simulations an element size of 5x5 mm is used giving a shell thickness in the contact formulation of 2 mm. Simulations were carried out using the shell thickness in the contact formulation equal to the initial thickness of the shell. The predicted behaviour of the bumper beam-longitudinal system is compared with the baseline model in Figure 8-10. From the figure it can be concluded that the use of the actual thickness in the contact algorithm in LS-DYNA had none or little influence on the force level and thus on the behaviour of the bumper beam-longitudinal system.

The thickness of the shell will change during deformation, this thickness change is per default not included in the contact formulation of LS-DYNA. Simulations were performed taking into consideration changes in thickness in the contact formulation. The results show, Figure 8-11, that there is no effect of considering the change of thickness in the contact algorithm. Jensen (2005) also obtained similar results when studying the square tubes subjected to axial loading.

8.1.5 Element formulation type

In the simulations, Belytschko-Tsay (type 2) (Hallquist, 2003) shell elements were used. This element formulation type is very CPU efficient and thus a natural choice. Two other element formulation types were tested,

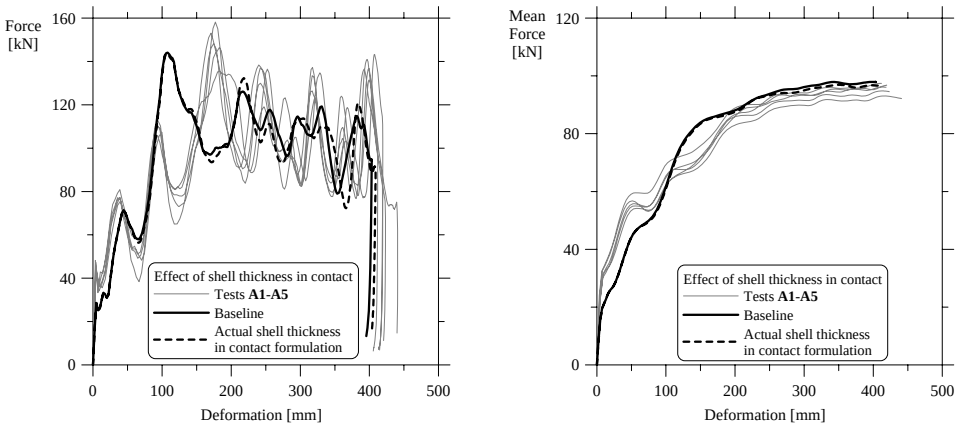

(a) (b)

Figure 8-10 Effect of actual shell thickness in contact formulation: (a) force-deformation and (b) mean force-deformation.

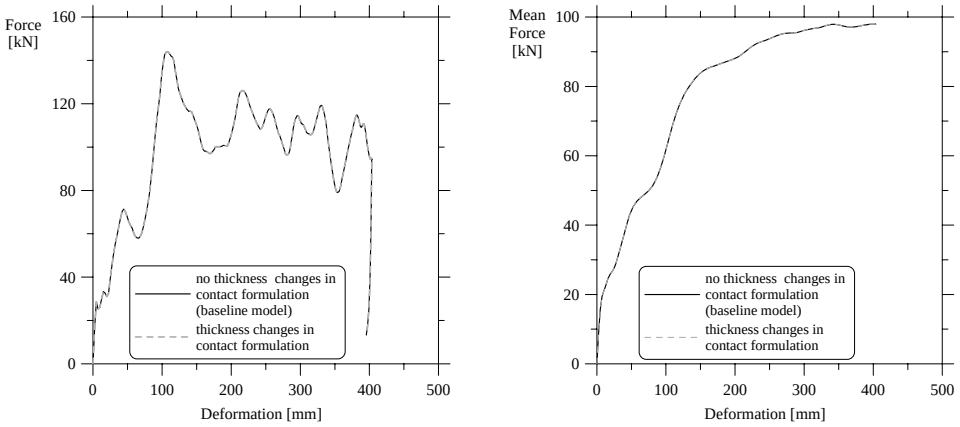

(a) (b)

Figure 8-11 Effect of considering thickness changes in contact formulation: (a) force-deformation and (b) mean force-deformation.

namely Hughes-Liu (type 1) (Hallquist, 2003) and a fully integrated element formulation (type 16) (Hallquist, 2003).

In the simulations with type 1 and type 16 element formulations - five through-thickness integration points were considered as in Belytschko-Tsay (default) formulation. The Hughes-Liu element formulation also uses one point quadrature as in Belytschko-Tsay element (Hallquist, 1998). Thus there is no need to worry for the element erosion when the fracture criterion is satisfied. If this value (three out of five) is used in the fully integrated element formulation (type 16) then a large group of elements was deleted. This over-predicts the fracture in the system, which is not physical. The reason is that type 16 uses 2x2 quadrature instead of a one-point quadrature, and thus the elements have a total of 20 integration points. To avoid deletion of such large group of elements when employing the fully integrated element formulation, the element deletion criterion has been changed from three out of five to twelve out of twenty.

As can be seen from Figure 8-12, when using the Hughes-Liu elements

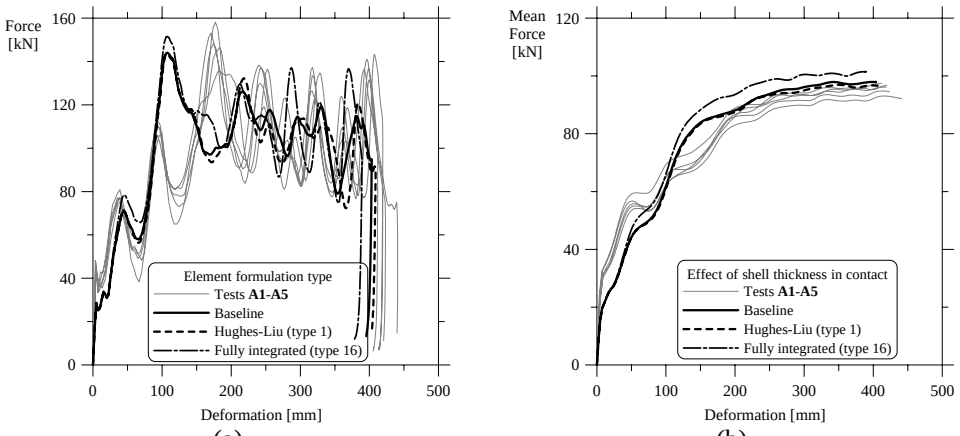

Figure 8-12 Effect of element formulation type on the crash behaviour of bumper beam-longitudinal system: (a) force-deformation and (b) mean force-deformation.

(type 1) the predicted behaviour of the bumper beam-longitudinal system was the same as that predicted by the default element formulation. On the other hand, the use of the fully integrated element type 16 led to an increase in the mean force level and, hence, a reduced permanent deformation compared to the baseline model, see Figure 8-12(a),

From the simulations with different element formulation types, it can be concluded that the choice of element type has some influence on the force level, especially fully integrated element type 16.

8.1.6 Through-thickness integration points

In Section 7.3 it was noted that the number of lobes developed in the impacted longitudinal in the simulations was two shorter compared to the tests. Here it is investigated whether the number of lobes might be increased by increasing the number of through-thickness integration points. However, it should be kept in mind that the computation time and cost is most proportional to the increased number of integration points.

In the baseline model five through-thickness integration points was used. Additional simulations were performed with seven and nine through-thickness integration points. The maximum through-thickness integration points that can be used in a shell are ten, due to the limitation of the Lobatto integration rule, see Hallquist (2003).

The predicted response of the bumper beam-longitudinal system when increasing the through-thickness integration points is compared to the baseline model in Figure 8-13, while in Figure 8-14 permanent deformation profiles of the impacted longitudinals are shown. It was expected that the number of lobes would increase because of the increased number of computations through the thickness of the shell, and thus the element could bend/buckle more easily. The force-deformation characteristics in Figure 8-13(a) indicates that an increased number of through-thickness integration

points have no influence for the predicted response of the system at hand. The mean force-deformation plots are fairly close with the baseline prediction, Figure 8-13(b). The permanently deformed profiles in Figure 8-14 show that there is a slight change in the deformation mode during the formation of last-but-one buckle, when using seven and nine through-thickness integration points. This could be the probable reason for the drop in the force level at a deformation of about 350 mm, see Figure 8-13(a), when compared to the baseline model.

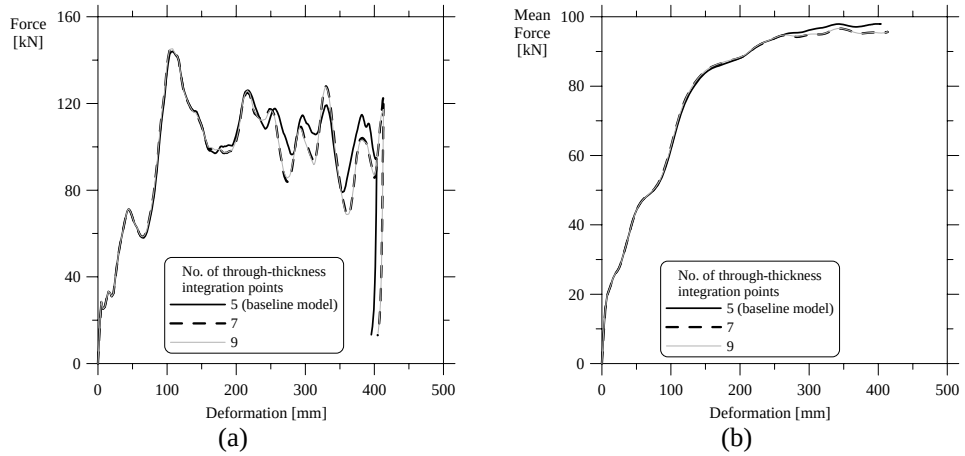

Figure 8-13 Effect of increasing the number of through-thickness integration points on the crash behaviour of bumper beam-longitudinal system: (a) force-deformation and (b) mean force-deformation.

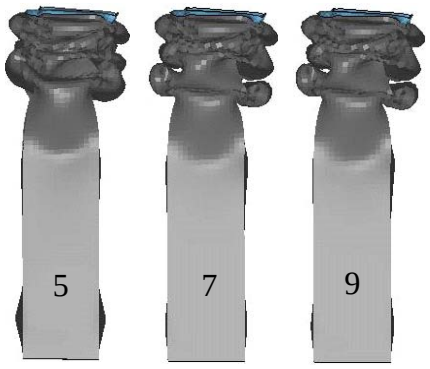

Figure 8-14 Permanent deformed shapes of longitudinals when increasing the number of through-thickness integration points.

8.1.7 Mesh size

The longitudinal members absorb the energy by buckling of the side walls. The buckling phenomenon is sensitive to the mesh size. In order to check the mesh sensitivity of the bumper beam-longitudinal system a simulation was performed. The mesh of the impacted longitudinal was modified, since it absorbs most of the energy.

To obtain the fine mesh in the impacted longitudinal an element split operation (Hallquist, 2003) was performed. In this operation each element was splitted into four small elements, thus the obtained elements have a size of approximately 2.5x2.5 mm^2. The element split operation was performed on the whole longitudinal including the HAZ, expect for the end rows of elements. The first and last row elements were meshed manually to avoid the problem of merging the nodes between the HAZ and interface plate and between the longitudinal and the fixture.

The predicted behaviour of the bumper beam-longitudinal system with

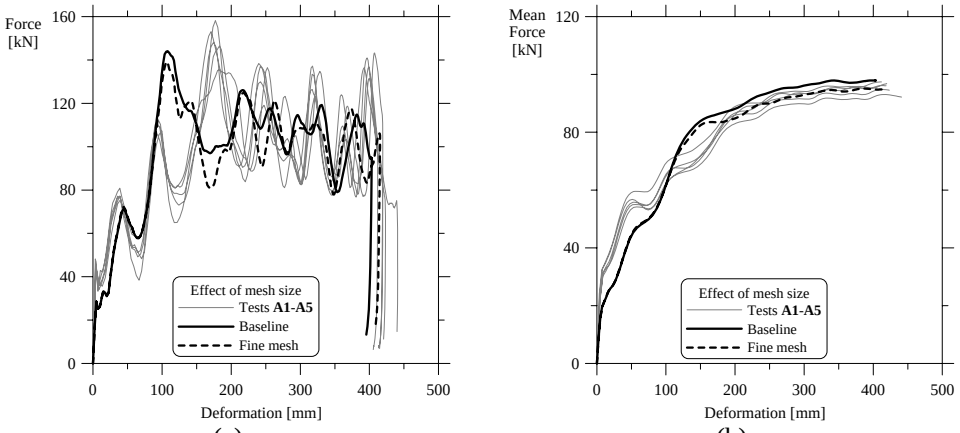

Figure 8-15 Effect of mesh size on the crash performance of bumper beam-longitudinal system (a) force-deformation and (b) mean force-deformation.

refined mesh is included in Figure 8-15. As seen, that the behaviour of the system is sensitive to the mesh size. Compared to the baseline model, the permanent deformation in the system is increased due to a lower mean force level, Figure 8-15(b). However, no change in the deformation mode was observed, and the number of lobes developed in the impacted longitudinal was the same as in baseline model. The increase in permanent deformation is due to the effective compression of the buckles (lobes).

8.1.8 Adaptive meshing

The adaptive meshing study was actually performed before adding the fillet material in the HAZ in Section 8.1.2.3. Although that increased thickness helped in predicting the through-thickness shear crack correctly, the propagating tearing crack at the intersection between the lower flange and the web was not captured. The basic reason behind employing the adaptive meshing was mainly to predict the fracture modes at the non-impacted end and in the mid-section (i.e. bending failure in the webs and flanges) of the bumper beam, see Figure 7-7. It was assumed that the present element size ($5x5\ mm^2$) was too large and thus the reason why the simulations failed to predict the fracture. Hence, with an intention to predict these failure modes simulations with adaptive meshing was performed on the baseline model. The adaptive meshing was applied only for the bumper beam using the *CONTROL_ADAPTIVE card in LS-DYNA (Hallquist, 2003).

By default LS-DYNA utilizes an h-adaptivity for shell elements. In the h-adaptive method, the elements are sub-divided into smaller elements whenever an error indicator shows that sub-division of the elements will provide improved accuracy. For the present simulations the maximum refinement level is set to 2 and a thickness strain error indicator is used. This means that whenever the adaptive re-meshing thickness criterion is satisfied the element is divided into four sub-elements. More details about the use of adaptive meshing can be found in Hallquist (2003).

It was observed that nothing was gained from the use of adaptive meshing in predicting the through-thickness shear crack and the bending failure in the mid-section of the bumper beam. Thus, no images of bending failure in the bumper beam are presented. The force-deformation and mean force-deformation plots are respectively compared in Figure 8-16(a) and (b) with respect to the baseline model.

The deformation of the bumper beam-longitudinal system when using the adaptive meshing was similar to that observed in the baseline model. The fracture modes observed at the non-impacted end of the bumper beam in the experiment and that predicted in the simulations using the *CFS** and CL fracture criteria with a fixed and adaptive mesh with the *CFS** fracture criterion are shown in Figure 8-17. The propagating tearing crack at the intersection between the lower flange and the web, that was suppressed in the baseline model and also when using Cockcroft-Latham fracture criterion, is accurately predicted with the adaptive mesh. The adaptive re-meshing that occurred across the cut-out section of the bumper beam due to adaptivity can also be seen. The simulations failed to predict the through-thickness shear failure at the non-impacted end of the bumper beam, without

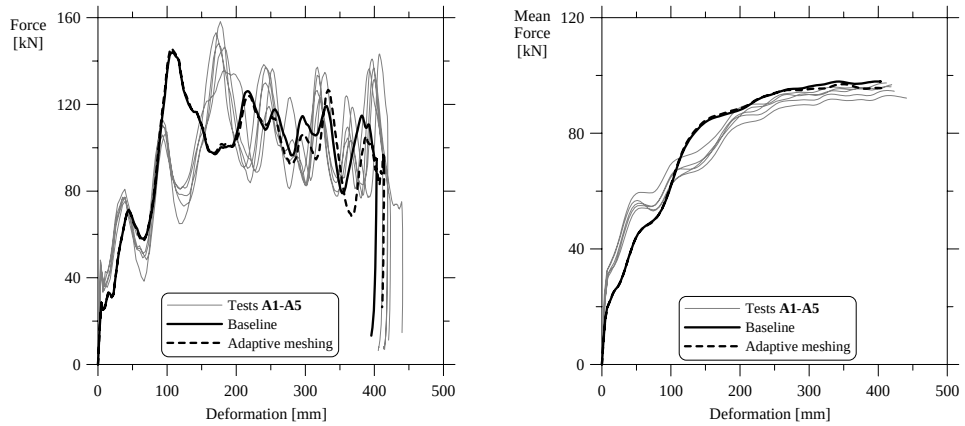

Figure 8-16 Influence of adaptive meshing on the crash behaviour of bumper beam-longitudinal system: (a) force-deformation and (b) mean force-deformation.

combining the adaptive meshing with increased thickness in the elements situated within the fillet weld.

The fracture mode predicted (in Section 8.1.2.3) at the non-impacted end of the bumper beam is shown in Figure 8-17(e). This image is mainly used to compare the fracture that was predicted when employing adaptive meshing. The two last images of Figure 8-17, i.e. (e) and (f) reveal that the use of adaptive meshing helps in predicting a more clear fracture path due to the sub-division of the elements in critical areas.

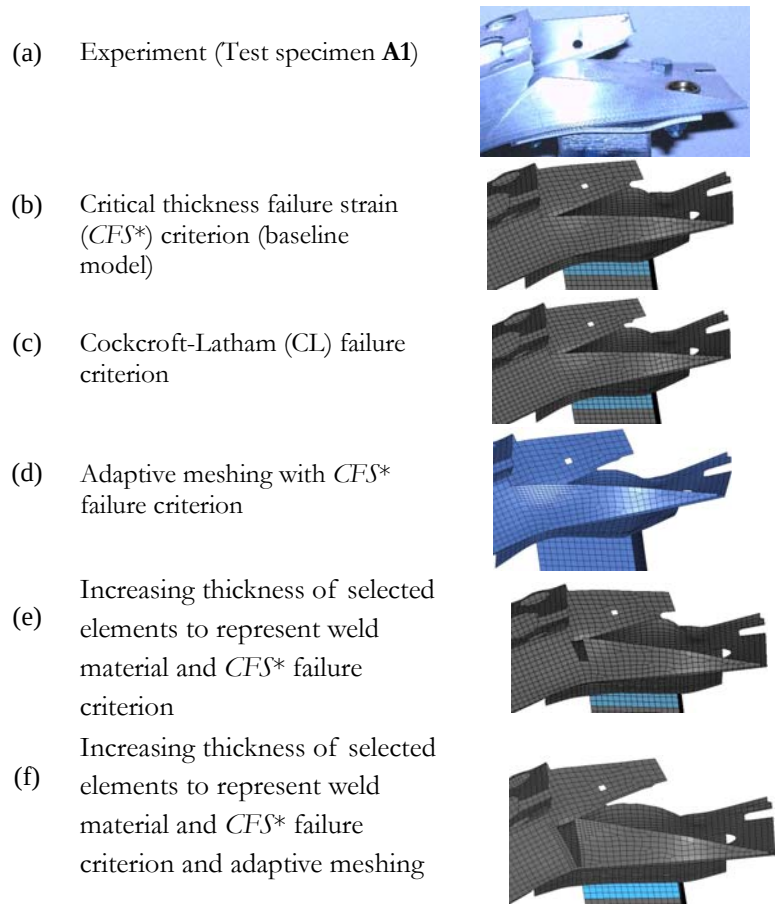

Figure 8-17 Comparison of fracture at the non-impacted end of the bumper beam, experiment vs. numerical simulations.

The force-deformation and mean force-deformation plots are compared with the baseline model in Figure 8-18. Up to the formation of the first two lobes in the impacted longitudinal, the adaptive meshing had no influence. The curves with and without adaptive meshing started to deviate at a deformation of 150 mm. The system without adaptive meshing had a higher peak force, which was almost the same height as the initial peak force. Whereas the system with adaptive meshing the force level was lower than the initial peak. This is due to the erosion of the elements at the intersection of the lower flange and the web. Simultaneously, re-meshing took place near the cut-out region of the bumper beam. From the force-deformation plots, Figure 8-18(a), one can see that the lobes developed in the impacted longitudinal was progressive with increased permanent deformation, see Figure 8-19. The mean force of the system decreased considerably, Figure 8-18(b), compared to the baseline model and the system without adaptive meshing. The deformation mode of the impacted longitudinal has changed from mixed mode to progressive folding mode with the application of adaptive meshing, when modelling them as close as possible to the reality, i.e. increasing the thickness of the selected rows of elements in the HAZ to represent the fillet material addition due to welding.

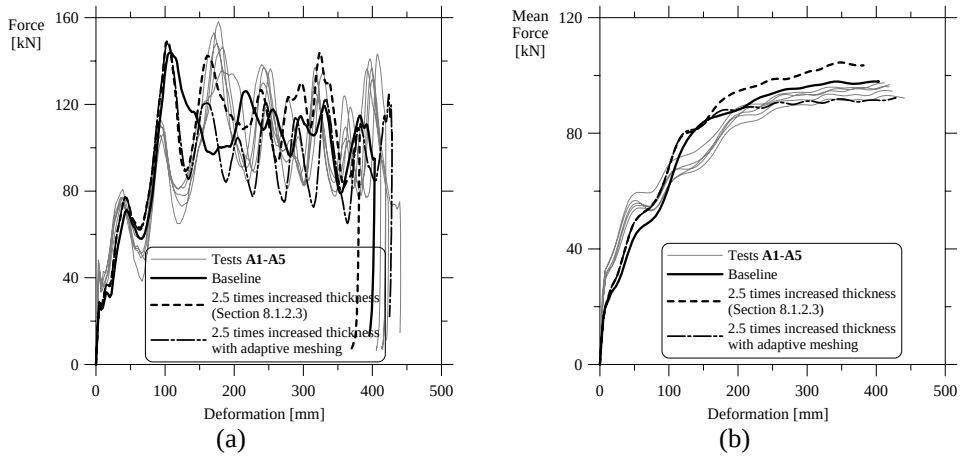

Figure 8-18 Influence of increasing the thickness of selected elements to represent weld material addition and also use of adaptive meshing (a) force-deformation and (b) mean force-deformation.

The use (or application) of adaptive meshing shows that the element size should be in the order of the thickness of the elements to predict the fracture at least in the critical areas.

8.2 Test series C

For test series **C** the predicted deformation mode of the system was close to that observed in the tests, but the mean force level was underestimated compared to the tests, see Section 7.6. Thus, the only sensitivity study performed on test series **C** was the influence of strain-rate effects. As in the previous section, here also the response predicted by MAT-41(*CFS**) is chosen as the "baseline" model.

In the baseline model the material (longitudinal AA6060-T1) is assumed to be strain-rate insensitive and no strain-rate data was available since no experiments were performed on this alloy. However, Enjalbert (2003) performed material tests on AA6060-T6 and has shown that it has a small strain-rate sensitivity. Even though it is small it may have an influence on the mean force level. Enjalbert (2003) performed tensile tests on specimens

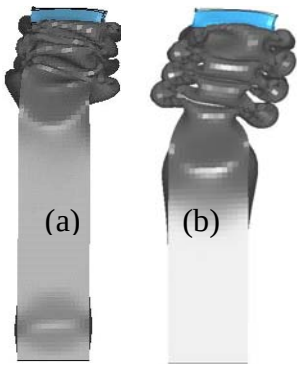

Figure 8-19 Permanent deformation shapes of the impacted longitudinal when increasing the thickness of selected elements to represent weld material addition (a) without and (b) with adaptive meshing of the bumper beam.

cut from aluminium alloy 6060-T6 tube with 4.5 mm wall thickness in a hydraulic testing machine and in a "Split Hopkinson Tension Bar" similar to the programme reported in Section 3.2.1. Figure 8-20 shows the reported strain-rate sensitivity at different levels of plastic strain.

As can be seen there is small positive strain-rate sensitivity for AA6060-T6. To take strain-rate effects into account, Equation (2.27) was used. The parameters are listed in Table 8-1.

The response of test series **C** when considering the strain-rate sensitivity parameters for temper T6, is plotted together with the baseline model in Figure 8-21. From the force-deformation and mean force-deformation plots in Figure 8-21(a) and (b), respectively, it is clear that there is some influence of strain-rate on the behaviour of the system. The mean-force level is increased with the inclusion of rate effects, and matches exactly with the tests at the final deformation.

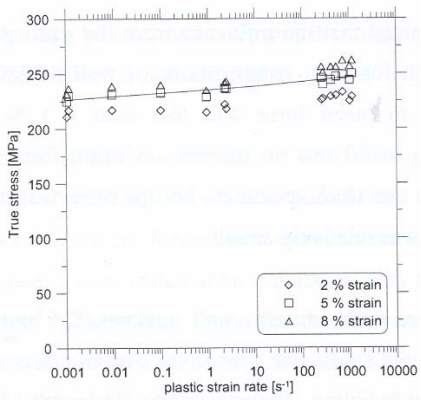

Figure 8-20 Strain-rate sensitivity in AA6060-T6 (Enjalbert, 2003).

Table 8-1 Strain-rate parameters for AA6060-T6.

Alloy - Temper	$\dot{\varepsilon}_0$ [s^{-1}]	C [-]
AA6060-T6	1.0	0.001

8.3 Test series D

Test series **D** is similar to test series **A**, but with increased impact velocity. The sensitivity studies are performed because in Section 7.7.1 the numerical simulations predicted much higher peaks in the force-deformation characteristics, and thus the mean force level deviated significantly from the tests, see Figure 7-18. The main aim for the sensitivity studies in this section is to improve the mean force level with reduced peaks in the force-deformation characteristics. Thus the test series **D** sensitivity studies were related to physical parameters only. One of these was to check the influence of not modelling the HAZ (i.e. without the HAZ), while the other was to increase the modelled HAZ length (20 mm) to the natural buckling length (95 mm), as in Section 8.1.2. To perform the sensitivity studies, the model in Section 7.7 was chosen as the "baseline" model.

8.3.1 Without the HAZ

The predicted behaviour of the system when the HAZ was not modelled is

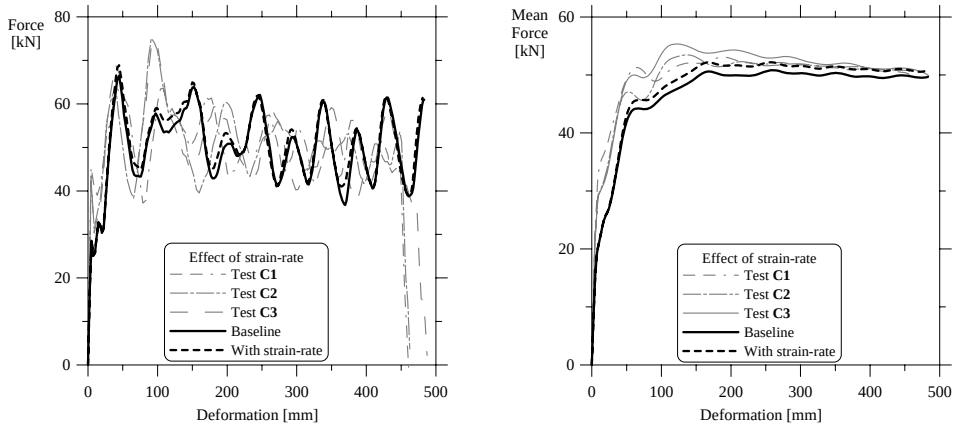

Figure 8-21 Strain-rate effects on the response of test series **C** (a) force-deformation and (b) mean force-deformation.

shown in Figure 8-22 together with the tests and the baseline model. The peak force remained the same as in baseline model for the present system. Whereas the peak force level increased slightly when the HAZ was removed from the model for series **A**. This can be due to the different impact velocities in test series **A** and **D**. The predicted deformation modes without modelling the HAZ in test series **D** and **A** followed the same course. The mean force of the system decreased compared to the baseline model and is close to the tests, Figure 8-22(b).

The final deformed shapes of the bumper beam-longitudinal systems with and without the HAZ are shown in Figure 8-23(a) and (b) respectively. As with the series **A** one can observe that the deformed end of the impacted longitudinal has some rotational effects compared to the baseline model.

8.3.2 Increasing the HAZ length

In the previous section it was observed that the mean force of the system decreased when the HAZ was not modelled. However, the mean force-deformation curve in Figure 8-22(b) deviated much in the first part of the

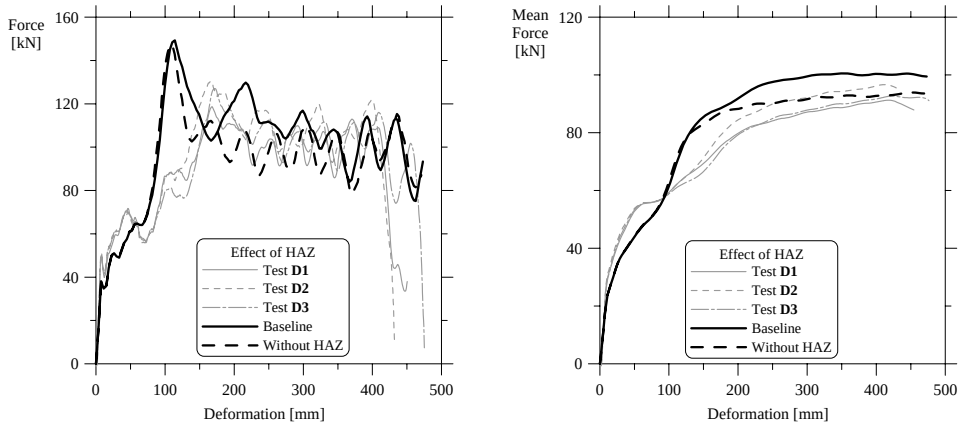

Figure 8-22 Influence of HAZ on the crash behaviour of test series **D**, (a) force-deformation and (b) mean force-deformation.

impact due to the higher force level before it reached a value close to the tests. The peak force level that occurred in the force-deformation characteristics is the cause for the above deviation. With an intention to reduce the initial peak force level, simulations were performed with an increased HAZ length, 95 mm, which corresponds to the elastic buckling length of the longitudinal. The predicted response of the bumper beam-longitudinal system with 95 mm HAZ length in the impacted longitudinal only is compared with the baseline model and the tests in Figure 8-24. As can be seen from the force-deformation characteristics in Figure 8-24(a), the peak force level is decreased considerably when the HAZ length was modelled as 95 mm instead of 20 mm. This peak force level is almost equal to that obtained in the tests. The early occurrence of the peak was, however, not avoided. The mean force-deformation curves in Figure 8-24(b), shows that the predicted mean force level by the 95 mm HAZ value coincides with

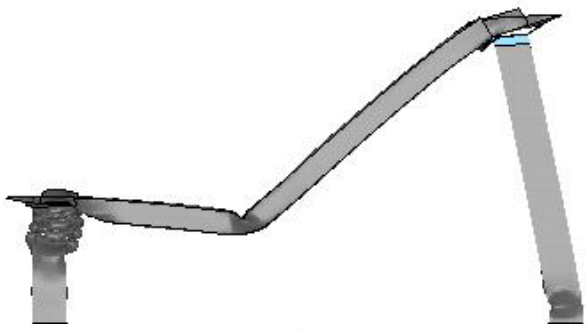

(a)

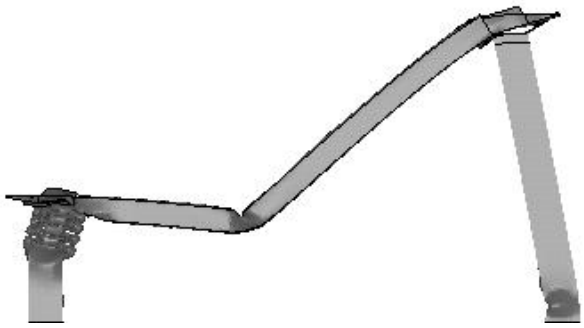

(b)

Figure 8-23 Final deformation shapes of test series **D** from the simulations (a) with HAZ (baseline model) and (b) without HAZ.

the experimental curves, except for some deviations in the first part of the impact.

The permanent deformation shapes of the bumper beam-longitudinal system with 20 mm HAZ and 95 mm HAZ are shown in Figure 8-25(a) and (b) respectively. From Figure 8-25(b) one can see that the deformed end of the impacted longitudinal has more rotation compared to the baseline model.

To conclude, for accurate prediction of test series **D** behaviour it is preferable to model the HAZ length equal to 95 mm, i.e. the elastic local buckling length, instead of 20 mm.

8.4 Summary of sensitivity studies

Table 8-2 gives the relative CPU cost for the different sensitivity parameters investigated in this study. Studying the CPU cost directly may be misguiding as it is very dependent on the number of cycles needed in the simulation. The number of cycles in one simulation may be significantly

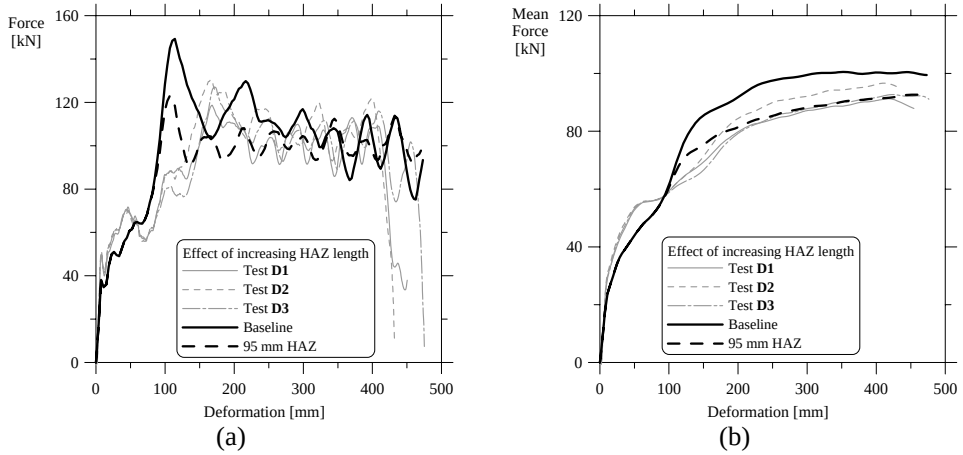

Figure 8-24 Influence of increasing the HAZ length from 20 mm to elastic local buckling length of 95 mm on the crash behaviour of test series **D**, (a) force-deformation and (b) mean force-deformation.

increased if one element experiences a large decrease in size. Thus the relative CPU cost per cycle for the investigated parameter and the baseline model is presented.

As seen, the use of element type 16 leads to a significant increase in the relative CPU cost. The next significant parameter is the adaptive meshing. When using adaptive meshing the relative CPU cost increases almost with a factor twice of the baseline model. On the other hand, decreasing the mesh size only in the impacted longitudinal, increases the relative CPU cost by 50%. For all other parameters the increase in relative CPU cost is 5% or less.

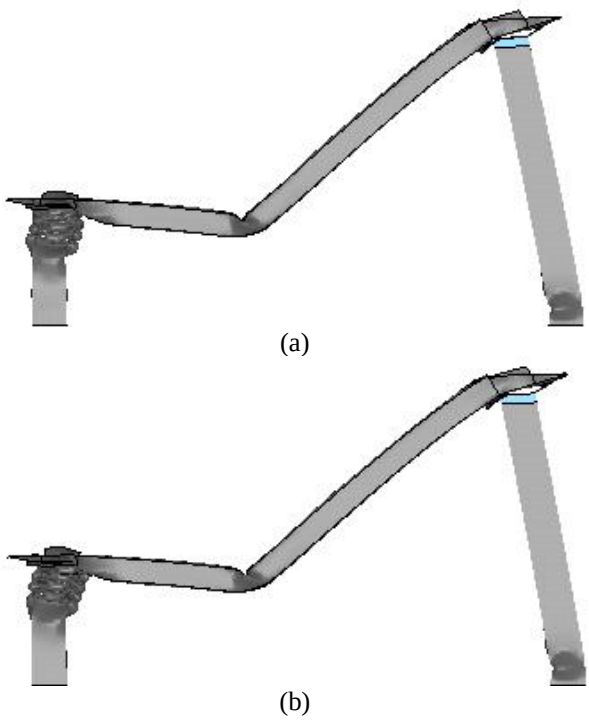

(a)

(b)

Figure 8-25 Final deformation shapes of test series **D** from the simulations (a) with 20 mm HAZ (baseline model) and (b) with 95 mm HAZ.

8.5 Process effects on material level

The simulations results presented in Chapter 7 and in the previous sections are based on a geometry of the bumper beam that is generated from forming simulations, see Chapter 6. Thus, in the bumper beam model the thickness changes from the forming process has been taken into consideration, while the process effects on the material have not been included. In conjunction with damage models and failure prognosis, and for the accurate prediction of instability and failure, the consideration of forming history is crucial for crash relevant parts that have been subjected to high strains during forming (Wang and Holzner, 2002). As mentioned earlier, the process effects on the material are not routinely included in industrial product development. The primary focus of the present section was on whether the observed material effect in Section 3.5, could result in any further improvement in the predicted behaviour of the bumper beam-longitudinal system.

Table 8-2 Relative CPU cost.

	Test series **A**	Test series **B**	Test series **C**	Test series **D**
Strain-rate	1.09	-	1.12	-
Without the HAZ	1.01	-	-	1.01
Increasing the HAZ length	0.99	-	-	1.02
Increasing thickness of selected row of elements	0.99	-	-	-
Increasing thickness of selected row of elements with adaptivity	1.95	-	-	-
Cockcroft-Latham fracture criterion	0.99	-	-	-
Self contact	0.99	-	-	-
Element type 16	2.45	-	-	-
Element type 1	1.05	-	-	-
Through-thickness integration points 7	1.01	-	-	-
Through-thickness integration points 9	0.99	-	-	-
Mesh size	1.45	-	-	-
Adaptive meshing	1.93	-	-	-

As previously mentioned, anisotropy development due to pre-stretching is not included in the model. The process effect is considered being an isotropic phenomenon related to increased precipitation speed within the denser dislocation forests arising whenever the material has been plastically pre-deformed. Thus, within the model the process effect in the crash analysis has been linked to the scalar effective plastic strain resulting from a forming analysis, i.e. pre-deformation (Lademo et al., 2005).

The simulations when considering the process effects on the material level for the bumper beam were performed using both 1- and 12- hour batch data, (Section 3.5), for test series **A**. In order to compare the predicted behaviour of the bumper beam-longitudinal system the baseline model defined in Section 8.1 was used.

Figure 8-26 shows the predicted behaviour of the bumper beam-longitudinal system with and without the process effects on the material level. As can be seen from Figure 8-26(a), there is no difference between the analysis results with and without process effects. If there was any effect of process

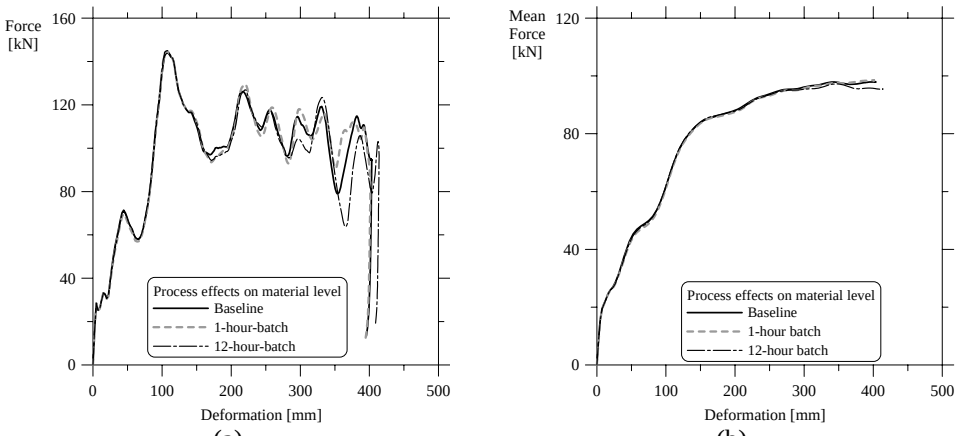

Figure 8-26 Influence of process effects on the crash performance of test series **A**, (a) force-deformation and (b) mean force-deformation.

parameters then these effects should appear in the initial stage, related to crushing of the bumper beam (process effects are considered only for the bumper beam). Further, the mean force-deformation curves (Figure 8-26(b)), as well as the deformation modes in the longitudinal, Figure 8-27 are the same in simulations with and without process effects.

From the simulations it can be concluded that the consideration of process effects on material level for such complex system has no significant influence. Further, assuming that the numerical model has sufficient predictive capability it is noted that the test series **A** is robust, since variations in material parameters do not noteworthy influence the system performance.

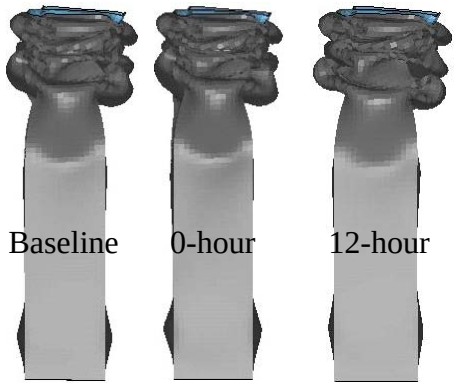

Figure 8-27 Deformation modes of impacted longitudinal with and without process effects on the material level in the bumper beam, test series **A** simulations.

Chapter 9 Conclusions and Recommendations

The objectives of this study were to increase the physical understanding of the different phenomena taking place during the offset impact of an automotive bumper beam-longitudinal system as well as to validate a modelling procedure for the system's crash performance. The objective was achieved through material tests, full-scale system tests and non-linear FE-analyses.

The work included an experimental and a numerical study of a bumper beam-longitudinal system at 40% offset impact, where longitudinals of two different alloys (AA7003 and AA6060) and two temper conditions (T79 and T1) were varied along with two impact velocities of 10 m/s and 15 m/s. The longitudinals in AA7003-T79, AA7003-T1 and AA6060-T1 were selected, whereas the bumper beam chosen was in AA7108-T6. The effect of material and temper condition on the energy absorbing characteristics of the bumper beam-longitudinal system was studied. Further, the influence of yield criterion and the process effects on the crash performance of the bumper beam-longitudinal system was studied using the non-linear FE-code LS-DYNA.

9.1 Conclusions

The following conclusions can be drawn from the present work:

Results from the material tests in Chapter 3 indicated that:

- The bumper beam material AA7108 has significant anisotropy in strength, plastic flow and ductility in both tempers (W and T6).

- The AA7003 material shows less anisotropy in strength and plastic flow compared to AA7108, but shows large anisotropy with respect to the ductility.
- Considerable anisotropy in ductility has been observed for the AA6060-T1 material, without much difference in the strength levels.
- The strain-rate affects the materials' flow stress significantly for AA7108-T6 and AA7003-T79. The increase in material strength in the strain-rate range 10^{-4} s^{-1} - 10^{3} s^{-1} is 15% for AA7108-T6 and 25% for AA7003-T79.
- There is a well-defined effect of the amount of pre-stretching in W-temper on the properties of the AA7108 bumper beam material. The strength and specimen elongation decrease for increasing pre-strain. Further, an increased tendency of a "quasi-brittle" through-thickness shear failure i.e. a reduced material/local ductility was observed as a function of the pre-strain.

Experimental work on the bumper beam-longitudinal systems showed that:

- The robustness of the system was very dependent on the yield strength and temper condition of the longitudinals used.
- Test series **A** revealed that the total impact energy was effectively utilised in deforming the system without the activation of the reaction wall crashboxes. The five parallel experiments of test series **A** showed robust performance with similar force-deformation characteristics.
- A non-robust response was observed for test series **B**, i.e. different collapse modes were found in parallel tests with similar longitudinals under similar impact test conditions. The longitudinal members had a tendency to develop lobes randomly

along the length, since the material had higher strain-hardening properties.

- The bumper beam's cross-section did not collapse completely in test series **C**. In the three parallel tests the same deformation mode was observed and the fracture observed was much less compared to other test series.
- Test series **D** were equal to series **A** except for an increased impact velocity. These systems showed highly repetitive and robust performance. The specimens further experienced less material failure compared to test series **A**.
- For the same amount of deformation, test series **A** and **D** absorbed almost the same amount of energy, which was higher than the one for test series **B** and **C**.

Results from the numerical simulations indicated that:

- The user-defined material model was capable of representing the material behaviour accurately with respect to strength, strain-hardening and strain-rate sensitivity.
- Tensile test simulations in 45°- and 90°-direction were not performed. However, for the 0°-direction explicit simulation of the tensile specimen failed to predict the material ductility correctly for the bumper beam material. The implicit analysis predicted a ductility that was close to the tests.
- The force- and mean force- deformation characteristics predicted by the user-defined material model with the critical thickness strain fracture criterion were close to the experiments for test series **A**. However, the folding mode in the impacted longitudinal deviated from the experiments.
- For test series **B** the simulations failed to predict the deformation and fracture modes that were observed in the experiments.

- Though the predicted deformation mode in the impacted longitudinal was similar to that observed in the experiments of test series **C**, the numerical model underestimated the mean force level. Inclusion of strain-rate sensitivity led to accurate predictions.
- For the increased impact velocity in test series **D** the simulations predicted much higher peaks in the force-deformation characteristics compared to the experiments and thus over-estimated the mean force.
- Sensitivity studies revealed that (when the fillet material was modelled) the propagating tearing and the through-thickness shear cracks at the cut-out region of the non-impacted end of the bumper beam was predicted using the adaptive meshing technique.
- Consideration of the process effects on strength and strain-hardening did not show any significant influence on the predicted behaviour of the bumper beam-longitudinal system. The process effects with respect to the reduced material ductility (i.e. the increased tendency of "shear fracture") was not investigated.
- The simulations failed to predict the bending failure in the bumper beam.

9.2 Recommendations for further work

Based on the present work the following subjects need further investigation:

- The non-robust behaviour observed in test series **B** should be studied more closely.
- In the numerical simulations, when modelling the HAZ for test series **C**, the stability of the system was lost. On the other hand, the system without the HAZ predicted a more dominant buckle on

the non-impacted longitudinal. The factors influencing this should be explored.

- Effect of modelling the initial imperfections on the buckling mode of the longitudinals should be studied.
- In order to capture the bending failure in the bumper beam the process effects on the material level that are linked to the reduced ductility should be investigated.
- A more refined fracture criterion may be required in order to predict the failure zones accurately in the bumper beam.

References

Abramowicz W., (2003). *Thin-walled structures as impact energy absorbers*. Thin-walled Structures 41,91-107.

Achani D., Hopperstad O.S. and Lademo O.-G., (2005). *Assessement of anisotropic yield criteria for extruded aluminium alloys: experimental and numerical study*. International Journal of Plasticity (Submitted).

Alghamdi A.A.A., (2001). *Collapsible impact energy absorbers: an overview*. Thin-walled Structures 39(2), 189-213.

Aretz H., (2004). *Applications of a new plane stress yield function to orthotropic steel and aluminium sheet metals*. Modelling and Simulation in Materials Science and Engineering 12,491-509.

Barata da Rocha A., Barlat F. and Jalinier J.M., (1984). *Predicition of the forming limit diagrams of anisotropic sheets in linear and non-linear loading*. Materials Science and Engineering 68,151-164.

Barlat F., (1987). *Crystallographic texture, anisotropic yield surfaces and forming limits of sheet metals*. Materials Science and Engineering 91,55-72.

Barlat F., Becker R.C., Hayashida Y., Maeda Y., Yanagawa M., Chung K., Brem J.C., Lege D.J., Matsui K., Murtha S.J. and Hattori S., (1997a). *Yielding description for solution strengthened aluminum alloys*. International Journal of Plasticity 13(4), 385-401.

Barlat F., Brem J.C., Yoon J.W., Chung K., Dick R.E., Lege D.J., Pourboghrat F., Choi S.-H. and Chu E., (2003). *Plane stress yield function for aluminum alloy sheets-Part 1: theory*. International Journal of Plasticity 19,1297-1319.

Barlat F., Maeda Y., Chung K., Yanagawa M., Brem J.C., Hayashida Y., Lege D.J., Matsui K., Murtha S.J., Hattori S., Becker R.C. and

Makosey S., (1997b). *Yield function development for aluminum alloy sheets*. Journal of the Mechanics and Physics of Solids 45(11-12), 1727-1763.

Belytschko T., Liu W.K. and Moran B. (2000). *Nonlinear Finite Elements for Continua and Structures*. John Wiley & Sons Ltd., West Sussex. ISBN 0-471-98774-3.

Berstad T., Lademo O.-G., Pedersen K.O. and Hopperstad O.S. (2004). *Formability modeling with LS-DYNA*. In: 8th LS-DYNA International Users Conference. Detroit.

Bjørneklett B.I. and Myhr O.R. (2003). *Material design and thermally induced triggers in crash management*. International Body Engineering Conference. Tokyo.

Bottcher C.-S. and Frik S. (2003). *Consideration of manufacturing effects to improve crash simulation accuracy*. In: 4th European LS-DYNA Users Conference. Ulm.

Bressan J.D. and Williams J.A., (1983). *The use of a shear instability criterion to predict local necking in sheet metal deformation.* International Journal of Mechanical Sciences 25(3), 155-168.

Bridgman P.W. (1952). *Studies in Large Plastic Flow and Fracture with Special Emphasis on the Effects of Hydrostatic Pressure*. McGraw-Hill, New York.

Cafolla J., Hall R.W., Norman D.P. and McGregor I.J. (2003). *"Forming to crash" simulation in full vehicle models.* In: 4th European LS-DYNA Users Conference. Ulm.

Clausen A.H. and Auestad T. (2002). Technical report R-16-02. Department of Structural Engineering, Norwegian University of Science and Technology, Trondheim.

Clausen A.H., Hopperstad O.S. and Langseth M., (2000). *Stretch bending of aluminium extusion for car bumpers*. Journal of Materials Processing Technology 102,241-248.

Cockcroft M.G. and Latham D.J., (1968). *Ductility and workability of metals*. Journal of the Institute of Metals 96,33-39.

Dagson N. (2001). *Influence of the forming process on the crash response of a roof fail component*. Master Thesis, Department of Solid Mechanics, Linköping University, Linköping.

Dieter G.E. (1988). *Mechanical Metallurgy*. McGraw-Hill, Singapore.

Dutton T., Iregbu S., Sturt R., Kellicut A., Cowell B. and Kavikondala K., (1999). *The effect of forming on the crashworthiness of vehicles with hydroformed frame siderails*. SAE Paper No 1999-01-3208,3354-3360.

Dutton T., Richardson P., Knight A. and Sturt R. (2001). *The inlfuence of residual effects of stamping on crash results*. In: 3rd European LS-DYNA Users Conference. Paris.

Enjalbert P. (2003). *Strain-rate sensitivity of aluminium alloy AA6060-T6*. MSc Thesis. Department of Structural Engineering, Norwegian University of Science and Technology, Trondheim.

Euro NCAP., (2002). *Available from internet*. http://www.euroncap.com/

Frank T. and Gruber K., (1992). *Numerical simulation of frontal impact and offset collisions*. CRAY Channels, Cray Research Inc,2-6.

Hähner P. and Rizzi E., (2003). *On the kinematics of Portevin-Le Chatelier bands: theoretical and numerical modelling*. Acta Materialia 51(12), 3385-3397.

Hallquist J.O. (1998). *LS-DYNA Theoretical Manual*. Livermore Software Technology Corporation, California.

Hallquist J.O. (2003). *LS-DYNA Keyword User's Manual v 970*. Livermore Software Technology Corporation, California.

Hanssen A.G., Auestad T., Langseth M. and Tryland T., (2005). *A note on development of a 3-component load cell for structural impact testing*.

International Journal of Mechanics and Materials in Design (Accepted for publication).

Hanssen A.G., Auestad T., Tryland T. and Langseth M., (2003a). *The kicking machine: A device for impact testing of structural components*. International Journal of Crashworthiness 8(4), 1-8.

Hanssen A.G., Porcaro R., Aalberg A. and Langseth M. (2003b). *Identification of modeling of self-pierce rivet failure for crash analyses*. In: Assemblages: des Matèriaux à la Structure. Edited by Aubin, Degallaix, Desplanques and Tanghe, Presented at the Colloque Nationale MECAMAT, 20-24 January, Aussios.

Hill R. (1950). *The Mathematical Theory of Plasticity*. Clarendon Press, Oxford.

Hooputra H., Gese H., Dell H. and Werner H., (2004). *A comprehensive failure model for crashworthiness simulation of aluminium extrusions*. International Journal of Crashworthiness 9(5), 449-463.

Hopperstad O.S., Berstad T., Ilstad H., Lademo O.-G. and Langseth M. (1998). *Effects of the yield criterion on local deformations in numerical simulation of profile forming*. In: Metal Forming 98. Birmingham.

Hosford W.F. and Caddel R.M. (1993). *Metal Forming: Mechanics and Metallurgy*. PRT Prentice Hall. ISBN 0-13-588526-4.

Jensen Ø. (2005). *Behaviour of aluminium extrusion subjected to axial loading*. Dr.ing. Thesis, Department of Structual Engineering, Norwegian University of Science and Technology, Trondheim. ISBN 82-471-6872-3.

Johnson W. and Reid S.R., (1978). *Metallic energy dissipating systems*. Applied Mechanics Reviews 31(3), 277-288.

Johnson W. and Reid S.R., (1986). *Update to "Metallic energy dissipating systems" [AMR 31 (1978):277-288]*. Applied Mechanics Update 315-319,

Johnson W. and Walton A.C., (1983). *An experimental investigation of the energy dissipation of a number of car bumpers under quasi-static lateral loads*. International Journal of Impact Engineering 1(3), 301-308.

Jones N. (1997). *Structural Impact*. Cambridge University Press, Cambridge, Paperback edition. ISBN 0-521-62890-3.

Jones N., (2003). *Several phenomena in structural impact and structural crashworthiness*. European Journal of Mechanics A/Solids 22,693-707.

Khan A.S. and Huang S. (1995). *Continuum Theory of Plasticity*. John Wiley & Sons, Inc., New York.

Kim H., Hong S., Hong S. and Huh H. (2003). *The evaluation of crashworthiness of vehicles with forming effect*. In: 4th European LS-DYNA Users Conference. Ulm.

Kim K.P. and Huh H., (2003). *Collpase analysis of auto-body structures considering the effect of fabrication*. Key Engineering Materials 233-236,737-742.

Kokkula S., Hopperstad O.S., Langseth M. and Lademo O.-G. (2003). *Explicit and implicit analysis of beams subjected to impact loading with axial restraints*. In: Proceedings of the 16th Nordic Seminar on Computational Mechanics in combination with the Pål Bergan Anniversary Seminar. Edited by Mathisen, Kvamsdal and Okstad, Tapir Uttrykk, Trondheim.

Kokkula S., Langseth M., Hopperstad O.S. and Lademo O.-G. (2005). *Behaviour of an automotive bumper beam-longitudinal system at 40% offset impact: An experimental and numerical study*. In: Proceedings of the International Conference on Impact Loading of Lightweight Structures. Edited by Alves and Jones, WIT press, Southampton.

Lademo O.-G. (1999). *Engineering models of elastoplasticity and fracture for aluminium alloys*. Dr.ing. Thesis, Department of Structual

Engineering, Norwegian University of Science and Technology, Trondheim. ISBN 82-471-0367-2.

Lademo O.-G., Berstad T., Eriksson M., Tryland T., Furu T., Hopperstad O.S. and Langseth M., (2005). *A model for process-based crash simulation*. Submitted for journal publication.

Lademo O.-G., Berstad T., Hopperstad O.S. and Pedersen K.O. (2004a). *A numerical tool for formability analysis of aluminium alloys. Part I: Theory*. In: Proceedings of the 10th International Conference on Metal Forming. Edited by Kusiak, Hartley, Majta, Pillinger and Pietrzyk, Steel Grips, Suppl Metal Forming 2004, Kraków.

Lademo O.-G., Berstad T., Tryland T., Furu T., Hopperstad O.S. and Langseth M. (2004c). *A model for process-based crash simulation*. In: 8th LS-DYNA International Users Conference. Detroit.

Lademo O.-G., Hopperstad O.S. and Langseth M., (1999). *An evaluation of yield criteria and flow rules for aluminium alloys*. International Journal of Plasticity 15,191-208.

Lademo O.-G., Hopperstad O.S., Malo K.A. and Pedersen K.O., (2002). *Modelling of plastic anisotropy in heat-treated aluminium extrusions*. Journal of Materials Processing Technology 125-126,84-88.

Lademo O.-G., Pedersen K.O., Berstad T. and Hopperstad O.S. (2004b). *A numerical tool for formability analysis of aluminium alloys. Part II: Experimental validation*. In: Proceedings of the 10th International Conference on Metal Forming. Edited by Kusiak, Hartley, Majta, Pillinger and Pietrzyk, Steel Grips, Suppl Metal Forming 2004, Kraków.

Lee S.-H., Han C.-S., Oh S.-I. and Wriggers P., (2001). *Comparative crash simulations incorporating the results of sheet forming analyses*. Engineering Computations 18(5-6), 744-758.

Lemaitre J. and Chaboche J.-L. (1990). *Mechanics of Solid Materials*. Cambridge University Press.

Marciniak Z., Duncan J.L. and Hu S.J. (2002). *Mechanics of Sheet Metal Forming*. Butterworth-Heinemann, Oxford. ISBN 0-7506-5300-0.

Marciniak Z. and Kuczynski K., (1967). *Limit strains in the processes of stretch-forming sheet metal*. International Journal of Mechanical Sciences 9,609-620.

Mercer C.D., Nagtegaal J.D. and Rebolo N. (1995). *Effective application of different solvers to forming simulations,*. In: Proceedings of the Simulation of Materials Processing: Theory, Methods and Applications. Edited by Shen and Dawson, Balkema.

Phantom C., (2004). *Available from Internet:*. http://www.visiblesolutions.com/ cited 2004-10-30,

Photron C., (2005). *Available from internet*. http://www.photron.com/ cited 2005-04-05,

Portevin A. and Le Chatelier F., (1923). *Sur un phénomène observé lors de l'essai de traction d'alliages en cours de transformation*. Comptes Rendus de l'Academie des Sciences 176,507-510.

prEN 1999-1-1. (2004). *Eurocode 9: Design of aluminium structures. Part 1.1: General structural rules*. CEN, rue de Stassart 36,, Brussels.

Pugsley A. and Macaulay M.A., (1978). *Cars in collision-safe structures*. New Scientist 78(596-598),

Reid J.D., (1996). *Crashworthiness of automotive steel midrails: Thicknes and material sensitivity*. Thin-walled Structures 26(2), 83-103.

Reid S.R., (1993). *Plastic deformation mechanisms in axially compressed metal tubes used as impact energy absorbers*. International Journal of Mechanical Sciences 35(12), 1035-1052.

Reyes A., Hopperstad O.S., Hanssen A.G. and Langseth M., (2004). *Modeling of material failure in foam-based components*. International Journal of Impact Engineering 30(7), 805-834.

Reyes A., Hopperstad O.S., Lademo O.-G. and Langseth M. (2005). *Characterization of materials*. Project report MODIF, Department of Structural Engineering, Norwegian University of Science and Technology, Trondheim.

Robinson G.M., (1997). *Finite element modeling of load cell hysteresis*. Measurement 20(2), 103-107.

Sharp M.L., Jombock J.R. and Shabel B.S., (1978). *Structural performace of aluminium bumpers*. SAE Paper No 780140,569-575.

Shen Y.Z., Oh K.H. and Lee D.N., (2004). *The effect of texture on the Portevin-Le Chatelier effect in 2090 Al-Li alloy*. Scripta Materialia 5(4), 285-289.

Shieh R.C. (1975). *Strain rate sensitivity effects on crash response and dynamic yield moment formulas for crash prediction of automobile bumpers*. In: Proceedings of 16th Structures Structural Dynamic and Material Conference. American Institute of Aeronautics and Astronautics.

Sowerby R. and Duncan J.L., (1971). *Failure in sheet metal in biaxial tension*. International Journal of Mechanical Sciences 13,217-229.

Tang S.C., (1979). *Computer modeling of bumper impact resistance*. SAE Paper No 790991,3309-3319.

TrueGrid® Manual (2001). *Version 2.1.0*. XYZ Scientific Applications, Inc.

Tvergaard V., (1978). *Effect of kinematic hardening on loaclized necking in balanced biaxially stretched sheets*. International Journal of Mechanical Sciences 20,651-658.

Wang X. and Holzner M. (2002). *Strategic development of crash simulation*. In: 2nd Freiburg Workshop for Material and Structural Behaviour at Crash Process (CRASH-MAT 2002). Presentations Compact Disc, Freiburg.

Welo T. (1996). *Bending of aluminium extrusions for automotive applications: a commentary on practical and theoretical aspects*. In:

Proceedings of the 6th International Aluminium Extrusion Technology Seminar. Edited by Werner, Chicago.

Yeh J.R., Summe T.L. and Seksaria D.C. (1999). *The development of an aluminum failure model for crashworthiness design*. In: Crashworthiness, Occupant Protection and Biomechanics in Transportation Systems. Edited by Mahmood, Barbat and Baccouche, ASME, New York.

Appendix-A: Test series A

Test specimen **A2**

Table A-1 Description of impact events for test specimen **A2** see Figure A-1 and Figure A-2.

Time (ms)	Description
$t_1 = 0$	Impact of the bumper beam-longitudinal system started
$t_2 = 9$	The bumper beam cross-section collapsed completely before t_2 and at the same time buckling initiation in the impacted longitudinal started
$t_3 = 15$	A propagating tearing crack along the edge of upper flange and web of the bumper beam started before time t_3
$t_4 = 25$	Due to the straining caused by the bumper beam a local plastic hinge developed in the non-impacted longitudinal at time t_4
$t_5 = 38$	A through-thickness shear crack at the non-impacted end of the bumper beam developed at time t_5
$t_6 = 76$	At time t_6 the crashboxes on the reaction wall were almost activated

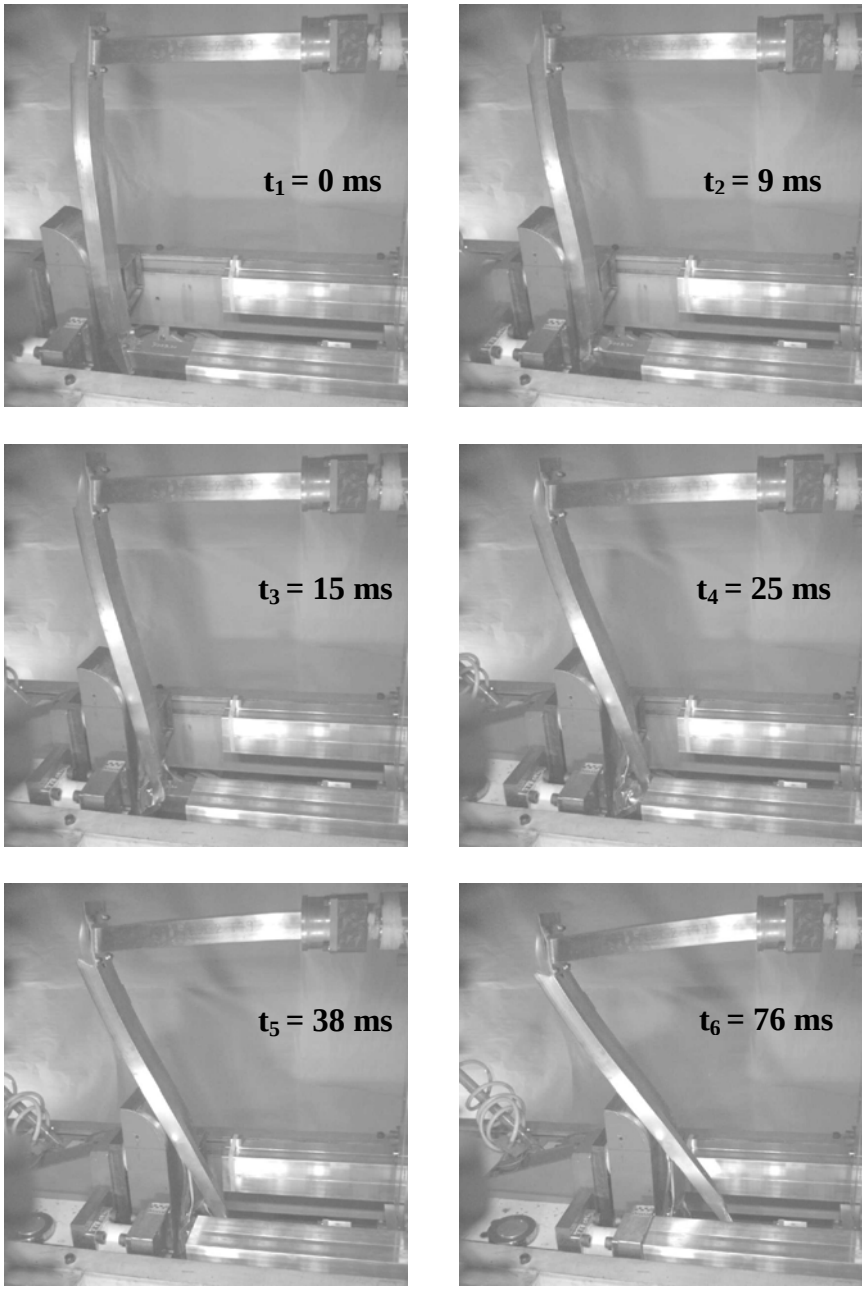

Figure A-1 Photos taken from high speed video recording for test specimen **A2**.

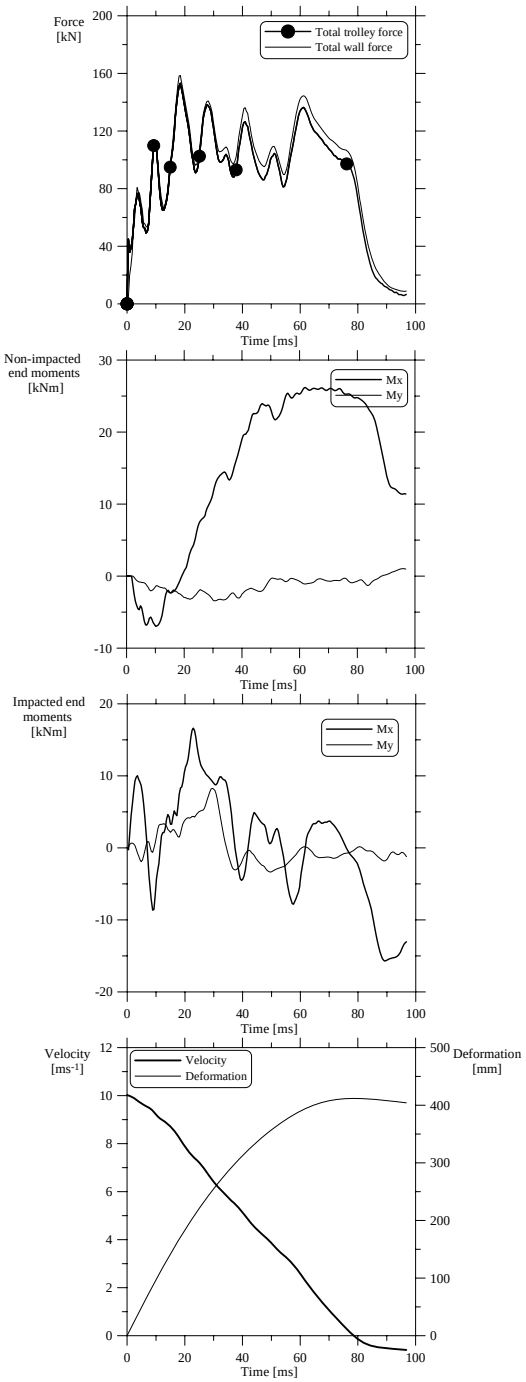

Figure A-2 Loadcell data for test specimen **A2**.

Test specimen **A3**

Table A-2 Description of impact events for test specimen **A3** see Figure A-3 and Figure A-4.

Time (ms)	Description
$t_1 = 0$	Impact of the bumper beam-longitudinal system started
$t_2 = 9$	The bumper beam cross-section has collapsed completely before t_2 and at the same time buckling initiation in the impacted longitudinal started
$t_3 = 20$	A plastic hinge in the mid-section of bumper beam developed at time t_3
$t_4 = 50$	Weld failure occurred between the interface plate and longitudinal on the non-impacted end at time t_4
$t_5 = 64$	Due to the straining caused by the bumper beam a local plastic hinge developed in the non-impacted longitudinal at time t_5 at its clamped end
$t_6 = 84$	At time t_6 the crashboxes on the reaction wall were almost activated

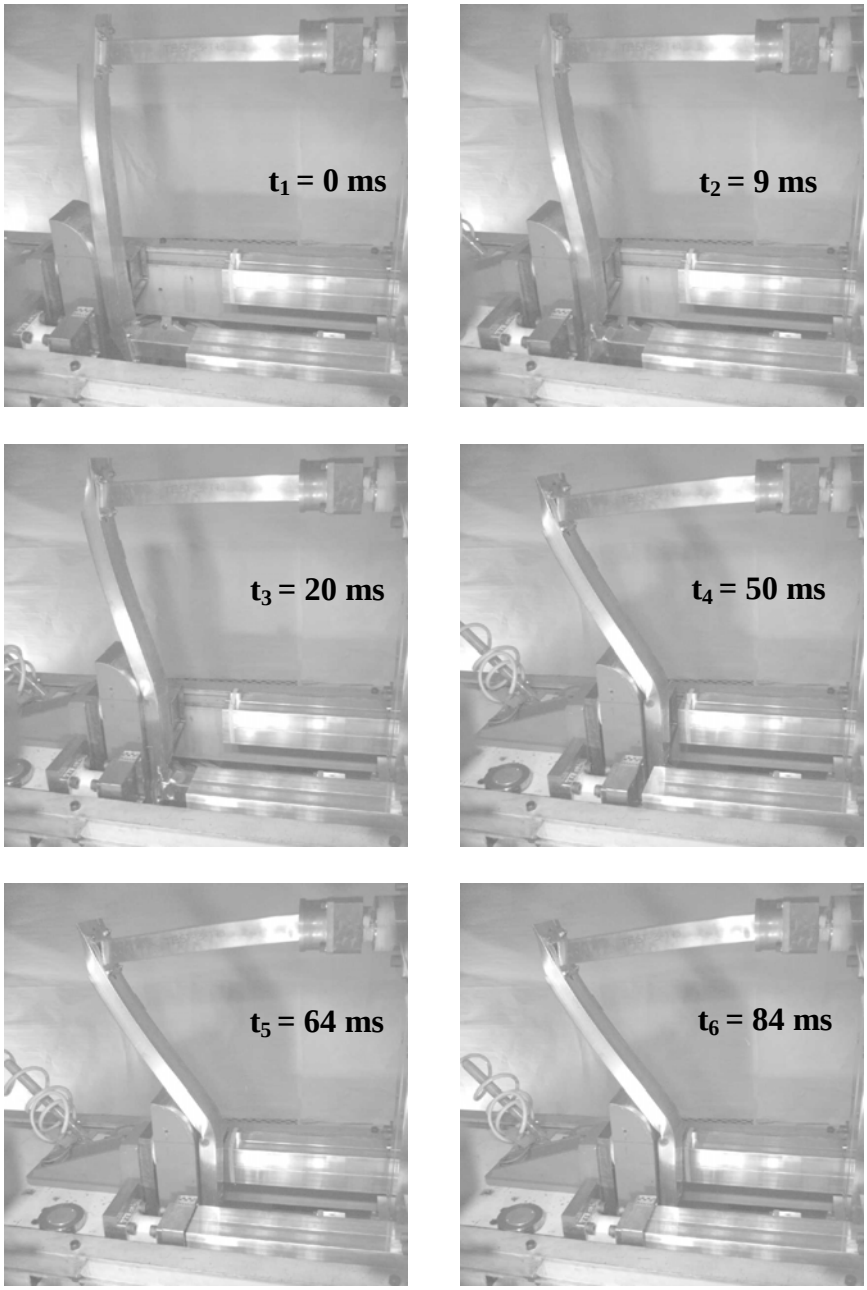

Figure A-3 Photos taken from high speed video recording for test specimen **A3**.

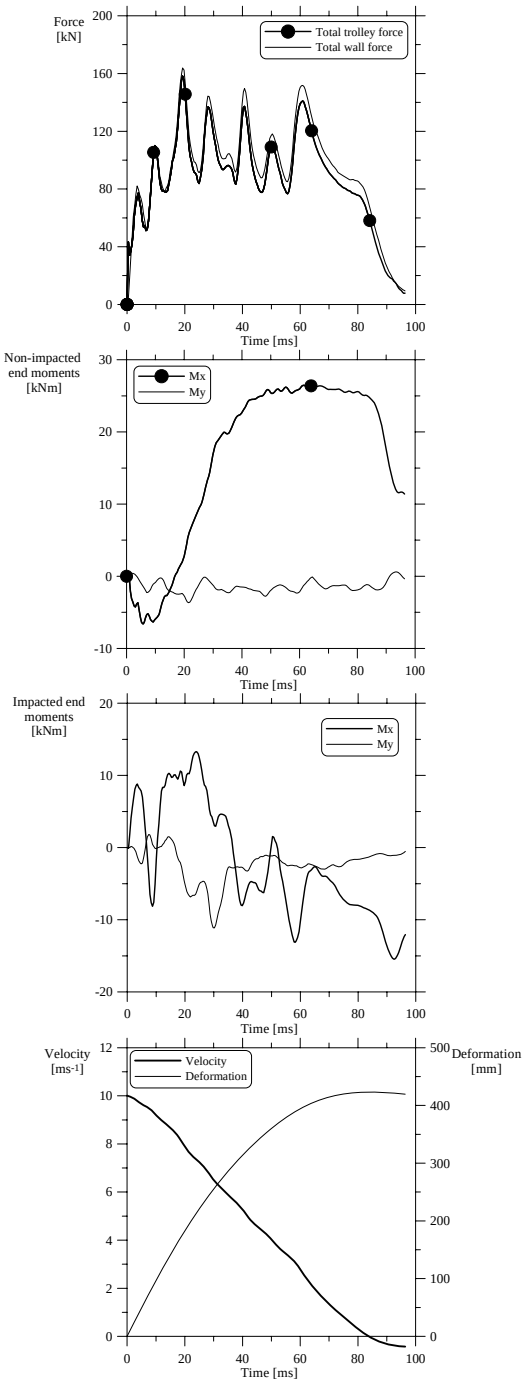

Figure A-4. Loadcell data for test specimen **A3**.

Test specimen **A4**

Table A-3 Description of impact events for test specimen **A4** see Figure A-5 and Figure A-6.

Time (ms)	Description
$t_1 = 0$	Impact of the bumper beam-longitudinal system started
$t_2 = 6$	A propagating tearing crack along the edge of upper flange and the web started at time t_2
$t_3 = 9$	At time t_3 buckling in the impacted longitudinal started at some distance from the HAZ
$t_4 = 27$	A through-thickness shear crack developed in the bumper beam on non-impacted end at time t_4
$t_5 = 52$	Due to the straining caused by the bumper beam a local plastic hinge developed in the non-impacted longitudinal at time t_5, at its clamped end. A plastic hinge in the mid-section of bumper beam appeared before t_5
$t_6 = 81$	At time t_6 the crashboxes on the reaction wall were almost activated

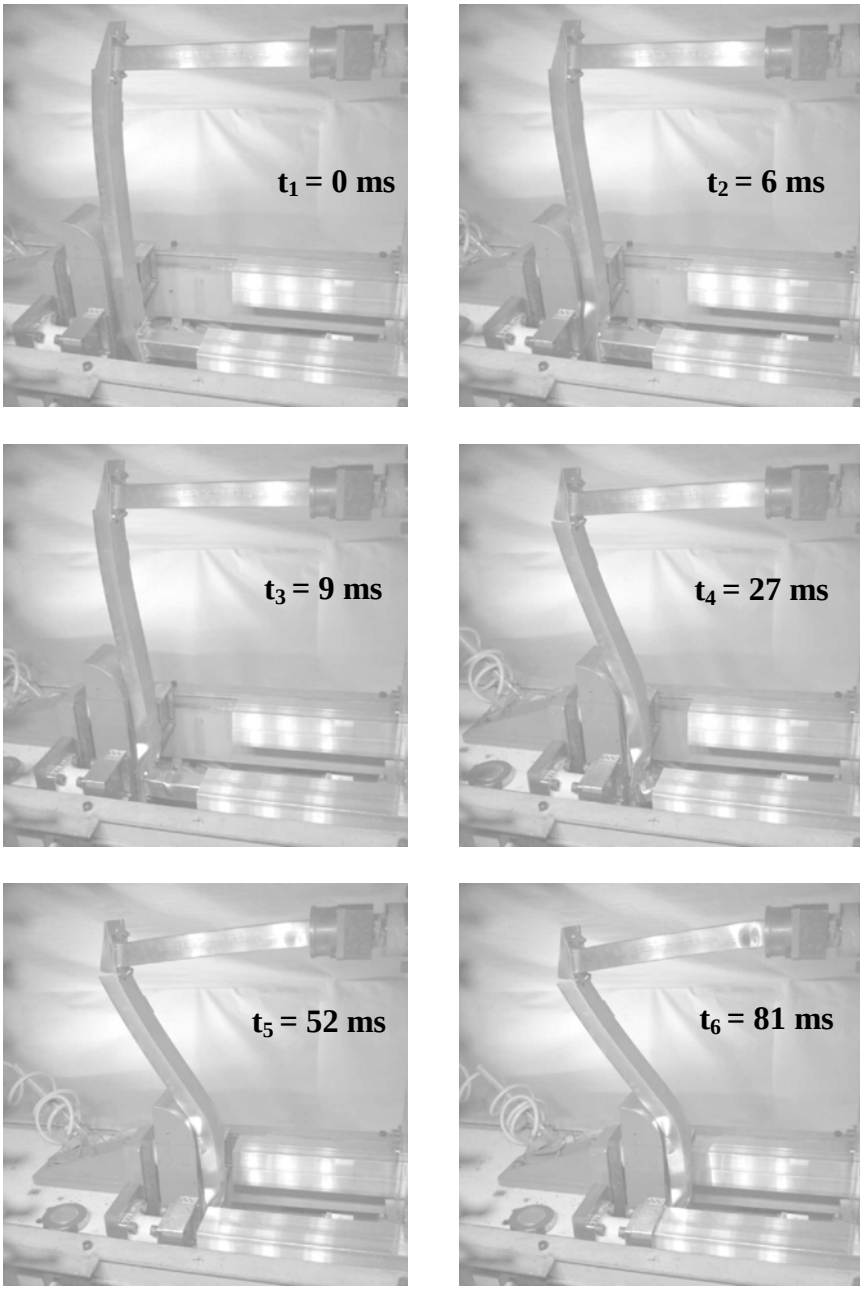

Figure A-5 Photos taken from high speed video recording for test specimen **A4**.

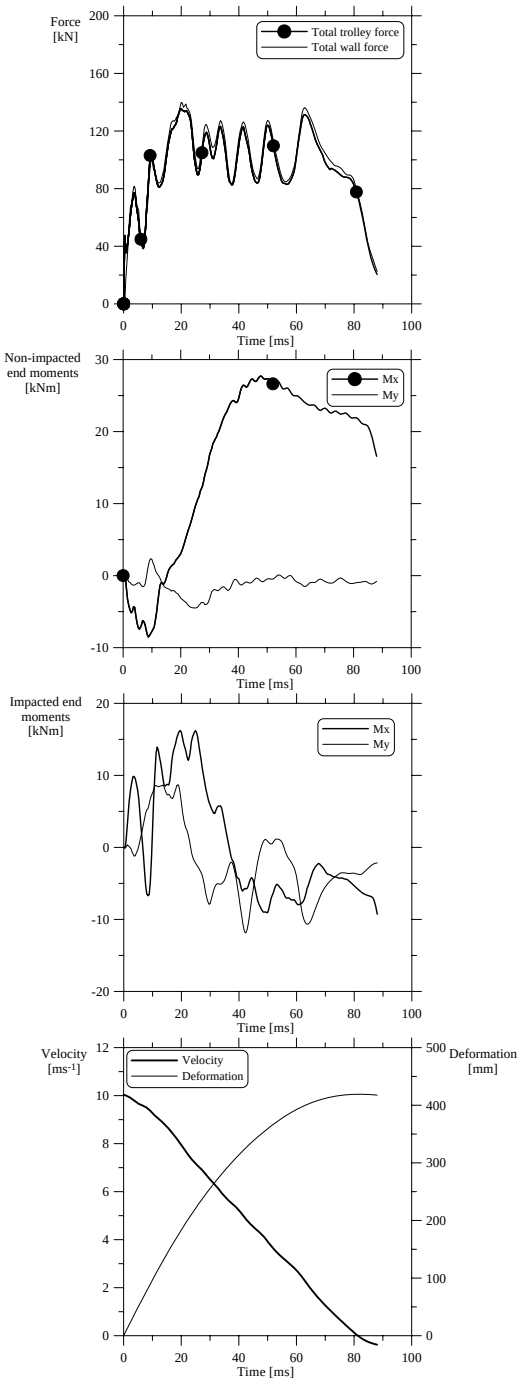

Figure A-6 Loadcell data for test specimen **A4**.

Test specimen **A5**

Table A-4 Description of impact events for test specimen **A5** see Figure A-7 and Figure A-8.

Time (ms)	Description
$t_1 = 0$	Impact of the bumper beam-longitudinal system started
$t_2 = 9$	The bumper beam cross-section collapsed completely before t_2 and at the same time buckling initiation in the impacted longitudinal started
$t_3 = 16$	A plastic hinge in the mid-section of bumper beam developed at time t_3
$t_4 = 24$	A through-thickness shear crack at the non-impacted end of the bumper beam developed at time t_4
$t_5 = 54$	Due to the straining caused by the bumper beam a local plastic hinge developed in the non-impacted longitudinal at time t_5
$t_6 = 81$	At time t_6 the crashboxes on the reaction wall were almost activated

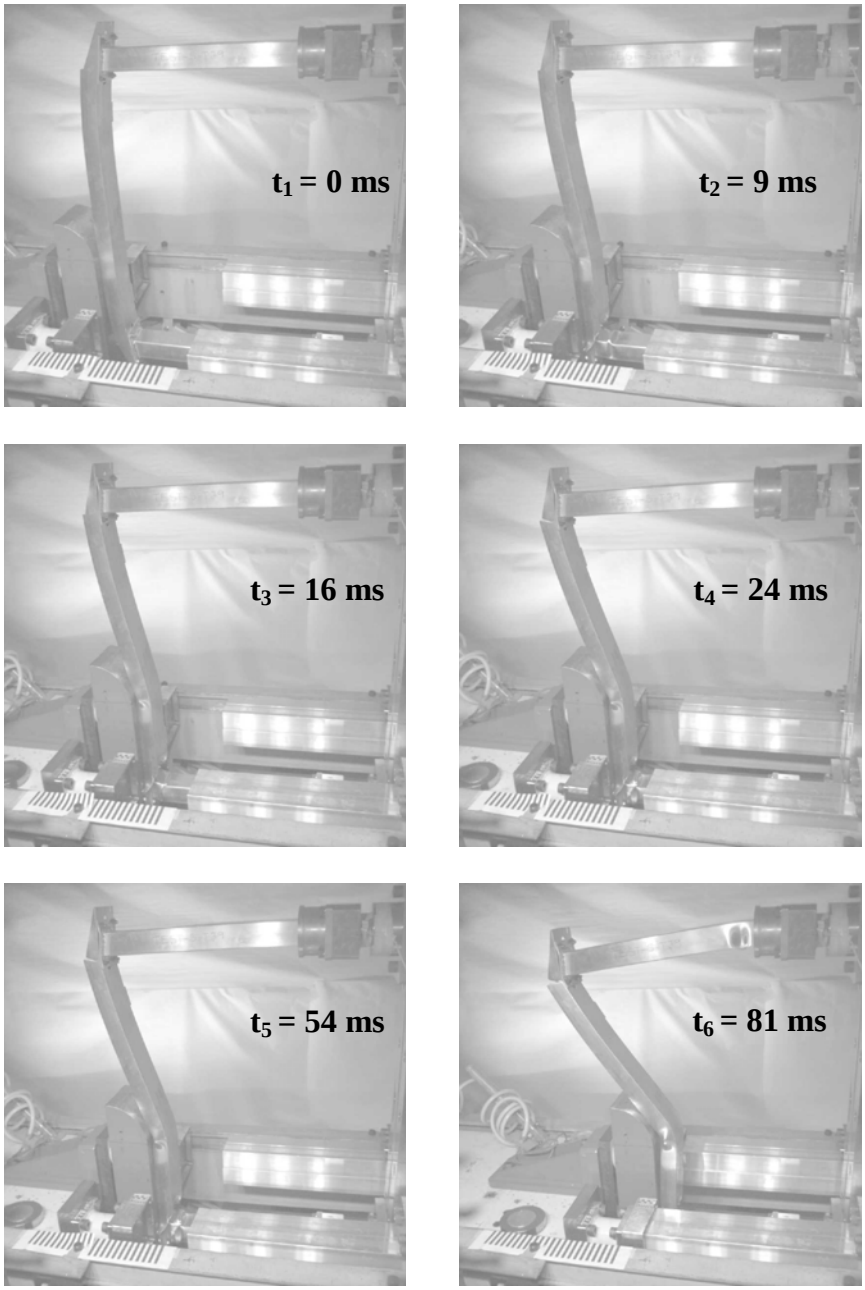

Figure A-7 Photos taken from high speed video recording for test specimen **A5**.

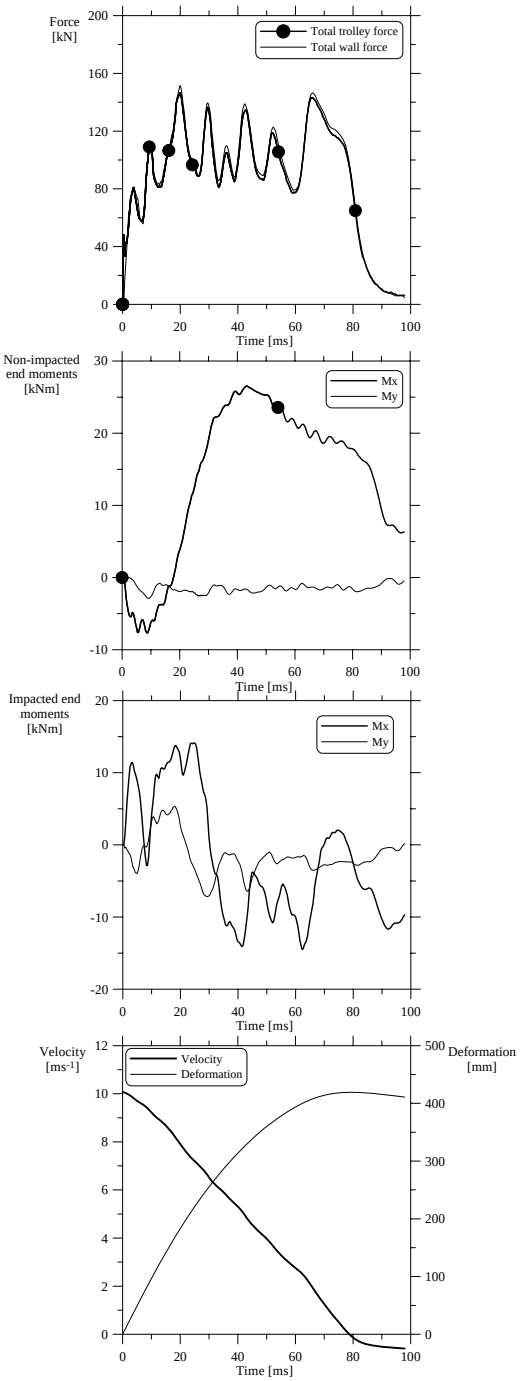

Figure A-8 Loadcell data for test specimen **A5**.

Appendix-B: Test series B

Test specimen **B2**

Table B-1 Description of impact events for test specimen **B2** see Figure B-1 and Figure B-2.

Time (ms)	Description
$t_1 = 0$	Impact of the bumper beam-longitudinal system started
$t_2 = 10$	The bumper beam cross-section collapsed completely before t_2 and at the same time buckling initiation in the impacted longitudinal started
$t_3 = 21$	A plastic hinge in the mid-section of bumper beam developed at time t_3
$t_4 = 41$	A through-thickness shear crack at the non-impacted end of the bumper beam developed at time t_4
$t_5 = 49$	Rotation of the deformed longitudinal at the impacted end started before time t_5
$t_6 = 65$	At time t_6 the crashboxes on the reaction wall were almost activated

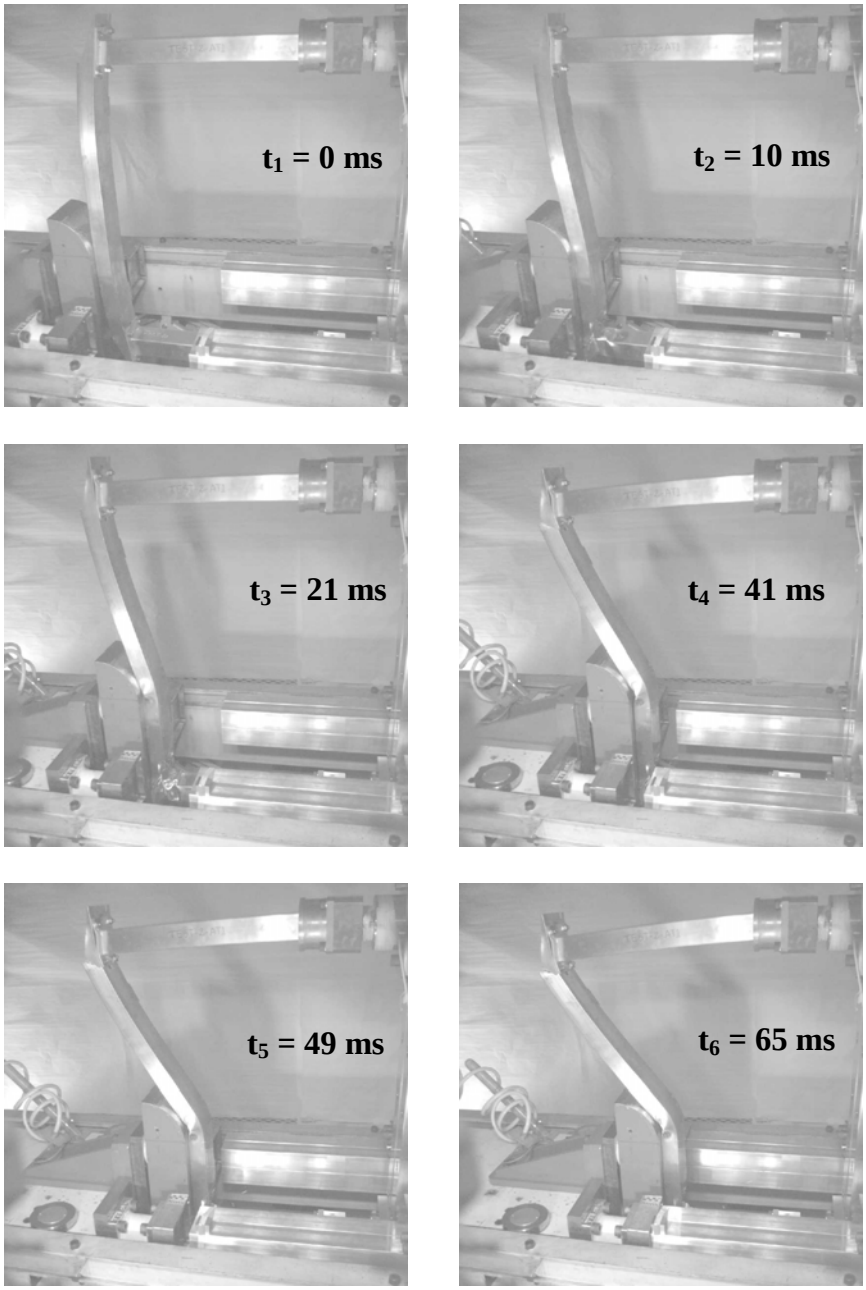

Figure B-1 Photos taken from high speed video recording for test specimen **B2**.

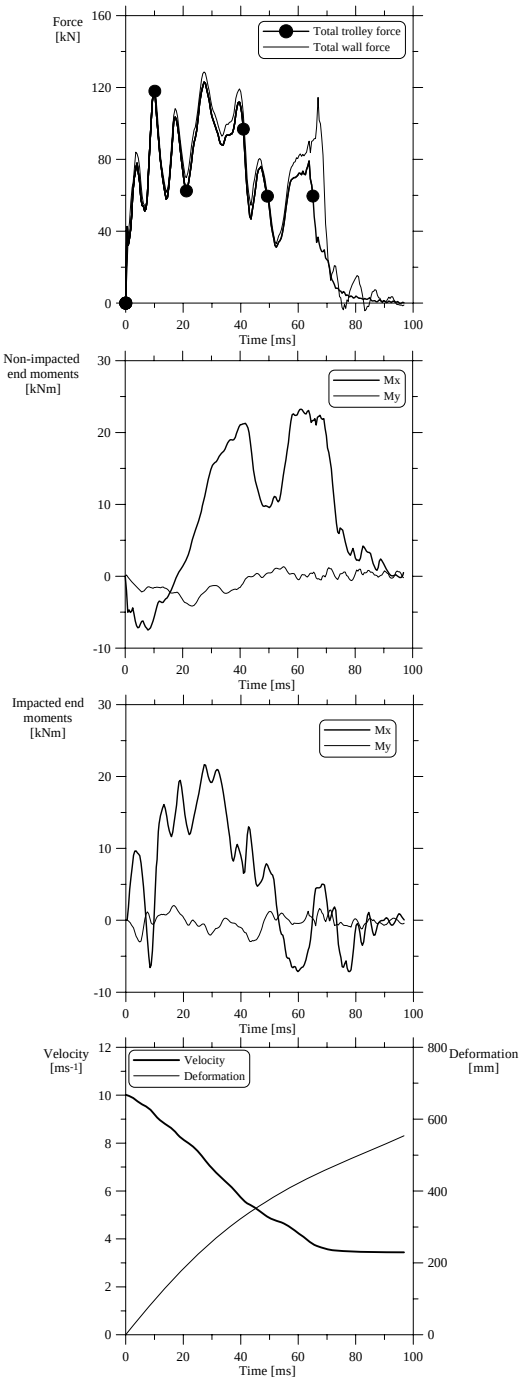

Figure B-2 Loadcell data for test specimen **B2**.

Test specimen **B3**

Table B-2 Description of impact events for test specimen **B3** see Figure B-3 and Figure B-4.

Time (ms)	Description
$t_1 = 0$	Impact of the bumper beam-longitudinal system started
$t_2 = 9$	The bumper beam cross-section collapsed completely before t_2 and at the same time buckling initiation in the impacted longitudinal started
$t_3 = 20$	A propagating tearing crack in the bumper beam started at time t_3
$t_4 = 30$	Rotation of the deformed longitudinal at the impacted end started before time t_4
$t_5 = 37$	A through-thickness shear crack at the non-impacted end of the bumper beam developed at time t_5
$t_6 = 65$	At time t_6 the crashboxes on the reaction wall were almost activated

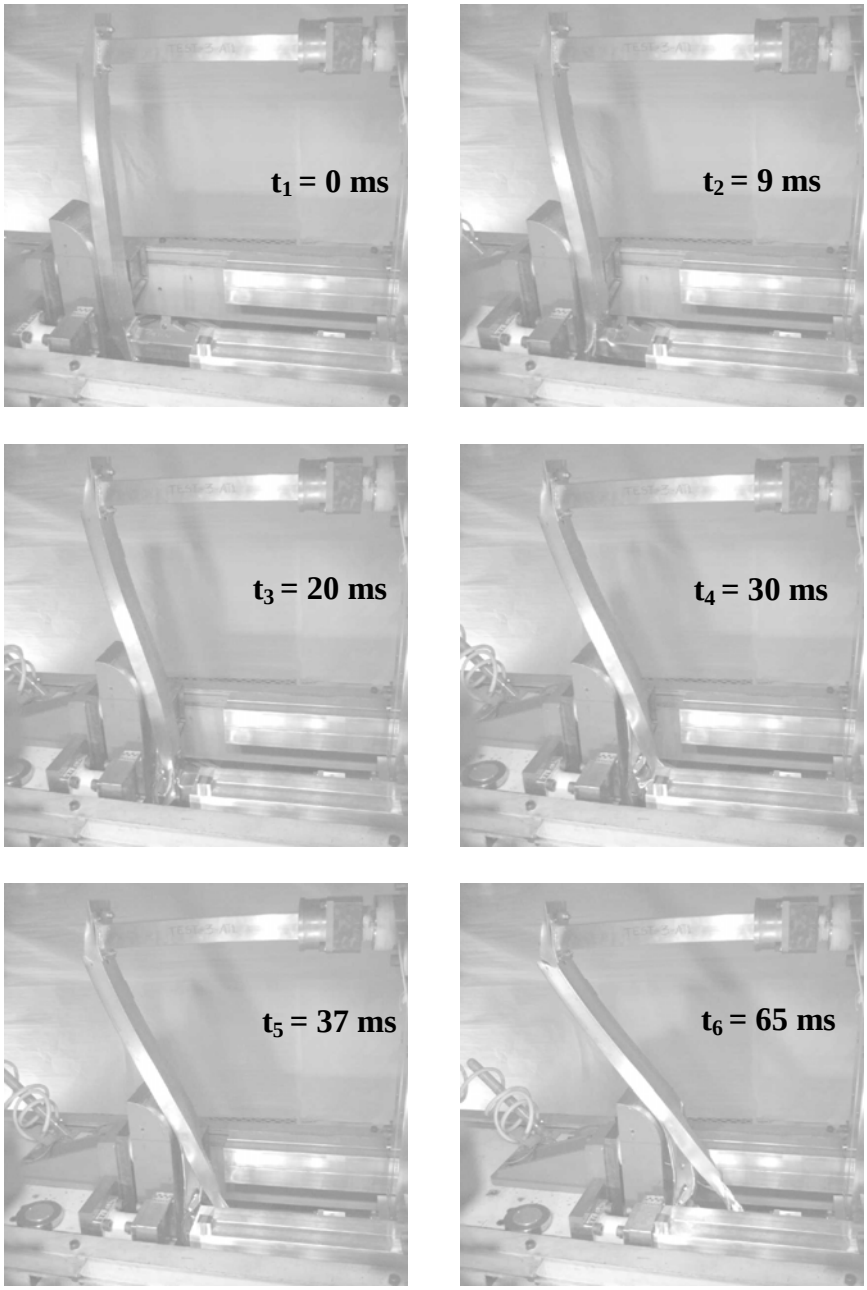

Figure B-3 Photos taken from high speed video recording for test specimen **B3**.

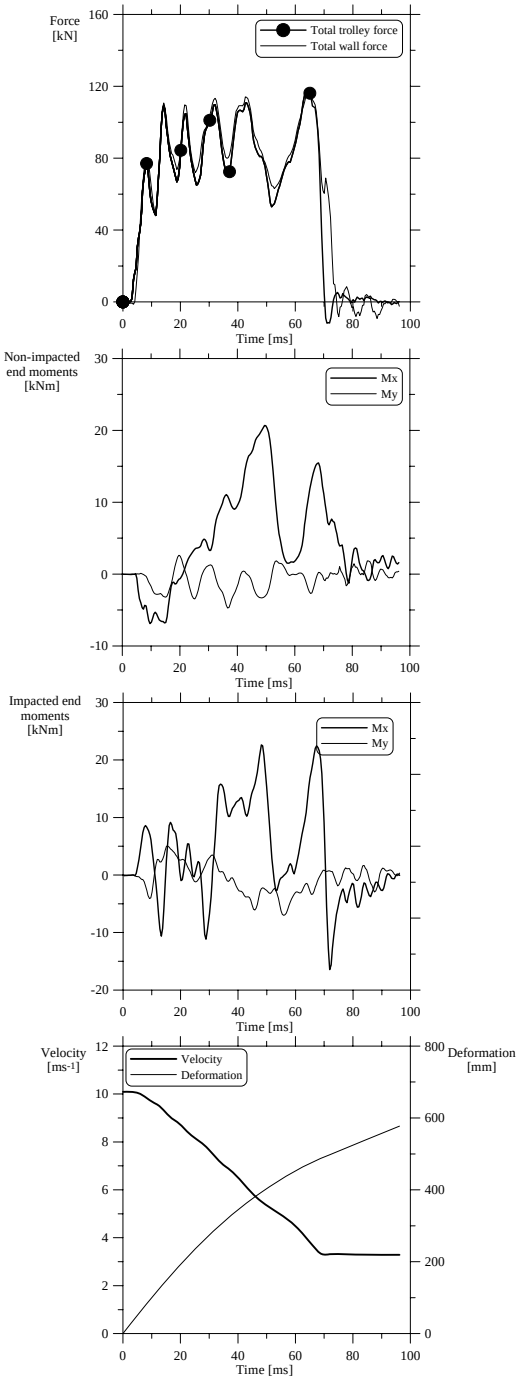

Figure B-4 Loadcell data for test specimen **B3**.

Appendix-C: Test series C

Test specimen **C2**

Table C-1 Description of impact events for test specimen **C2** see Figure C-1 and Figure C-2.

Time (ms)	Description
$t_1 = 0$	Impact of the bumper beam-longitudinal system started
$t_2 = 4$	The buckling initiation in the impacted longitudinal started at time t_2, without considerable collapse of the bumper beam cross-section
$t_3 = 9$	A plastic hinge in the mid-section of bumper beam started to develop at time t_3
$t_4 = 16$	A local plastic hinge developed close to the HAZ in the non-impacted longitudinal at time t_4, instead of developing the through-thickness shear crack at the non-impacted end of the bumper beam
$t_5 = 48$	Due to the straining caused by the bumper beam a local plastic hinge developed in the non-impacted longitudinal at time t_5
$t_6 = 55$	At time t_6 the crashboxes on the reaction wall were activated

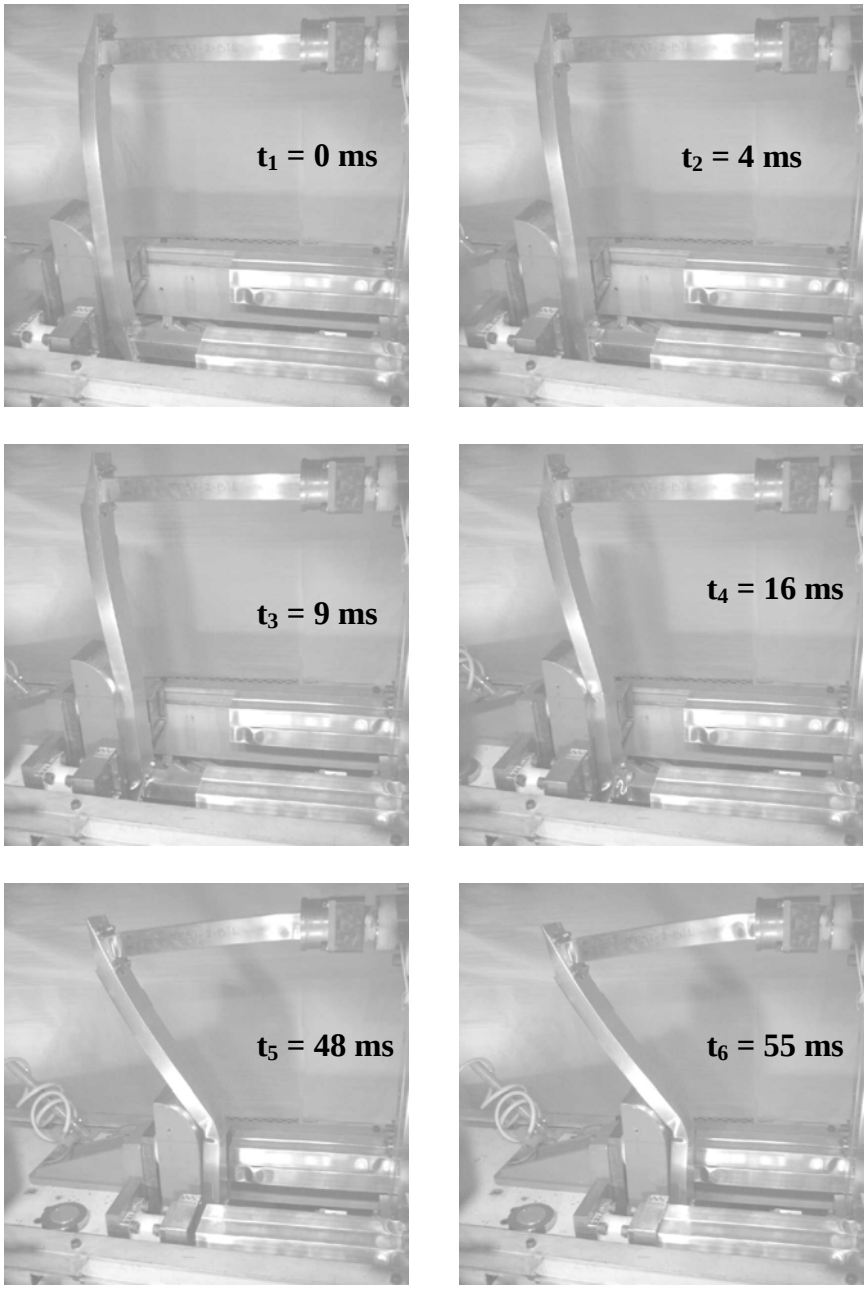

Figure C-1 Photos taken from high speed video recording for test specimen **C2**.

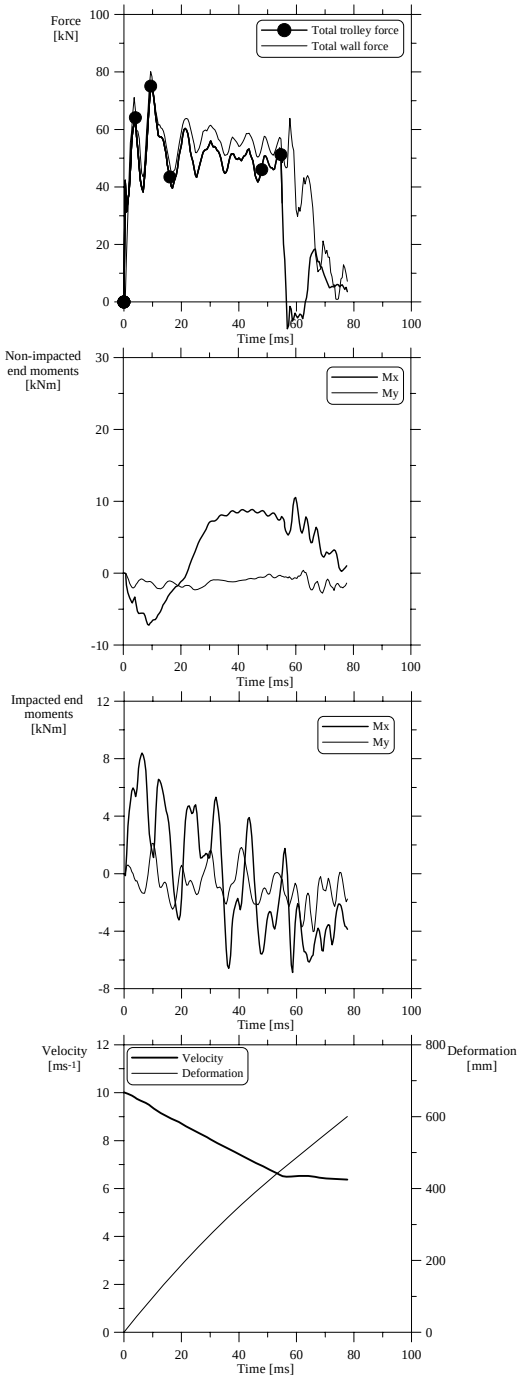

Figure C-2 Loadcell data for test specimen **C2**.

Test specimen **C3**

Table C-2 Description of impact events for test specimen **C3** see Figure C-3 and Figure C-4.

Time (ms)	Description
$t_1 = 0$	Impact of the bumper beam-longitudinal system started
$t_2 = 4$	The buckling initiation in the impacted longitudinal started at time t_2, without considerable collapse of the bumper beam cross-section
$t_3 = 10$	A plastic hinge in the mid-section of bumper beam started to develop at time t_3
$t_4 = 26$	A local plastic hinge developed close to the HAZ in the non-impacted longitudinal at time t_4, instead of developing the through-thickness shear crack at the non-impacted end of the bumper beam
$t_5 = 48$	Due to the straining caused by the bumper beam a local plastic hinge developed in the non-impacted longitudinal at time t_5
$t_6 = 59$	At time t_6 the crashboxes on the reaction wall were activated

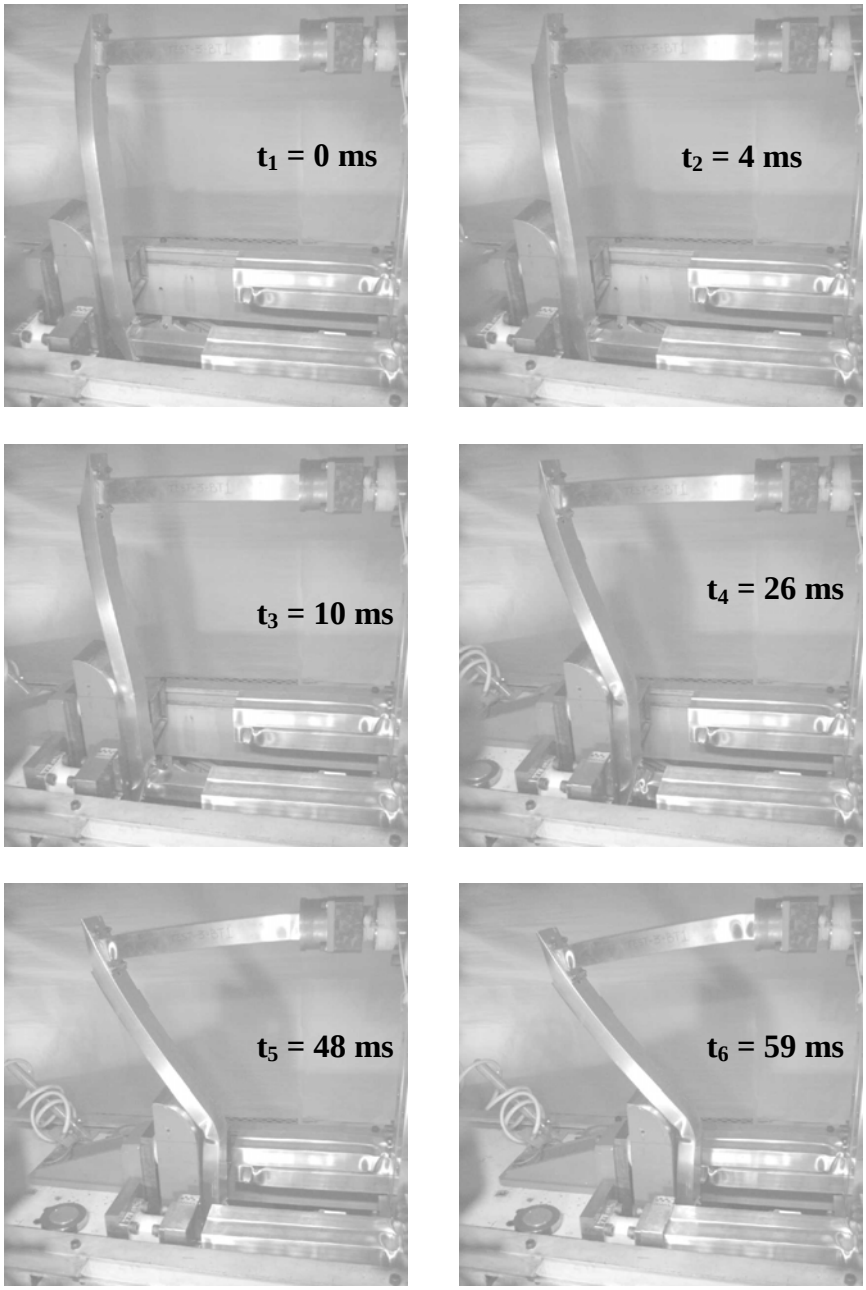

Figure C-3 Photos taken from high speed video recording for test specimen **C3**.

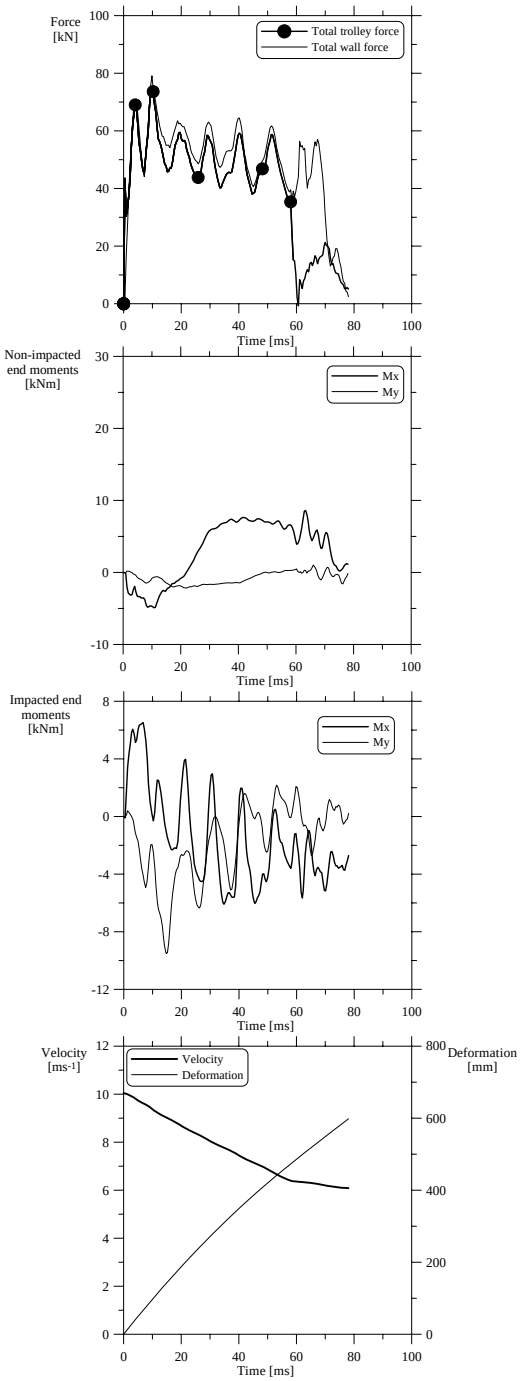

Figure C-4 Loadcell data for test specimen **C3**.

Appendix-D: Test series D

Test specimen **D2**

Table D-1 Description of impact events for test specimen **D2** see Figure D-1 and Figure D-2.

Time (ms)	Description
$t_1 = 0$	Impact of the bumper beam-longitudinal system started
$t_2 = 4$	The bumper beam cross-section collapsed completely and buckling initiation in the impacted longitudinal started at time t_2
$t_3 = 13.5$	A plastic hinge in the mid-section of bumper beam developed at time t_3
$t_4 = 26$	A through-thickness shear crack at the non-impacted end of the bumper beam developed at time t_4
$t_5 = 29.5$	Due to the straining caused by the bumper beam a local plastic hinge developed in the non-impacted longitudinal at time t_5 at its clamped end
$t_6 = 32$	At time t_6 the crashboxes on the reaction wall were activated

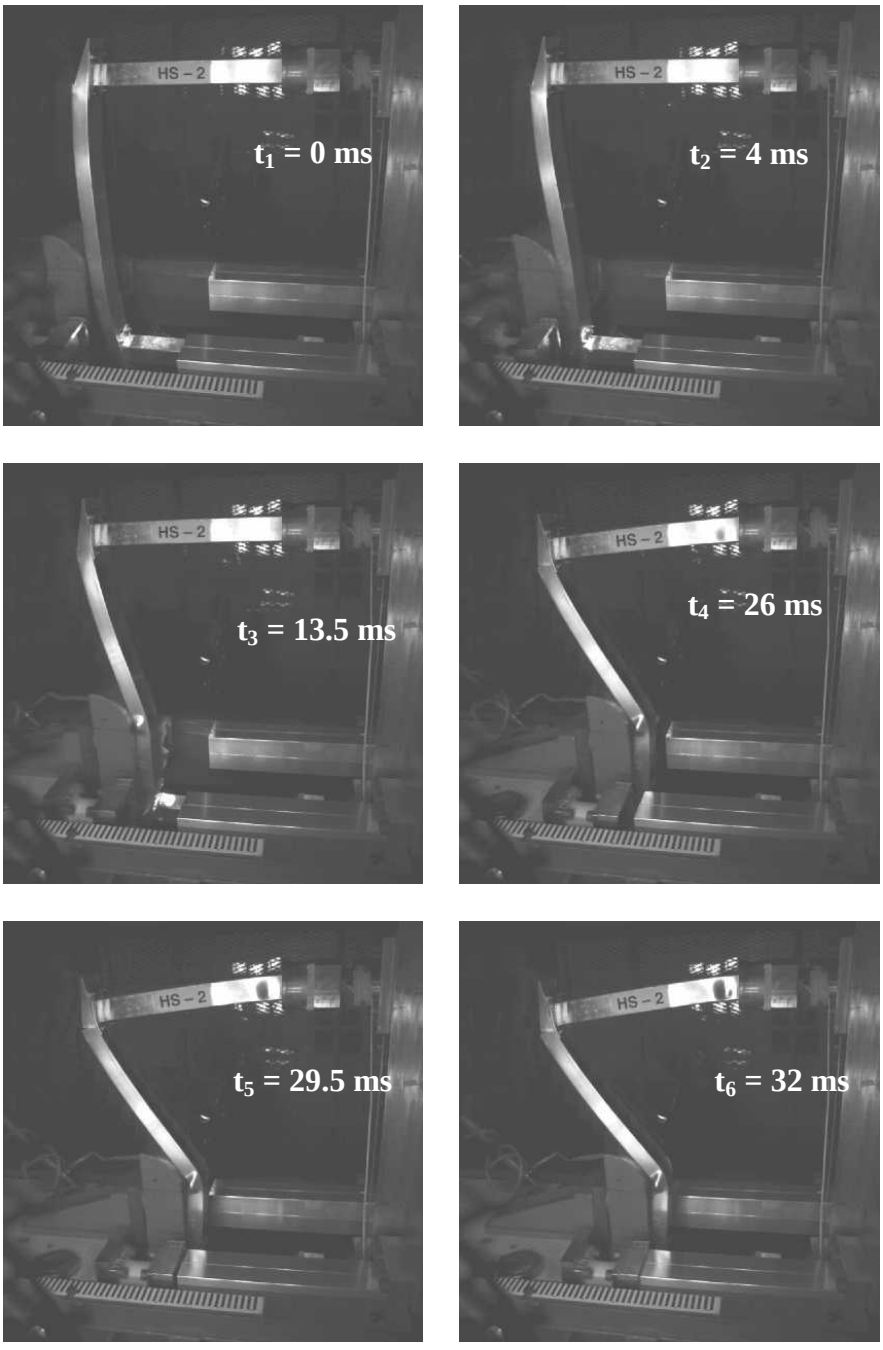

Figure D-1 Photos taken from high speed video recording for test specimen **D2**.

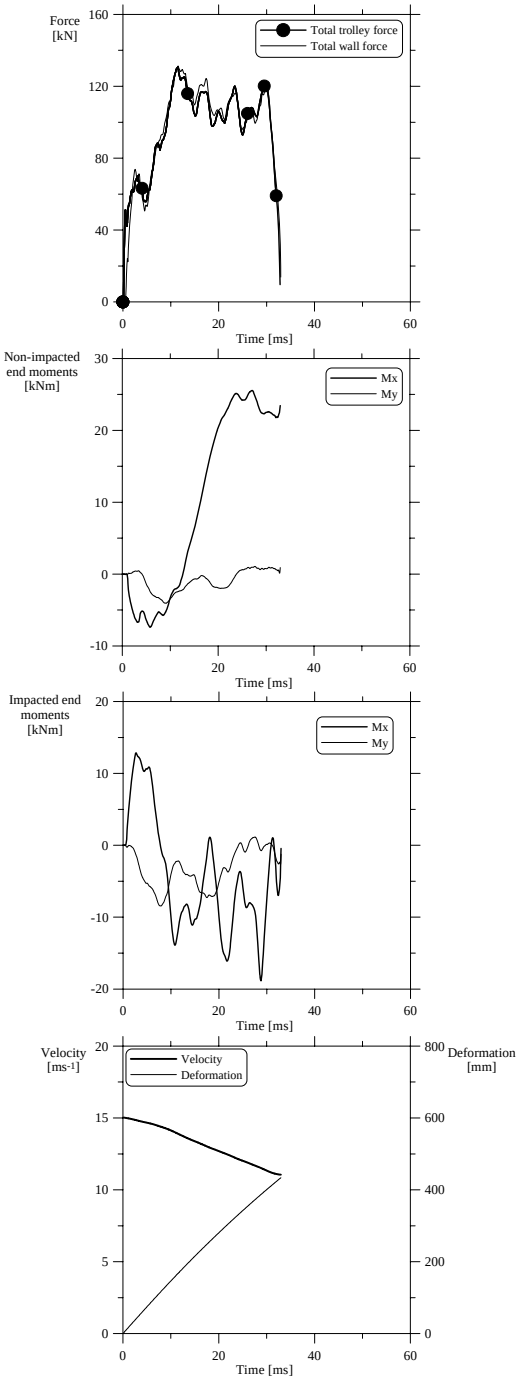

Figure D-2 Loadcell data for test specimen **D2**.

Test specimen **D3**

Table D-2 Description of impact events for test specimen **D3** see Figure D-3 and Figure D-4.

Time (ms)	Description
$t_1 = 0$	Impact of the bumper beam-longitudinal system started
$t_2 = 4$	The bumper beam cross-section collapsed completely and buckling initiation in the impacted longitudinal started at time t_2
$t_3 = 14$	A plastic hinge in the mid-section of bumper beam developed at time t_3
$t_4 = 25.5$	A through-thickness shear crack at the non-impacted end of the bumper beam developed at time t_4
$t_5 = 27$	Due to the straining caused by the bumper beam a local plastic hinge developed in the non-impacted longitudinal at time t_5 at its clamped end
$t_6 = 35$	At time t_6 the crashboxes on the reaction wall were activated

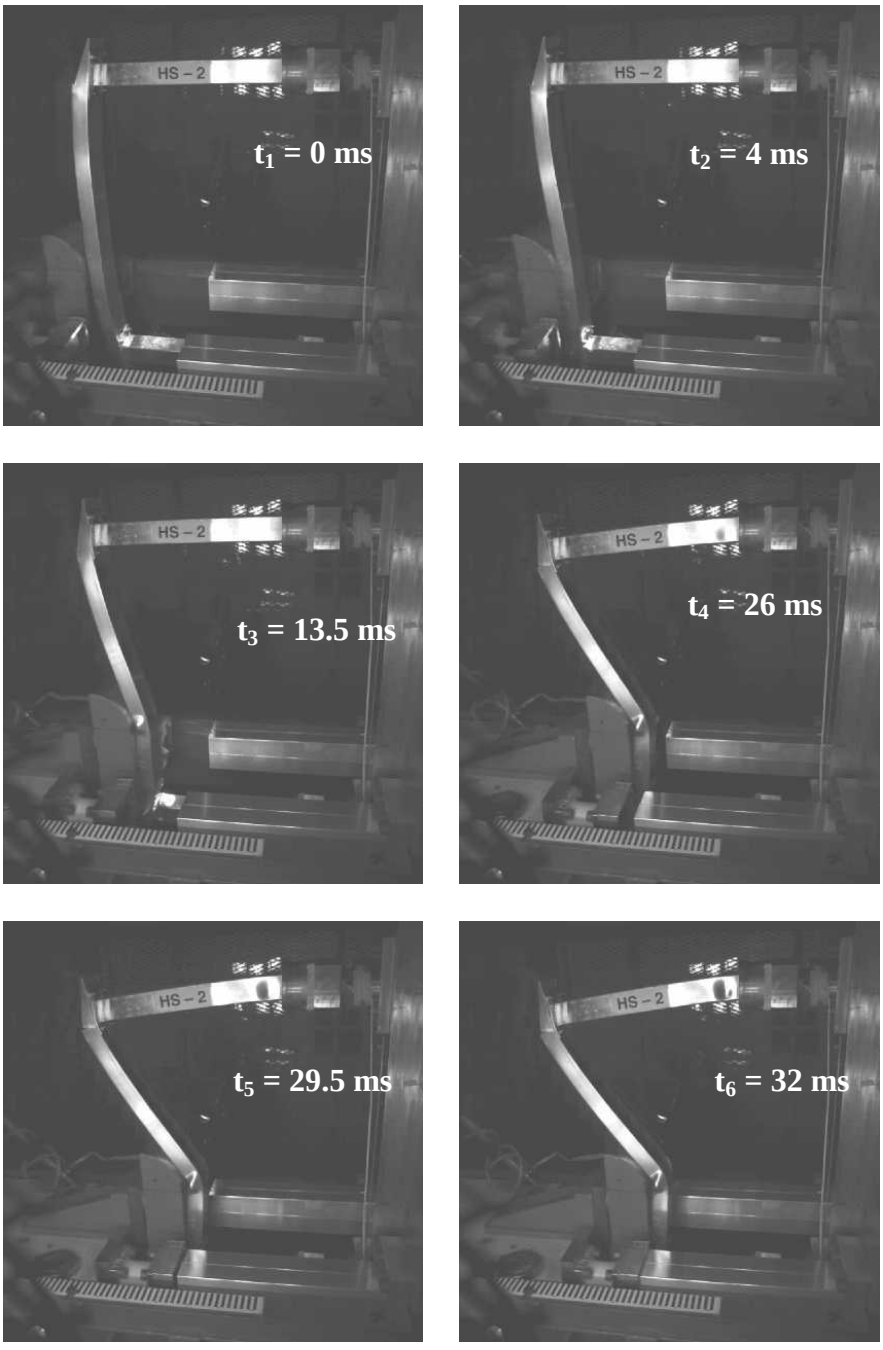

Figure D-3 Photos taken from high speed video recording for test specimen **D3**.

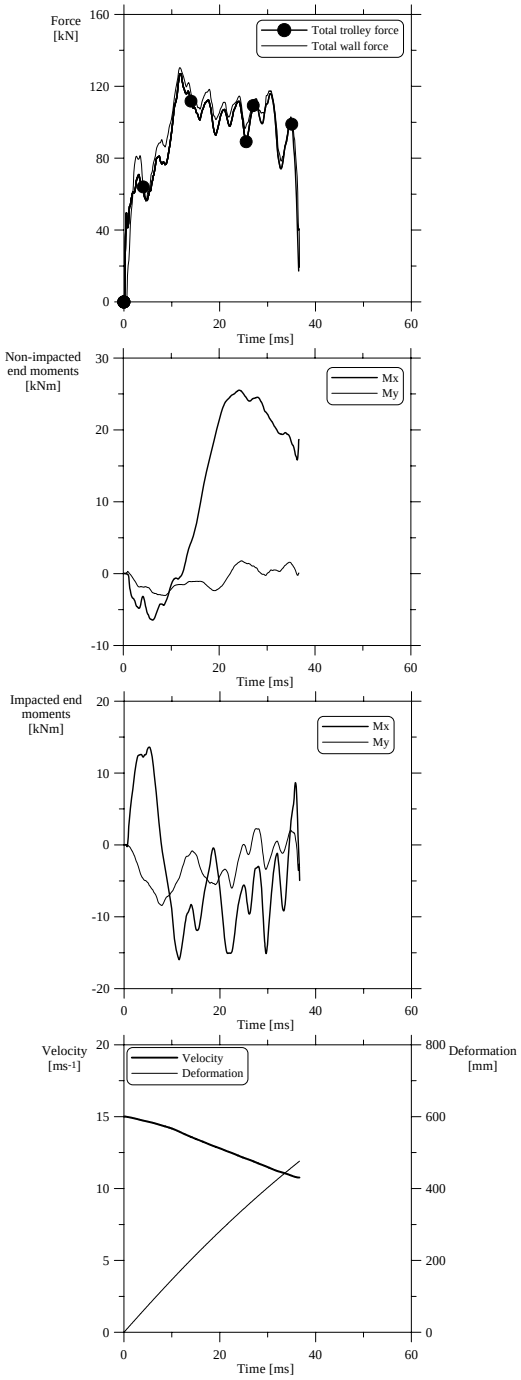

Figure D-4 Loadcell data for test specimen **D3**.

DEPARTMENT OF STRUCTURAL ENGINEERING
NORWEGIAN UNIVERSITY OF SCIENCE AND TECHNOLOGY

N–7491 TRONDHEIM, NORWAY
Telephone: +47 73 59 47 00 Telefax: +47 73 59 47 01

"Reliability Analysis of Structural Systems using Nonlinear Finite Element Methods",
C. A. Holm, 1990:23, ISBN 82-7119-178-0.

"Uniform Stratified Flow Interaction with a Submerged Horizontal Cylinder",
Ø. Arntsen, 1990:32, ISBN 82-7119-188-8.

"Large Displacement Analysis of Flexible and Rigid Systems Considering Displacement-Dependent Loads and Nonlinear Constraints",
K. M. Mathisen, 1990:33, ISBN 82-7119-189-6.

"Solid Mechanics and Material Models including Large Deformations",
E. Levold, 1990:56, ISBN 82-7119-214-0, ISSN 0802-3271.

"Inelastic Deformation Capacity of Flexurally-Loaded Aluminium Alloy Structures",
T. Welo, 1990:62, ISBN 82-7119-220-5, ISSN 0802-3271.

"Visualization of Results from Mechanical Engineering Analysis",
K. Aamnes, 1990:63, ISBN 82-7119-221-3, ISSN 0802-3271.

"Object-Oriented Product Modeling for Structural Design",
S. I. Dale, 1991:6, ISBN 82-7119-258-2, ISSN 0802-3271.

"Parallel Techniques for Solving Finite Element Problems on Transputer Networks",
T. H. Hansen, 1991:19, ISBN 82-7119-273-6, ISSN 0802-3271.

"Statistical Description and Estimation of Ocean Drift Ice Environments",
R. Korsnes, 1991:24, ISBN 82-7119-278-7, ISSN 0802-3271.

“Properties of Concrete Related to Fatigue Damage: with Emphasis on High Strength Concrete”,
G. Petkovic, 1991:35, ISBN 82-7119-290-6, ISSN 0802-3271.

“Turbidity Current Modelling”,
B. Brørs, 1991:38, ISBN 82-7119-293-0, ISSN 0802-3271.

“Zero-Slump Concrete: Rheology, Degree of Compaction and Strength. Effects of Fillers as Part Cement-Replacement”,
C. Sørensen, 1992:8, ISBN 82-7119-357-0, ISSN 0802-3271.

“Nonlinear Analysis of Reinforced Concrete Structures Exposed to Transient Loading”,
K. V. Høiseth, 1992:15, ISBN 82-7119-364-3, ISSN 0802-3271.

“Finite Element Formulations and Solution Algorithms for Buckling and Collapse Analysis of Thin Shells”,
R. O. Bjærum, 1992:30, ISBN 82-7119-380-5, ISSN 0802-3271.

“Response Statistics of Nonlinear Dynamic Systems”,
J. M. Johnsen, 1992:42, ISBN 82-7119-393-7, ISSN 0802-3271.

“Digital Models in Engineering. A Study on Why and How Engineers Build and Operate Digital Models for Decisison Support”,
J. Høyte, 1992:75, ISBN 82-7119-429-1, ISSN 0802-3271.

“Sparse Solution of Finite Element Equations”,
A. C. Damhaug, 1992:76, ISBN 82-7119-430-5, ISSN 0802-3271.

“Some Aspects of Floating Ice Related to Sea Surface Operations in the Barents Sea”,
S. Løset, 1992:95, ISBN 82-7119-452-6, ISSN 0802-3271.

“Modelling of Cyclic Plasticity with Application to Steel and Aluminium Structures”,
O. S. Hopperstad, 1993:7, ISBN 82-7119-461-5, ISSN 0802-3271.

“The Free Formulation: Linear Theory and Extensions with Applications to Tetrahedral Elements with Rotational Freedoms”,
G. Skeie, 1993:17, ISBN 82-7119-472-0, ISSN 0802-3271.

“Høyfast betongs motstand mot piggdekkslitasje. Analyse av resultater fra prøving i Veisliter'n”,
T. Tveter, 1993:62, ISBN 82-7119-522-0, ISSN 0802-3271.

“A Nonlinear Finite Element Based on Free Formulation Theory for Analysis of Sandwich Structures”,
O. Aamlid, 1993:72, ISBN 82-7119-534-4, ISSN 0802-3271.

“The Effect of Curing Temperature and Silica Fume on Chloride Migration and Pore Structure of High Strength Concrete”,
C. J. Hauck, 1993:90, ISBN 82-7119-553-0, ISSN 0802-3271.

“Failure of Concrete under Compressive Strain Gradients”,
G. Markeset, 1993:110, ISBN 82-7119-575-1, ISSN 0802-3271.

“An Experimental Study of Internal Tidal Amphidromes in Vestfjorden”,
J. H. Nilsen, 1994:39, ISBN 82-7119-640-5, ISSN 0802-3271.

“Structural Analysis of Oil Wells with Emphasis on Conductor Design”,
H. Larsen, 1994:46, ISBN 82-7119-648-0, ISSN 0802-3271.

“Adaptive Methods for Non-Linear Finite Element Analysis of Shell Structures”,
K. M. Okstad, 1994:66, ISBN 82-7119-670-7, ISSN 0802-3271.

“On Constitutive Modelling in Nonlinear Analysis of Concrete Structures”,
O. Fyrileiv, 1994:115, ISBN 82-7119-725-8, ISSN 0802-3271.

“Fluctuating Wind Load and Response of a Line-Like Engineering Structure with Emphasis on Motion-Induced Wind Forces”,
J. Bogunovic Jakobsen, 1995:62, ISBN 82-7119-809-2, ISSN 0802-3271.

“An Experimental Study of Beam-Columns Subjected to Combined Torsion, Bending and Axial Actions”,
A. Aalberg, 1995:66, ISBN 82-7119-813-0, ISSN 0802-3271.

“Scaling and Cracking in Unsealed Freeze/Thaw Testing of Portland Cement and Silica Fume Concretes”,
S. Jacobsen, 1995:101, ISBN 82-7119-851-3, ISSN 0802-3271.

“Damping of Water Waves by Submerged Vegetation. A Case Study of Laminaria Hyperborea",
A. M. Dubi, 1995:108, ISBN 82-7119-859-9, ISSN 0802-3271.

“The Dynamics of a Slope Current in the Barents Sea”,
Sheng Li, 1995:109, ISBN 82-7119-860-2, ISSN 0802-3271.

”Modellering av delmaterialenes betydning for betongens konsistens”,
Ernst Mørtsell, 1996:12, ISBN 82-7119-894-7, ISSN 0802-3271.

“Bending of Thin-Walled Aluminium Extrusions”,
Birgit Søvik Opheim, 1996:60, ISBN 82-7119-947-1, ISSN 0802-3271.

“Material Modelling of Aluminium for Crashworthiness Analysis”,
Torodd Berstad, 1996:89, ISBN 82-7119-980-3, ISSN 0802-3271.

“Estimation of Structural Parameters from Response Measurements on Submerged Floating Tunnels”,
Rolf Magne Larssen, 1996:119, ISBN 82-471-0014-2, ISSN 0802-3271.

“Numerical Modelling of Plain and Reinforced Concrete by Damage Mechanics”,
Mario A. Polanco-Loria, 1997:20, ISBN 82-471-0049-5, ISSN 0802-3271.

“Nonlinear Random Vibrations - Numerical Analysis by Path Integration Methods”,
Vibeke Moe, 1997:26, ISBN 82-471-0056-8, ISSN 0802-3271.

“Numerical Prediction of Vortex-Induced Vibration by the Finite Element Method”,
Joar Martin Dalheim, 1997:63, ISBN 82-471-0096-7, ISSN 0802-3271.

“Time Domain Calculations of Buffeting Response for Wind Sensitive Structures”,
Ketil Aas-Jakobsen, 1997:148, ISBN 82-471-0189-0, ISSN 0802-3271.

“A Numerical Study of Flow about Fixed and Flexibly Mounted Circular Cylinders”,
Trond Stokka Meling, 1998:48, ISBN 82-471-0244-7, ISSN 0802-3271.

“Estimation of Chloride Penetration into Concrete Bridges in Coastal Areas”,
Per Egil Steen, 1998:89, ISBN 82-471-0290-0, ISSN 0802-3271.

“Stress-Resultant Material Models for Reinforced Concrete Plates and Shells”,
Jan Arve Øverli, 1998:95, ISBN 82-471-0297-8, ISSN 0802-3271.

“Chloride Binding in Concrete. Effect of Surrounding Environment and Concrete Composition”,
Claus Kenneth Larsen, 1998:101, ISBN 82-471-0337-0, ISSN 0802-3271.

“Rotational Capacity of Aluminium Alloy Beams”,
Lars A. Moen, 1999:1, ISBN 82-471-0365-6, ISSN 0802-3271.

“Stretch Bending of Aluminium Extrusions”,
Arild H. Clausen, 1999:29, ISBN 82-471-0396-6, ISSN 0802-3271.

“Aluminium and Steel Beams under Concentrated Loading”,
Tore Tryland, 1999:30, ISBN 82-471-0397-4, ISSN 0802-3271.

“Engineering Models of Elastoplasticity and Fracture for Aluminium Alloys”,
Odd-Geir Lademo, 1999:39, ISBN 82-471-0406-7, ISSN 0802-3271.

“Kapasitet og duktilitet av dybelforbindelser i trekonstruksjoner”,
Jan Siem, 1999:46, ISBN 82-471-0414-8, ISSN 0802-3271.

“Etablering av distribuert ingeniørarbeid; Teknologiske og organisatoriske erfaringer fra en norsk ingeniørbedrift”,
Lars Line, 1999:52, ISBN 82-471-0420-2, ISSN 0802-3271.

“Estimation of Earthquake-Induced Response”,
Símon Ólafsson, 1999:73, ISBN 82-471-0443-1, ISSN 0802-3271.

“Coastal Concrete Bridges: Moisture State, Chloride Permeability and Aging Effects”,
Ragnhild Holen Relling, 1999:74, ISBN 82-471-0445-8, ISSN 0802-3271.

“Capacity Assessment of Titanium Pipes Subjected to Bending and External Pressure”,
Arve Bjørset, 1999:100, ISBN 82-471-0473-3, ISSN 0802-3271.

“Validation of Numerical Collapse Behaviour of Thin-Walled Corrugated Panels”,
Håvar Ilstad, 1999:101, ISBN 82-471-0474-1, ISSN 0802-3271.

“Strength and Ductility of Welded Structures in Aluminium Alloys”, Miroslaw Matusiak, 1999:113, ISBN 82-471-0487-3, ISSN 0802-3271.

“Thermal Dilation and Autogenous Deformation as Driving Forces to Self-Induced Stresses in High Performance Concrete”,
Øyvind Bjøntegaard, 1999:121, ISBN 82-7984-002-8, ISSN 0802-3271.

“Some Aspects of Ski Base Sliding Friction and Ski Base Structure”,
Dag Anders Moldestad, 1999:137, ISBN 82-7984-019-2, ISSN 0802-3271.

“Electrode Reactions and Corrosion Resistance for Steel in Mortar and Concrete",
Roy Antonsen, 2000:10, ISBN 82-7984-030-3, ISSN 0802-3271.

“Hydro-Physical Conditions in Kelp Forests and the Effect on Wave Damping and Dune Erosion. A Case Study on Laminaria Hyperborea”,
Stig Magnar Løvås, 2000:28, ISBN 82-7984-050-8, ISSN 0802-3271.

“Random Vibration and the Path Integral Method”,
Christian Skaug, 2000:39, ISBN 82-7984-061-3, ISSN 0802-3271.

“Buckling and Geometrical Nonlinear Beam-Type Analyses of Timber Structures",
Trond Even Eggen, 2000:56, ISBN 82-7984-081-8, ISSN 0802-3271.

“Structural Crashworthiness of Aluminium Foam-Based Components”, Arve Grønsund Hanssen, 2000:76, ISBN 82-7984-102-4, ISSN 0809-103X.

“Measurements and Simulations of the Consolidation in First-Year Sea Ice Ridges, and Some Aspects of Mechanical Behaviour”,
Knut V. Høyland, 2000:94, ISBN 82-7984-121-0, ISSN 0809-103X.

“Kinematics in Regular and Irregular Waves Based on a Lagrangian Formulation”,
Svein Helge Gjøsund, 2000-86, ISBN 82-7984-112-1, ISSN 0809-103X.

“Self-Induced Cracking Problems in Hardening Concrete Structures”, Daniela Bosnjak, 2000-121, ISBN 82-7984-151-2, ISSN 0809-103X.

“Ballistic Penetration and Perforation of Steel Plates”,
Tore Børvik, 2000:124, ISBN 82-7984-154-7, ISSN 0809-103X.

“Freeze-Thaw Resistance of Concrete. Effect of: Curing Conditions, Moisture Exchange and Materials”,
Terje Finnerup Rønning, 2001:14, ISBN 82-7984-165-2, ISSN 0809-103X.

“Structural Behaviour of Post Tensioned Concrete Structures. Flat Slab. Slabs on Ground”,
Steinar Trygstad, 2001:52, ISBN 82-471-5314-9, ISSN 0809-103X.

“Slipforming of Vertical Concrete Structures. Friction between Concrete and Slipform Panel”,
Kjell Tore Fosså, 2001:61, ISBN 82-471-5325-4, ISSN 0809-103X.

“Some Numerical Methods for the Simulation of Laminar and Turbulent Incompressible Flows”,
Jens Holmen, 2002:6, ISBN 82-471-5396-3, ISSN 0809-103X.

“Improved Fatigue Performance of Threaded Drillstring Connections by Cold Rolling”,
Steinar Kristoffersen, 2002:11, ISBN: 82-421-5402-1, ISSN 0809-103X.

“Deformations in Concrete Cantilever Bridges: Observations and Theoretical Modelling",
Peter F. Takâcs, 2002:23, ISBN 82-471-5415-3, ISSN 0809-103X.

“Stiffened Aluminium Plates Subjected to Impact Loading",
Hilde Giæver Hildrum, 2002:69, ISBN 82-471-5467-6, ISSN 0809-103X.

“Full- and Model Scale Study of Wind Effects on a Medium-Rise Building in a Built up Area”,
Jónas Thór Snæbjørnsson, 2002:95, ISBN82-471-5495-1, ISSN 0809-103X.

“Evaluation of Concepts for Loading of Hydrocarbons in Ice-Infested Water”,
Arnor Jensen, 2002:114, ISBN 82-417-5506-0, ISSN 0809-103X.

“Numerical and Physical Modelling of Oil Spreading in Broken Ice”,
Janne K. Økland Gjøsteen, 2002:130, ISBN 82-471-5523-0, ISSN 0809-103X.

“Diagnosis and Protection of Corroding Steel in Concrete”,
Franz Pruckner, 20002:140, ISBN 82-471-5555-4, ISSN 0809-103X.

“Tensile and Compressive Creep of Young Concrete: Testing and Modelling”,
Dawood Atrushi, 2003:17, ISBN 82-471-5565-6, ISSN 0809-103X.

“Rheology of Particle Suspensions. Fresh Concrete, Mortar and Cement Paste with Various Types of Lignosulfonates”,
Jon Elvar Wallevik, 2003:18, ISBN 82-471-5566-4, ISSN 0809-103X.

“Oblique Loading of Aluminium Crash Components”,
Aase Gavina R. Reyes, 2003:15, ISBN 82-471-5562-1, ISSN 0809-103X.

“Utilization of Ethiopian Natural Pozzolans”,
Surafel Ketema Desta, 2003:26, ISSN 82-471-5574-5, ISSN:0809-103X.

“Behaviour and Strength Prediction of Reinforced Concrete Structures with Discontinuity Regions”,
Helge Brå, 2004:11, ISBN 82-471-6222-9, ISSN 1503-8181.

“High-Strength Steel Plates Subjected to Projectile Impact. An Experimental and Numerical study”,
Sumita Dey, 2004:38, ISBN 82-471-6281-4 (elektr. Utg.), ISBN 82-471-6282-2 (trykt utg.), ISSN 1503-8181.

“Alkali-Reactive and Inert Fillers in Concrete. Rheology of Fresh Mixtures and Expansive Reactions”,
Bård M. Pedersen, 2004:92, ISBN 82-471-6401-9 (trykt utg.), ISBN 82-471-6400-0 (elektr. utg.), ISSN 1503-8181.

"On the Shear Capacity of Steel Girders with Large Web Openings",
Nils Christian Hagen, 2005:9 ISBN 82-471-6878-2 (trykt utg.), ISBN 82-471-6877-4 (elektr. utg.), ISSN 1503-8181.

"Behaviour of Aluminium Extrusions Subjected to Axial Loading",
Østen Jensen, 2005:7, ISBN 82-471-6872-3 (elektr. utg.), ISBN 82-471-6873-1 (trykt utg.), ISSN 1503-8181.

"Thermal Aspects of Corrosion of Steel in Concrete",
Jan-Magnus Østvik, 2005:5, ISBN 82-471-6869-3 (trykt utg.) ISBN 82-471-6868 (elektr.utg), ISSN 1503-8181.

"Mechanical and Adaptive Behaviour of Bone in Relation to Hip Replacement. A Study of Bone Remodelling and Bone Grafting",
Sébastien Muller, 2005:34, ISBN 82-471-6933-9 (trykt utg.) (ISBN 82-471-6932-0 (elektr.utg), ISSN 1503-8181.

"Analysis of Geometrical Nonlinearities with Applications to Timber Structures",
Lars Wollebæk, 2005:74, ISBN 82-471-7050-5 (trykt utg.), ISBN 82-471-7019-1 (elektr. Utg.), ISSN 1503-8181.

"Pedestrian Induced Lateral Vibrations of Slender Footbridges",
Anders Rönnquist, 2005:102, ISBN 82-471-7082-5 (trykt utg.), ISBN 82-471-7081-7 (elektr.utg.), ISSN 1503-8181.

"Initial Strength Development of Fly Ash and Limestone Blended Cements at Various Temperatures Predicted by Ultrasonic Pulse Velocity",
Tom Ivar Fredvik, 2005:112, ISBN 82-471-7105-8 (trykt utg.), ISBN 82-471-7103-1 (elektr.utg.), ISSN 1503-8181.

"Behaviour and Modelling of Thin-Walled Cast Components",
Cato Dørum, 2005:128, ISBN 82-471-7140-6 (trykt utg.), ISBN 82-471-7139-2 (elektr. utg.), ISSN 1503-8181.

"Behaviour and Modelling of Selfpiercing Riveted Connections",
Raffaele Porcaro, 2005:165, ISBN 82-471-7219-4 (trykt utg.), ISBN 82-471-7218-6 (elektr.utg.), ISSN 1503-8181.

“Behaviour and Modelling of Aluminium Plates Subjected to Compressive Load”,
Lars Rønning, 2005:154, ISBN 82-471-7169-1 (trykt utg.), ISBN 82-471-7195-3 (elektr.utg.), ISSN 1503-8181.